Alma Mater Studiorum – Università di Bologna

DOTTORATO DI RICERCA

Disegno e metodi dell'ingegneria industriale

Ciclo XX

ING-IND/15

DESIGN AND DEVELOPMENT OF NEW PRESSURE SENSORS FOR AERODYNAMIC APPLICATIONS

Presentata da: Dott. Ing. Alessandro Rossetti

Coordinatore Dottorato   **Relatore**

Prof. Ing. Franco Persiani   Prof. Ing. Alessandro Talamelli

Esame finale - Maggio 2008

Keywords

Capacitive pressure sensors
Fluidynamic
FEM
Air data system

Sail
Aerodynamic
FEM
Wireless network

Contents

Preface

This thesis reports on two different projects that were carried out during the three years of Doctor of the Philosophy course.

In the first years a project regarding **Capacitive Pressure Sensors Array for Aerodynamic Applications** was developed in the Applied Aerodynamic research team of the Second Faculty of Engineering, University of Bologna, Forlì, Italy, and in collaboration with the ARCES laboratories of the same university. Capacitive pressure sensors were designed and fabricated, investigating theoretically and experimentally the sensor's mechanical and electrical behaviours by means of finite elements method simulations and by means of wind tunnel tests. During the design phase, the sensor figures of merit are considered and evaluated for specific aerodynamic applications. The aim of this work is the production of low cost MEMS-alternative devices suitable for a sensor network to be implemented in air data system.

The last two year was dedicated to a project regarding **Wireless Pressure Sensor Network for Nautical Applications**. Aim of the developed sensor network is to sense the weak pressure field acting on the sail plan of a full batten sail by means of instrumented battens, providing a real time differential pressure map over the entire sail surface. The wireless sensor network and the sensing unit were designed, fabricated and tested in the faculty laboratories. A static non-linear coupled mechanical-electrostatic simulation, has been developed to predict the pressure versus capacitance static characteristic suitable for the transduction process and to tune the geometry of the transducer to reach the required resolution, sensitivity and time response in the appropriate full scale pressure input A time dependent viscoelastic error model has been inferred and developed by means of experimental data in order to model, predict and reduce the inaccuracy bound due to the viscolelastic phenomena affecting the Mylar® polyester film used for the sensor diaphragm. The development of the two above mentioned subjects are strictly related but presently separately in this artwork.

Capacitive Pressure Sensors Array for Aerodynamic Applications

© Alessandro Rossetti

Introduction

Whenever aerodynamic characteristic of bodies immerged in a flow field are required the wider diffuse experimental procedure employed, is the measurements of the aerodynamic force components, by means of dynamometric balance, in wind tunnels. Nevertheless the aerodynamic force and the components in which it usually expressed, such as lift and drag in the aeronautical field, or drive and lateral force in yacht sail applications, are strictly related to shear stresses and normal stresses. The measurement of shear stress can be very challenging because it is a parameter of small magnitude, while static pressure is commonly sensed by means of static ports drilled in the body surface and connected by means of a series of small tubes to various kind of transducers. Thus in spite of the complications involved in the set up procedure required to performed such action, pressure measurements are of great importance in fluidynamic and in many fields of engineering and industrial applications. Moreover the constant progress in fluid dynamics numerical codes and the ever increasing computational power of modern computers has not diminished the need for detailed space and time resolved measurements, both to provide boundary conditions and to validate the results. This emphasises the importance of precise measurement instruments. Despite the large amount of literature on the subject, whenever sensors are used in the real operative environment to monitor pressures on large domains and in highly unsteady flows, there are still problems in using classical techniques due, for instance, to the cost of each single transducer, their intrusiveness or their time response. A common specification in most of the above applications is related to the large size of the surfaces that has to be monitored, leading to the use of a large number of robust and conformable sensors in order to achieve the required spatial resolution. In this scenario, a real-time pressure distribution represents an important means for the analysis of the aerodynamic behaviour of the body and for its correct trim. The main characteristic of the developed pressure sensor strip are strictly connected to air data systems and to an alternative role and layout of probes in such systems. Air data systems consist of aerodynamic and thermodynamic sensors and associated electronics. The sensor measures characteristic of the air surrounding the vehicles and convert this information into electrical signal, by means of transducers, that are subsequently processed to derive flight parameters such as: true airspeed, mach number, free stream static pressure, pressure altitude, free stream outside temperature, air density, angle of attack and angle of sideslip. In modern aircrafts, data coming from on board sensors are of fundamental importance to provide information to the pilot, to implement Fly-by-Wire systems, and to achieve automatic flight control, indispensable in tele-controlled vehicles or in unmanned ones. Not differently from most conventional measurement practices developed in engineering, air data measurements have traditionally relied on the use of a few specialized, highly accurate, transducers seeking the most direct readout of the quantities of interest. The instrumentation is usually based on a few sensors such as pitot tubes, vanes, or multifunction devices integrating tube-slot type probes with self-aligning capabilities located at specific points of the aircraft body. Conventional air data system are developed around the sensing probe. Even if widely diffused and successfully used, this approach may suffer few drawbacks: different probe types may be needed for reading different physical quantities, leading to device proliferation; the high accuracy required on the individual probes may result in high costs, the probe technology or location requirements may make the installation intrusive; the probe placement may result critical with regard to perturbation and wake effects within the flight envelope, moreover the use of a small number of probes may affect availability and reliability, in conclusion conventional systems are all designed trying to minimize

the amount of required sensor data. The air data system application for which the sensor developed in this artwork has been developed is targeted to move the emphasis from the transducers to the signal processing, following the methods described in [1]. Rather than using few specialized probes, a redundantly large number of low cost transducers of the same type is exploited, in a framework where information processing enables the inference of many related quantities from a homogeneous set of raw measurements. Here, diversity among many raw pressure readings taken on the aircraft surface are used to decouple speed and flight attitude angles and aid accurate measurement. Thanks to the large number of probes that will be used, sensors can be designed favoring the reduction of cost and intrusivity over other merit factors such as measurement sensitivity and accuracy. The following sensor properties are therefore required: small dimensions to increase spatial accuracy; low environment-invasion-level; high rejection ratio to temperature, altitude and dampness; robustness and last but not least low cost. According to these considerations a capacitive differential pressure sensor strip has been design with low cost material such has polymide and polyester and assembled by means of micromechanical circuit board technology PCB [2], which represents a valid alternative to most sensitive and accurate pressure sensor based on Micro-Electrical-Mechanical-Systems (MEMS), technology [3], [4], [5]. PCB devices can be used other than connecting electronic components but also as a means for electro-mechanical transduction, being supported by materials such as polyimides and polyesters, which are now available in thin films of a few microns. These preliminary remarks give the motivation to investigate which characteristics of sensitivity, resolution and precision can be achieved by the proposed sensor. For these purpose the sensor has been design, constructed and finally tested to validate the capability of acquiring pressure data on a surface of a body immersed in an air flow. Sensors are based on the following principle: a fluid dynamic variable causes a mechanical stress that deforms a polyimide membrane, on which one electrode is placed. The electrode displacement generates an electrical capacitance variation, which is acquired and processed. Sensor figures of merit such as sensitivity, resolution, accuracy and drift are exploited during the design phase to achieve the optimum construction. As a first testing application, sensors have been used to obtain the pressure distribution along a two dimensional wing airfoil placed inside the wind tunnel.

4

Chapter 1

Air data system literature review

An air data system consist of aerodynamic and thermodynamic sensors and associated electronics. The sensor measures characteristic of the air surrounding the vehicles and convert this information into electrical signal, by means of transducers, that are subsequently processed to derive flight parameters. Typical flight parameters calculated by air vehicles include calibrated airspeed , true airspeed, mach number, free stream static pressure, pressure altitude, baro-corrected altitude, free stream outside temperature, air density, angle of attack and angle of sideslip. These information are used for flight displays for autopilots, for weapon system fire control computations and for the control of cabin air pressurization system. Air data system are an outgrowth of the first pneumatically driven instruments such as air speed indicator and altimeter used in early aviation. These kind of instruments performed computations by means of non linear spring mechanism incorporated into specially designed bellows, which expanded and contracted in response to changes in sensed pressures, thereby moving the dials of the flight instruments. Subsequently analog computers where interposed between the pressure sensor and the flight instruments, and servo-driven cams or nonlinear potentiometers computed parameters such as altitude, airspeed, and mach number. The evolution of microprocessor technology shifted all the computations and data management to digital based processing and tends to obsolete the air-data computer as a separate entity. In fact new avionics architectures are incorporating aid data function into other subsystems such as inertial/GPS navigations units or are packaging the air data transducers into flight control computers. As far as air data functions are packaged, they provide flight critical information and therefore are implemented with appropriate redundancy and automated fault detection and isolation.

1.1 Conventional Intrusive Probes

All of the air data parameters that are relevant to flight performance are derived by sensing h pressure , temperatures, and flow direction surroundings the vehicles. Free stream pressure and temperatures are required for the computations of static air temperature, altitude, airspeed, and Mach number. Because air is moving past the aircraft, the pressure at various places on the aircraft's skin may be slightly higher or lower than the free stream. Conventional probes are devoted to sense static pressure by means of static ports probes, total pressure via the pitot tube, total temperature via the temperature probe, and local flow direction via the angle of attack and sideslip vanes. All of these sensing elements except for the flush mounted static port, are intrusive because they disturb the local airflow. In flight testing of new aircraft, integrated air data booms are often used to mount combinations of these probes forward of the flow which normally contacts the aircraft skin. The angle of attack and angle of sideslip vanes are self aligning, they measure the direction of local flow. Total pressure must be measured at the front opening on the pitot tube which extend directly into the airflow, but at an angle with respect to the relative wind. That angle defined by the sideslip angle does not produces any significant inaccuracies as long as it doesn't exceed +/- 10 degrees. In applications where the angle of attack and sideslip are large, then specials booms

5

containing a gimballed pitot tube can be used, such tubes contain wind vanes or may be servo driven to align the relative wind.

1.2 Static and total pressure measurements

Static pressure is the absolute pressure of the still air surrounding the aircraft. To obtain a sample of static air in a moving aircraft static port or series of holes are drilled in a plate on the side of the fuselage or on the side of the pitot tube probe which extend into the tree air stream. These sensed static pressures will differ from the free-stream values. That difference is referred to as the static defect. The location of static ports is selected by wind-tunnel tests and by tests at numerous locations on actual aircraft. The location of a static port on helicopters or on fixed wing aircraft that operate at very high angles of attack is especially difficult because of unusual local flow phenomena. Even with an optimum static source location, a large static defect usually remains, which is a function of Mach number. angle of attack: and aircraft configuration such as flap deployment, wing stores, etc. Because static defect is predictable, it can be corrected in the air-data computations. Techniques for correcting such errors can be employed As far as the sensing of total pressure in concerned this is sensed by means of a pitot tube such device is electrically heated to prevent ice formation. Pipes in the aircraft, referred to as the pneumatic plumbing carry the sensed pressure to transducers associated with the air-data computations and also to direct-reading airspeed indicators. Since the 1970 large aircraft carry direct reading, pneumatic instruments at the crew stations to backup the computer-driven instruments. In subsonic flight, a pitot tube's recovery of total pressure is reasonably accurate for typical variations in angle of attack and Mach number; hence, compensations to correct static defect are generally not required. At supersonic speeds, the pressure sensed within the tube is ideally the pressure that develops behind a normal shock wave. Design and calibration of the pitot tube orifice to achieve the desired shock wave is difficult, so measurement errors in total pressure are higher at supersonic speeds and must be compensated. Total pressure is used to compute calibrated airspeed V, and Mach number M.
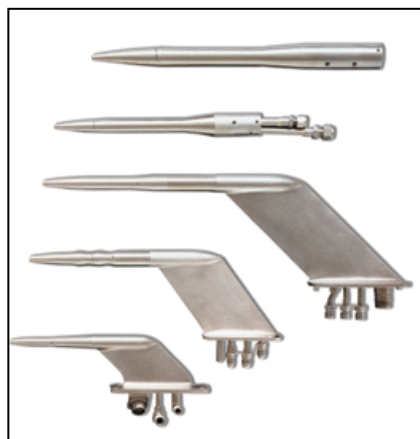
Figure 1.1 : Different kind of aircraft pitot tubes

1.3 Air temperature measurements

Outside air temperature referred to as static air temperature Ts, and sometimes OAT, is required for the computation of true airspeed. It is also used in the computation of air density, which is required for some types of fire-control aiming solutions aiming solutions. The temperature measured by a thermometer on the exterior of an moving aircraft is higher than the free-stream air temperature

6

because of frictional heating and compression of the air impinging on the thermometer Temperature probe, is typically installed to point along the local streamline and compresses the impacting air to zero speed. thus causing a total or stagnation temperature to exist at the thermometer. To avoid time lags in the temperature measurement a leakage hole at the near of the probe allows for a rapid air change. Probes may be mounted on the wing tips. Vertical tails, forward fuselage, or other locations where the local Mach number is the same as the free stream Mach for all expected flight attitudes and speeds. A recovery factor accounts for frictional heating, re-radiation, and non isentropic compression of the air. The recovery factor is measured empirically, and when independent of Mach number and angle of attack, it does not contribute to any errors in the computation of static air temperature. Temperature probes are available with recovery factor values ranging from about 0.7 to greater than 0.99. The thermometers is usually a small coil of wire whose resistance varies with temperature. The resistance variation is detected in a bridge circuit, whose excitations and signal processing are located in a signal-conditioning box or the computer. Moisture, water ingestion, and icing are significant error sources that are reduced by a variety designed techniques, including heaters.

1.4 Angle of attack and sideslip

Angle of attack is the angle, in the normally vertical plane of symmetry of the aircraft. at which the relative wind meets an arbitrary longitudinal datum line or the fuselage. The pivoted vane, illustrated in Fig.1.2 measures local flow angle and is the most commonly used method of measuring the angle of attack and sideslip they are often part of an independent stall warning or stall control system. Maximum angle of attack boundaries define the aircraft's low-speed flight envelope. Since such systems are flight critical redundant sensors are usually installed. Engine inlet controls also uses incidence measurements that tend to be safe-critical in supersonic flight. In normal operation, sideslip is approximated by a body mounted lateral accelerometer positioned and displayed on the pilot's ball bank indicator. Automatic flight control systems compute sideslip from inertial measurements and include sideslip control as part of their lateral-directional control loops. With fast computers, angle of attack and sideslip can be estimated from the aircraft force and moment equations and the more commonly available inertial and airspeed measurements. Analytically derived angle of attach may supplement a vane sensor for redundancy.
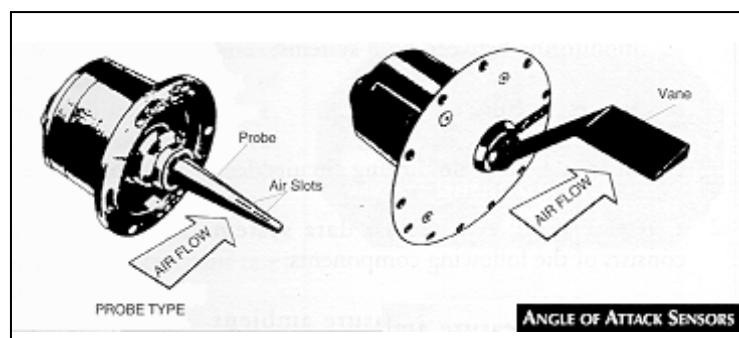
Figure 1.2 : Pivoted vanes

7

1.5 Air data computers

A typical central air-data computer (CADC) is a box containing : the pressure Transducers, associated excitation circuitry, and signal-conditioning circuitry the computer; and the output drivers that are compatible with interfacing subsystems. The box containing these elements includes fittings that allow the pitot and static pressure lines to connect to the computer's internal pressure transducers. Its inputs are the pitot and static pressure tubes, a temperature probe signal (for the bridge circuit), a barometric setting. The air-data equations are solved in the processor subassembly, which contains the CPU, data storage memory. The air data software includes a considerable number of built-in test and monitoring algorithms for establishing the validity of all sensor inputs and processing. Thus the inputs provided by the air data system conventional probes (asymptotic static and total pressure, static temperature, local angle of incidence and sideslip are feed in the CADC which computes fundamental flight parameters: pressure altitude, true air speed, Mach number, air density, incidence and sideslip angle. As microprocessors became smaller and cheaper, it became possible to package them with probes and transducers. The result is a distributed air-data system that replaces the CADC. A key feature is the packaging of signal-processing functions with or adjacent to the probes. Mechanization of such systems may be with smart probes whose integral electronics provide the probe and transducer calibrations. plus the digital interface, Fig. 66 illustrates this concept with a dual-redundant probes and vanes. Such an architecture provides corrected pressure, temperature. and angle-of-attack data to a flight control computer that computes altitude, Mach, calibrated, and true airspeed. It can also compute other standard air-data parameters and transmit them to flight management computers, or other subsystem. A major advantage of distributed architecture is the eliminations of pneumatic plumbing to the CADE boxes. Reliability and maintenance problems, including water drains, are eliminated. Electrical wiring weighs less than tubing and the electrical transmission of pressure information eliminates lags associated with long lengths of tubing. As example the Boeing 777 has a partly distributed air-data architecture. Miniature air data processing modules are located in the vicinity of the probe on the aircraft structure. The modules contain transducers and signal-processing circuitry. They compensate the transducers, control probe heaters, and interface with the aircraft's data bus. A module's output transmits to the aircraft's integrated inertial-air-data unit by means of a data bus.

1.6 Special design

Helicopter air-data systems differ from their fixed-wing counterparts primarily in the implementation of airspeed measurements at low speeds, including the inference of winds while the aircraft is hovering. The conventional pitot tube and pressure transducers become ineffective as air speed drops below about 40 knots. Static-source errors in helicopters tend to be difficult to compensate because of rotor downwash that differs significantly in and out of ground effect. Fixed- wing aircraft do not compensate their static source errors in ground effect (during landing and take off) and neither do helicopters. In the mid-1970, the U.S. Army flight tested many devices that were designated to measure low airspeed omnidirectionally [18 19 20], [1 14 15 16 17 45] of them the rotating anemometer, the vortex counter, and the down wash detector are the most employed.

1.6.1 Rotating anemometer

This device measures the magnitude of the pressure change caused by a change in airspeed when the aircraft airspeed is near zero. Such systems are called low omnidirectional system. A variation

8

of this concept embeds airflow sensors and associated pressure transducers within the rotor blade. Blade-mounted sensors have been tested experimentally, and they have been considered for the United States Army's Comanche helicopter and; Russian attack helicopters. In Fig 1.3 is shown a schematic representation of a rotating anemometer where two total port are present. The total pressure difference sensed by the two ports is proportional to the port speed induced by the rotor angular speed, and therefore amplificated over what would be seen by a conventional pitot tube.
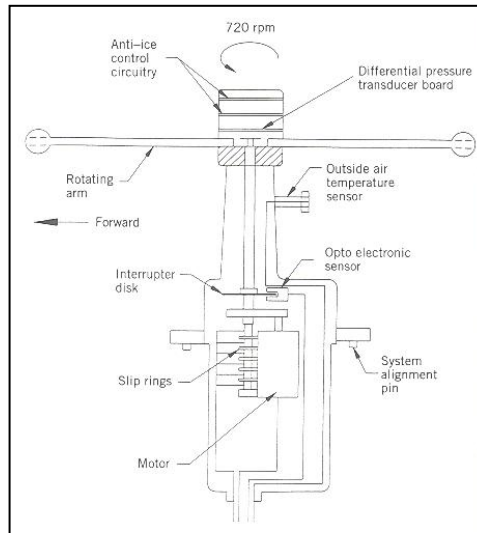
Figure 1.3 : Rotating anemometer, [22]

At large bank angles. The computed velocity is no longer accurate, and the solution is ignored, In level flight the component of the velocity computed , are used to estimate the wind vector which is important in fire control equations.

1.6.2 Vortex Sensing

The sensor measures vortices shed by fluid flow over a deliberately-inserted obstruction. The frequency of vortices is proportional to the air speed. This method has been used to measure low airspeed in helicopters and in ground vehicles control systems. A similar version was used on models of the AH-64D aircraft. The theory of the vortex sensor dates back to Von Karman studies. The frequency of vortex formations from each side of the obstruction is given by Eq. 1.1

$$f = S(\frac{V}{d})$$
(1.1)

Where f id the Strouhal number, V the air velocity and d the width of the obstruction. The value of f has been experimentally determined for a variety of obstructions widths and fluid properties. The sensitivity of this device is about 1 knots. One method of measuring vortex frequency direct an ultrasonic beam through the vortex trail The rotational velocity of the vortices combine vectorially with the sonic ray velocity, causing the sonic rays to be deflected. This causes an amplitude modulation of the received energy at the vortex frequency. To measure the horizontal velocity vector, an orthogonal sensor is required. As in all helicopters, the airspeed sensors should be mounted above the rotor for minimum downwash effects.

9

1.6.3 The swelling pitot tube below rotor

The swelling pitot tube was developed in united Kingdom: it is currently in use on the AH-1S and AH64D, and other attack helicopters. It was tested extensively by the United States Army in the 1970s. A gimballed pitot tube contains a vane arrangement that causes the tube to align with the airflow within the downwash field emanating from the rotor blades. Changes in the airflow field vector are correlated with changes in true airspeed. With appropriate angular pick-offs to measure vane orientation, the true airspeed is estimated using a calibration associated with each aircraft and its rotor system. In Fig. 1.4 the induced flow velocity. The velocity vector V, is normal to the rotor tip path plane, Vi sin(i) is proportional to the thrust component that overcomes aircraft drag and causes a forward velocity. The vector diagram is expressed by :

$$V_i \sin(i) + V_H = V \cos \alpha \tag{1.2}$$

A swiveling probe aligns with the resultant flow velocity V, sensing both its Magnitude and angle of attack and sideslip .
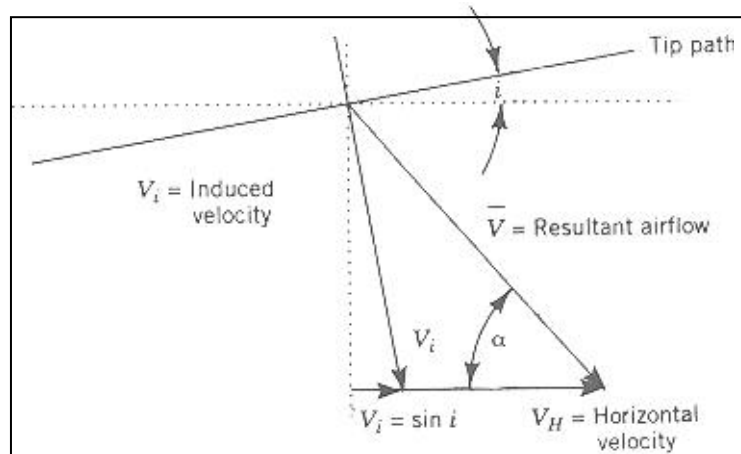
Figure 1.4 : Flow field vector for swivelling probe

The principle of the probe is that Vi sin(i) is a repeatable function of horizontal airspeed, irrespective of thrust, weight, vertical speed sideslip angle, center of gravity, but varies only with ground proximity. Hence, a radar altimeter measurement is required to accommodate the ground effect. The basic sensing equations are

$$V \cos \alpha = f(V_H)$$

$$V_x = V_H \cos \beta \tag{1.3}$$

$$V_y = V_H \sin \beta$$

where β is the yaw angle also measured by the swiveling probe. Placing a pitot tube in the downwash flow held avoids the need to measure the low pressure existing near hover since the minimum downwash airflow V_i will always be greater than about 15 knots. Also, aligning the pitot lube with the airflow eliminates alignment errors in both the pitot and static pressures. In Fig. 1.5 is shown a view of the swiveling probe.
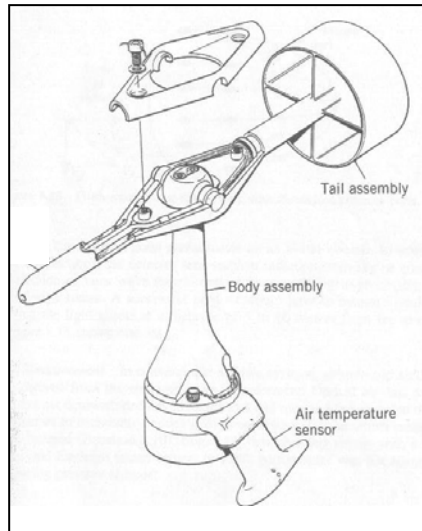
Figure 1.5 : Air speed and direction sensor, swivelling probe,[22]

1.7 Optical Air data system

1.7.1 Laser velocimetry

Non intrusive optical methods of flow visualization have been part of wind tunnel test instrumentation Since the l970s, optical techniques have also emerged as viable air-data systems. motivated by radar observability penalty of intrusive probes and by the unsuitability of intrusive probes for hypersonic flight, Optical sensors are usually located within the vehicles and look out through the local flow into the tree stream. Laser velocimetry that measure the Doppler shift from backscatter of naturally occurring aerosol particles have been tested on aircraft since the l970s in experiments related to the detection of clear air turbulence. During l980s and early l980s several laser velocimeters were marketed to calibrate intrusive air-data systems; Nasa has experimented with them for hypersonic applications. In most applications, three orthogonal sensors are used in which the laser beam is split into three components beams. Each is focused at certain distance from the aircraft's skin to be in undisturbed flow (typically several meters away). Lens are used to converge the beam, with optimum polarization and geometric characteristic for maximizing backscattered response.
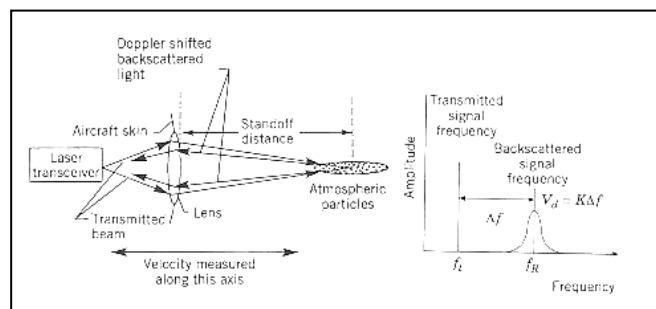
Figure 1.6: Laser Doppler velocimetry

The reflected or "backscattered" signal is Doppler shifted from the transmitted frequency by an amount proportional to the relative velocity between the aircraft and the undisturbed atmosphere.

11

Backscattered signals are mixed with the transmitted signals using interferometers. Test results show accuracy of one knot or better at altitudes where particle (aerosol) density is adequate. Aerosol densities and particle sizes vary with altitude, time, and volcanic eruption. Testing has shown that there is adequate aerosol density up to about 10000 meters Blending the inertial velocity vector with an optically derived true airspeed vector allows operation at higher altitudes. In 1996, laser velocimeters met the civil and military eye-safety standards, although there may be some question regarding the intensity of the focused region, The trend is toward improved signal processing and low-power laser beams.

1.7.2 Particle Time of Flight Method

Another laser-based airspeed-measurement technique estimates the time of flight required for aerosol particles to traverses the distance between two laser beams, in Fig. 1.7. Two sheets of laser light separated by a distance of a few centimetres, are transmitted through a window in the aircraft's skin. The light sheets are in the YZ-plane, so they measure the velocity component Vx. Airborne particles generate signals in each of the two detectors that can be timed or correlated; hence true airspeed can be determined.
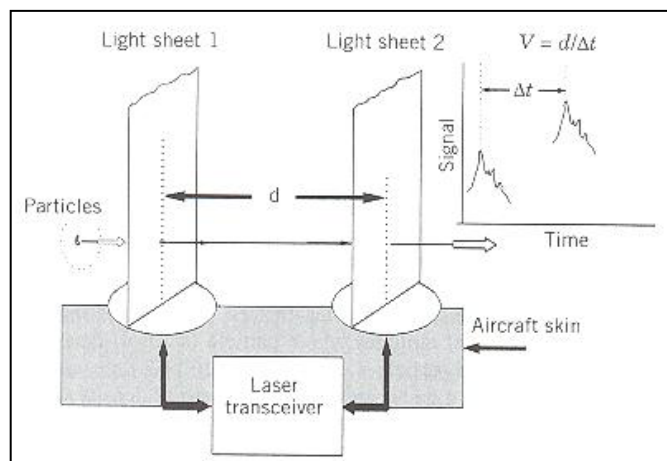
Figure 1.7: Particle time of flight method of measuring airspeed, [22]

In addition to particle reflections, the detector sees ambient radiation from sky or ground. Thus selection of laser wave length, optical filters, and signal-processing are difficult design issues. A successful product would have to measure particles penetrating the light sheets at a distance of 5 to 10 meters from the aircraft skin.

1.8 Hi angle of attack flush air data system

At high-angles of attack it is difficult to accurately measure air data using traditional sensing devices such as nose booms. Moreover a nose boom installation would alter the basic flow characteristics of the aircraft nose. S.A. Withmore [21], developed a non intrusive high angle of attack flush air data sensing system was installed and flight tested on the F-18 High Alpha Research Vehicle at the NASA Dryden Flight Research Facility. As shown in Fig. 1.8 This system consists of a matrix of 25 pressure orifices arranged in concentric circles on the nose of the vehicle to determine angles of attack and sideslip, Mach number, and pressure altitude.
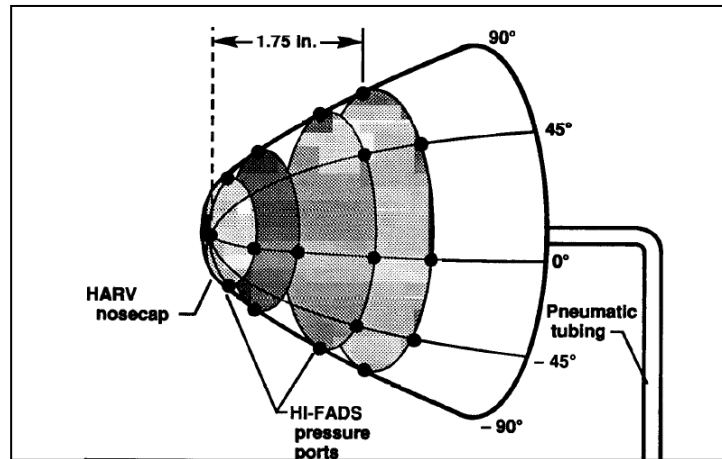
Figure 1.8: Fibreglass reinforced plastic nose cap with pressure orifice. [20]

The configuration of the nose has a simple hardware arrangement with the basic fixture being a small fibreglass reinforced plastic nose cap. A set of 25 0.06-in. diameter pressure orifices, arranged in annular rings, was drilled in the nose cap. Flight tests were conducted using a 25-port arrangement with ports arranged in 4 rings and a single nose tip port. The rings were distributed in a symmetric radial pattern about the nose cap axis of symmetry. Analyses were performed using all 25 orifices and a subset of 9 orifices. The high-angle-of-attack flush air data sensing system was calibrated and demonstrated using reference air-data generated by way of minimum variance estimation techniques which blended air data measurements from two wingtip air data booms with inertial velocities, aircraft angular rates and attitudes, precision radar tracking, and meteorological analyses. Although analyses were not performed onboard in real-time, the High Alpha Research Vehicle high-angle-of attack flush air data sensing system and resulting air data algorithms were validated as being real-time capable using flight data in ground based simulations. The sensing system was shown to give excellent results. Empirical verification was performed over a large portion of the High Alpha Research Vehicle flight envelope with a Mach number range from 0.15 to 1.20 and an angle-of-attack range from -8.0 to 55.0°. Angle of sideslip excursions covered the range from - 15.0 to 15.0°.

Chapter 2

A Pressure Sensor for aerospace applications

The Aeronautical pressure sensor reported in the following section has been developed in strict collaboration with other colleagues and in particular the project has been led off by Dott. M. Zagnoni, from the Phd thesis of whom [23], many results are reported for completeness, the project has then carried on by the author and the results are added on in the following chapters. The sensor is a conformable thin film strip, designed for aerodynamic applications and is basically a capacitive differential pressure transducer, built in PCB technology, aimed at monitoring the pressure profile on an aerodynamic body. During last few years, printed circuit board (PCB) technology has greatly improved, achieving the photolithographic resolutions of silicon planar technology in the earlier 1970s; this allows the design of low cost precision transducers and, for instance, being able to satisfy most of the specifications required in fluid dynamics. The pressure field in which the proposed sensor is able to operate ranges in ±2000Pa with a resolution of units of Pa. The sensors must be suitable for conforming to the profile surface and must be characterised by a total thickness that will not alter the fluid flow condition. This requirement is satisfied if the sensor is comprised within the boundary layer of the profile. Moreover, accidental impacts with particles at high velocity in the fluid must not damage the sensor. Capacitive sensing has been chosen because of distinct advantages when compared to other, such as higher sensitivity, lower power consumption and better temperature performance. Moreover, the use of PCB technology has advantages over other approaches: it naturally allows the hosting of electronic sensing and signal processing components by means of smart packaging, such as the chip on board (COB) technology. Last but not least the differential pressure sensor approach has been preferred to absolute pressure sensors for overcoming altitude problems due to barometric pressure gradients.

2.1 Sensor working principle

The pressure sensor system presented is meant to produce an electric output related to the pressure distribution that is applied to the sensor strip surface. The fluid dynamic variables act on the deformable part of the sensors, where an electrode is placed, which, changing its geometry, leads to an electrical capacitance variation. The latter can be electronically read in order to collect a set of surface pressure points, through a multiplexed switch capacitor sensing scheme. A diagram of the system is reported schematically in Fig. 2.1.

14
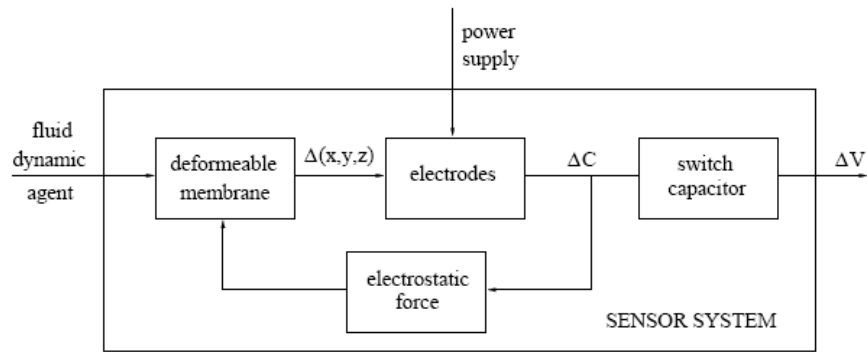
Figure 2.1: Electro-mechanical system measurement diagram.

The sensitive unit consists of a three layer structure in a stack Fig. 2.2: Base, Spacer and Conductive Membrane. The Base layer is a rigid copper-clad glass-fibre composite layer. This layer hosts as many pads as pressure measurement points. Pads represent the lower plate of every capacitor. A guard ring is designed between the pad and the routes, for reducing coupling effects between different capacitors. Finally, VIAs (particular D) enable the addressing of every pad through the connection to a flat cable. The Spacer layer is a rigid glass-fibre copper-clad composite layer which is glued both to the top of the base layer and to the bottom of the membrane layer, forming the cavity within the diaphragm is deflected by the pressure input.
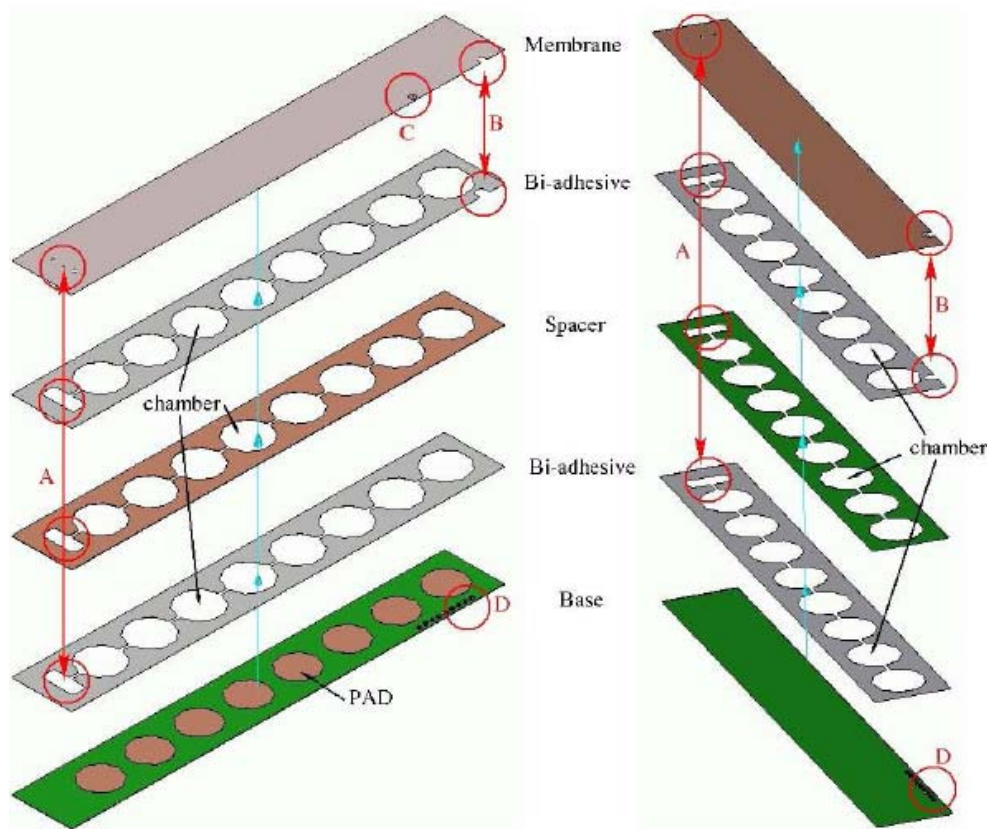
Figure 2.2: Pressure sensor strip structure: exploded top view (left side), exploded bottom view (right side). Membrane, spacer and base are connected by means of bi-adhesive layers. A: small chamber for allowing the pressure reference to flow in the spacer chamber. B: spacer guard ring electrical connection. C: membrane electrical connection. D: base electrical connections.

15

All unity chambers are connected by miniaturised pipes, patterned in the spacing layers, in order to share the same internal pressure, forming a unique bigger chamber. The copper layer acts as a guard ring for reducing the coupling effects between the upper electrode on the membrane and the routes on the base. The Membrane layer is a 25 µm thick deformable copper-clad (17 µm) Kapton®
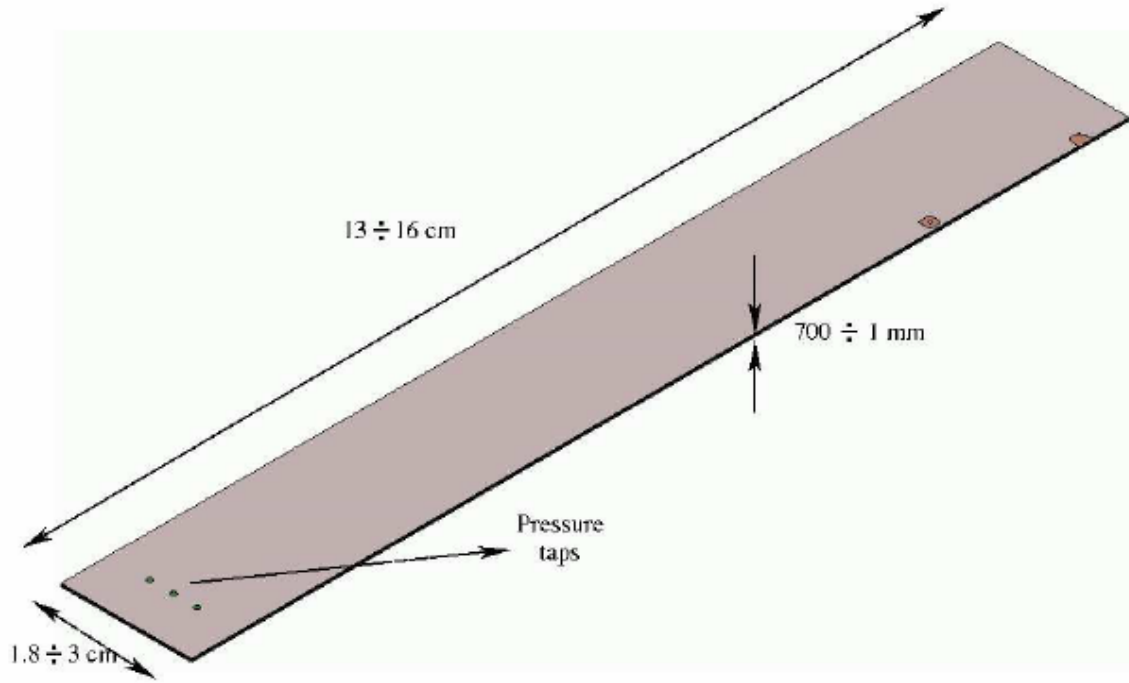
Figure 2.3: Pressure sensor strip structure: assembled view and dimensions.

polyimide composite layer. Small holes (particular A) are drilled on the proximity of one the ends of the sensor, before the first sensing element and act as a pressure reference. A VIA (particular C) is designed for the connection of the upper electrode, through the same flat cable used for connecting the base. Layers are attached to each other by means of some 50 µm thick bi-adhesive tape, patterned in the same shape as the spacing layer. As shown in particular A of Fig. 2.2, a small chamber is drilled for allowing the pressure reference to be shared in every sensing element chambers. Particular B and C show how the spacer guard ring and the membrane can be electrically connected. The device length and width can be set according to the application: the measurements and simulations reported here in this work are related to devices that are from 13 to 16 cm long and from 1.8 to 3 cm wide. The total thickness is comprised within 700 µm and 1 mm, as shown in Fig. 2.3. As illustrated in Fig. 2.4, the membrane at each point of sensing deforms itself downward or upward with respect to the static pressure reference taken by means of the holes. Since the membrane area is usually much smaller than the aerodynamic surface to be monitored, the corresponding pressure distribution over the deformable film can be considered constant with a good approximation, however the importance of the surface occupation of every sensing element in terms of spatial resolution becomes evident. Fig. 2.5 shows a possible application in which sensors can be employed. Depending upon the angle of attack α and upon the free stream velocity V, the

16
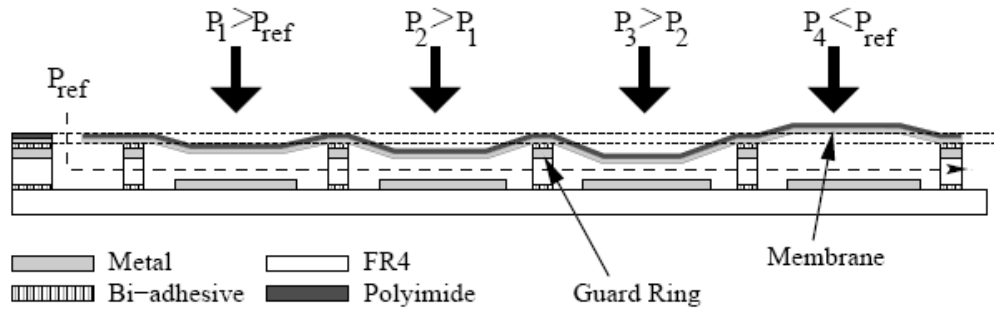
Figure 2.4: Differential pressure sensor strip principle of operation. Membranes deflect upward or downward with respect to the gradient of pressure between the outside and inside of the chamber.
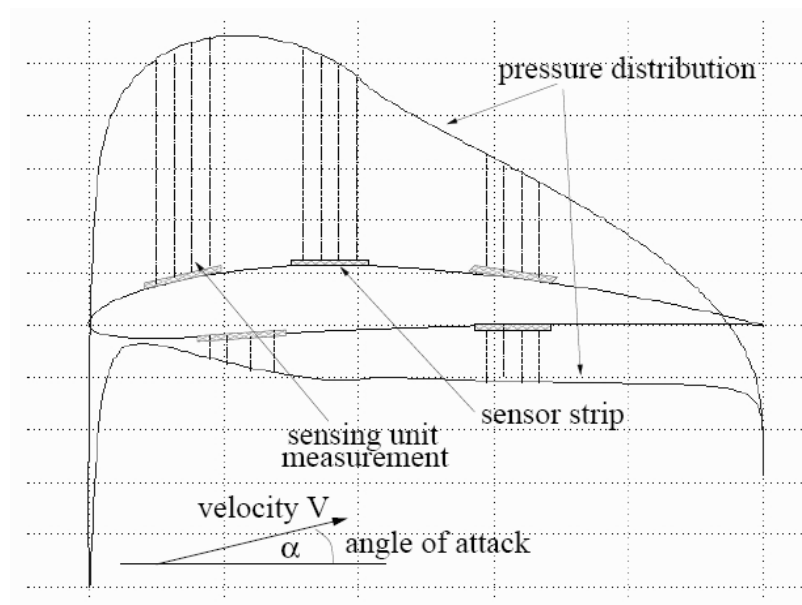
Figure 2.5: Application example: monitoring pressure distribution over a wing profile. The pressure distribution over the profile depends on free stream velocity V and angle of attack α: a variation in the (α, V) field leads to a different pressure pattern.

2.2 Analytical sensor model

In order to obtain an accurate sensor design approach, a better understanding of every step of transduction, from the physical point of view, is required for modelling the sensor and for identifying the parameters. As a general remark, a cylindrical structure is chosen for the sensing element, as shown in Fig. 2.2. Such geometry considerably simplifies the model description, since a three dimensional axial symmetric configuration can be easily expressed in two dimensions, allowing much simpler equations to be considered both for the mechanical and the electric model representation. In the following paragraphs three aspects will be take into account and described in order to depict the model: the mechanical deflection behaviour of the membrane, the viscoelastic behaviour of the polyimide and the final relationship existing between the pressure and the capacitance variation.

17

2.2.1 Large deflection

To be able to describe the mechanical behaviour of the diaphragm whenever small mechanical perturbations are applied, classical mechanical theory of deformation can be used, where a linear stress-strain relationship for matters (Hooke's law) describes the linear displacement of plates with respect to the exerted pressure. In the case of a circular diaphragm, the bending properties of the plate depend on its thickness as compared to the other dimensions. Three kinds of plates must then be considered: thin plates with small deflections, thin plates with large deflections and thick plates. Whenever large deflections are obtained, a specific theory has to be taken into account [23]. In fact, the increase of bending of a circular plate creates a strain in the middle plane that cannot be neglected in cases where the deflections are no longer negligible with respect to the plate thickness, but still small with respect to the other dimensions. The presence of the middle plane strain causes supplementary stresses with respect to the conventional elastic theory and it must be taken into consideration in deriving the differential equations. This geometrical effect causes non linearity between stress and deflection the more a plate is stressed, the less it deflect. Sensors membrane, because of its thickness, is supposed to be described by the large deflections theory for thin plates with a good approximation. Since the deflections surface, in such a case, is symmetrical with respect to the centre of the plate, the displacement of a point in the middle plane can be resolved in two components: a component u in radial direction and a component w perpendicular to the plane of a plate Fig. 2.6.a .
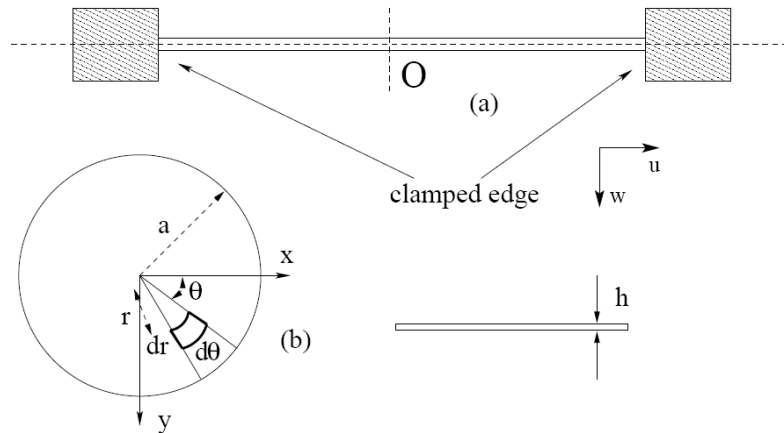
Figure 2.6: Thin plate two dimensional representation: a) displacement coordinates system (u,w); b) infinitesimal element of a plate of radius a and thickness h.

It can be demonstrated[1] that the strain in the radial direction is:

$$\varepsilon_r = \frac{du}{dr} + \frac{1}{2}\left(\frac{dw}{dr}\right)$$ (2.1)

while the strain in the tangential direction is:

$$\varepsilon_t = \frac{u}{r}$$ (2.2)

Considering the equations of equilibrium of an element of the plate Fig. 3.6.b and taking the projections along the axis, it derives that:

18

$$\frac{d^2u}{dr^2} = -\frac{1}{r}\frac{du}{dr} + \frac{u}{r^2} - \frac{1-v}{2r}\left(\frac{dw}{dr}\right)^2 - \frac{dw}{dr}\frac{d^2w}{dr^2} \tag{2.3}$$

$$\frac{d^3u}{d^33} = -\frac{1}{r}\frac{d^2w}{dr^2} + \frac{1}{r^2}\frac{dw}{dr} - \frac{12}{h^2}\frac{dw}{dr}\left[\frac{du}{dr} + v\frac{u}{r} + \frac{1}{2}\left(\frac{dw}{dr}\right)^2\right] \tag{2.4}$$

where v is the Poisson's ratio of the uniform material the plate is made of. Equations 3.3 and 3.4 can be integrated numerically by starting from the centre of the plate and advancing by small increments in the radial direction. A more useful relationship for an appropriate calculation of the deflections can be obtained by applying the energy method [23]. Considering the circular plate of radius a be clamped at the edge, as in Fig. 3.6, and be subject to a uniformly distributed pressure p. Assuming the shape of the deflected surface is represented by the same equation as in the case of small deflections:

$$w = w_0\left(1 - \frac{r^2}{a^2}\right)^2 \tag{2.5}$$

where r is the radius coordinate whose origin is set in the centre of the membrane and w0 the maximum deflection. The relationship of the displacement with respect to pressure is given by:

$$w_0 = \left(\frac{pa^4}{64D}\frac{1}{1 + 0.488\dfrac{w_0^2}{h^2}}\right) \tag{2.6}$$

$$D = \frac{Eh^3}{12(1-v^2)_0} \tag{2.7}$$

where, E is the modulus of elasticity, v is the Poisson's ratio and h is the plate thickness. Eq. 2.6 is typically used for w_0 greater than 0.5h and it shows how the rigidity of the plate increases with respect to the deflection, so that w0 is no longer proportional with respect to the pressure, as in the elastic theory where w_0 take the form in Eq. 2.8. In the case of very thin plates, where w_0 may become very large in comparison with h, a useful approximated relationship is given by the following formula [25]:

$$w_0 = \frac{pa^4}{64D} \tag{2.8}$$

$$w_0 = K_1 a\sqrt{\frac{pa}{Eh}} \tag{2.9}$$

where k_1 is an experimental constant that must be chosen dependent on the material and on the kind of anchorage in a range $0.5 - 1$. Eq. 2.9 is derived from the method proposed by A. Nadai [25], where the resistance of the plate to bending can be neglected and it can be treated as a flexible membrane, whose equations are:

$$\frac{d^2u}{dr^2} + \frac{1}{r}\frac{du}{dr} - \frac{u}{r^2} = -\frac{1-v}{2r}\left(\frac{dw}{dr}\right)^2 - \frac{dw}{dr}\frac{d^2w}{dr^2} \qquad (2.10)$$

$$0 = \frac{12}{h^2}\frac{dw}{dr}\left[\frac{du}{dr} + v\frac{u}{r} + \frac{1}{2}\left(\frac{dw}{dr}\right)^2\right] - \frac{1}{Dr}\int_0^r prdr \qquad (2.11)$$

The relationship 2.9 shows that the deflection changes as the cube root of the intensity p. For the tensile stresses at the centre of the membrane and at the boundary, the same solution gives respectively:

$$(\sigma_r)_{r=0} = K_2\sqrt[3]{\frac{Ep^2a^2}{h^2}} \qquad (2.12)$$

$$(\sigma_r)_{r=a} = K_3\sqrt[3]{\frac{Ep^2a^2}{h^2}} \qquad (2.13)$$

which show how even the relationship between the load, the stresses and the geometry parameters becomes highly non linear, k_2 and k_3 are experimental constant to be chosen between $0.3-0.5$. The above equations are useful tool for a rough estimation of the sensor behaviour. Nevertheless, the sensor membrane is formed by composite material that cannot be considered homogeneous. As reported in recent papers [26], novel formulae and analytical solutions can be extracted for describing sandwich structure stiffness. A sandwich structure consists of a lightweight core material sandwiched between one or two stiff facings, as the ones normally employed in PCB technology. Based upon the key assumption of iso-strains for the face and core material, the effective longitudinal elastic modulus can be obtained directly through the rule of mixtures, which yields:

$$E_s = E_F f_F + E_C f_C \qquad (2.14)$$

where E_S, E_F and E_C represent, respectively, the effective elastic modulus of the integrated sandwich composite, the face material, and the core material; f_F and f_C stand for the volume fractions of the face material and the core material, respectively. A similar expression can be written for the Poisson's ratio:

$$v_s = v_F f_F + v_C f_C \qquad (2.15)$$

where v_S, v_F and v_C are the effective Poisson's ratio of the integrated sandwich composite, the face material, and the core material respectively. Assuming to approximate the sensor membrane with an homogeneous material whose mechanical properties can be obtained by Eq. 2.15 and Eq. 2.16 and considering pressure values up to 2 kPa, membrane deflections can be derived by Eqs. 2.6 and 2.9 for a plate thickness of tens of μm. Using the above referred expressions, it turns out that circular shaped membranes, having radius of about 1 cm, can show deflections in the order of hundreds of microns in the given pressure ranges. Unfortunately, this theory is very satisfactory in the case of a homogeneous material, but not for composite laminates, where FEM non-linear algorithms need to be used to refine sensors design.

2.2.2 Creep

Any material subjected to an external load can be considered, in the range of small deformations at ambient temperature whenever the internal stresses don't exceed the yield and therefore can be treat as linear elastic solids. This assumption implies that the Hooke's law can be used and that there is no time-dependent relationship between stress and strain. When a material is subjects to tension exciding the yield point or to lower tension but at high temperature then the relationship between stress and strain strongly depends on the size of the applied load, on the temperature, and crucially on time. This effect is usually referred to as viscoelasticity [27]. Materials as metals or ceramic manifest viscoelastic phenomena at very high temperature and load while other materials as polymers or polyester are still concerned with this phenomena at ambient temperature and low stress levels. An important implication of viscoelastic behaviours is that the stress-strain characteristic cannot be rigorously considered a static (i.e. memory-less, though nonlinear) relationship, as depicted in Sec. 2.2.1. Conversely, the stress-strain characteristic exhibits behaviours that appear highly non linear, even for small deformations, and that, most importantly, depends on the derivatives of the stress and strain functions. This phenomenon is well evidenced by the analysis of two cases.
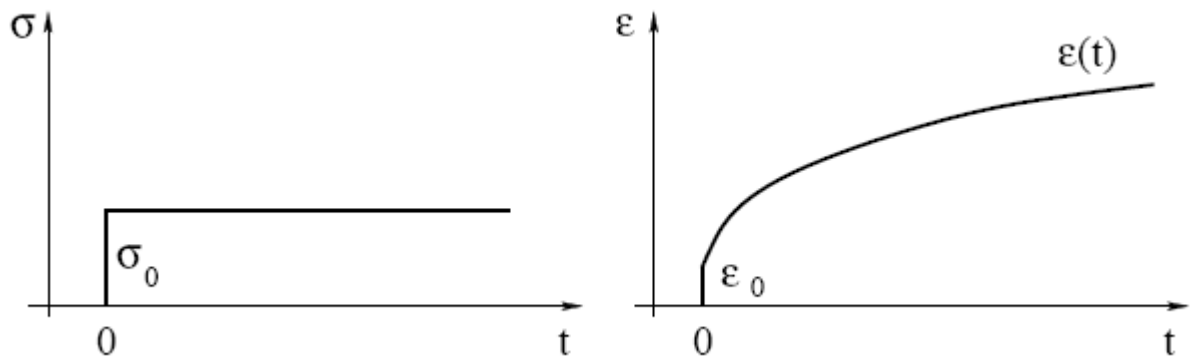
Figure 2.7: Response to an applied constant stress.

As shown in Fig. 2.7, if a stress function step is applied to a sample of material subject to creep, a sudden elastic strain is followed by a viscous and time dependent strain with an increasing trend. This phenomenon is referred as "compliancy" as is defined as:

$$D(t) = \frac{\varepsilon(t)}{\sigma_0} \tag{2.16}$$
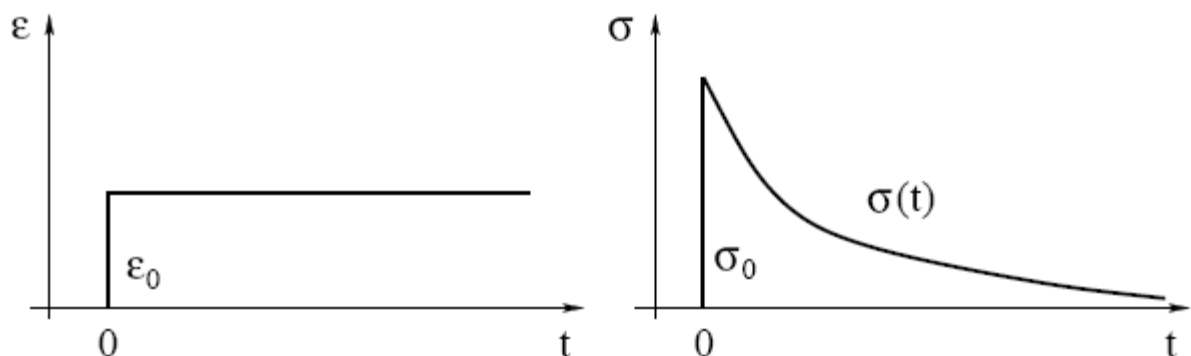
Figure 2.8: Response to an applied constant strain.

Conversely, if a strain step is applied, the stress decreases as a monotonic function (Fig. 2.8) and is commonly referred as "relaxation", defined as:

$$E(t) = \frac{\sigma(t)}{\varepsilon_0} \qquad (2.17)$$

This type of behaviour is usually present in polyimides at ambient temperature and for stress bigger than 1 MPa [28] and is conventionally known as creep, where the common trends followed by materials are shown in Fig. 2.9. In viscoelastic material the stress is a function of strain and time and so may be described by an equation of the form:

$$\sigma = f(\varepsilon, t) \qquad (2.18)$$

This is known as a non-linear viscoelasticity, but as it is not amenable to simple analysis it is frequently approximated by the following form:

$$\sigma = \varepsilon \cdot f(t) \qquad (2.19)$$

This response is the basis of linear viscoelasticity and simply indicates that for a fixed value of elapsed time the stress will be directly proportional to the strain.
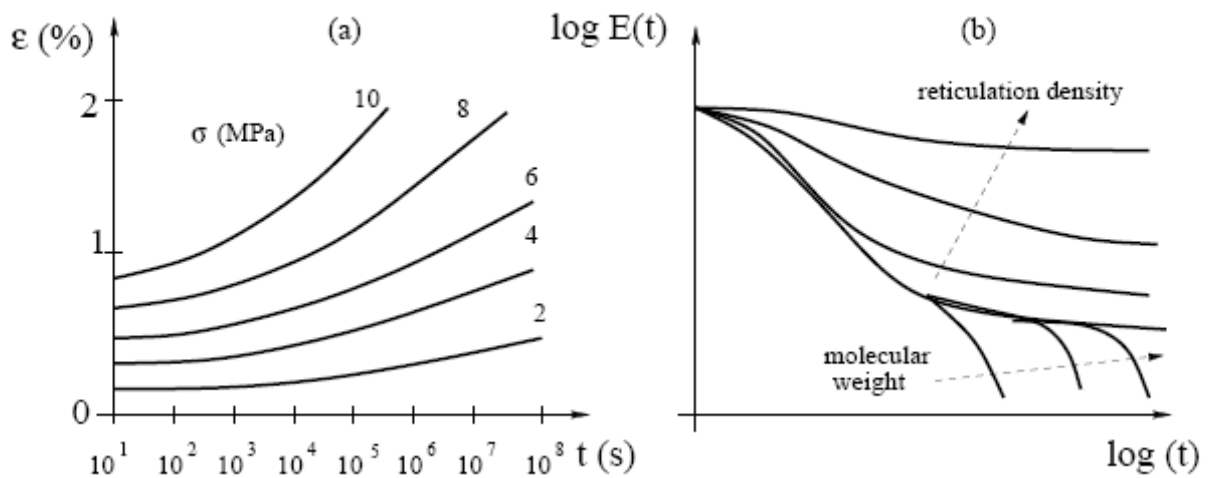
Figure 2.9: a) Creep deformation for different applied stresses. b) Qualitatively behaviour of the relaxation modulus as function of time and molecular structure.

However, this doesn't imply that the time function is linear. First of all, it can be observed that the mechanical deformation of a body subject to creep phenomena is a function of the entire loading history of the body itself. In other terms, thanks to viscoelasticity the system gains memory: all previous loading steps contribute to the final response, as shown in Fig. 2.10.
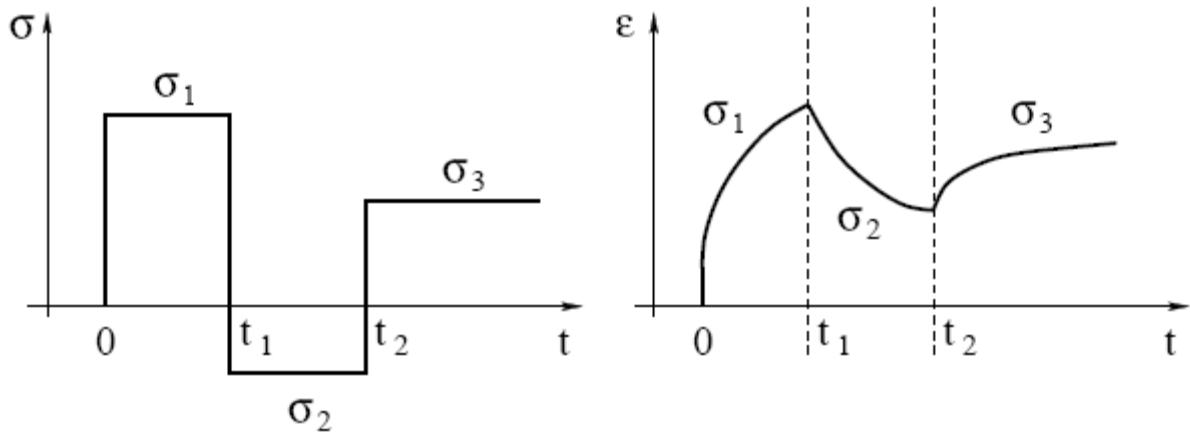
Figure 2.10: Presumed creep response when different stresses are applied

The Boltzmann superposition principle is a useful means of analysing the creep deformation resulting from several distinct loading or unloading steps of strain or stress [29]. Creep affects the proposed structure, causing membrane deflections of some µm, manifesting themselves in time-scales of tens of minutes. The above observation implies that in order to know the exact response of a structure subject to creep, a model of its excitation should be available, describing the evolution in time of input stress (or strain). This is normally not possible in fluid dynamic applications where the input loading and its dynamic is unknown. In this case, the best that can be achieved is a bound on the maximal deviation that creep may introduce with regard to static models such as those in Sec. 2.2.1. Such bound can be roughly interpreted as an uncertainty that should be taken into account when using the sensor as a measurement device in a dynamic environment. A convenient way to obtain such bound consists of realising that creep can be approximately classified as a low-pass phenomenon, so that a typical experiment to estimate its extent consists of applying, at t = 0, a step-like excitation in stress spanning the whole allowable stress range and in evaluating the difference between the response at t = 0+ and the response at t →∞, where, of course, t→∞ means a temporal value for which the experiment can be considered settled or the viscoelastic effect has reached more than 90 % of his relaxation behaviour. Intuitively, any structure subject to a slowly varying load will deform deviating from a non-viscoelastic response by no more than such a quantity (the slower the load dynamics, the lower the deviation). The major reason to practise this kind of analysis is to understand how actions on the geometry and materials employed in the sensor fabrication can re-duce the extent of the viscoelastic response and thus tighten the error bounds. In the modeling of creep [30], one should consider that by taking into account the viscoelastic phenomena: the deformation model of a membrane changes from a static, non-linear, time-invariant model to a dynamic, non-linear, time-invariant model. In other terms, one could in principle model the viscoelastic behaviour by introducing time derivatives into the system of partial equations that rule the membrane deformation. In practise, it is generally convenient not to do so. In many conditions it is handier to model creep by using equations where time-varying parameters take care of describing the dynamical effects. A particularly effective way of doing so is by the introduction of a time de-pendent module of elasticity, obtained starting from Kapton[®] data sheets [28]. As shown in Fig. 2.11, from strain versus time curves, given by different applied stresses, the corresponding time dependent modulus of elasticity have been.

23
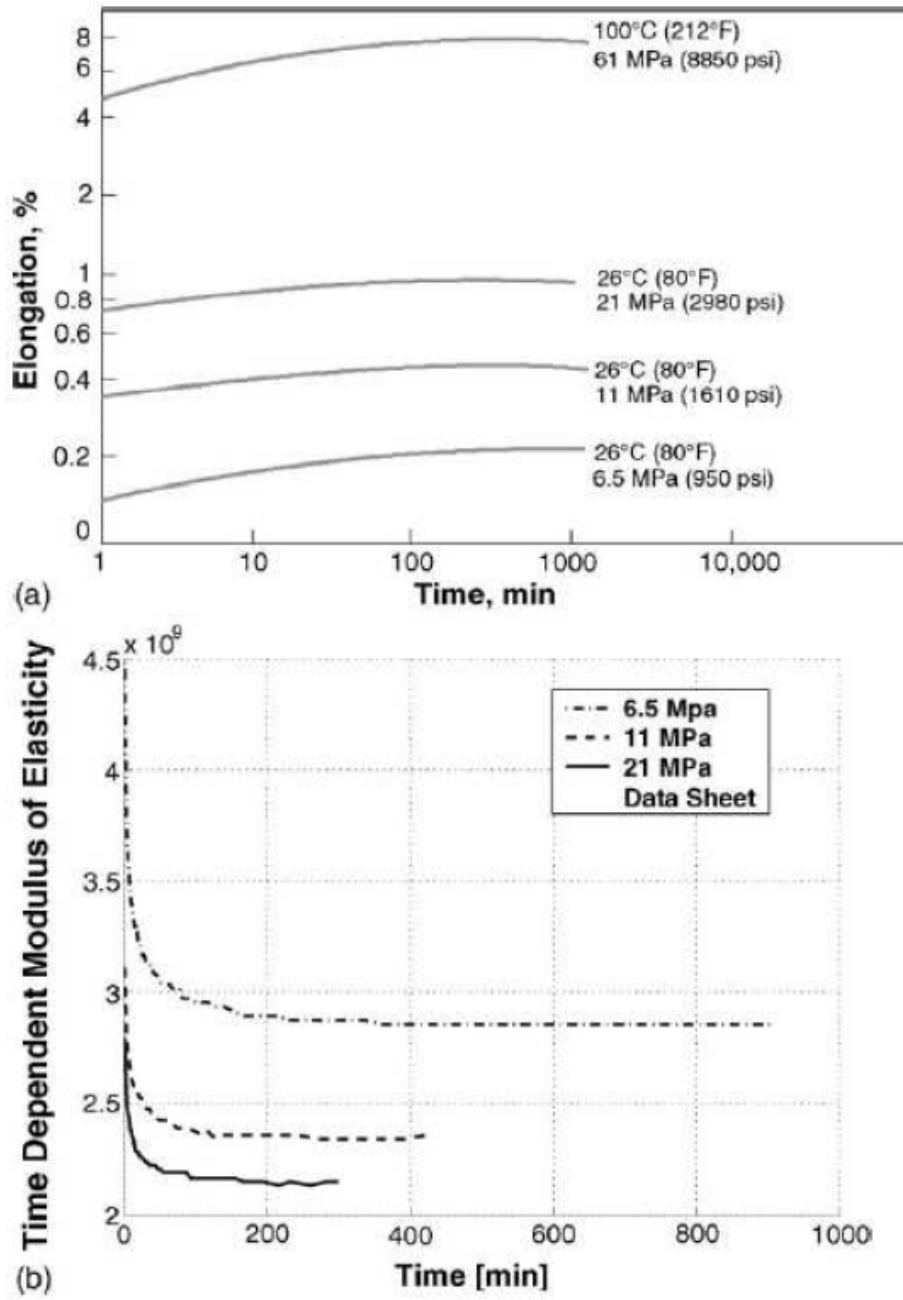
Figure 2.11: Kapton® creep: a) strain versus time behaviour from datasheet for particular temperature and stress conditions. b) time dependent modulus of elasticity Eτ(t), as described in Eq. 2.18 for particular temperature and stress conditions.

calculated, interpolating the strain curves, as:

$$E_\tau(t) = \frac{\sigma_i}{\varepsilon_i(t)} \qquad (2.20)$$

24

where εi(t)is the time dependent strain, σi is the corresponding stress and the index irepresents different values of stresses and temperature conditions. The approach is convenient because it leads to equation sets which fit more easily into an analytical and conventional FEM simulation structure than models with explicit time derivatives. In other terms it allows creep to be obtained by a sequence of static simulations referring to different time instants. These curves (Fig. 2.11.b) have been fitted minimising the root mean square difference between Eq. 2.14 and the sum of exponential and a constant, truncating the series at the fourth term:

$$E_\tau(t) = \sum_j \left(A_{ij} e^{B_{ij} t} \right) + k_i \tag{2.21}$$

where A_{ij} , B_{ij} and K_i parameters are representative of the elastic and viscous behaviour of the membrane in particular condition of exerted stress and temperature. The expressions obtained in Eq. 3.18 will be used for time dependent mechanical simulations and for analytical approximation in the design phase. The approach followed is an alternative and easier way to reproduce creep behaviour without differential equations, basing the estimation of the coefficients of Eq. 2.21 by means of interpolation, depending upon the stress and the temperature. Since the maximum membrane relaxation, due to creep, is obtained for the maximum pressure value, a time dependent capacitance variation can then be calculated until the transient response can be considered as finished or no longer relevant for the proposed application.

2.2.3 Electro-mechanical model

A complete, though approximate, relationship between the pressure applied on the sensor membrane and the electric capacitance can be obtained, considering the axial symmetry of the sensor and a parallel plate capacitor structure with electrodes of the same area, as shown for a similar structure and small deflections in [62]. The capacitance C is given by:

$$C = \iint \frac{\varepsilon}{d_0 - w(r)} f dr d\vartheta \tag{2.22}$$

For a moving circular diaphragm sensor, like the one considered in Sec. 3.1, the capacitance can be expressed as in Eq.2.22 where ε is the permittivity and do the initial distance between the plates when no pressure is applied; w(r) is the deflection of the diaphragm as obtained in Eq. 2.6 while the expression of w_0 is the one obtained in Eq. 2.5. Due to the axial symmetry of the structure there is no dependence on the angle θ. When solving the Eq. 2.22, three domains must be taken in to account: the first, where the pressure makes the diaphragm deflect inwards, giving a positive deflection for the equation considered in Sec. 2.2.1; the second, where the pressure is equal to 0 and the classic equation for a flat capacitor must be used; and, finally, the third, where the pressure makes the diaphragm deflect outwards, giving a negative deflection for the equation considered in Sec. 2.2.1. For inward deflection, the capacitance C_{inw} is given by:

$$C_{inw} = \int_0^a \frac{2\pi\varepsilon}{d_0 - w_0\left(1 - \dfrac{r^2}{a^2}\right)^2} r dr \tag{2.23}$$

that gives, after a few simplification, the following result:

$$C_{inw} = -\left[\frac{\pi\varepsilon a^2}{\sqrt{w_0 d_0}}a\tanh\left(\sqrt{\frac{w_0}{d_0}\left(\frac{a^2-r^2}{a^2}\right)}\right)\right]_0^a \qquad (2.24)$$

and substituting expression 2.9, it gives:

$$C_{inw} = -\frac{\pi\varepsilon a^2}{\sqrt{d_0 k_1 \sqrt[3]{\frac{pa^4}{Eh}}}}a\tanh\left(\sqrt{\frac{k_1\sqrt[3]{\frac{pa^4}{Eh}}}{d_0}}\right) \qquad (2.25)$$

For outward deflections it can be found similarly that the capacitance C_{outw}:

$$C_{outw} = \int_0^a \frac{2\pi\varepsilon}{d_0 + w_0\left(1-\frac{r^2}{a^2}\right)^2}r\,dr \qquad (2.26)$$

which gives, after a few simplifications, the following result:

$$C_{outw} = -\left[\frac{\pi\varepsilon a^2}{\sqrt{w_0 d_0}}a\tan\left(\sqrt{\frac{w_0}{d_0}\left(\frac{a^2-r^2}{a^2}\right)}\right)\right]_0^a \qquad (2.27)$$

and substituting expression 2.9, gives:

$$C_{outw} = -\frac{\pi\varepsilon a^2}{\sqrt{d_0 k_1 \sqrt[3]{\frac{pa^4}{Eh}}}}a\tanh\left(\sqrt{\frac{k_1\sqrt[3]{\frac{pa^4}{Eh}}}{d_0}}\right) \qquad (2.28)$$

It must be considered that if the sensor structure is like the one depicted in Fig. 2.4, the lower plate of the capacitor has a smaller surface of radius R_{low} with respect to the upper one, of radius a. This changes the integration boundaries to [0,Rlow] and the expressions of Eqs. 2.25 and 2.28 result in:

$$C_{inw} = \frac{\pi\varepsilon a^2}{\sqrt{d_0 k_1 \sqrt[3]{\frac{pa^4}{Eh}}}}a\tanh\left(\sqrt{\frac{k_1\sqrt[3]{\frac{pa^4}{Eh}}}{d_0}}\right) - \frac{\pi\varepsilon a^2}{\sqrt{d_0 k_1 \sqrt[3]{\frac{pa^4}{Eh}}}}a\tanh\left(\sqrt{\frac{k_1\sqrt[3]{\frac{pa^4}{Eh}}}{d_0}\frac{a^2-R_{low}^2}{a^2}}\right) \qquad (2.29)$$

and:

26

$$C_{outw} = \frac{\pi\varepsilon a^2}{\sqrt{d_0 k_1 \sqrt[3]{\frac{pa^4}{Eh}}}} \, a\tanh\left(\sqrt{\frac{k_1\sqrt[3]{\frac{pa^4}{Eh}}}{d_0}}\right) - \frac{\pi\varepsilon a^2}{\sqrt{d_0 k_1 \sqrt[3]{\frac{pa^4}{Eh}}}} \, a\tanh\left(\sqrt{\frac{k_1\sqrt[3]{\frac{pa^4}{Eh}}}{d_0}}\frac{a^2 - R_{low}^2}{a^2}\right) \quad (2.30)$$

Eqs. 2.25, 2.28, 2.29 and 2.30 give the pressure-capacitance characteristics of the sensor, where the expression 2.13 is used for the Young's modulus E. Considering the expression 2.20, the creep behaviour in the membrane is evaluated with a first order approximation, using two different values for the Young's modulus, E_{Max} and E_{Min}. These values are given at $t=0$ and $t\rightarrow\infty$, respectively, while an averaged value of the time dependent Young's modulus, E_{Av}, can be used for evaluating the sensor characteristics. For instance, referring to Fig. 2.11.b, three different elastic moduli can be evaluated as follows:

$$E_{Max} = E_{copper} f_{copper} + E_{MaxKapton} f_{MaxKapton}$$

$$E_{Av} = E_{copper} f_{copper} + E_{AvKapton} f_{Kapton} \quad (2.31)$$

$$E_{Min} = E_{copper} f_{copper} + E_{MinKapton} f_{Kapton}$$
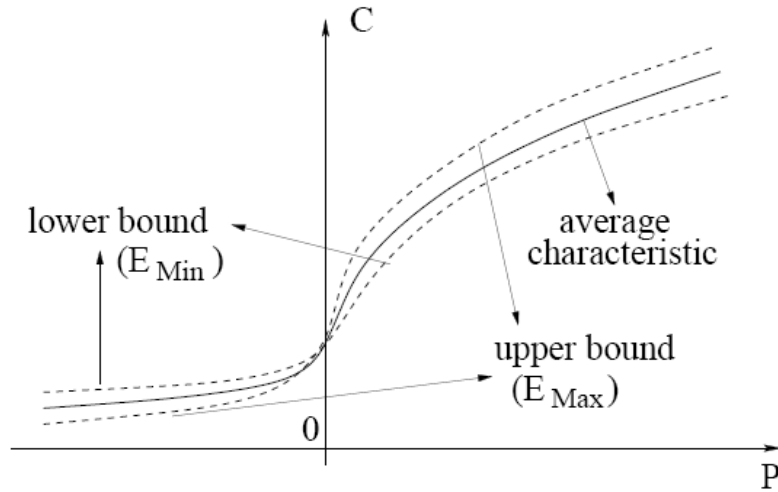
Figure 2.12: Analytical averaged sensor characteristic prediction (continuous line) limited by viscoelastic boundary condition (dashed line).

The sensor characteristic, as shown in Fig. 2.12, is then represented as an average characteristic (continuous line) with an upper and lower bound (dashed line), which mark the viscoelastic zone in which the membrane can assume values for the given pressure range and for a predefined maximum amount of time. Because of the approximations made for expressing Eqs. 2.25, 2.28, 2.29 and 2.30, like 2.5, 2.9, 2.20 and 2.29, these equations can only be used for approaching the optimum design of the sensor, allowing the understanding of the parameter influence on the sensor figures of merit.

Chapter 3

Finite element method simulations

Aim of FEM simulations is to describe more efficiently the physical and structural sensor features, cause the analytical formulation of the sensor behaviour might be not sufficiently accurate to achieve a good design of the device due to the non linearity present both in the pressure-deflections transduction and in the electric capacitance relationship, other approximations are then introduce by means of the model used in the rule of mixtures, these topics lead to a non neglectable error in the capacitance integration. Since the output of the sensor is a capacitive information, coupled electrical and mechanical simulation have to be taken into account. Fortunately, simple hand calculations show that, in contrast with typical MEMS structures, electrostatic force is negligible with respect to external forces inducing mechanical deformation: for a parallel circular plate capacitor with a radius of 1 cm, the distance between armatures should be tens of μm for obtaining an electrostatic force, in air, equivalent only to 5 Pa for an applied difference of potential of 5V. As a consequence, electrostatic simulations may follow mechanical ones without coupling. On the other hand, an important difficult issue is due to viscoelastic behaviour of polymers, that an over-simplified analysis could lead to large errors. This problem is usually referred to as creep and its modeling was described in Sec.3.2.2.

3.1 Pressure input variables

The monitoring of the pressure pattern over wings, is the fluid dynamic environment, chosen for the proposed sensor. To be able to set the FSI (full scale input) the sensor will face, a first analysis, concerned with the typical pressure distribution of a bi-dimensional profile has been performed .
A NACA 0012 wing's profile was chosen as the aerodynamic body of investigation: the 4-digit numbering system for a NACA wing profile is based on the section geometry. The first integer indicates the maximum value of the mean-line ordinate in per cent of the chord. The second integer indicates the distance from the leading edge to the location of the maximum camber in tenths of the chord. The last two integers indicate the section thickness in per cent of the chord. A simple algorithm based on the panel method can be used for computing 2D inviscid, incompressible, irrotational flow solutions. This method is based on the boundary layer equation described in [32]. It uses Thwaites equations for the laminar part of the flow and Head's equations for the turbulent part. Michel's criterion is used to locate transition and the drag coefficient is computed using the Squire-Young formula [33]. The results obtained with the panel method model are accurate for pressure distribution but not enough for the evaluation of the shear stresses, which are not considered in this phase. In more advanced developments, like Xfoil [34], the model is slightly more complicated, and the solution is more robust and closer to experimental results. Another possibility to calculate the pressure distribution around a wing profile is to use the Thin Airfoils Theory. From the Bernoulli's equation it is possible to show that the local pressure coefficient Cp is linked with the local flow velocity by the following equation:

$$C_p = \frac{p - p_{\text{inf}}}{0.5\rho_f V^2} = 1 - \frac{v^2}{V^2} \tag{3.1}$$

where V is the free steam velocity, p_{inf} is the pressure in a point where the fluid is not affected by the aerodynamic object and p and v are the pressure and the velocity around the profile, respectively. This coefficient gives are related to the pressure variation with respect to the value that it finds on free stream flow.
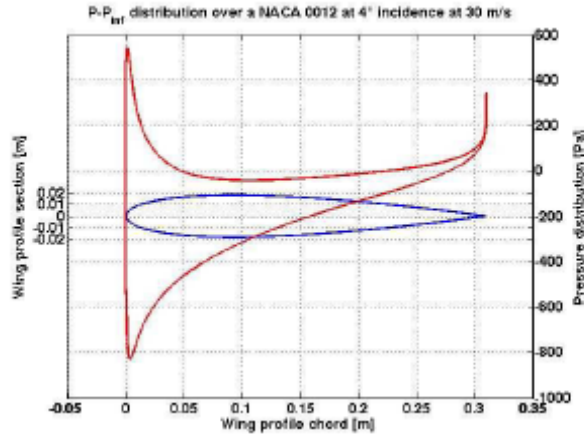
Figure 3.1 : Pressure coefficient on airfoil

The calculated values for the NACA 0012 profile are referred to low Reynolds numbers (in the range of $0.1 \cdot 10^6 - 2 \cdot 10^6$). Considering the pressure values in Fig. 3.1, a pressure range has been chosen starting from 15% and going to the 80% of the chord, and represents the area of the airfoil for the sensors application. Pressure values cover a range of about $50 - 2000$ Pa and the pressure gradient is always monotonic both for the upper and lower side of the profile. As a final remark, considering Eq. 3.2 and Eq. 3.3:

$$\delta \cong \left(\frac{\upsilon L}{V} \right)^{0.5} \tag{3.2}$$

$$\text{Re} = \frac{\rho V L}{\mu} \tag{3.3}$$

it turns out that the range of boundary layer thickness as for the chosen application varies from 300 μm up to 700 μm for free stream velocity ranging from 10 to 50 m/s according to a chord length of 31 cm. These specifications, together with that of the altitude, justify the sensor structure, shown in Chapter 2.

3.2 Numerical FEM simulation

From the many possible FEM packages now available, Femlab [35] has been chosen as the finite elements software. The simulation is organised in the following mode: first, the sensor axial-symmetric geometry Fig. 3.2 is solved for the large mechanical deflection problems considering an average value for the Young Modulus of the polyimide membrane in a static simulation Fig. 3.3, that gives as a result the membrane deflection for different constant values of uniformly applied pressure on the membrane. The time dependent behaviour due to the creep contribution is then established for different time instants (from 0 up to 7200 seconds, with 120 seconds steps) as shown in Fig. 3.4 only for significant instants. With this approach the sensor characteristic in absence of creep is obtained
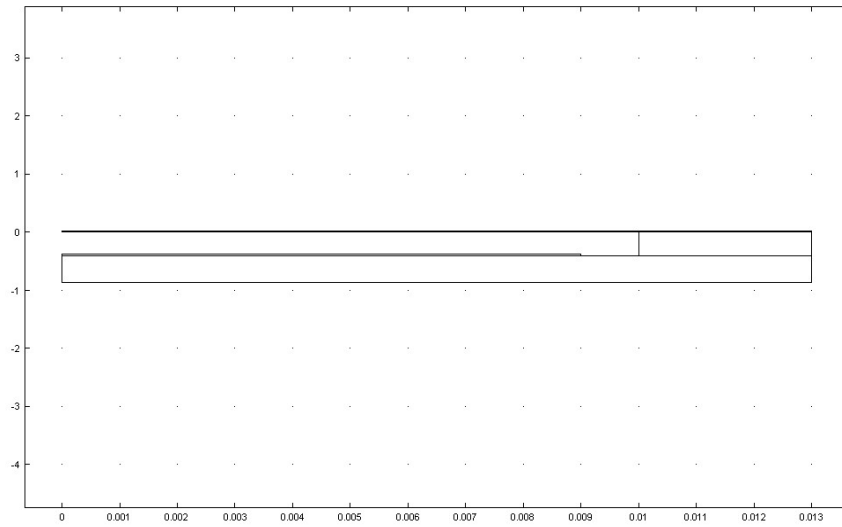
Figure 3.2 : Sensor axial-symmetric geometry

and afterward the time dependent behaviour is added as an error and calculated as a worst case from the time window considered (2 hours). This procedure is described theoretically in Secs. 3.2.1 and 3.2.2. The solution for the mechanical static large deflections problem is obtained by solving the equilibrium equations for an axially symmetric problem, revealing that the creep behaviour can not be neglected and appears as a bigger and different contribution (Sec. 4.3) with respect to the analytical formula 2.22, proposed in Sec.2.2.3, because of the stresses present in the membrane. The capacitance value is obtained solving the electrostatic problem for the deformed membrane configuration obtained from the static and time dependent mechanical simulations solution (Fig. 3.4). Femlab solves for large deflections using a strain-displacement relation, knownas Green or Green-Lagrange strains [36] and defined as:

$$\varepsilon_{GL} = \frac{1}{2}\left(\frac{l^2 - l_0^2}{l_0^2}\right)$$
(3.4)

30
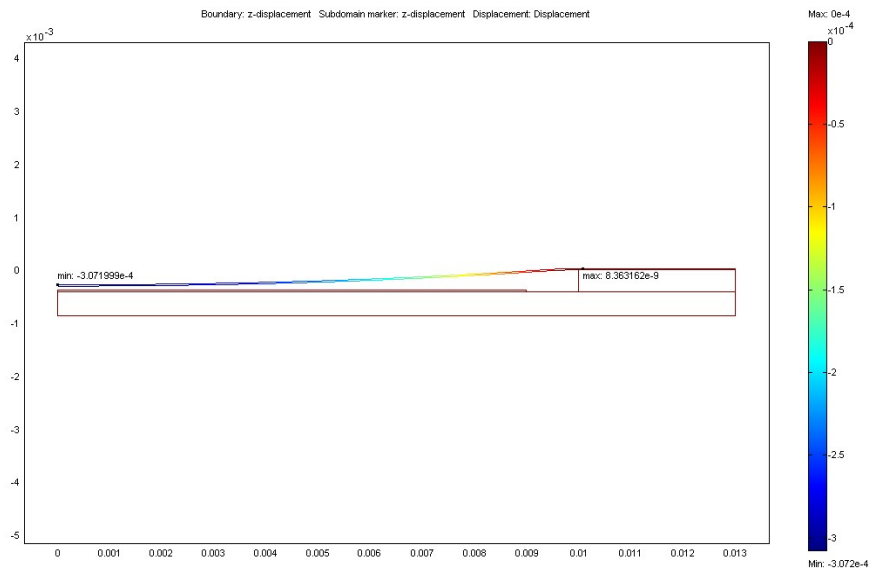
Figure 3.3: FEM simulations graphical results. Mechanical simulations: stress pattern and membrane deflection.
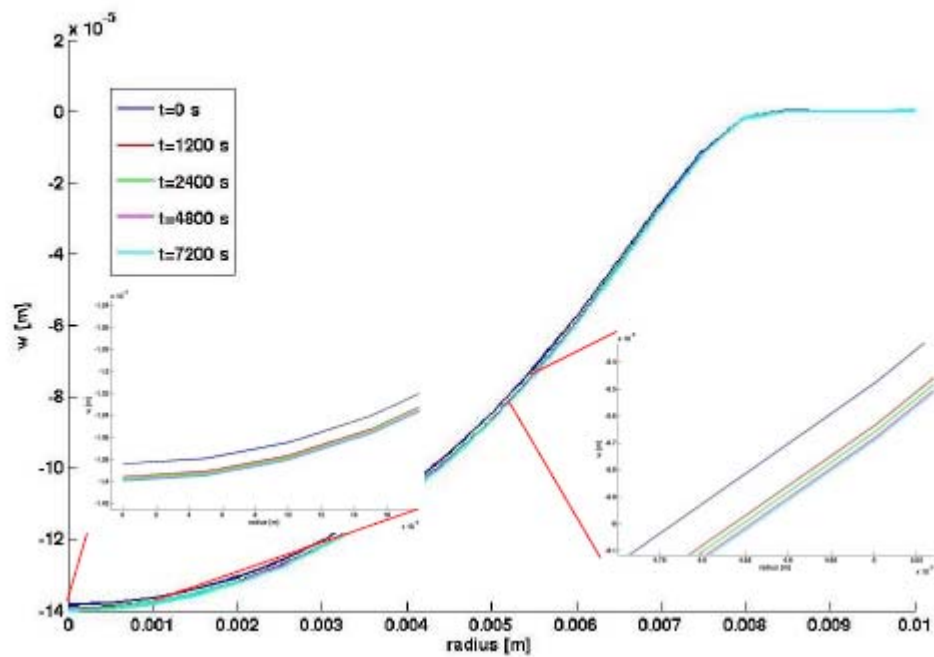
Figure 3.4: Time dependent behaviour of the membrane for a constant applied pressure at different instants showing the drift effect produced by creep.

31
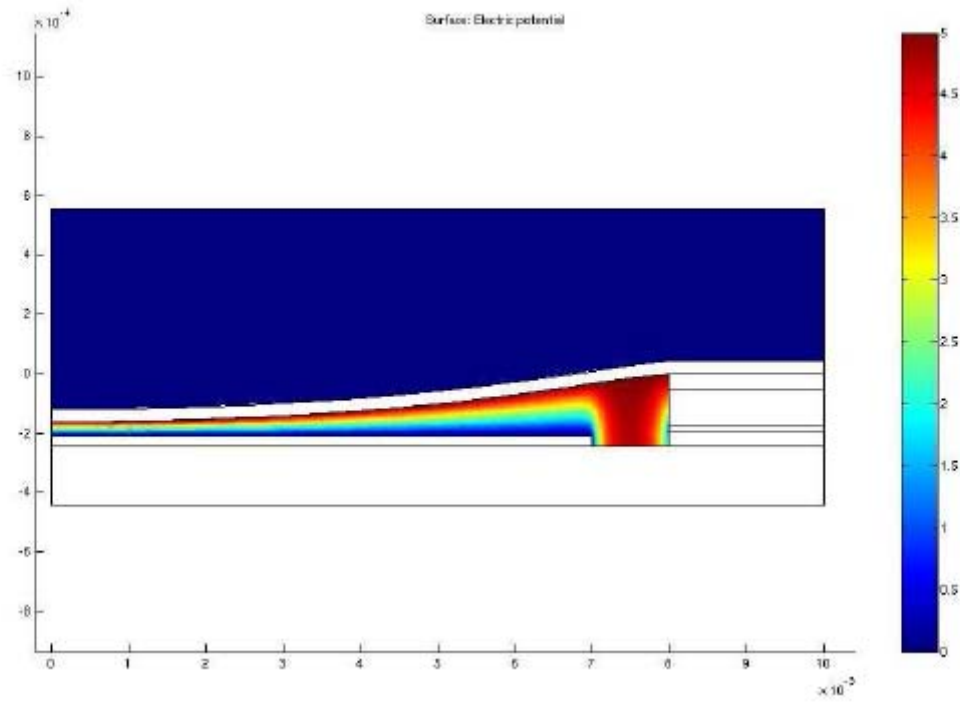
Figure 3.5: FEM simulations graphical results. Electrostatic simulation: electric potential pattern due to the change in membrane geometry.

where ε is the deformation, l_0 is the initial length and l the deformed length. This formula has been used in place of classical engineering strains, defined as:

$$\varepsilon = \left(\frac{l - l_0}{l_0} \right) \tag{3.5}$$

Furthermore, Cauchy stresses, defined as:

$$\sigma_C = \frac{F}{A} \tag{3.6}$$

are replaced by second Piola Kirchoff stress:

$$\sigma_{PK} = \frac{1}{lo} \frac{F}{A} \tag{3.7}$$

where σ is the stress, F the force and A the surface area. This model has been used for the whole structure, even for the parts that are subjected to small deformations: this is because the large deflections model is valid with a good approximation also for small displacements. By means of static simulations the stresses on the membranes have been calculated. As it will be better explained in the following section, the creep values obtained by analytical formula are not satisfactory enough and FEM simulations are needed to enrich the model with more accurate viscoelastic results. To this aim, a time dependent large deflections FEM model was made, using a sum of exponential in time modulus of elasticity, as reported in Sec. 2.2.2 . As a last step, for any deformed geometry obtained by mechanical FEM analysis, the Poisson equation:

32

$$\nabla^2 V = -\frac{\delta}{\varepsilon} \tag{3.8}$$

in the domain defined by the internal chamber of the sensor is solved for the space charge density δ variable, where V is the electrostatic potential and ϱ the permittivity. Integrating δ over the plate area of the sensor, the total capacitance C is obtained as:

$$C = \frac{Q}{V} = \frac{2\pi}{V} \int_0^R \delta(r) r dr \tag{3.9}$$

where R is the radius of the electrode. To summarise, from this analysis the sensor membrane deflections are calculated as the response to the respective applied pressure distribution, finding out the capacitance variation, due to the geometrical changing, caused by the input and by the viscoelastic effect.
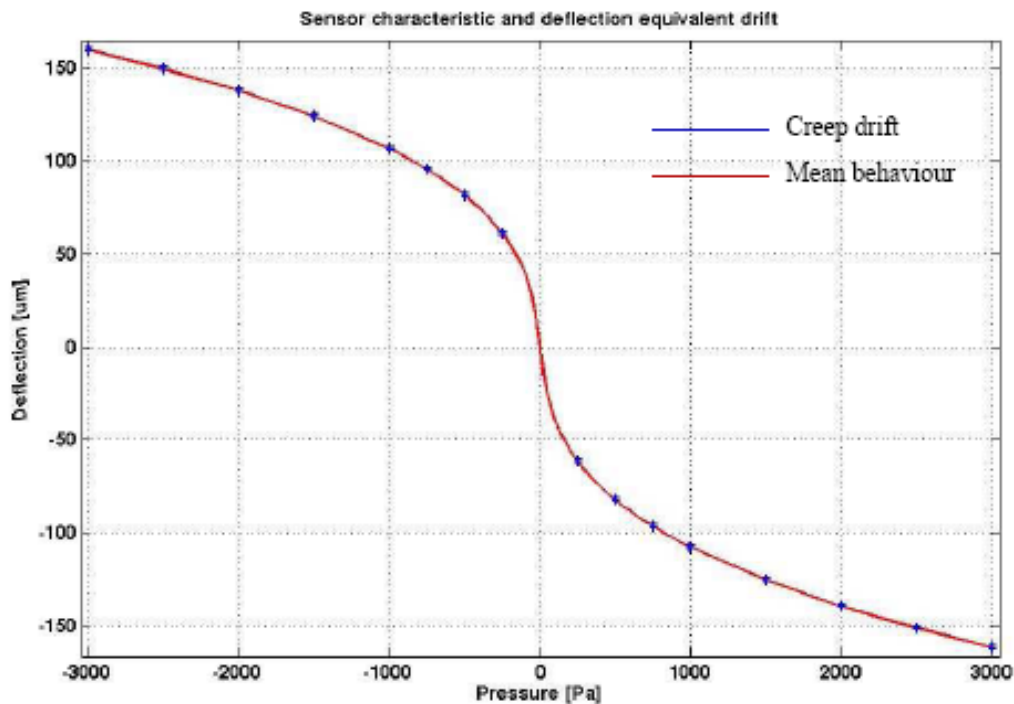
Figure 3.6: Sensor characteristic obtained by FEM simulation for membrane displacement: the average behaviour of the sensor (red) with the drift creep imprecision intervals (blue) for some specific pressure values.

The sensor characteristic obtained by FEM simulations is reported in Fig. 3.6 and Fig. 3.7.
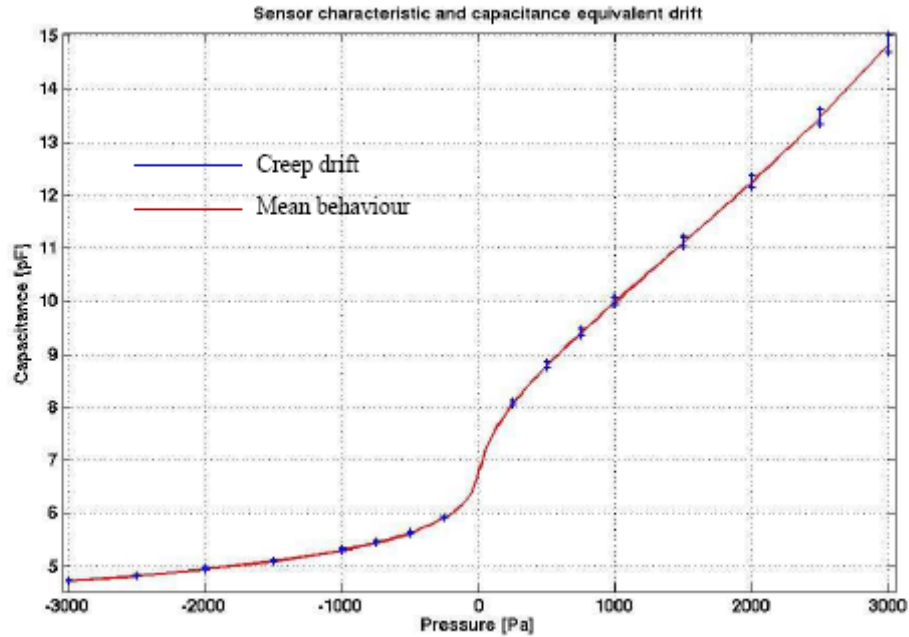
Figure 3.7: Sensor characteristics obtained by FEM simulation for membrane capacitance: the average behaviour of the sensor (red) with the drift creep imprecision intervals (blue) for some specific pressure values.

3.3 Comparison between analytical and FEM solution

This section is intended for making comparisons between the different aspects of the analytical solutions with respect to the FEM solutions, taking into account the main approximations made during the analysis that leads to a close form for the sensor characteristic. Since FEM simulations are usually more accurate but definitely more time consuming than simple equations, an inspection about the information that can be extracted by the procedures illustrated in the previous chapters is fundamental. In fact, during the design, it is important to handle the sensor parameters for optimisation and for the addressing to a specific application, knowing which element and which model can influence qualitatively and quantitatively the output, in order to define a design approach based on the accuracy of the model used.

3.3.1 Consideration of the large deflection model

Large deflection theory was explained in Sec. 2.2.3. There are three approximations introduced for the proposed analysis: the first is related to the membrane behaviour of the plate, the second is due to the rule of mixtures and the last is the one necessary for obtaining a close solution of the integral (Eq. 2.23) and given in the expression 2.5. The first two approximations can only be validated together and not independently, making a comparison between the maximum displacement of the membrane obtained by the FEM results and the Eq. 2.9, where Eq. 2.14 is used as an equivalent elastic modulus of a uniform material that holds the same properties as the composite.

34
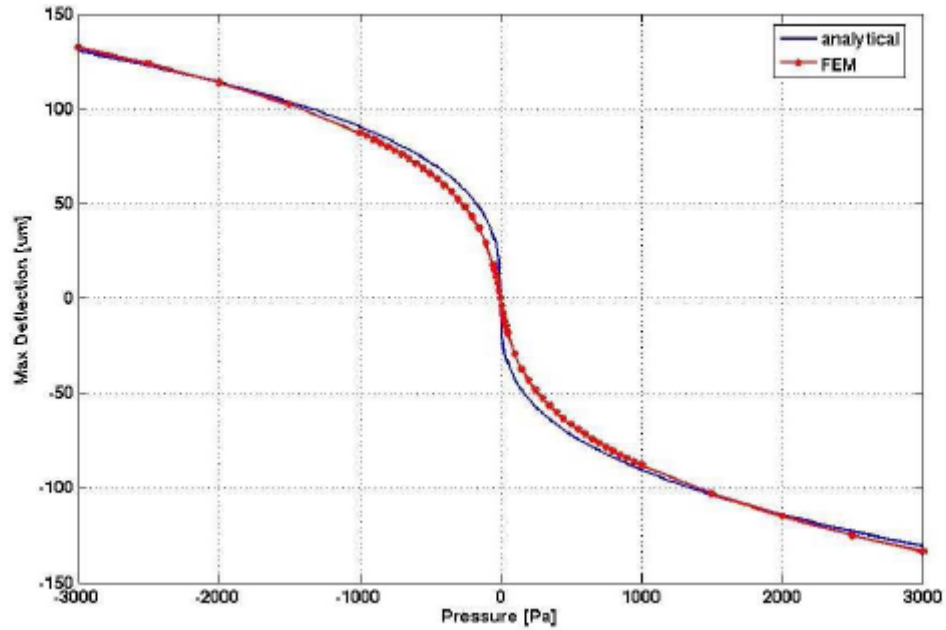
Figure 3.8: Comparison of the maximum displacement of the sensor membrane between the FEM and the analytical solution for k1 = 0.822.

As reported in Fig. 3.8, the maximum displacement, that manifests itself in the centre of the plate, is modeled by the approximated analytical formula and FEM simulation with a not too similar behaviour for pressure values that are in the range of the rest position (± 1000 Pa). Conversely, for pressure values above 1000 Pa, where the deflections are greater than twice the membrane thickness, a very similar behaviour is shown. This effect is furthermore presented by the percent error plot between the difference of the two displacement values while referring to the full scale, in Fig. 3.9, for a given geometry of the sensor.
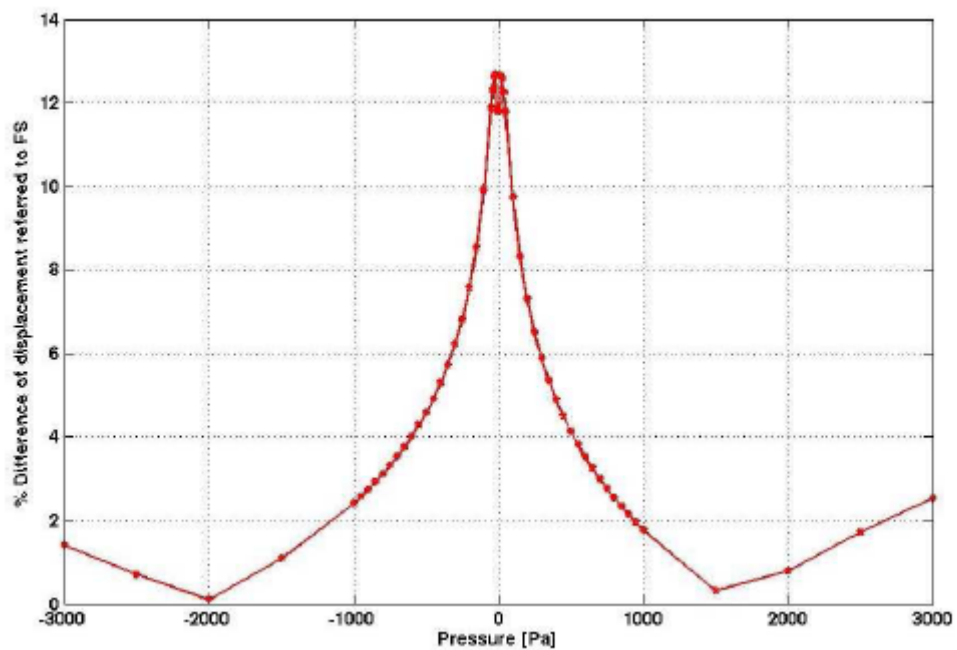
Figure 3.9: Percent error referred to the full scale (FS) between the analytical and FEM solution for the maximum displacement.

35

The two solutions presents different behaviour depending on the pressure that is applied to the membrane. A possible explanation can be found in the clamped edge condition chosen for the plate when obtaining Eq. 2.9. This constraint is in fact the one that set the boundary condition for solving the differential equation shown in Eq. 2.3 and Eq. 2.4 for the estimation of the maximum displacement w_0. The FEM solution appears more smooth, characterised by a lower slope around the zero with respect to the analytical one. This behaviour must not be surprising, because of the kind of equations used for considering large deflections rather than small deflections. Moreover, it is also possible that considering a uniform material with an elastic modulus obtained by the rule of mixture could lead to further imprecision when the large deflection theory is used for describing small deflections. Finally, a significant approximation is introduced by Eq. 2.5, which represents the shape of the membrane deformation. As stated in the previous chapter, this is an expression used for small deflections and is useful for the integration of the electric capacitance in a close form. As shown in Fig. 3.10, two different behaviours of the membrane shape deformation are compared, for two different pressure values representative for low (a) and high (b) sensor range of inputs, considering the analytical solution and the FEM simulation.
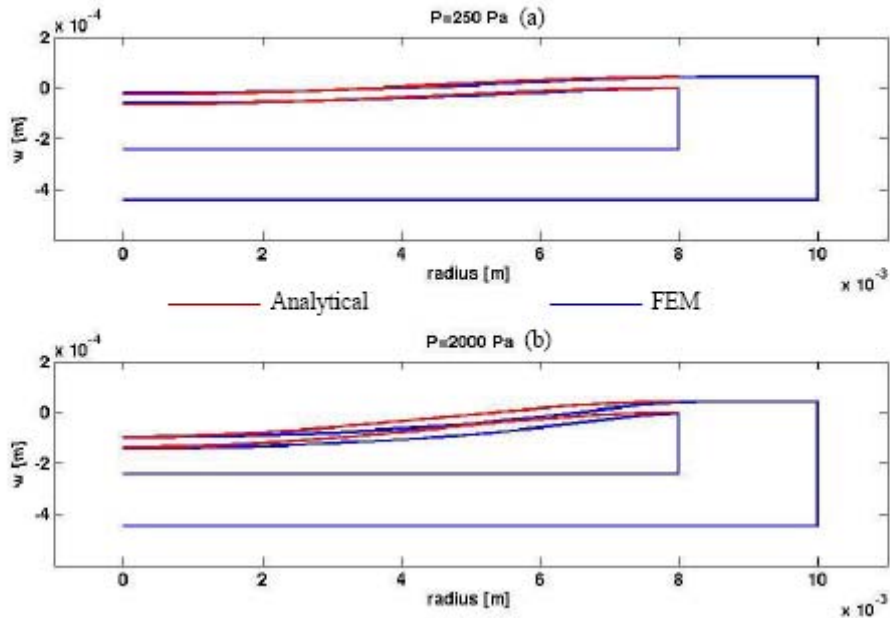
Figure 3.10: Membrane shape deformation: comparison between the analytical solution (k1 = 0.822) and the FEM simulation for two different pressure values representative for low (a) and high (b) input.

For a low-range input (from 10 to 100's of Pa), Eq. 2.5 models with a good accuracy the membrane deflection, but for higher pressure values (above 1000 Pa) the deformation near the edges lacks of precision due to the small deflection approximation. In that region, the loads are distributed differently because of the large deflection theory [37]. In fact, because of the stress that rises due to the strain in the middle plane, the plate carries part of the applied load as a diaphragm in direct tension. This tension may be balanced by radial tension at the edges if the edges are held or by circumferential compression if the edges are not horizontally restrained. This behaviour has to be taken into account every time the deflection becomes approximately larger than about one-half the plate thickness.

3.3.2 Consideration of the electric model

The electric model obtained by Eq. 2.29 and Eq. 2.30 presents a significant difference with the one obtained by FEM simulation (Fig. 3.7), as shown in Fig. 3.11, especially for pressure values that lead the plates to get closer. Some considerations are expressed hereafter for justifying the results obtained:
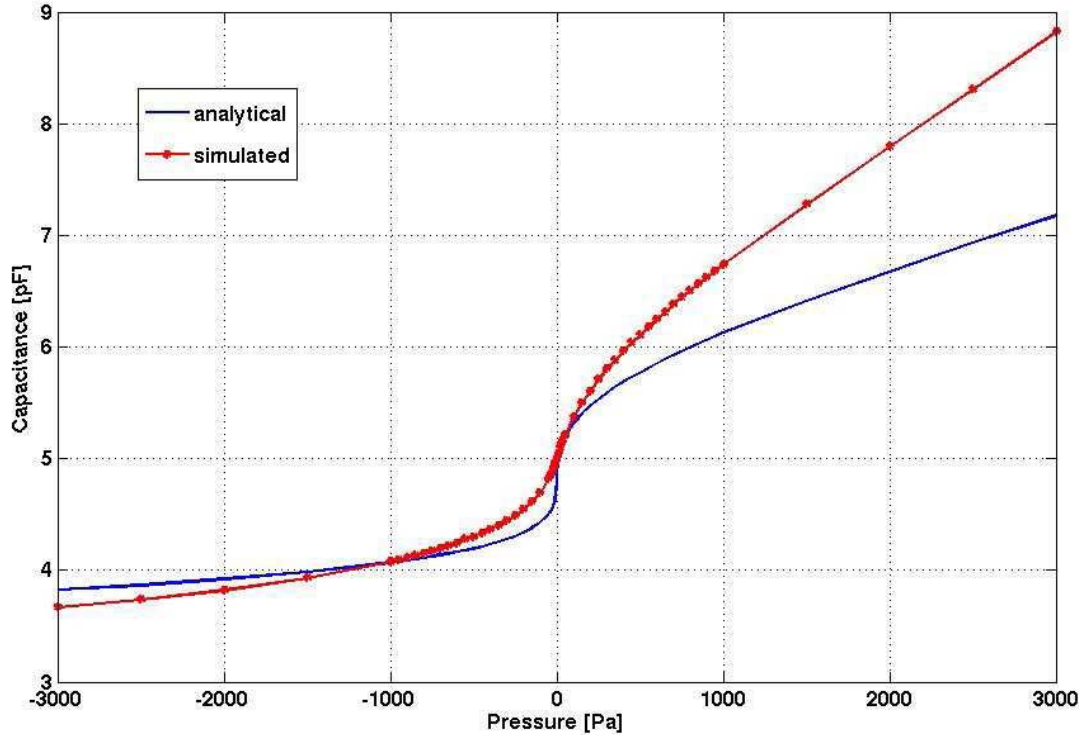
Figure 3.11: Sensor pressure-capacitance characteristic comparison between analytical and FEM model.

as shown in Fig. 3.10, the approximation used for describing the membrane deflection is not extremely accurate for high pressure values, leading only to a qualitative estimation of the membrane behaviour in such a range; the analytical expression for the electric capacitance takes into account a configuration with a capacitor formed by two electrodes with the same radius, which is not the case for the proposed geometry, where the upper plate is larger than the lower one. Fringing fields, caused by the latter difference and by the guard ring in the spacing layer, are so responsible for different results, introducing errors due to previous second orders electrostatic approximations; the strong non-linearity of the capacitance relationship is given by the hyperbolic dependence of the capacitance by the plate separation. This is the reason why the analytical model differs for positive pressures more than for the negative ones whenever Eq. 3.10 leads to an inaccurate description of the membrane deformation near the edges; moreover, the imprecision at low pressures around the membrane resting position (Fig. 3.8) obtained in terms of maximum displacement is also propagated in terms of capacitance. As stated previously, even if the analytical model fails in a quantitative description of the sensor output with respect to the FEM model, it remains a useful mean for a qualitative interpretation of it and allows the designer to understand which effects are produced by changing the sensor parameters.

37

3.3.3 Consideration of the viscoelastic model

Modeling viscoelasticity accurately appears to be one of the most important goals to achieve for the correct sensor design. It is clear from Sec. 3.2 how this feature can influence the sensor behaviour in terms of drift and alter the sensor precision. This polymer property also appears to be the main characteristic that differentiates the presented sensor design from the MEMS one. An accurate modeling of the creep behaviour is of significant importance for minimising the undesired effect produced, both from the theoretical and from the numerical point of view: the first for a qualitative description and the latter for a correct estimation of the sensor figures of merit.

3.3.4 Creep behaviour of a uniform polymer plate

The analytical method proposed in Sec. 2.2.1 and Sec. 2.2.2 is first applied to a polyimide membrane, which is carrying different constant loads and its deflection. The stress variations are numerically evaluated by the FEM simulation and finally compared with the theory. Fig. 3.12 shows the geometry considered in the FEM simulation. Fig. 3.13 reports on the maximum displacement variation for an applied constant and uniform pressure on a polyimide membrane, where we can consider the Young's modulus as decreasing in time due to the viscoelastic effect. In Fig. 3.13 (a) it is shown how the maximum displacement w_0 increases with time, according with Eq. 2.9, due to the decreasing of the elastic modulus E with time.
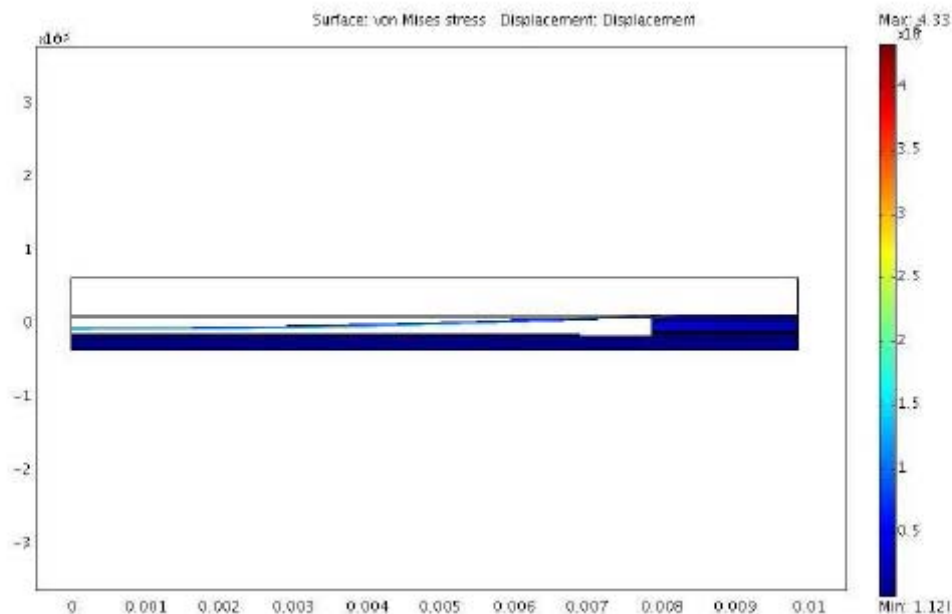
Figure 3.12: Uniform polyimide membrane deflection due to a constant applied uniform load.

In Fig. 3.13 (b) the complementary behaviour of the radial stress in the plate is shown, which decreases with time for a constant load, according to Eq. 3.7, where E is directly proportional to σ. Fig. 3.14 shows how the maximum deflection variation due to creep, calculated as the $w_{0Max} - w_{0Min}$ $= w_{0(EMin)} - w_{0(EMax)}$ (Sec. 2.2.3), behaves for different pressure values for an increasing trend. The FEM results respect qualitatively the behaviour shown by Eq. 2.9, where the inverse proportionality between w_0 and E enhances the variation Δw_0 for ever increasing loads. In fact, the following equation:

$$\Delta w_0 = w_{0Max} - w_{0Min} = k_1 a^3 \sqrt{pa/h} \left(\sqrt[3]{\frac{1}{E_{Min}}} - \sqrt[3]{\frac{1}{E_{Max}}} \right) \qquad (3.10)$$

shows that Δw_0 increases with a monotonic trend together with the pressure. Fig. 3.15 represents the behaviour of the stress variation in the membrane (valid both for the mean and the maximum stress in the plate).
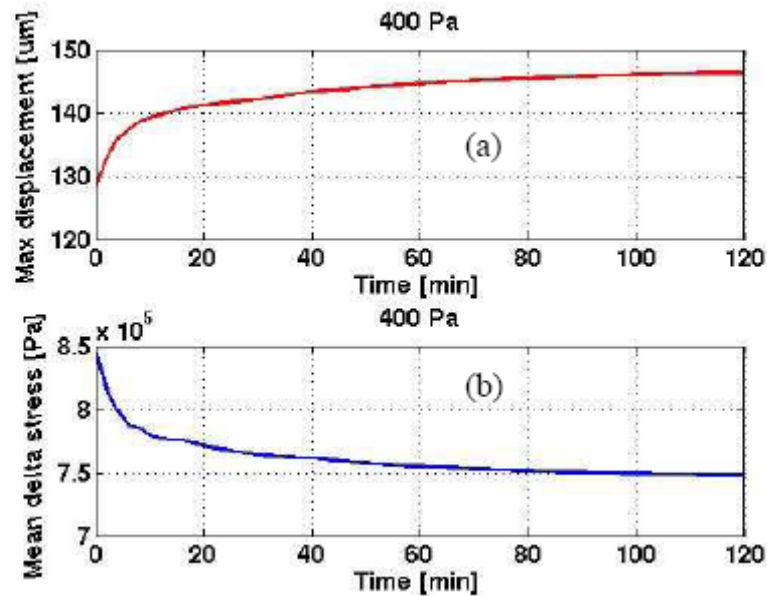
Figure 3.13: Uniform polyimide membrane time dependent behaviour due to a constant applied uniform load: (a) maximum deflection; (b) mean stress.
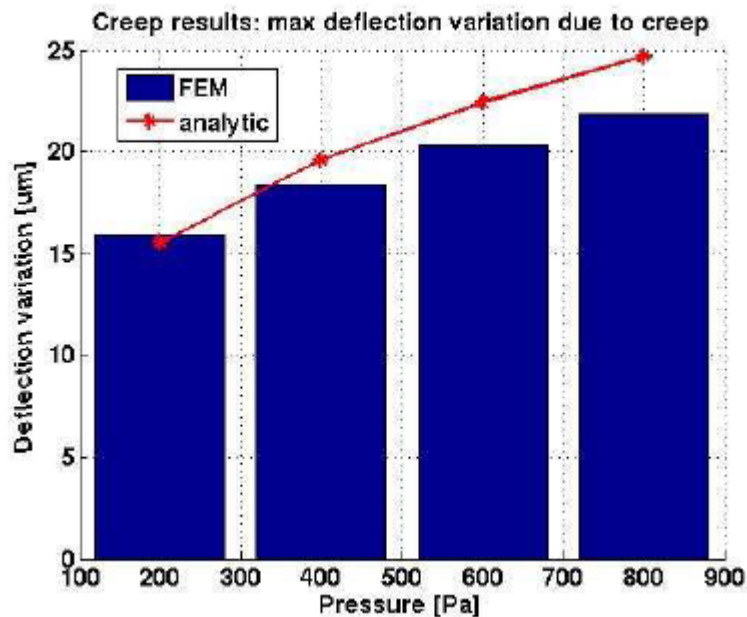
Figure 3.14: Maximum deflection variation of a polyimide membrane due to creep with respect to the pressure.

39

Comparing the FEM simulation with the analytical expression:

$$\Delta\sigma = \sigma_{Max} - \sigma_{Min} = k_2 a^3 \sqrt{p^2 a^2 / h^2} \left(\sqrt[3]{E_{Min}} - \sqrt[3]{E_{Max}} \right) \qquad (3.11)$$
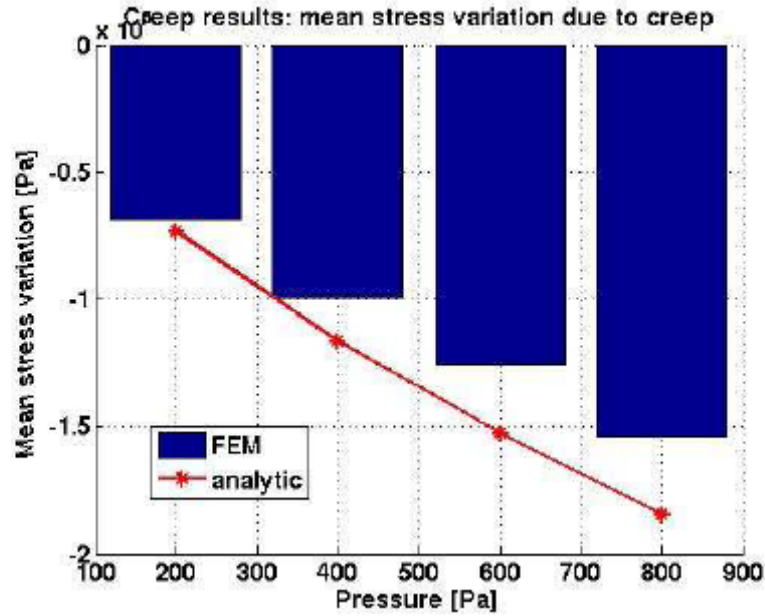
Figure 3.15: Mean stress variation inside a polyimide membrane due to creep with respect to the pressure.

obtained from Eq. 3.7. Similarly the increasing monotonic behaviour of the negative stress variation with respect to an increasing pressure trend is shown.

3.3.5 Creep behaviour of a composite plate

When considering the creep effect on a composite membrane a different trend is obtained with respect to a polymeric uniform material described in the previous subsection. The rule of mixture then fails in describing the deflection variation because of the copper layer that behaves conversely with respect to the polyimide membrane. As shown in Fig. 3.16, the maximum displacement of the membrane always increases with time, but a significant difference is present in stress distribution between the two layer of polyimide and copper respectively. While the polyimide is "relaxing", according to the previous subsection, the metal layer is becoming "more stressed", even if the load remains constant. Fig. 3.17 reports the stress variation for an increasing pressure trend. The bigger the pressure, the larger the deflection (as reported in Fig. 3.8), but also the larger the stress variation in the composite membrane, with an increasing trend for the copper layer and a decreasing one for the polyimide layer. This effect is responsible for the maximum displacement variation behaviour
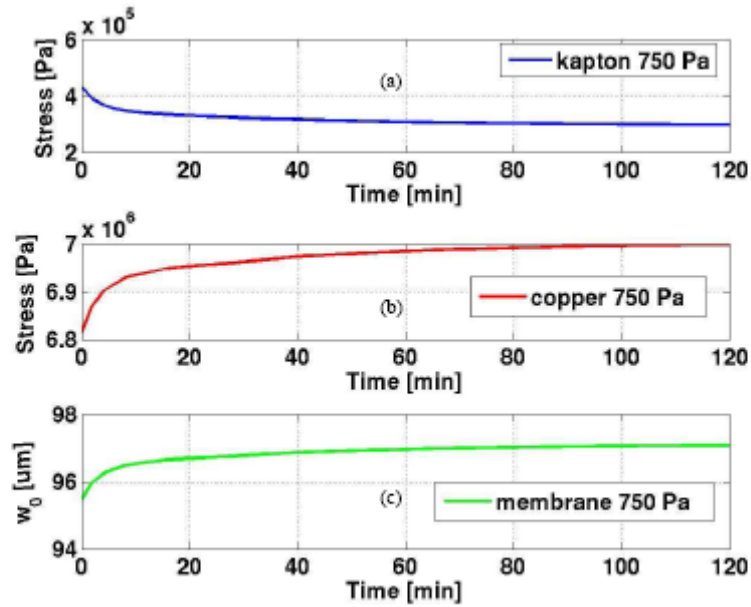
Figure 3.16: Composite membrane time dependent behaviour due to a constant applied uniform load: (a) polyimide mean stress; (b) copper mean stress; (c) membrane maximum deflection.
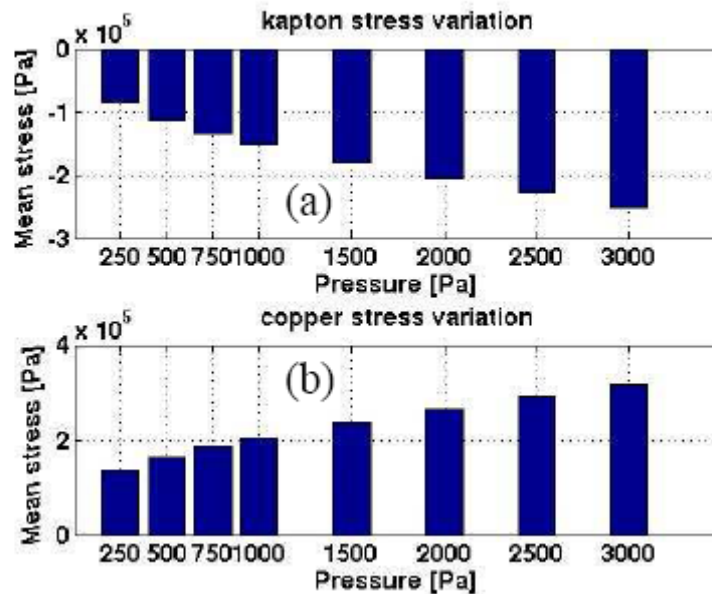
Figure 3.17: Mean stress variation inside a composite membrane due to creep with respect to the pressure: (a) copper behaviour; (b) polyimide behaviour.

Δw_0, reported in Fig. 4.18. Conversely, with what was demonstrated in the subsection regarding the uniform polyimide membrane, the Δw_0 trend is no longer monotonic with the pressure and appears with a greater contribution for low pressure values rather than for higher ones.
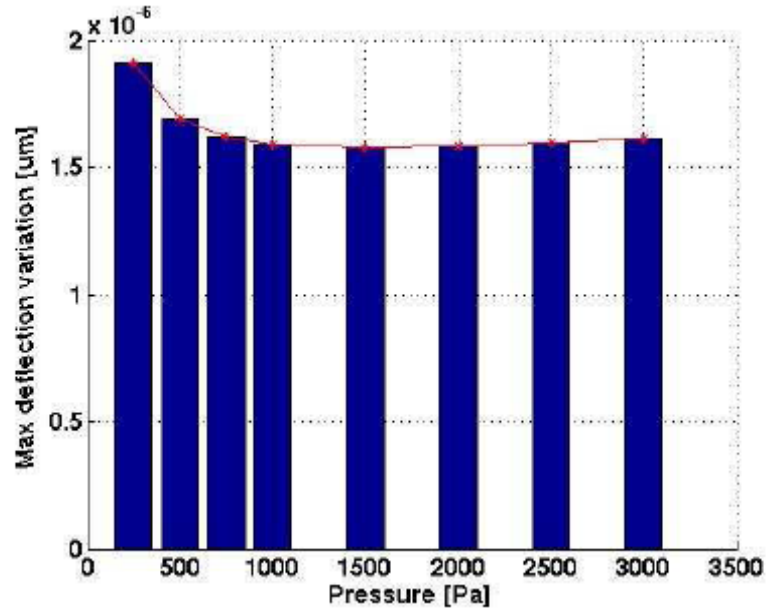
Figure 3.18: Maximum displacement variation of a composite membrane due to creep with respect to the pressure: the red line depicts the decreasing (first) and increasing (later) behaviour of the variation with respect to an increasing pressure trend.

Considering Eq. 2.9 and Eq. 3.7, the following can be extracted:

$$w_0 = cost\left(\frac{\sigma}{E}\right)^{\frac{3}{5}}$$
(3.12)

In the copper layer, the elastic modulus remains constant and evaluating Δw_0 from Eq. 3.12 as:

$$\Delta w_0 = w_{02} - \sigma_{01} = cost\left(\frac{\sigma + \Delta\sigma}{E}\right)^{\frac{3}{5}} - cost\left(\frac{\sigma}{E}\right)^{\frac{3}{5}}$$
(3.13)

for different σ and for different stress variation $\Delta\sigma$, it can be found how Δw_0 is influenced by the stress value and its variation, depending on their numerical values. This is a direct consequence of the polyimide relaxation that creates an opposite phenomenon in the copper layer. Fig. 3.19 shows the dual dependence of Δw_0 from σ and $\Delta\sigma$ for the ranges of interest. A better understanding of the phenomenon can be obtained from

42
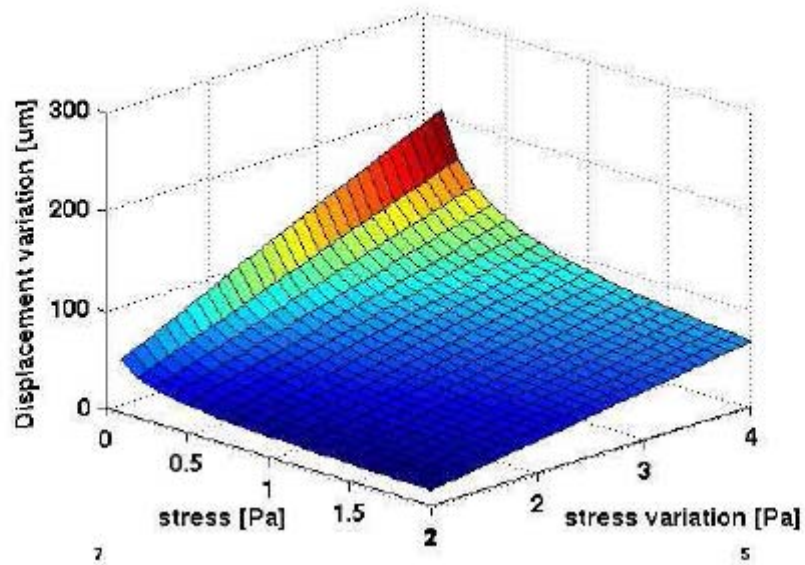
Figure 3.19: Maximum displacement variation of a composite membrane with respect to the stress and the stress variation due to the relaxation of the polyimide membrane that makes the stress in the copper layer to arise.

Fig. 3.20, where every parameter is alternatively fixed. Δw_0 presents a strong decreasing non-linear dependence by σ and an increasing linear dependence by $\Delta\sigma$.
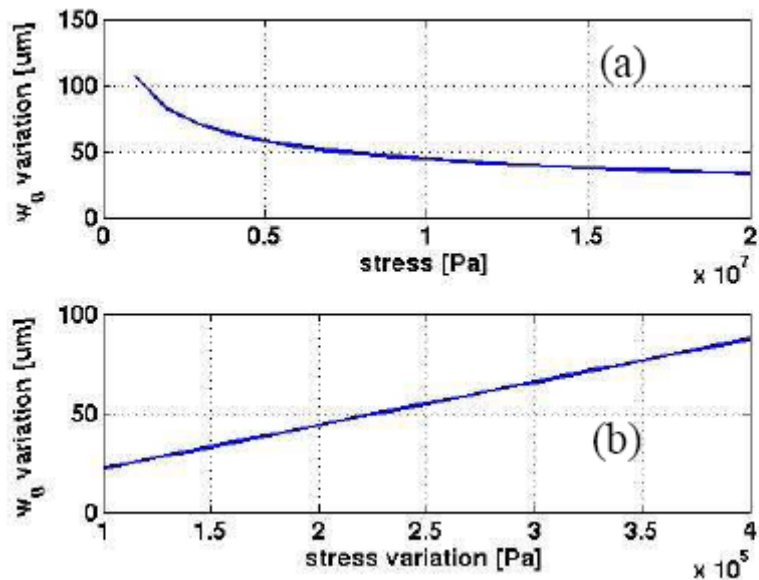
Figure 3.20: Maximum displacement variation of a composite membrane with respect to the stress and the stress variation respectively: (a) stress; (b) stress variation. Δw_0.

The superimposition of this two effects explains the curve obtained by the FEM simulation in Fig. 3.18 (red line). As a general remark, it can be concluded that because of the interlinked effect of the large deflections and of the relaxation behaviour of the polyimide layer, a final and significant

43

"stiffening" of the membrane is obtained in the copper layer, leading to a bigger drift in terms of deflection variation for lower pressure values than for higher ones. Finally, the drift effect presents a monotonic increasing trend, reported in terms of electric capacitance variation (Fig. 3.21), due to the strong non-linearity of the capacitance relationship with respect to the plate distance, where a small variation of this quantity around the equilibrium position results in a big capacitance variation when the electrodes are significantly close to each other.
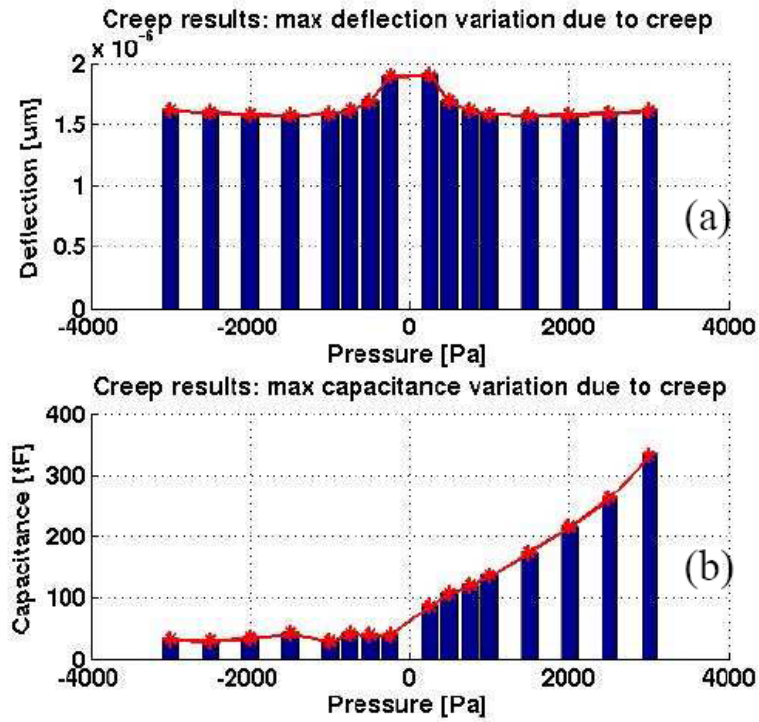
Figure 3.21: Maximumdisplacement variation (a) and capacitance variation (b) of a composite membrane due to creep with respect to the pressure.

Chapter 4

Aeronautical pressure sensor fabrication

4.1 Materials

Standard printed circuit board material layers were used for assembling the device, providing not only the means for communicating electrically the sensitive units to the read out circuitry through standard lithographic techniques, but especially for achieving the transduction. Polyimide is commonly used for obtaining flexible connections in devices where a moveable part is utilised, i.e. inject printers, due to its resistance to cyclic stresses. Bi-adhesive tapes were used for assembling the three main part of the sensor (base, spacer and membrane), while the more rigid part of the sensor was made out of woven fibreglass epoxy layers, which, due to their thickness, guarantee the conformability of the structure on non planar surfaces.

4.1.1 Polyimide

Polyimide are a very interesting group of incredibly strong and astoundingly heat and chemically resistant polymers, which are often used for replacing glass and metals, such as steel, in many demanding industrial applications. They can also be used in circuit boards, insulation, fibres for protective clothing, composites, and adhesives. Aromatic heterocyclic polyimides are typical of most commercial polyimides, such as DuPont's Kapton®. These polymers have such incredible mechanical and thermal properties that they are used in place of metals and glass in many high performance applications in the electronics, automotive, and even the aerospace industries. These properties come from strong intermolecular forces between the polymer chains. In this work, a composite laminate AKAFLEX KCL, made of a Kapton® VN layer and copper layer, whose thickness was 25 μm and 17 μm respectively, was used for the sensitive membrane and purchased by August Krempel Soehne GMBH & CO.KG (Germany).

4.1.2 Epoxy resin

FR4 laminate is the usual base material from which plated-through-hole and multilayer printed circuit boards are constructed. "FR" means Flame Retardant, and Type "4" indicates woven glass reinforced epoxy resin. The laminate is constructed from glass fabric impregnated with epoxy resin and copper foil, which is commonly supplied in thicknesses of approximately 18 μm or 35 μm. Foil is generally formed by electrodeposition, with one surface electrochemically roughened to promote adhesion. FR4 laminate displays a reasonable compromise of mechanical, electrical and thermal properties. Dimensional stability is influenced by construction and resin content. Generally, heavyweight glass fabric gives a more dimensionally stable material, although it is necessary to use

lightweight fabrics for high layer count multilayer circuits laminate Three types of FR4 laminate have been employed :

- FR4 DURAVER NEMA 156   : 510 μm of thickness with 35 μm copper thickness (both side)
- FR4 DURAVER-E-CU 104ML : 200 μm of thickness with 35 μm copper thickness (both side)
- FR4 DURAVER-E-CU 104ML : 125 μm of thickness with 17 μm copper thickness (both side)

4.1.3 Bi-adhesive

M3 VHB 9469 double coated adhesive was used for assembling the sensor layers. VHB tapes are usually employed for bonding a variety of substrates, including most metal, sealed wood and glass, as well as many plastics. They are characterised by specific features such as high tensile strength, high shear and peel adhesion, resistance to solvent and moisture, low outgassing and conformability. The tape is double coated by two 50 μm protective layers, presenting a total thickness of 130 μm (± 10% tolerance) and was purchased by 3M, Industrial Adhesives and Tapes Division (US).

4.2 Methods

The sensor fabrication consists of two steps: the first that produces the base, the spacing and the membrane layer of the pressure sensors, while the second step concerns the assembling of the parts. Every layer is obtained by standard PCB fast prototyping techniques

Conductive routing

Spacer   Base   Base
                Top   Bottom
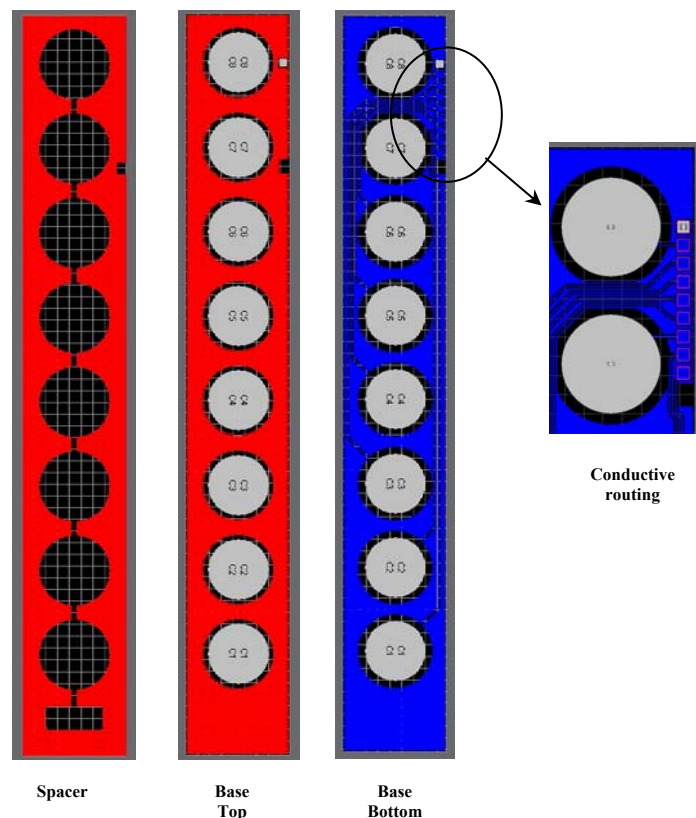
Figure 4.1: Pressure sensor layers gerber file representation A particular of the base tracks is shown, where every pad connection is surrounded by tracks acting as a guard ring for decoupling the every transduction in the different pads.

This first phase was processed by the manufacturer through the gerber files. The layers were bonded together by bi-adhesive films. To perform the layer bonding we built a particular assembler device working with a vacuum table. The base is a double sided copper layer of (200 um of thickness with 35 um copper thickness). A simple representation of this part is shown in Fig. 4.1. The circular pads (lower capacitor electrodes) can be electrically connected by the Vias pads on the bottom side. The spacing is composed of a layer of FR4 156 (125 um of thickness): on the upper and the lower face of this layer is set a bi-adhesive tap (3M, 200Mp), in order to create the internal chamber, the sandwich is milled after the application of the adhesive on both side of the spacing layer, without peeling off the remaining external coating protection. Finally, the membrane is a polyimide double-sided copper-clad layer of Kapton; to create the pressure taps 3 holes are drilled in the membrane. The differential capacitive strip sensor built in our laboratories it's a multilayer structure. To create every sensor layers a particular fast prototype machine : LPKF Protomat S62 has been used, Fig 4.2.

Figure 4.2: LPKF S60

This machine by means of milling tools, it's able to draw, on a FR4 substrate or other materials (sheets of plastic, aluminium, copper) electronic circuit, and mechanical structures. The LPKF is a three axis machine able to work with a maximum of 10 different tools in the same job, creating holes of different diameters and drawing lines with a width of 100 um with a precision of 10 um working on the horizontal surface (X,Y).

4.3 Base Fabrication

The BASE layer is an FR4 substrate covered by a double layer of copper. The copper thickness on each side of FR4 is 35um, the Fr4 thickness is 200 um. After the creation of the project by means of an electronic CAD, the sensor sketch is exported into the prototype machine management software. The fast prototyping machine area is able to milling seven sensor layers at once. The three different layers have been realized and bonded in the assembly procedure all at once, and subsequently divided by each others. In the BOTTOM side of the base layer the electronic paths and the pads necessary to carry out the electronic signals are present Fig. 4.3 (a). In the TOP side of the base layer the fix electrodes of the capacitors are milled. The signal of every fixed electrodes in the upper side is routed to the electric paths on the bottom, by means of cooper coated drills Fig 4.3 (b).
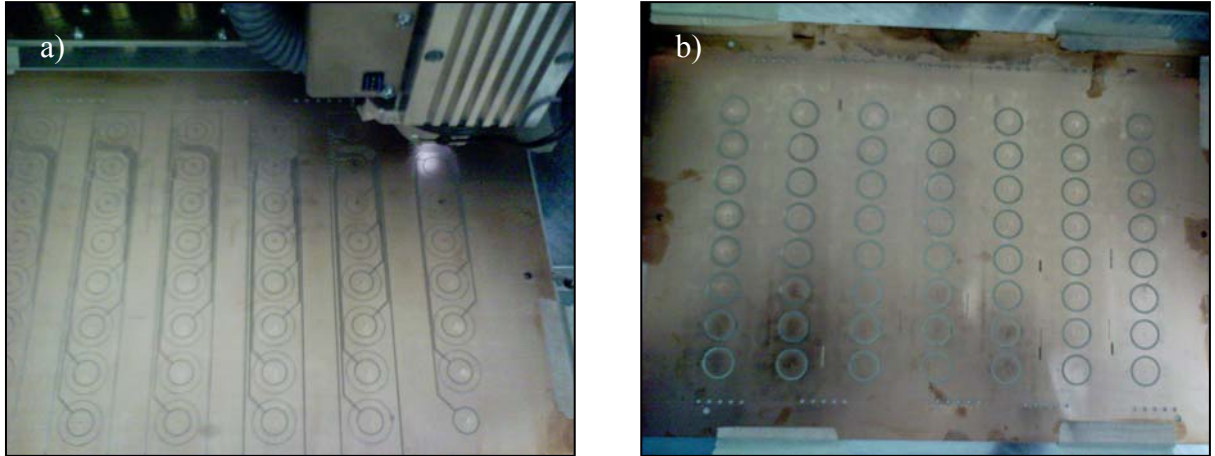
Figure 4.3 : a) Base layer bottom side with signal routing, b) Base layer top side with circular fix electrode

Any copper coated drills has been sealed from the external environment by means of a Kapton® layer to avoid air to penetrate inside the cavity of every sensing unit. The Kapton® layer is also useful to preserve, the electronics pathes in the bottom side of the base, from oxidation Fig 4.4.
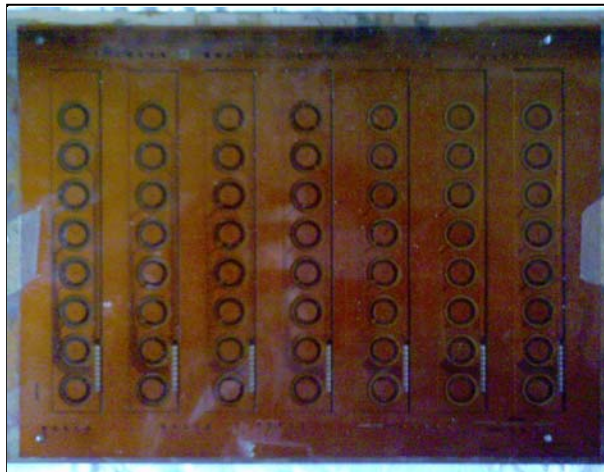
Figure 4.4 : Bottom side BASE sensor covered by Kapton layer

4.4 Spacer fabrication

Spacer is a rigid glass-fibre layer, used to crate the internal sealed chamber of any sensing unit. All unity chambers are connected by miniaturised pipes, patterned in the spacing layers, in order to share the same internal pressure, forming a unique bigger chamber. The spacer layer is an FR4 substrate where the copper layers has been chemically removed, the Fr4 thickness is 200um, this layer when bonded to the base create the inner circle cavities wherein the circular electrode are present and the membrane is deflected. The layers bonding is performed with a thin acrylic bi-adhesive layers both for the base-spacer and the spacer-membrane junction, thus the bi-adhesive layer has been first bond in upper and lower side of the FR4 spacer layer before the milling process, acting in this way the spacer and the two bi-adhesive layers are shaped at once Fig 4.5.

48

Figure 4.5 : Spacer structure covered by bi-adhesive tape

4.5 Membrane fabrication

The membrane layer is a 25 μm thick deformable copper-clad (17 μm) Kapton® polyimide composite layer. Small holes are drilled on the proximity of one the ends of the sensor, before the first sensing element and act as a pressure reference. A VIA is designed for the connection of the upper membrane electrode, through the same flat cable used for connecting the base electrode.

4.6 Assembly Device

The assembly procedure has been performed by means of a special assembler built in laboratory of the faculty. The assembly device is presented in Fig. 4.6 (a), it is compose by three floor of which just the middle one is movable. The bottom floor is fixed on the ground and by means of three reference pivots allows the alignment of the base layer settled on it. The movable floor is actuated by a circular crank handle, and it also house three reference pivots to perform the layers alignments. Moreover the movable floor is a suction surface, in fact it is connected, by means of a rectangular sealed chamber and a circle plug, to an extractor fan. It is thus possible to lay, subsequently both the spacer and membrane layers to the movable floor, and to lower the floor to perform first the base –spacer junction and then the spacer-membrane junction, to complete the assembly procedure. In Fig. 4.6 (b) the assembler device completely lowered is shown.
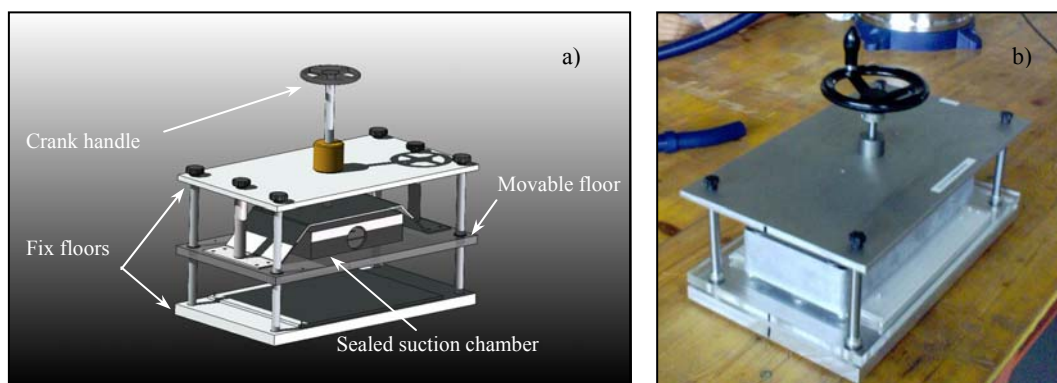
Figure 4.6 : a) Base layer bottom side with signal routing, b) Base layer top side with circular fix electrode

4.7 Base – Spacer junction

The base spacer junction is performed aligning the sheet containing the seven base layer, above the fix floor, through the three reference pivot; the base layer is arrange to share the top side (the one with the fix electrode) towards the movable floor Fig. 4.7 (a). The spacer layer is aligned above the movable suction floor 4.7 (b), the bi-adhesive protective film is removed and subsequently the movable floor is lowered to perform the bonding process. To obtain an optimum adhesion, the bonding surface must be well unified, clean and dry. At room temperature, approximately 50% of the ultimate strength will be achieved after 20 minutes and 100% after 72 hours. In Fig 4.8 the base and spacer layers are shown after the bonding process; the top side of the spacer still present the bi-adhesive protection film that will be removed in the following spacer-membrane junction.
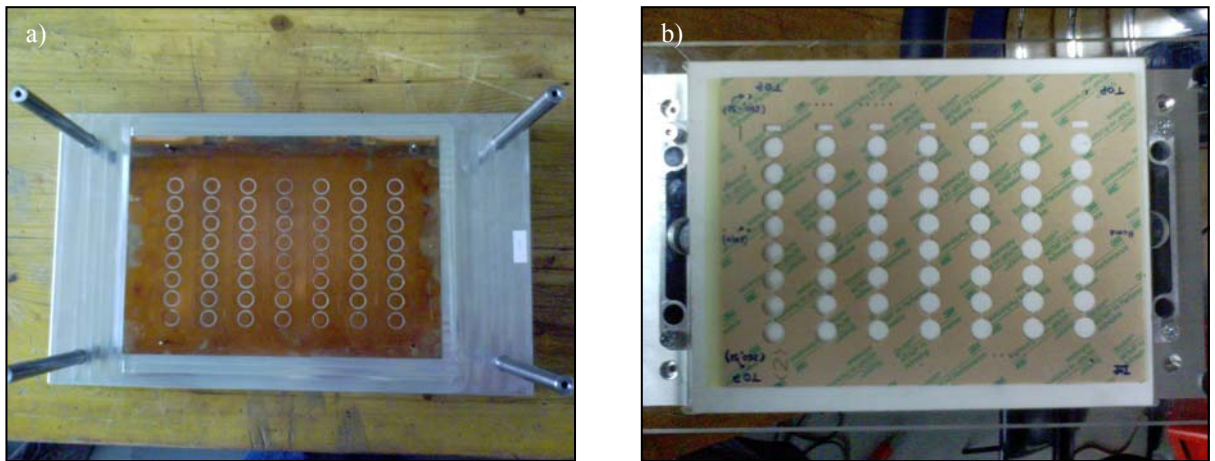
Figure 4.7 : a) Base layer top side, b) Spacer layer bottom side with bi-adhesive tape
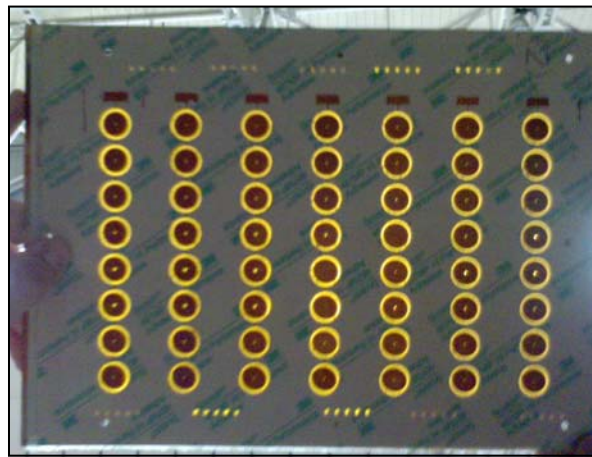
Figure 4.8 : Base layer bottom side with signal routing

4.8 Spacer– Diaphragm junction

The spacer membrane junction is performed aligning the previously bonded base and spacer layers above the fix floor; the bi-adhesive protection film is removed from the upper side of the spacer. The membrane layer is aligned above the movable floor and is arrange to share the bottom

conductive side toward the bi-adhesive layer, the suction performed by means of the suction surface ensure the planar shape of the flexible membrane.
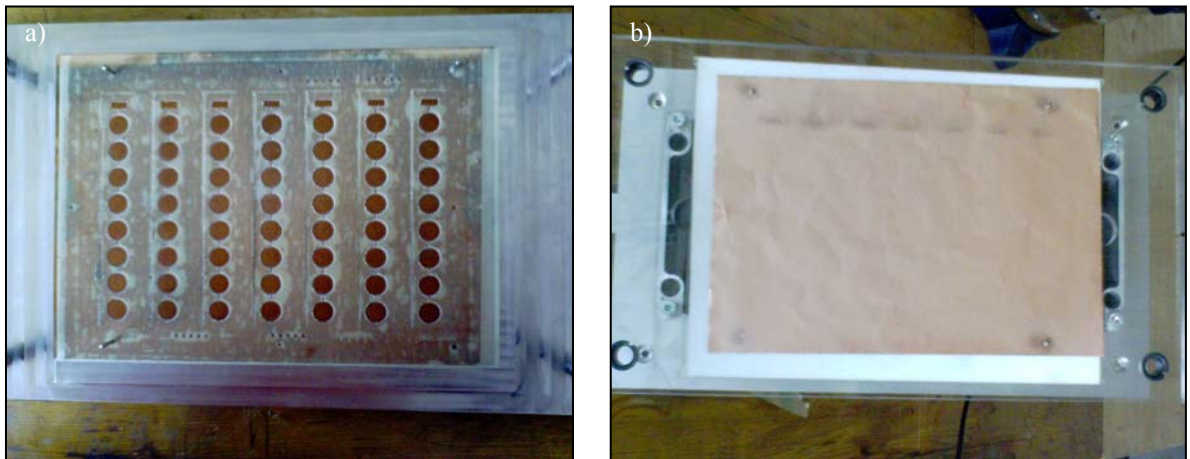
Figure 4.9: a) Base layer bottom side with signal routing, b)Membrane bottom side, the cooper layer will be bond above the spacer top side

Subsequently the movable floor is lowered to perform the bonding process, in Fig. 4.9 (a) and (b) the bottom and the top side of the assembled array are shown.
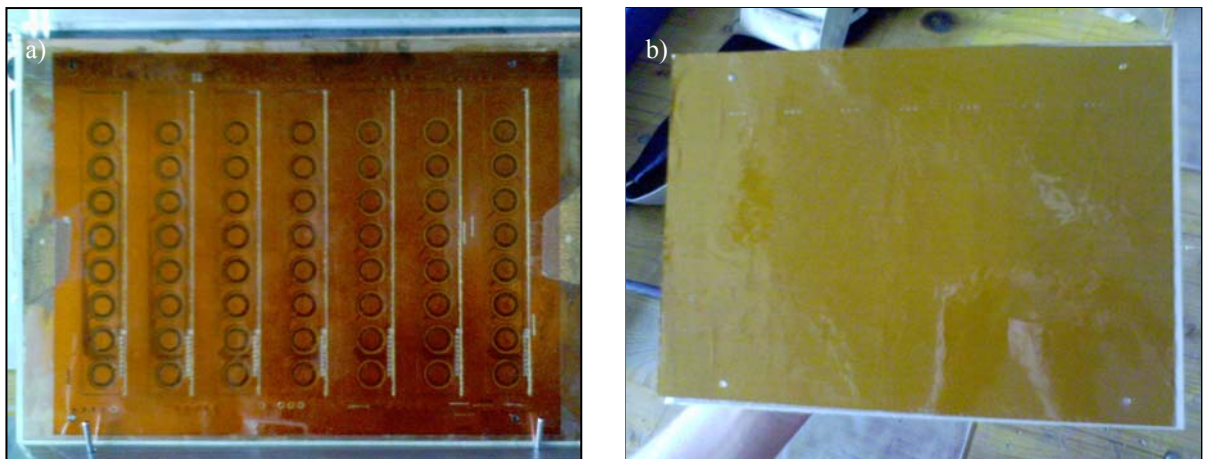
Figure 4.10 : a) Base layer bottom side with signal routing, b) Membrane top side

Finally the array of strip sensor is aligned inside the PCB prototyping machine to separate along the edge the single sensor unit. In Fig 4.11 one of the final strip sensor fabricated is presented.

Figure 4.11 : Base layer bottom side with signal routing

Chapter 5

Experimental results

Two series of sensor prototypes were tested in the wind tunnel of the II faculty of engineering. The first sensor series prototypes were build by a PCB Swiss manufacturer[1] while the second one were completely fabricated in our laboratory as described in chapter 4. Two types of analysis were set up. The first test was intended to validate the large deflections and the creep simulation models for the sensitive unit in the array: this was obtained by applying several pressure values (in a range from tens to hundreds of Pa) on the device membrane by means of sealed chambers that allow an independent measurement to be conducted on each sensing unit. The second test was set up to assess the performance of the strip and its functionality on a wing profile.

5.1 Experimental setup

The experimental tests performed were aimed to obtain the static characteristics of the sensor, and to test the long term behaviour of the sensor in order to depict the viscoelastic behaviour of the sensor membrane. The setup, shown in Fig. 6.1, is composed of a wind tunnel, a Pitot tube, sealed chambers for applying loads independently on the sensor membranes, a conventional silicon-based pressure transducer, an LCR meter, the read-out electronic circuit and a Labview interface control system. In order to apply different pressure values on the membranes, a system made of a wind tunnel and a Pitot tube was used. Low pressure values, such as those in a range of units to hundreds of Pa, are in fact very difficult to obtain statically
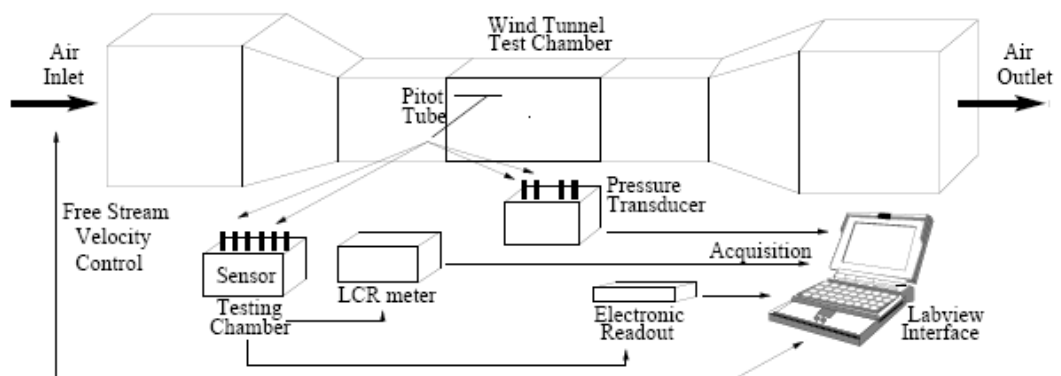
Figure 5.1 : Sealed chambers setup for performing static characteristic acquisition and creep measurements on the sensors array

to obtain statically acting on small volume variations because of the temperature drift and of the pressure waves propagation, which create instabilities in the resulting thermodynamic pressure. This problem was avoided by using, as a referenced applied load, the dynamic pressure obtained from a Pitot tube inserted in the wind tunnel test chamber. Varying the wind tunnel free stream flow velocity, various pressure values can be achieved as the difference between the static pressure and the total pressure, as represented in Fig. 5.2.
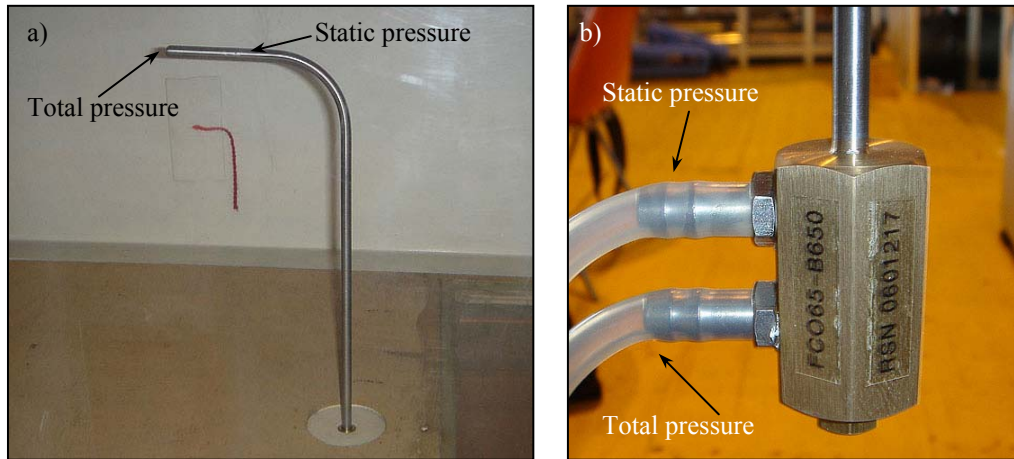
Figure 5.2 : Pitot tube inside the test chamber (a), Total and static pressure pipe (b)

Fig. 5.3 shows one of the PVC airproof devices built in one of the laboratory facilities by means of a numeric-controlled milling machine. The PVC device is composed by a base, Fig. 5.3 where the sensor is leaned, and a lid where two sealed chamber have been milled; in the smaller sealed chamber by means of three static taps in the forward part of sensor, the reference pressure is led inside the internal chambers of any sensing units, while in the larger sealed chamber a different pressure value is led, thus any sensing unit share the same differential pressure.
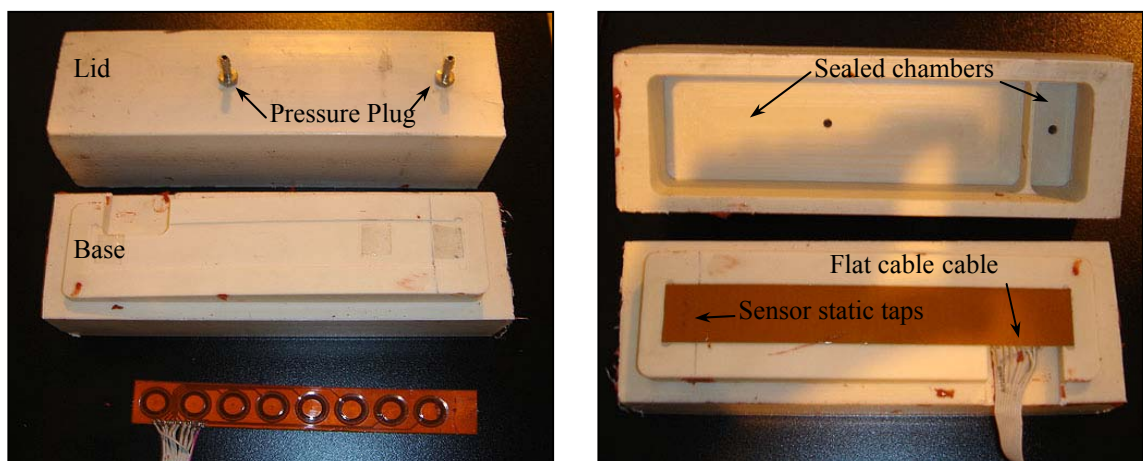
Figure 5.3 : PVC airproof devices

Every capacitor of the sensor is connected electrically to an instrument by mean of a flat cable, soldered to the array. A conventional silicon pressure transducer, a Setra® Capacitive Instruments, connected to an National Instrument acquisition board, is used to measure the pressure .

53
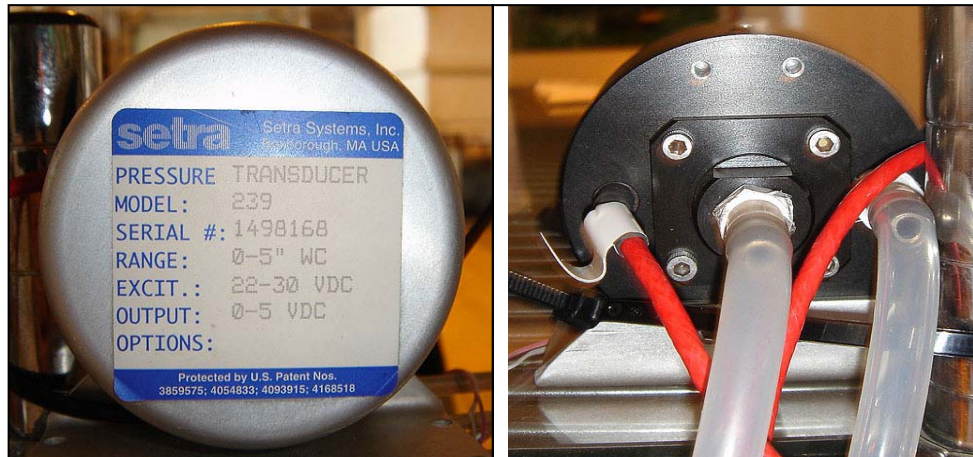
Figure 5.4 : Setra® pressure transducer front and back view

The data acquisition was performed by mean of a LCR meter Fig 5.5 and by means of a capacitive sensitive electronic circuit. The LCR meter is used to measure directly the capacitance values in order to assess the accuracy of the characteristic evaluated by the theory and by the FEM simulations. The circuit measurement was performed for an estimation of the parasitic and for optimising the circuit parameter in order to maximise the sensitivity of the electronic.. Data have been sampled by a National Instrument PCI-6070E High Performance 1.25 MS/s 12-bit multifunction acquisition board, controlled by a Labview program Fig 5.5 , written in order to rule automatically the whole setup.
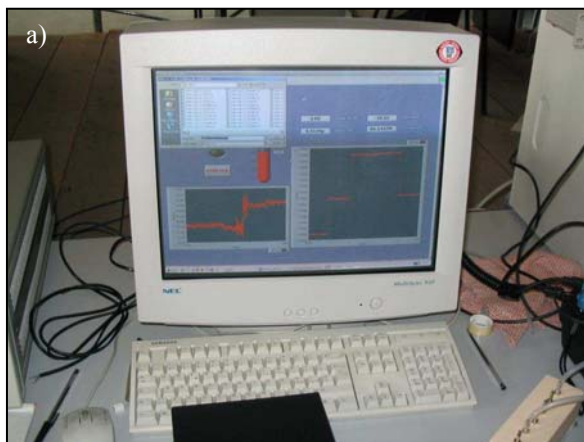
Figure 5.5 : Programmed Labview interface (a), Agilent 4284A Precision LCR meter (b)

5.1.1 Static characteristic – Swiss type series sensor

A set of different constant pressure values were exerted on the sensor membrane, each value being applied for an acquisition period of about sixty second , by mean of the sealed PVC device shown in Fig. 5.3. The static sensor characteristic and the creep drift was obtained by the modelling procedure described in chapter 3. The experimental characteristic is thus obtained and compared with static simulations, as represented in Fig. 5.6, showing good agreement and confirming the FEM models as a reliable mean for the sensor design.

54
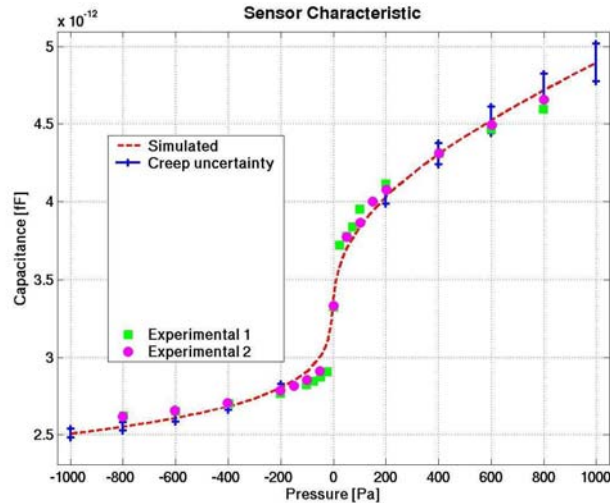
Figure 5.6 : Experimental and Simulated characteristic, creep uncertainty

A calibration still remains necessary for providing the sensors capacitance pressure relationship. This is a non linear relationship, that strongly depends upon geometries, uncertainties due to materials and process tolerances. This affect the curve in terms of initial conditions and capacitance variations, because of the highly non linear large deflection formula and the hyperbolic relationship of the capacitance with respect to the plate separation. Sensors have shown a resolution of 2 Pa in a ± 2k Pa range ±1% of full range precision, due to the creep drift.

However, the high non-linearity of the pressure-capacitance relationship must be analysed with more accuracy defining the drift imprecision on the output referred to every point of measurement, due to the fact that creep is a stress-modulus related phenomenon and a different deflection variation is then expected depending upon the stress present in the membrane. This can be taken into account considering a linear creep theory and adjusting the equivalent time-dependent elastic modulus E(t) with a linear coefficient, proportional to the stress present in the specimen. For instance, a look-up table of time-strain curves related to several stress values, as the one presented in Fig. 3.9 in chapter 3, and extracted from Kapton® [59] data sheet, should be written. A numerical procedure based on experimental data is presented in chapter 9 to develop an error model suitable to predict the inaccuracy bound due to viscoelastic phenomena.

5.1.2 Creep measurement - Swiss type series sensor

In Fig 5.7 the response to a constant load of an ideal sensor and the response of a sensor affected by viscoelastic phenomena When a constant pressure load is applied it is possible to distinguish two superimposed dynamics: an instantaneous response due to the elasticity of the membrane and a slower one due to the viscoelastic behaviour. In order to simulate the latter phenomenon, a time dependent modulus of the elasticity was used, as described in chapter 3. With this approach, any experimental testing or feedback analytical procedure is required to find out FEM model parameters: any coefficient can be extracted directly from material data sheets with a good approximation, though for achieving more accurate results, a dedicated reference table for every membrane geometry is required, through which a more accurate description can be given depending upon the stress present in the membrane.

Ideal Sensor
Applied Pressure = constant

Real Sensor
Applied Pressure = constant

(a)

(b)
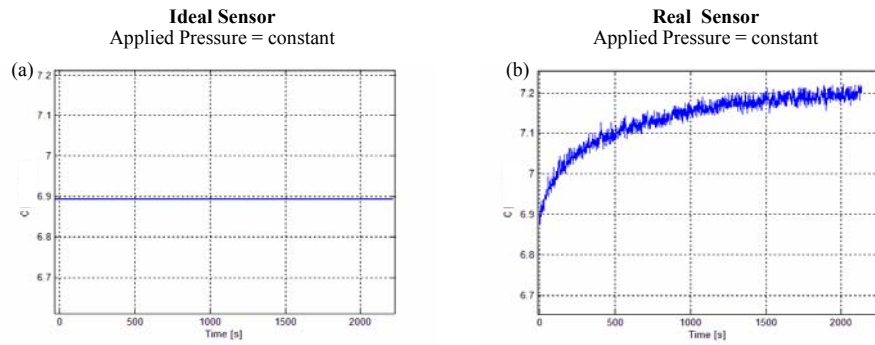
Figure 5.7 : Response to a constant load of an ideal sensor (a), and the response of a sensor affected by viscoelastic phenomena (b).

As shown in Fig. 5.8, the simulation fits to the experimental viscoelastic behaviour with a 1% error in the worst case, at the very beginning of the experiment (0-300 seconds). The proposed method, being based on the estimation of the global variation due to creep for a constant applied load, can be considered a reliable procedure for the simulation of the viscoelastic effects.
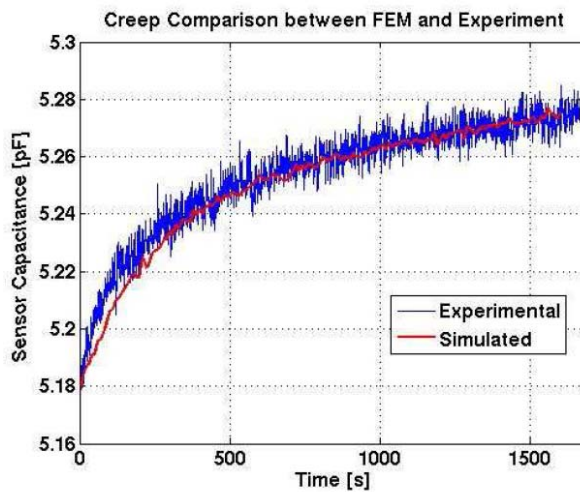
Figure 5.8 : Capacitive response due to membrane viscous behaviour: comparison between experiment and simulation.

In order to understand the viscolelastic behaviour of the sensor a series of long term experimental tests has been carried out. The experiments was performed by applying four different steps of constant pressure over the membrane, for the whole time interval required to reach an asymptotic constant value of capacitance output. The four pressure loads imposed in the test procedure was +200, +400 +600 +800 Pascal. The loads chosen are defined positive when the membrane deflect itself inside the cavity of the sensor thus producing the higher value of capacity output.

56
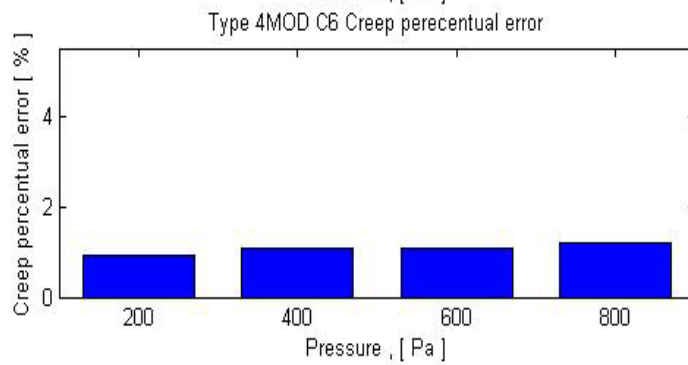
Figure 5.9 : Creep drift error

Positive constant pressure loads was chosen cause this is the condition where the time dependent viscoelastic deflection of the membrane is more amplified by the closer distance between electrodes. The creep drift error measurements performed in the tests has shown a maximum error of 1,1% of the FSO for a pressure of 800 Pascal

5.1.3 Static characteristic – Home built type sensor

The second series of experimental tests concerns with the home built senor. The fabrication process and the material employed are crucial issues in obtaining an affordable pressure sensing device; therefore a certain fabrication experience must be achieved. Tests on the first home built prototypes have revealed the lack of repeatability in the static characteristic behaviour of the eight sensing unit of which the strip is composed.
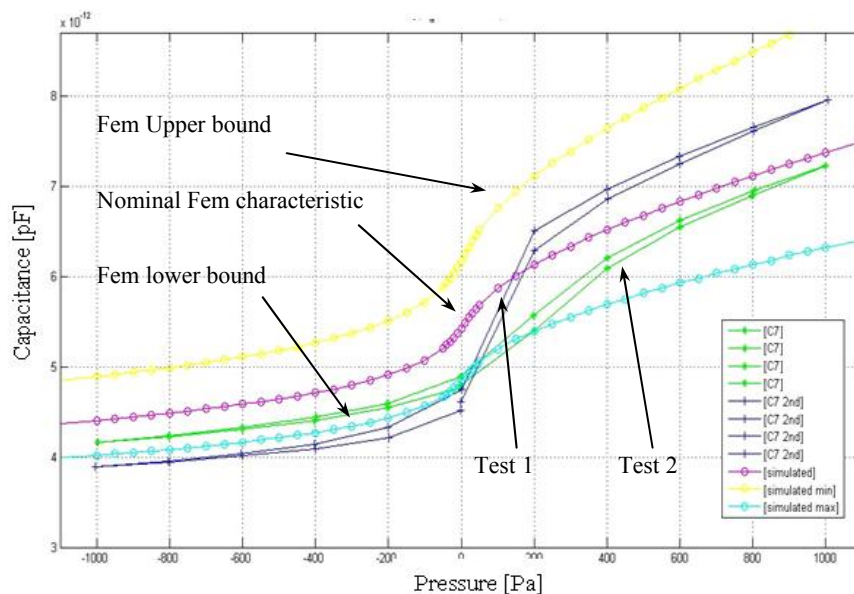
Figure 5.9 : Experimental an simulated static characteristic

In Fig. 5.9 two experimental static characteristics related to the same sensing unit are shown, moreover the Fem nominal characteristic and the two Fem bound related to materials tolerance are superimposed. The two experimental function, performed at different time instants, reveal a completely different behaviour, for low value of pressure between +/- 200 Pascal the function

57

slopes are different. At higher pressure value the slopes of the two tests share the same trend but the absolute value of capacity is different. Further investigation has revealed how the lack of long term repeatability is due to the lack of a pre-stress level in the diaphragm of the strip; this cause a lack of planarity in the membrane causing different membrane equilibrium shapes for low pressure value. To overcame the problems the assembly device described in chapter 4 has been modify to provide a certain pre-stress level in the Kapton diaphragm before bond it to the spacer layer Fig.5.10.
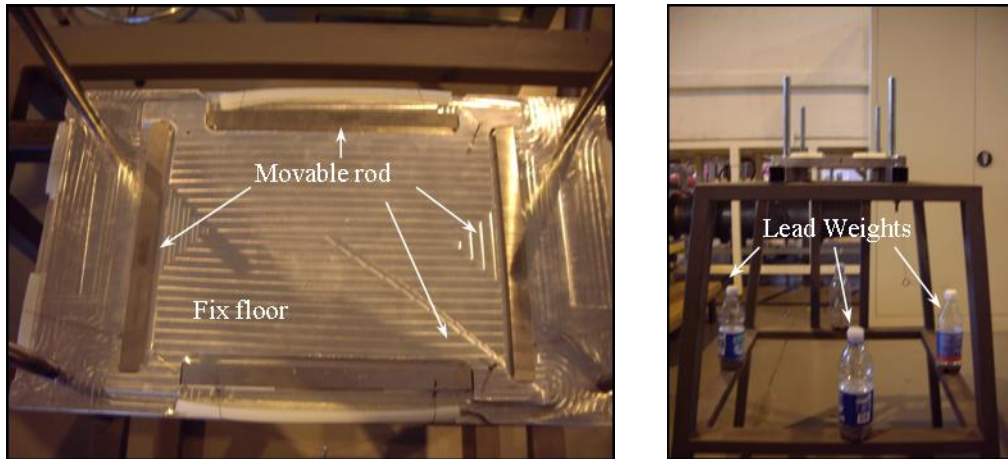
Figure 5.10 : Modified assembly device

Four movable rods have been set at the same level of the fix floor, in the assembly device; any rods was linked by means of lines to four known lead weights. The Kapton® sheet is first lean on the fix floor and bond with an adhesive tape to the four movable rods; the lead weights are then applied and the Kapton® is pre-stressed. Subsequently the spacer layer leaned on the movable suction floor describe in chapter 4, is lowered and bonded to the stretched diaphragm. New tests have been performed with the pre-stress diaphragms and an acceptable repeatability is gained Fig 5.11.
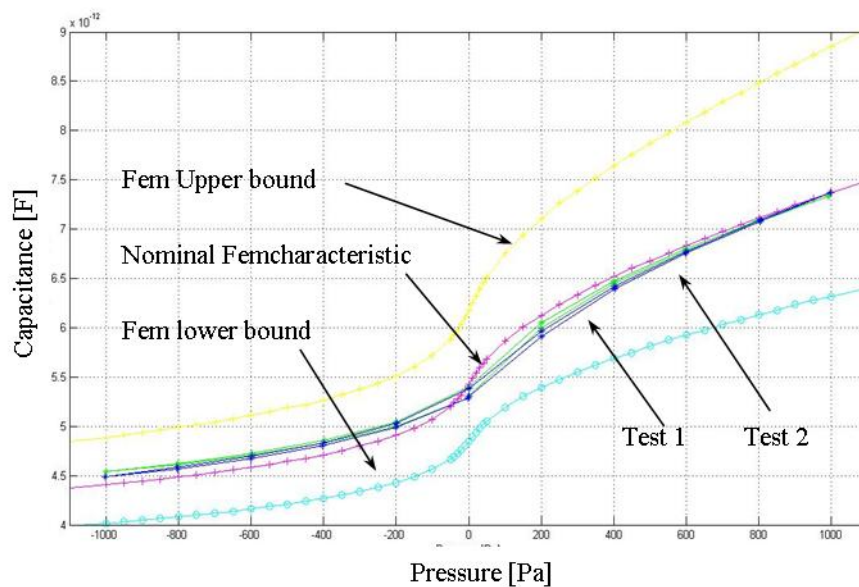
Figure 5.11 : Experimental and simulated static characteristics performed with stretched diaphragm

Unfortunately the pre-stress procedure doesn't guarantee an uniform strain of the kapton sheet moreover if a certain value of lead weight is exceed the sheet shape is not planar anymore. The pre-
58

stress assembly device so far described has been suitable to understand that a certain level of pre-stress is necessary to let the sensor be repeatable in the whole full scale input and stable when low pressure input values are applied, but to be able to understand the role of pre-stress a new device able to perform a known and repeatable stress-strain level in the diaphragm must be attained.

5.1.4 Creep measurement - Home built type sensor

As far as creep measurements on home built sensor are concerned these have been performed in the same manner, but tests reveal a worst viscoelastic behaviour if compared with the Swiss series sensor type.
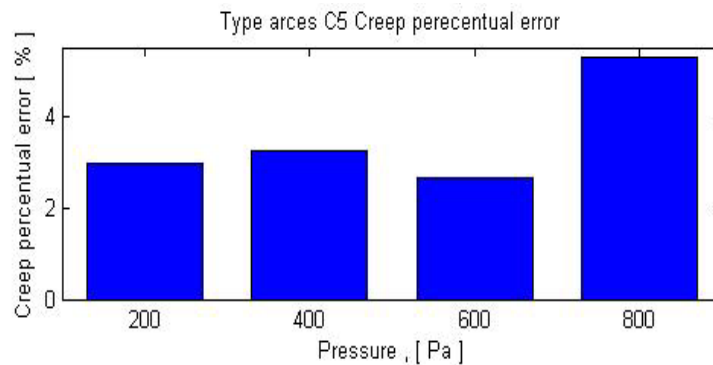
Figuere 5.12 : Creep drift error

The maximum creep drift is 5% of the full scale output for a pressure of 800 Pascal. The main reason for the worst behaviour of the home built sensor has been identified in the material employed in the fabrication of the device. In fact was not possible to find anymore on the market the same type of kapton used for the Swiss sensor type. Kapton as many polyamide products is made in a wide variety of blend and thickness and even if the Kapton-copper layer employed has the same thickness the mixture of copper bonded to the Kapton layer is slightly but crucially different. Depending upon the materials, viscoelastic behaviours can manifest at ambient temperature and for stress bigger than 1MPa [5,38] [16,17,29,30,31], As reported in [5,38,40-47][16,17,39-47], creep manifests primarily in two components of the sensor structure: the deformable membrane and the solder adhesive (or glue) used to bond the membrane to the sensor support. The membrane and the gluing substance show viscoelastic behaviour typically when polymeric (polyimides, resins) or composites materials (polymers and thin copper-clad films) are employed, and whenever the stress in the material (plastic, metal or alloy) approaches the yield stress, the viscoelastic behaviour is also strongly dependent on the temperature. Creep in polymers, at ambient temperature, is due to temporarily conformational rearrangements of the polymer macromolecules under an applied stress, leading to a time dependent deformation. This can be totally recovered [48,49] if the material yield stress inside the specimen is not exceeded. Instead creep in thin copper film $(0.1 - 10$ um thick at ambient temperature) can never be recovered, being due to dislocation of the copper crystals [49,50] and being strongly dependent on crystal size [51-53]. Crystal copper size is in turn strongly dependent on the chemical process used to bond the copper layer to the Kapton®. In conclusion the lack of an appropriate pre-stress level in the diaphragm and the different chemical process used to bond the copper layer to the new Kapton® sheet are the two main reason for the worst behaviour of the home built sensor if compared with the previous Swiss sensor series prototypes.

5.2 Wind tunnel setup

59

Tests on the real aerodynamic surface for which the strip sensor is design for, have been performed. The experimental test describe hereafter are referred to he Swiss sensor type. In order to test the functionality and the performance of the strip, a NACA 0015 wing profile was chosen for the first aerodynamic test to be performed. Experiments were made by building the setup shown schematically in Fig. 5.13. The sensors strip is positioned on a wing profile surface able to vary its incidence thus changing the pressure distribution above the upper and lower surface of the profile.
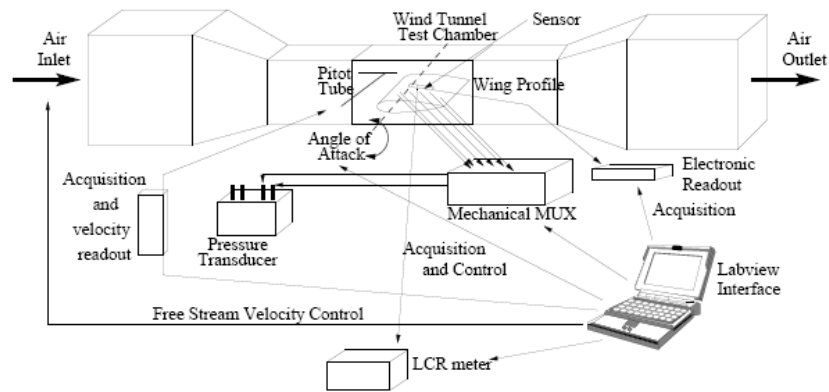
Figure. 5.13: Wind tunnel setup for acquiring sensor strip performance featuring an example of aerodynamic application.

Data can either be acquired by a readout circuit that can be placed inside the profile, or by an Agilent 4284A Precision LCR meter, providing direct measurements of capacitance variation. To compare the polyimide sensors measurements to a conventional technique, an orifice array has been drilled on the profile along the sensor strip and pneumatically linked to a Scanivalve® differential pressure transducer (Mechanical MUX). The advantage of using this type of aerodynamic body lies in the fact that, at a small angle of attack, the results coming from the two experimental techniques can be compared and validated with the results of numerical simulations. The setup instrumentation is ruled by a Labview program, built for the automation of the acquisition procedure. A modular decomposable PVC bi-dimensional wing, based on a NACA 0015 profile, was built in the laboratory facilities by means of a numeric-controlled milling machine, as shown in Fig. 5.14 (a). The strip is positioned in a recess on a wing profile surface in a special holder embedded in the profile (Fig. 5.14 b) and data can either be acquired by both a read out circuit and an LCR meter by means of different connections.
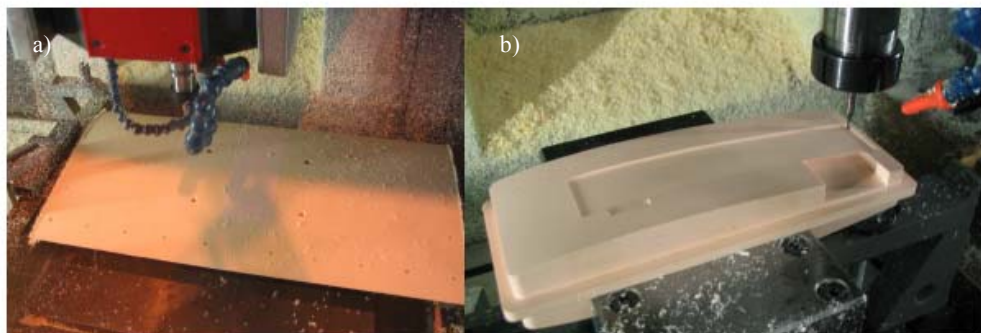
Figure 5.14: Decomposable NACA 0015 wing profile. Global view of the profile during milling (a). Particular of the sensor holder on the wing profile (b).

Circuitry can be hosted inside the profile in order to reduce parasitic and the noise level. The sensor, due to its conformability can assume the same curvature of the aerodynamic object, thus allowing a negligible perturbation of the aerodynamic environment. An array of pressure taps were drilled into the profile, along the sensor strip (Fig. 5.15 a), and pneumatically linked to a Scanivalve® differential pressure transducer (Fig. 5.15 b). The Labview software interface is programmed for acquiring pressure distribution from the electro-mechanical transducer simultaneously with the sensor, which can be interface by electronic or by a LCR meter. Before every acquisition run, the wind tunnel free stream velocity and the angle of attack of the profile is set. The advantage in using this type of aerodynamic body lies in the fact that, at small angle of attack, the results coming from the two experimental techniques can be compared and validated with the results of numerical simulations. In the last version of the setup, a stepper motor is used to change dynamically the angle of attack and in order to obtain a fully automated process of acquisition.
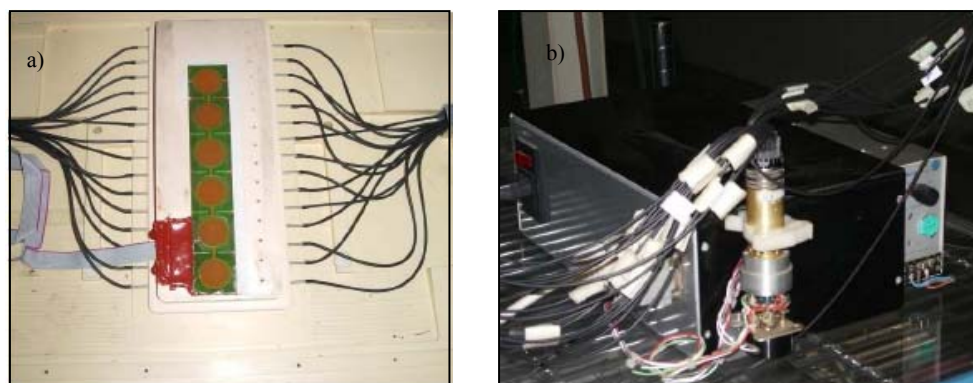
Figure 5.15 : Static tap above the Naca 0015 (a), Electro-mechanical MUX (b)

5.2.1 Wind tunnel measurement

Experiments were made in the wind tunnel for different angle of attack in a ± 8∘ range and for different free stream velocities up to 45 m/s. In Fig 5.16 the experimental set up is shown. Experimental wing profile pressure distribution data, acquired with the proposed device and conventional sensor output are reported in Fig. 5.17. For every strip membrane, the corresponding calibration characteristic curve C = fi(P), is inverted to directly represent the sensor response in terms of pressure values, where the subscript i stands as a marker for every membrane. The corresponding parasitic capacitance of each membrane must be subtracted to the characteristic capacitance curve before inverting the pressure-capacitance relationship since every value is different due to the topology of the cabling system. Experiments have been conduced for 15 min for every free stream velocity and angle of attack. The first sensor chamber measures no gradient and the other chambers measure an increasing pressure gradient.
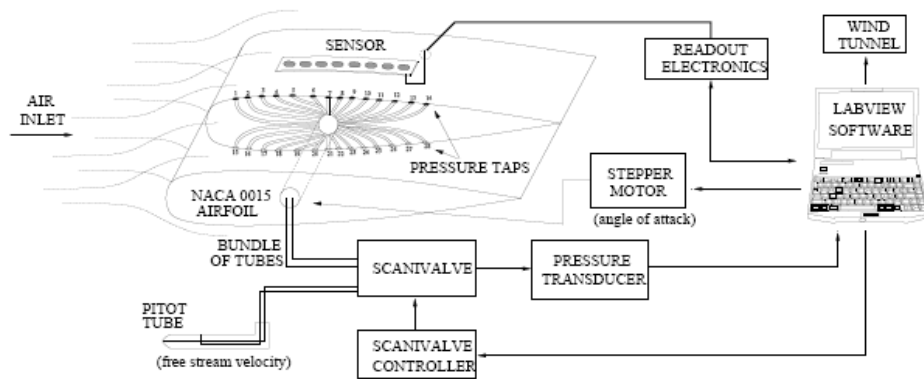
Figure.5.16 : Naca 0015 profile and wind tunnel set up

Important is the surface occupation of every unity block: the smaller the chamber's area, the higher is the spatial resolution, justifying the approximation of a constant pressure over a chamber membrane. Fig. 5.17 shows the pressure pattern, for a 5 degree angle of attack and 40 m/s free stream velocity, in the top and the bottom part of the wing in the central zone.
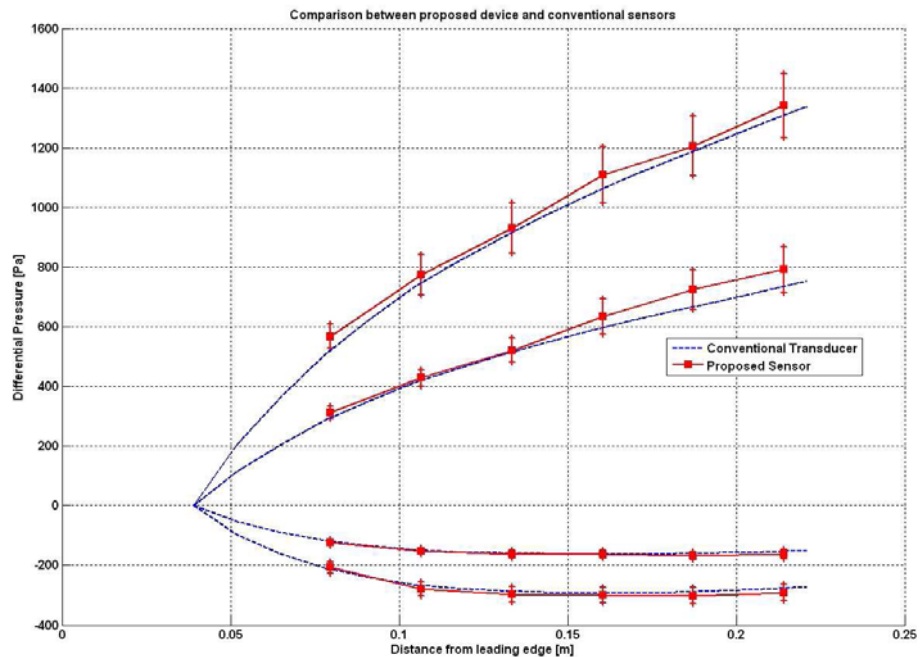
Figure.5.17 : Experimental pressure profile measurement obtained from the proposed device compared with Scanivalve transducer

Every pressure value represents only the pressure variation and it is necessary to add an offset to obtain the absolute value for the pressure. As described previously, the sensor structure is not able to measure an absolute pressure, but is able to work at every altitude. A solution with polymer membranes would be impracticable because of the pressure variation, which, due to the altitudes involved, would be much greater than hundreds of Pa.

5.3 Electronic circuit configuration

This part is reported in this work only for completeness and not in detail, because the project of developing the electronics was accomplished by other colleagues in the laboratory group and the author was involved in the circuit design only marginally, during testing and not in the design phase. Two different circuit configurations were developed for the read-out of the front and back-end of the sensor network. The first configuration was tested and data were acquired both with the chamber and the wind tunnel setup. The second configuration is still under development.
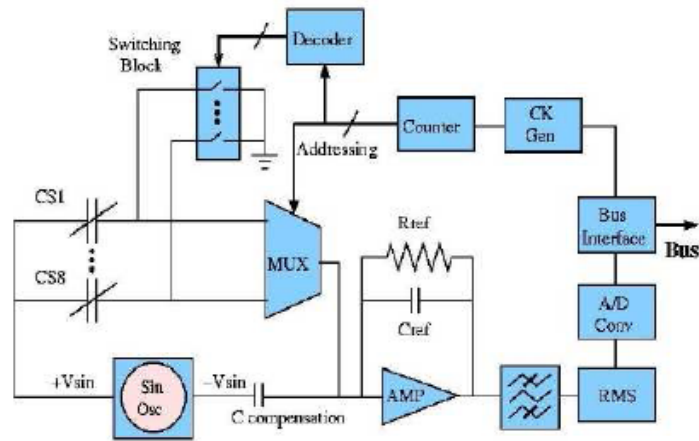
Figure 5.18 : AC sensing circuit diagram

Fig. 5.18 illustrates the electronic readout system, which is based on an AC sensing methodology. Its implementation relies on embedded off-the-shelf components and allows high sensitivity in the capacitance transduction. The core of the circuit is composed of a 20 kHz frequency oscillator built using a Wien-Bridge architecture, a charge amplifier, a second order band pass filter that generates an output waveform with a total harmonic distortion (THD) lower than 1% and a true RMS-to-DC converter. An 8-bit A/D converter coupled with a 1-Wire® interface converts analog signal into digital. In order to share these elements among all the transducers present on a strip, an analog multiplexer is also introduced, so that the strip capacitance can be selectively switched into and out of the charge amplifier. In order to reduce the interference and the noise due to capacitive coupling, the unused pads are grounded. Due to the above described capacitance switching method, the addressing of the individual sensing units by the bus master happens at two different levels. On one hand, by using the typical slave addressing methods offered by the 1-Wire® protocol, one addresses the strips as a whole. On the other hand, by sending appropriate data (i.e., commands) on the bus, one indicates to the strip which individual transducer to make active. The multiplexer is in fact driven by a state register/counter whose content can be updated in an incremental way. The clock signal of the counter is obtained by exploiting a channel of the A/D converter forced to operate as a digital output. A level transition generated on the above mentioned pin and properly elaborated with an ad hoc circuit, triggers the counter. Further logic assures the possibility of initialising the counter when required or whenever all the capacitive pads of the strip have been sensed. In the prototype realisation, the power supply to the strips is assured by a dedicated line. All the components have been chosen in order to reduce noise and power consumption. In this implementation the interface circuit has a 3 mA current consumption. The data acquisition algorithms by which the master unit manages the sensor network and the data acquisition from the sensor strips have been optimised in order to monitor all the network, maximising the data acquisition rate. The 1-Wire® bus can operate at two different communication rates: in standard mode (16.3 kbit/s) and in overdrive mode (142 kbit/s). The proposed architecture can use either mode, depending on the bus extension and is

scalable and reconfigurable to a variable number of sensor strips. At power up or whenever a re-initialisation is requested, a search algorithm running on master unit allows all the units of the network to be detected. If, due to some fault, there is a strip which is unable to transmit data, it can be identified and excluded from further monitoring processes. The initial monitoring condition is activated by a bus re set command. After initialisation, the system enters its monitoring loop. Here, to maximise data acquisition speed and reduce the addressing overhead, the addressing of all the strips, the selection of the specific sensing unit within each strip and the A/D conversion command are sent deploying the broadcast feature of the network. Eventually, all the data generated by strips, are sequentially collected by the central host.
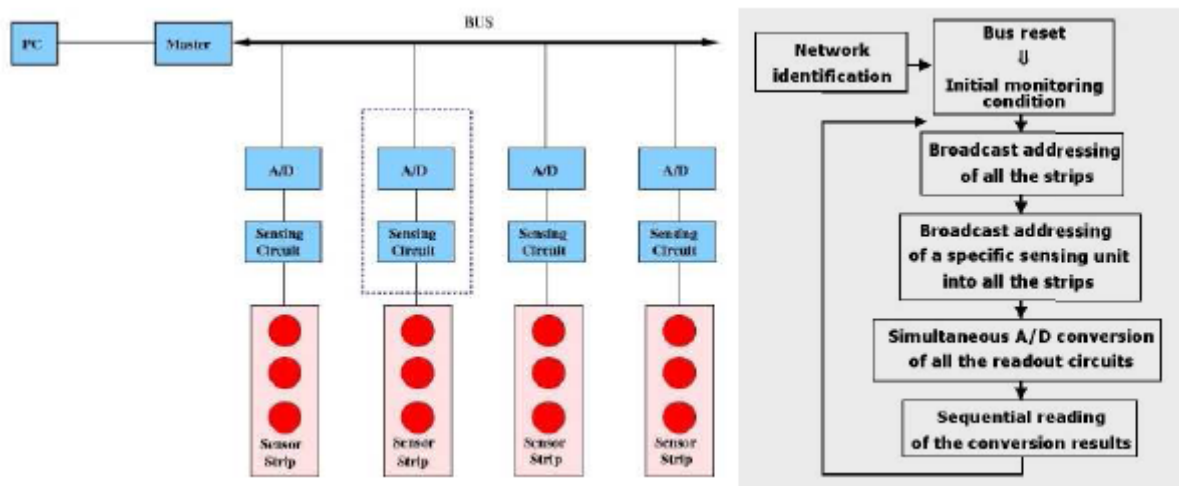
Figure.5.19 : Schematic representation of the acquisition system architecture (left). Flow chart of the main operations generated by host to control the acquisition system (right).

The operation sequence described above is schematically pictured in the block diagram in Fig. 6.19, where the initialisation and the normal readout loop are well distinguished. The latter is composed of a set of broadcast commands and a session of sequential data readings, continuously repeated in order to obtain the capacitive information associated to all the sensing units of the strips. Note that although the described process is optimised for the monitoring of the entire network, the architecture allows the acquisition system to be specifically set to other operative modes. For instance, one can easily focus the attention on a single specified sensor strip, or limit the algorithm to span a specific subset of the whole sensor network. With this, a high level of flexibility is achieved in the sensor management. The system, tested in conditions that emulate a real operating environment has shown a very high reliability level and a considerable sensitivity: a minimum capacitance variation of about 33 fF is detectable as a consequence of a pressure variation induced on the sensing unit of about 5 Pa. A good reliability in data transmission (100,000 consecutive correct data acquisition cycles) allows the strips to be distributed over wide surfaces in a continuous real-time monitoring process. The acquisition system is able to monitor sensor strips at a distance up to 50 meters if used at the standard protocol rate and up to 5 meters if used in the overdrive mode. The deterministic nature of the bus protocol also enables the estimation of the total time required to scan the whole sensor network. For instance, in a network composed of a single strip equipped with 8 individual transducers (our experimental setup), it is possible to have 10 full network scans per second in standard mode and 60 full network scans per second in overdrive mode. The proposed acquisition architecture has proved to achieve good measurement accuracy in real-time measurement making it a valid alternative to traditional mechanical pressure profile acquisition systems.

64

5.4 Frequency response

Pressure sensors are composed of an inertial element, a dampening element and an elastic element. It is possible to describe the sensor with a second order differential equation, as represented in Fig. 5.20. The equation that describes the system
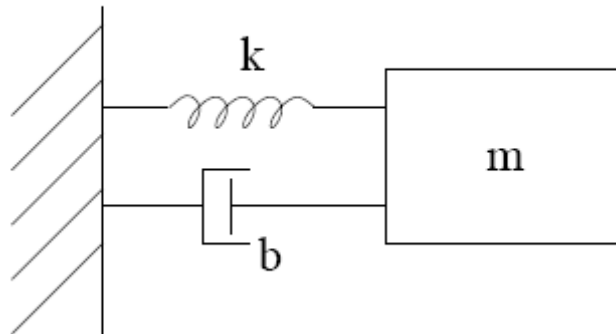
Figure 5.20 :

in absence of an external applied force is:

$$m\frac{d^2x}{dt^2} + b\frac{dx}{dt} + kx = 0 \tag{5.1}$$

whose poles are:

$$s_{1,2} = -\frac{b}{2m} +/- \sqrt{\frac{b^2}{4m^2} - \frac{k}{m}} \tag{5.2}$$

wheremis the mass, b is the damping factor and k represents the elastic behaviour. Since the latter parameters are always positive, the poles are always negative and the system solution is always stable. Moreover, depending on b,m and k values, the frequency responce changes: in particular, towards the resonance frequency, the input is amplified by many factors. Therefore, it is preferable to avoid noise vibration near this frequency. The resonance frequency for this system is ₁

$$\omega_n = \sqrt{\frac{k}{m}} \tag{5.3}$$

For pressure sensors, the coefficient b is unknown, but firstly it is sufficient to evaluate which frequencies are close to the resonance. m and k can be obtained from analytical calculation and from simulations. Fig. 5.21 shows the resonance frequency ranges of the pressure sensor, depending upon geometry and elastic behaviour. The frequency for pressure sensors is contained in a range from 216.5 to 1637.7 Hz. These values, that must be confirmed by experiments, show how the bandwith of the sensor can vary considerably and how important is the sizing of the sensor with respect to the nature of the application for what the sensor is intended. It appears evident how particular attention must be paid when designing the proposed structure for turbulent flow measurements.
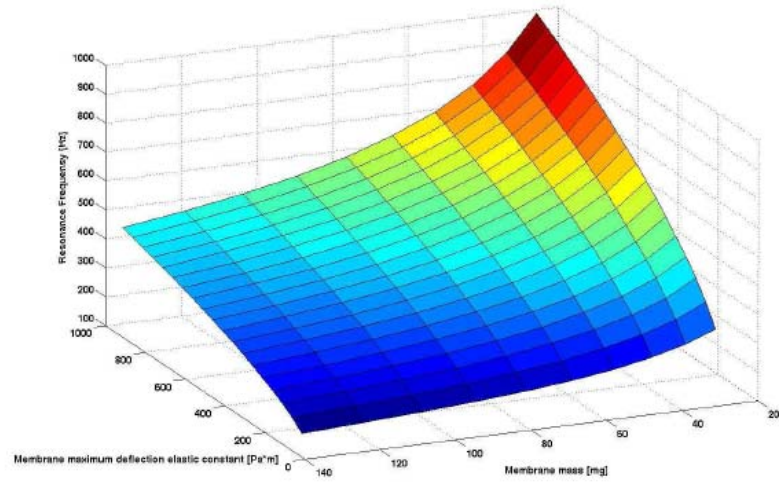
Figure 5.21: Resonance frequency domain for pressure sensors.

Chapter 6

Detection of aircraft parameters

Modern aircrafts require a vast amount of data coming from on board sensors, either to provide information to the pilot, to implement Fly-by-Wire (FBW) systems, or to achieve automatic flight control as in unmanned air vehicles (UAVs). Specifically, air data is fundamental to infer many high-level flight parameters, including the free-stream air speed and the attitude of flight. In this regard, it is worth considering that conventional measurement techniques tend to rely on a few specialized, highly accurate elements, in the form of Pitot tubes, electromechanical devices such as vanes, or multifunction units such as self aligning slot-type sensors [54], etc. In other terms, in conventional systems the emphasis is on the transducers, which should make the most direct measurements of the quantities of interest and make them ready available at a good precision. While undoubtedly successful, conventional techniques have a few drawbacks: (1) different probe types may be needed for reading different physical quantities, leading to device proliferation (at times hidden by the use of multi-functional probes [54]); (2) highly accurate probes are generally required, leading to high costs (possibly critical for certain classes of fliers); (3) probe installation may be intrusive, or constrained to very specific locations, or probes may be too bulky for small vehicles; (4) probe placement may be critical with regard to perturbation and wake effects (at times, to the point of requiring booms to bring probes outside the aircraft profile); (5) the use of a small number of sensing devices may make faults extremely critical. These issues are well recognized and a few attempts have been made to their solution. For instance, multi-hole/multifunctional probes have been introduced to infer a plurality of flight parameters at once [54,55]; techniques have been introduced to get free-stream parameters from measurement made on the air vehicle skin [21]; replicated systems have been introduced to enhance availability [56]. In this paper, a radically different approach is considered and experimented, where the above issues are avoided a-priori by moving the emphasis from the transducers to the signal processing . This is generally sensible, as the processing power made available to designers is rapidly increasing in magnitude and decreasing in cost. Rather than using a few specialized probes, many low cost transducers of the same type and providing homogeneous raw data are employed, showing that efficient signal processing can anyway assure the possibility of inferring a plurality of high-level parameters at an adequate accuracy. The sensors are designed favoring low cost and low intrusivity over other merit factors. Thanks to their large number, the system can be made tolerant of faults. Eventually, sensor placement constraints are relaxed, since the existence of regions of the flight envelope where some sensors are perturbed can be treated as a transient failure of a minority of units. For transducing, the proposal relies on conformable strips hosting capacitive pressure sensitive units, directly placed on the aircraft aerodynamic surfaces as shown in Fig. 6.1
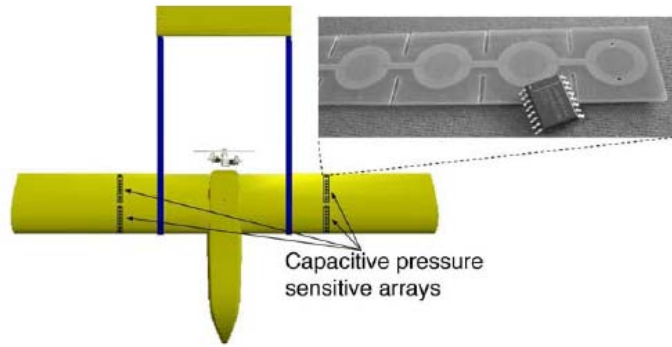
Figure 6.1 : proposed instrumentation to be applied on the aerodynamic surfaces of an aircraft

6.1 Sensing technologies

The proposed measurement system requires sensors capable of delivering partial views of the pressure gradients applied by the airflow over the aircraft surfaces. It is assumed that such views are provided in the form of vectors (indicated in this chapter with bold character) each of which represents a spatial discretization of the pressure gradient at some location. Fig. 6.2 helps to illustrate this assumption by showing an airfoil section where five sample "regions of interest" (R1 to R5) are marked. For each region R_j, specific spots $x_{j,0}$ to $x_{j,n}$ exist, contributing to the spatial discretization. With this, the sensor in charge of region R_j is expected to return a vector $\mathbf{P} = (Pj,1, \ldots, Pj,n-1)^T$ where entry $P_{j,i}$ represents the pressure difference between the spots $x_{j,I}$ and $x_{j,0}$. The vectors $\mathbf{P_j}$ can then be concatenated into a single vector of readings $\mathbf{R}$.
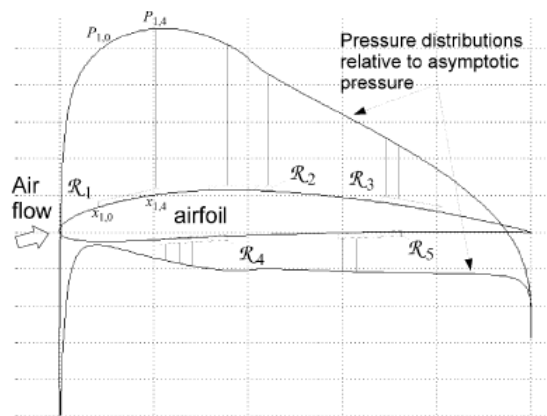
Figure 6.2 : Sample placement of "region of interest" and spots where information about pressure gradients over the airfoil is returned.
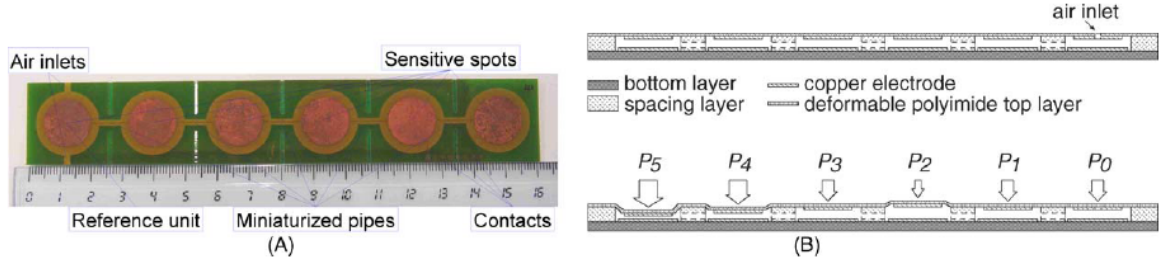
Figure 6.3 : Strip sensor array in PCB technology. Prototype photography (A); section and schematic operation (B)

Note that **R** does not represent a pressure gradient itself, as the pressure differences between the various locations Rj need not to be known. From the above, it should be clear that the requirements over the sensor sub-system are particularly mild. First of all, sensors can be differential as one is interested in pressure gradients and not in absolute distributions. This can greatly simplify the sensor design, neglecting absolute pressures which can significantly vary with altitude and meteorological conditions. Secondly, the sensors in charge of the many regions can be independent of each other as no pressure difference needs to be evaluated between them. Evidently, many technologies can be used for satisfying the above requirements. For instance, one could drill orifice arrays in the regions of interests and pneumatically link them to conventional multi-point pressure scanners [21,11]. Alternatively, one could think of sensors based on silicon micro-electromechanical systems (MEMS) and/or hybrid technologies [12]. In practice, however, one should make the sensor system as cheap, robust and easy to install as possible. To this aim, the sensor strips based on PCB technologies described in this thesis have been developed Fig. 6.3.

6.2 Theory of operation

From the above, it should be clear that m strip sensors with n sensitive spots each (n−1 pressure differences per sensor) represent m regions of interest and deliver a compound readout vector

$$R = \begin{pmatrix} \Delta\vec{P}_1 \\ \\ \\ \Delta\vec{P}_m \end{pmatrix} = \left(\Delta P_{1,1}, ..., \Delta P_{1,n-1}, \Delta P_{2,1}, ... \Delta P_{2,n-1}, ..., \Delta P_{m,n-1} \right)^T \tag{6.1}$$

The vector **R** thus holds l =m(n−1) elements where n can typically be any integer between two and a few tens.3 The signal processing aspects involve the definition of algorithms to properly consume this data and return high-level flight parameters including the free-stream air speed (V_∞) and the angle of attack (α). In general terms, one can think of a vector $\Phi = (V_\infty, \alpha)^T$ of quantities of interest with the provision of extending it to include the side-slip angle β too. The algorithms should exploit the functional tie that must exist between Φ and **R**, and which can be captured in most general terms as:

$$\vec{R} = F(\vec{\Phi}, \vec{E}) \tag{6.2}$$

69

where **E** is a vector of environmental parameters that might affect the tie (e.g. air density). In the following, dependence on **E** will be implicitly assumed without marking it, to keep the notation simpler.
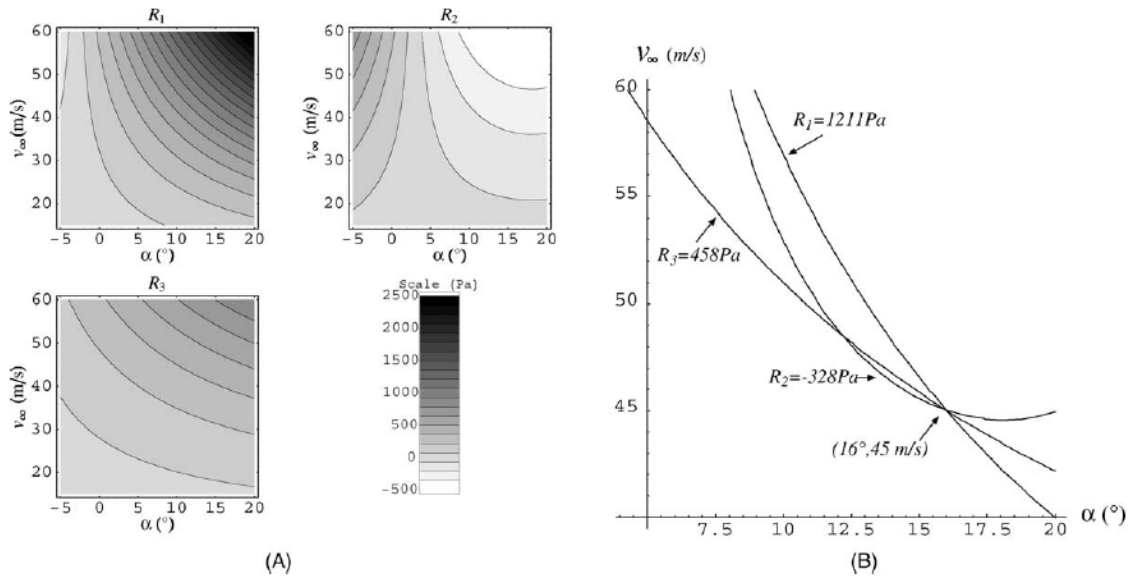
Figure 6.4 : (A) Contour plots of the various components of **F** for a test case where l = 3. (B) Corresponding graphical determination of attack angle and air speed for a readout vector **R** whose components are those on the corresponding isoclines. Test conditions: data obtained by simulation for a normalized NACA 0012 airfoil at room pressure and temperature. Airfoil is equipped with three two-units sensor strips: first strip on top surface, with sensing spots at $x_{1,0} = 0.2$m and $x_{1,1} = 0.4$m from leading edge; second strip on bottom surface with $x_{2,0} = 0.2$m and $x_{2,1} = 0.4$ m; third strip on top surface with spots at $x_{3,0} = 0.7$m and $x_{3,1} = 0.9$ m.

Note that knowledge about F can be obtained by various means, e.g. exploiting analytical methods (by fluid-dynamic modeling), by simulation or measurements (sampling the space of definition of **Φ** at significant points and applying interpolation) or by mixture of these techniques. Assuming that F is known, one should ideally use its inverse to compute **Φ** once a reading vector **R** is delivered by the sensor system. The determination of F is thus crucial and can be regarded as a calibration phase. For the moment, assume that F is known and C^1 in **Φ**. With this, the first issue to clear is to assess that F is invertible. In intuitive terms the inversion problem consists in taking the various components of F, as in Fig. 4(A), and in finding the intersection point of their isoclines corresponding to the components of the sensor readout vector $\mathbf{R} = (R_1, \ldots, R_l)^T$ as in $F_1(\mathbf{\Phi}) = R1, \ldots, Fl(\mathbf{\Phi}) = Rl$. This is shown in Fig. 4(B). From the example, it is evident that the invertibility of **F** cannot be generally assured. For instance, if in Fig. 4(B) one had considered only two isoclines (ignoring the output of a sensing unit), there would have been two intersection points and inversion ambiguity. For some specific sensor placements proving invertibility might be possible, but deriving invertibility conditions for arbitrary sensor placements and numbers would most likely be cumbersome. Fortunately, this is practically not needed as one can rely on the probability of F being not invertible to decrease extremely rapidly when the number of sensing units l is increased. In fact the diversity among the components of F makes it extremely hard not to be one-to-one when l is large. Hence, one can simply consider invertibility not be an issue as long as the proposed measurement system uses a sufficiently large number of sensing units, as it is actually meant to do. Once invertibility is assessed, one needs to consider how to exploit this property. In fact, naive inversion approaches cannot be practiced due to uncertainties affecting the readout of **R**.

70

Unavoidable measurement errors have the consequence that one cannot operate on **R** directly. Only "perturbed instances" **S** of **R** are available, built as

$$\vec{S} = \left(\Delta P_{1,1} + \varepsilon_{1,1}, ..., \Delta P_{1,n-1} + \varepsilon_{1,n-1}, \Delta P_{2,1} \varepsilon_{2,1}, ... \Delta P_{2,n-1} + \varepsilon_{2,n-1}, ..., \Delta P_{m,n-1} + \varepsilon_{m,n-1} \right)^T \qquad (6.3)$$

where the vector $\boldsymbol{\varepsilon} = (\varepsilon_{1,1}, \ldots , \varepsilon_{m,n-1})^T$ summarizes the reading errors. Keeping reference to the example in Fig. 4, their effect is to make it virtually impossible to have a single point where all the isoclines of the F components intersect. This fact can be seen from another perspective by considering that F maps points from $\mathbb{R}^q$ (where q is the dimensionality of $\boldsymbol{\Phi}$, e.g. (2)) to a subset D of $\mathbb{R}^l$ which is an l-dimensional manifold. As an example, Fig. 5(A) shows a possible image set of an interval $(V_\infty, \alpha)^T$ through F when l=3. In this light, one sees that reading errors make it unlikely for **S** to fall on the image set D of F, so that even knowing $F^{-1} : D \to \mathbb{R}^q$ one could not employ it to compute $\boldsymbol{\Phi}$. In conclusion, one is left with a classical estimation problem [59]. A very practical approach to its solution is maximum likelihood estimation (MLE). The approach requires knowing the probability density function (PDF) of **S** once $\boldsymbol{\Phi}$ is assumed to be deterministically set at a given value. Such PDF $\rho(\mathbf{S}; \boldsymbol{\Phi})$ is termed a likelihood function whenever it is viewed as a function of the unknown $\boldsymbol{\Phi}$ with **S** fixed. MLE is hence practiced by maximizing $\rho(\mathbf{S}; \boldsymbol{\Phi})$ in _$\Phi$when _S is given. In the specific estimation problem being tackled, the first step is to make reasonable hypothesis about the statistical distribution of $\boldsymbol{\varepsilon}$, since this enters the definition of $\rho(\mathbf{S}; \boldsymbol{\Phi})$. It seems reasonable to assume $\boldsymbol{\varepsilon}$ to be
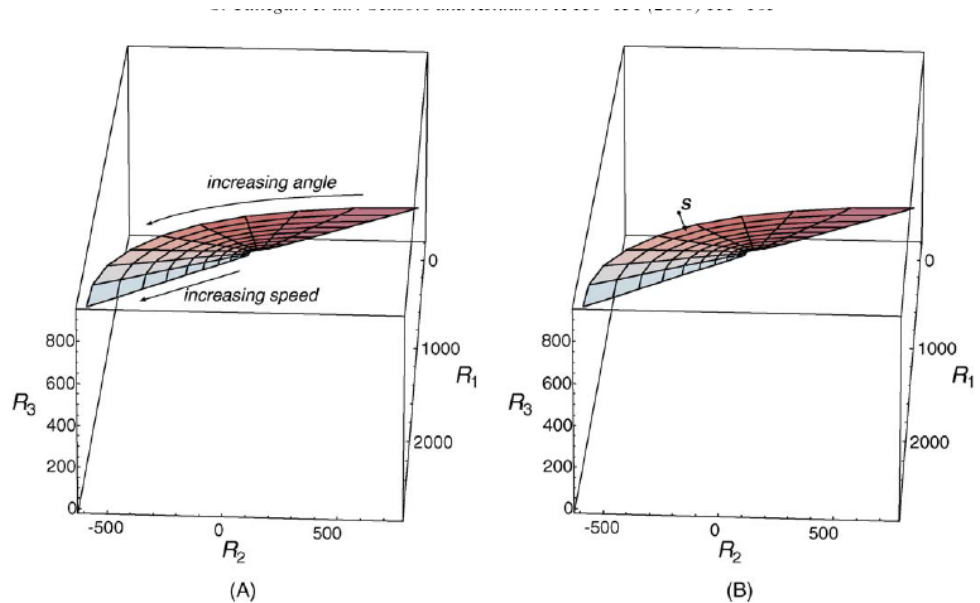
Figure 6.5 : (A) Image set of an interval in the _$\Phi = (V\infty, \alpha)$T plane through function F. Interval is definedby $\alpha \in [-5\circ,+8\circ]$ and $V\infty \in [15,60]$ m/s. (B) Projection operator used for the inversion of F when the reading vector is affected by measurement errors. Test conditions are the same as for the previous figure.

independent from $\boldsymbol{\Phi}$ (at least in a first order approximation). Furthermore, presuming that the various sensing units are identical and correctly built not to influence each other, it seems also reasonable to assume that the many $\varepsilon_{i,j}$ are independent identical distributed (IID) random variables, so that the first order statistics of $\boldsymbol{\varepsilon}$ can easily be factorized. Additionally, assuming that $\varepsilon_{i,j}$ are non-systematic, it seems reasonable to assume $\varepsilon_{i,j} \sim \mathcal{N}(0, \sigma_\varepsilon)$, i.e. that errors distribute normally with zero mean and a certain variance σ^2_ε . With all this:

71

$$\rho\left(\vec{S};\vec{\Phi}\right)=\frac{1}{(2\pi\sigma_\varepsilon^2)^{\frac{1}{2}}}\exp\left[-\frac{1}{2\sigma_\varepsilon^2}\sum_{i=1}^{l}\left(S_i-F_i(\vec{\Phi})\right)^2\right] \tag{6.4}$$

where Si and Fi are the components of **S** and F, respectively. Note that the sum in Eq 6.4 is just the squared euclidean distance $\|F(\boldsymbol{\Phi})-\mathbf{S}\|$. Hence, the maximization of Eq 6.4 can be conveniently restated as:

$$\mathrm{min}\,imize\,\left\|F(\vec{\Phi})-\vec{S}\right\| \tag{6.5}$$

The minimization can be performed numerically [60], for instance by gradient descent or Newton methods. However, if F is modeled by an interval-wise polynomial function, exact solutions may also be achievable. The MLE expression Eq. 6.5 lends to a further interpretation of the estimation mechanism. Since $F{-}1$ is not sufficient by itself for the inversion problem in presence of reading errors one needs a generalization $G : \mathbb{R}^l \to \mathbb{R}^q$ of F^{-1} in order to be able to deal with them. Since the proposed MLE framework – with the assumed error model – reduces to least square estimation by Eq. 6.5, the optimal solution is clearly represented by defining G as the combination of F^{-1} with an orthogonal projection operator **T** taking _S onto D as shown in Fig. 5(B). In other terms F^{-1} gets applied to the point of D closest to the reading **S**. While this interpretation is not convenient for the practical implementation of a computation algorithm, it can be useful for the prediction of estimation uncertainties.

6.3 System extension to fault detection and to fault tolerant operation

After the optimization Eq.6.5, the quantity object of minimization can be employed as a merit factor to qualify the estimation procedure. Under the assumption that the components of **ε** are IID and distributed according to N(0, σε), for each given **Φ**, the quantity $\|F(\boldsymbol{\Phi})-\mathbf{S}\|$ can be expected to be a random variable with a Chi-like distribution. Let us indicate by $\sigma^{(l)}_{CS}(x)$ the probability density function of the normalized Chi-square distribution with l degrees of freedom and define a quantity d_{max} so that:

$$\int_0^{d_{max}^2}\frac{1}{\sigma_\varepsilon^2}\rho_{CS}^{(l)}\left(\frac{x}{\sigma_\varepsilon^2}\right)dx=\vartheta \tag{6.6}$$

where θ is a quantity close to 1 (e.g. 99%). With this, the probability that a measure vector **S** leads to a $\|F(\boldsymbol{\Phi})-\mathbf{S}\| > d_{max}$ should be less than 1−θ (e.g. less than 1%). This consideration opens the way to a convenient fault detection mechanism for the proposed air data system. Whenever the quantity minimized in Eq. 6.5 exceeds a threshold (d_{max} or presumably a larger quantity to have some clearance), one knows that **S** is degraded by anomalously large errors. The latter might be caused by sensor faults, data transmission errors, or transient errors due to flow perturbations or wake effects. In mission-critical systems the ability to derive a reliability index from measured data can be a fundamental feature. Note that this comes as a direct benefit of the exploitation of a redundant sensor set where incoherence among the sensor readings can trigger alerts. If the sensor redundancy is large enough, the fault detection mechanism can be easily extended to achieve fault tolerance. In fact, when $\|F(\boldsymbol{\Phi})-\mathbf{S}\|$ is too large, one can progressively exclude some sensor readings from the estimation phase, until the minimization residue goes back to normality. At this point, the faulty part of the system is isolated.

6.3.1 System calibration

Having discussed the usage of function F for the estimation of $\mathbf{\Phi}$, it is worth considering the determination of F itself. Obviously, F depends on the particular shape of the aerodynamic surfaces on which the sensors are placed and on their particular locations. Note that the possibility of obtaining a closed-form F from physical models is generally hindered by the complications of fluid-dynamics. For instance, in [21] it was possible to rely on analytical models only thanks to the usage of particularly simple aerodynamic shapes. In this paper, F is approximated by using results from simulation and experimental data. Particularly, F is expressed by a $\underline{F}(\mathbf{\Phi},\mathbf{E},\mathbf{K})$ where $\underline{F}$ represents a fixed functional structure and $\mathbf{K}$ is a vector of calibration parameters. In other terms a compact model is sought for the physical phenomena. The choice of the structure $\underline{F}$ is extremely important as it strongly affects the possibility of accurately expressing $\underline{F}$ with a minimal number of parameters and to calibrate it by a minimal set of experimental data. Furthermore, the form of F influences the possibility of efficiently computing the minimization (5). As already mentioned, the latter can normally be performed by numerical methods such as gradient descent of Newton algorithms, but for particular expressions of $\underline{F}$ (e.g. interval-wise polynomial) exact solutions might also be achievable. The latter may result particularly advantageous thanks to the possibility of pre-determining computation times, which favors the set up of real-time systems. In this paper a preliminary approach has been pursued in order to get a proof of principle of the proposed techniques. This involves the definition of a limited region of $\_\Phi$ points admissible in a realistic flight envelope (e.g. $\alpha \in [-8°,8°]$ and $V_\infty \in [20,45]$ m/s). In this region, significant sample points are identified by uniformly stepping V_∞ and α. At these points, pressure data is obtained either by simulation or by wind tunnel experiments. This data is then used to obtain an optimal $\mathbf{K}$ by fitting techniques, when $\underline{F}$ is set to have an intervalwise polynomial form (3rd order). Fluid-dynamic considerations can then be used to introduce dependencies on environmental parameters such as temperature, barometric pressure, etc. Clearly, this approximation method is almost uninformed of the underlying fluid-dynamic phenomena, and as such open to many optimizations. In the future, more sophisticated approximation techniques should be introduced to reduce the sets of experimental data needed for calibration. With the current approach, sample algorithm implementations have shown that a commodity computer is capable of delivering a solution to the estimation problem in about 0.1 s when the readout space is 10-dimensional ($l = 10$). Such result is obtained by applying an unspecialized minimization algorithm in an interpreted software environment, so significant computation time reductions should be at hand.

6.3.2 Estimation of accuracy bounds

In order to proficiently exploit the techniques described in the previous section, one should be able to forecast how the sensors reading errors propagate onto the final $\mathbf{\Phi}$ values. It is intuitive that, due to the inherent non-linearity of the computations, errors must propagate differently in different areas of the flight envelope. A common index used in estimation theory is the Cramer–Rao lower bound (CRLB) [59]. Although it is a bound and not an exact variance evaluation, its usage can offer significant insight. Particularly, it alerts to the physical impossibility of finding unbiased estimators whose variance is less than its amount. In general terms the CRLB states that:

$$\mathrm{var}(\hat{\vartheta}_i) \geq \left[I^{-1}\left(\vec{\vartheta}\right) \right]_{i,i} \tag{6.7}$$

where $\mathbf{\theta}$ is the vector of the parameters to estimate, $\hat{\vartheta}_i$ is an estimated parameter and $\mathbf{I}$ is the Fisher information matrix defined as:

$$\left[I^{-1}(\vec{\vartheta})\right]_{i,j} = -E\left[\frac{\partial^2 \ln \rho(\vec{x};\vec{\vartheta})}{\partial \theta_i \partial \theta_j}\right] \tag{6.8}$$

where **x** is the vector of observations on which the estimation is based. The specialization of the CRLB to the estimation problem described above has a particularly compact form thanks to the hypotheses made on measurement errors: considering that the covariance matrix of the observations is diagonal with entries σ_ε^2 , that θ is Φ and that **x** is S, one has:

$$I^{-1}(\vec{\vartheta}) = \frac{1}{\sigma_\varepsilon^2} X \tag{6.9}$$

where X= (J[F])^{T}J[F] and J[F] is the Jacobian matrix of F. From this, when $\Phi = (V_\infty, \alpha)^T$

$$\sigma_{V\infty} \geq \sigma_\varepsilon \sqrt{[((J[F])^T J[F])^{-1}]_{1,1}} \tag{6.10 a}$$

$$\sigma_\alpha \geq \sigma_\varepsilon \sqrt{[((J[F])^T J[F])^{-1}]_{2,2}} \tag{6.10 b}$$

where $\sigma_{V\infty}$ and σ_α are the standard deviations to expect on V_∞ and α, respectively. It is also worth considering that in the particular application, the CRLB can be attained in an approximate sense. In other terms it can be used to forecast the effective accuracy that can be obtained from the proposed air data system, given the sensors characteristics (and thus σ_ε), number and location. Once accuracy specifications are provided for the whole system this can be precious to chose the sensors to adopt and to optimize their placement. The possibility to use Eq.6.10 as an excellent approximation of the effective performance of the MLE for the proposed application derives from **F** being locally not too far from linear (almost quadratic in V∞ and smooth in α). In geometrical terms, this can be seen by considering the framework of Fig. 5(B), where the estimation of Φ is obtained as $\mathbf{F}^{-1}(\mathbf{T}(\mathbf{S})) = \mathbf{G}(\mathbf{S})$. If **F** is not too far from linear, in the neighbour hood of any given Φ it can be approximated by its linearization $\mathbf{F}_{lin}$, expressed by the Jacobian J[F] at Φ. Note that the image set of $\mathbf{F}_{lin}$ is not D, rather the (hyper)plane D_{lin} tangent to D at $\mathbf{R} = F(\Phi)$.With this, one can approximate $\mathbf{G}(\mathbf{S})$ as $\mathbf{G}_{lin}(\mathbf{S}) = \mathbf{F}^{-1}_{lin}(\mathbf{T}_{lin}(\mathbf{S}))$ where $\mathbf{T}_{lin}$ is a projection operator taking **S** onto D_{lin}. Since the columns of **J[F]** define a basis for D_{lin}, a variation of **S**, $\Delta\mathbf{S}$, gets converted by $\mathbf{G}_{lin}$ into a variation of Φ that can be expressed as $\Delta\Phi = (\mathbf{J[F]}^T\mathbf{J[F]})^{-1}\mathbf{J[F]}^T \Delta\mathbf{S}$. With this formula, one can compute the covariance matrix for $\Delta\Phi$, assuming a diagonal covariance matrix $\sigma_\varepsilon^2 \mathbf{1}_l$ for **S** (where $\mathbf{1}_l$ is the l×l identity matrix). The covariance expression is:

$$\begin{aligned} E\left[\Delta\vec{\Phi}\Delta\vec{\Phi}^T\right] &= E[(J[F]^T J[F])^{-1}J[F]^T \Delta S \Delta S^T J[F](J[F]^T J[F])^{-1}] \\ &= (J[F]^T J[F])^{-1}J[F]^T \sigma_\varepsilon^2 \mathbf{1}_l J[F](J[F]^T J[F])^{-1} \\ &= \sigma_\varepsilon^2 (J[F]^T J[F])^{-1} \end{aligned} \tag{6.11}$$

i.e. it is equivalent to (10) when equalities are substituted for the inequalities in Eq. 6.10 and one is only interested in the variance (diagonal) terms of Eq. 6.11. Once the sensor accuracy is known and expressed as a standard deviation, formulas like Eq. 6.10 and Eq. 6.11 enable plots such as those of Fig. 6.6 to be drawn. Here, the pressure sensor accuracy is related to the global accuracy that can be obtained in the measurement of Φ, once the sensor placement is assigned. Obviously, the global accuracy that can be obtained depends on the specific point of the flight envelope where one operates. Notably, the accuracy is better at low angles of attack and at high speeds. This seems to be a major regularity, independent of the specific sensor placement being adopted. As a final remark,

74

note that the possibility of estimating the accuracy of the approach by a closed form expressions such as Eq. 6.10 and Eq. 6.11 can be fundamental in the practical design of an air data system. Particularly, expressions such as Eq. 6.10 and Eq. 6.11 enable the coding of optimization procedures where the placement of the sensors over the aerodynamic surfaces of an aircraft is incrementally adjusted until the best possible accuracy in the estimation of Φ is obtained.
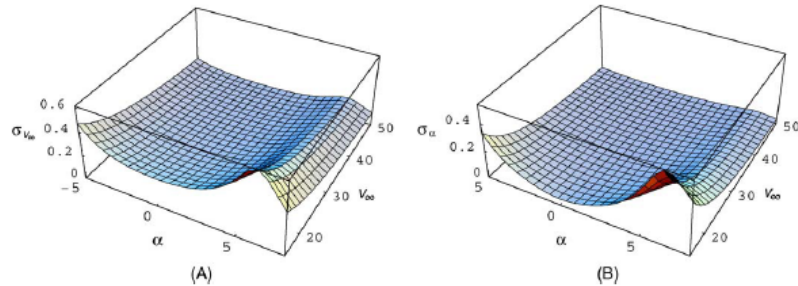
Figure 6.6 : Sample standard deviation surfaces obtained from Eqs. 6.10 and 6.11. (A) Standard deviation on V_∞; (B): standard deviation on α. Test conditions: data obtained by simulation for a NACA0012 airfoil (50 cm chord) equipped with two symmetrically placed strip sensors with nine sensitive spots each: first strip is on top surface of the airfoil, second strip on bottom; sensitive spots positions are at $x \cdot j = (5+2.5 \cdot j)$ cm from leading edge. The sensor resolution is assumed to be eight bits ($\sigma\varepsilon \approx 2$ Pa over a 1500 Pa range). The plots show the possibility of measuring the free-stream speed at an accuracy within ± 2m/s and the attack angle at an accuracy within $\pm 1\circ$ for this particular sensor setup.

6.4 Experimental results

The methodologies described in the previous section have been validated by three independent means, involving both numerical simulation and experiments practiced in a wind tunnel. The usage of three different validation tracks can be very advantageous since different experiment types permit different level of control of environmental information and are characterized by different pieces of return information. For instance, wind tunnel experiments offer realistic operating conditions, while simulation-based techniques allow strict control of second order aerodynamic effect and exclude that equipment set up problems can compromise the interpretation of data. Furthermore, experimental tracks that do not require the strip pressure sensors to be physically available make it possible to start experiments before prototypes sensors are available, enabling the concurrent development of the software and hardware parts of the proposed measurement system.

6.4.1. Simulation tests

By simulation one gets "ideal" input data to which numbers obtained by wind tunnel experiments can then be confronted for interpretation. Furthermore, simulation allows one to check the hypothesis that the CRLB can be used to forecast flight parameters uncertainties, without interference from second order aerodynamic phenomena. Finally, simulation provides data useful to drive and optimize the sensor design. The simulation tests herein reported consisted in the extensive application of Monte Carlo methods to accumulate sufficient information to derive the statistics of estimation errors. Simulation tests were practiced with the aid of the fluid-dynamic code Xfoil [61,34], linked to a Computer Algebra System by some ad hoc glue software. Particularly, the simulations procedure comprises the following steps:

1. A simulation setup is assigned, including an airfoil description, a sensor characterization and information about sensor placement over the airfoil.

2. Xfoil is first run to create calibration data and to generate an approximating function $\underline{\mathbf{F}}$ ($\mathbf{\Phi}$, $\mathbf{E}$, $\mathbf{K}$).

3. A cycle begins, including:

   - the generation of a random nominal $\mathbf{\Phi}$;

   - the usage of Xfoil to compute an ideal sensor reading vector $\mathbf{R}$ for such $\mathbf{\Phi}$;

   - the random perturbation of $\mathbf{R}$ to simulate measurement errors and to obtain a vector $\mathbf{S}$;

   - the estimation of a vector $\hat{\mathbf{\Phi}}$ from $\mathbf{S}$;

   - the recording of $\mathbf{\Phi}$ and the difference between the real $\mathbf{\Phi}$ and the estimated $\hat{\mathbf{\Phi}}$;

4. The cycle is repeated many times (>20,000).

5. At the end of the cycle standard deviations are computed for the estimation errors.

The above procedure confirmed the correctness of using the CRLB to forecast estimation uncertainties. Data obtained by simulation was coherent with analytically derived data such as that in Fig. 6.6.

Orifice placement from LE			
$x_{\cdot,0}$ 32 mm	$x_{\cdot,1}$ 45 mm	$x_{\cdot,2}$ 58 mm	$x_{\cdot,3}$ 71 mm
$x_{\cdot,4}$ 84 mm	$x_{\cdot,5}$ 97 mm	$x_{\cdot,6}$ 110 mm	$x_{\cdot,7}$ 123 mm
$x_{\cdot,8}$ 136 mm	$x_{\cdot,9}$ 149 mm	$x_{\cdot,10}$ 162 mm	$x_{\cdot,11}$ 175 mm
$x_{\cdot,12}$ 188 mm	$x_{\cdot,13}$ 201 mm	$x_{\cdot,14}$ 214 mm	$x_{\cdot,15}$ 227 mm
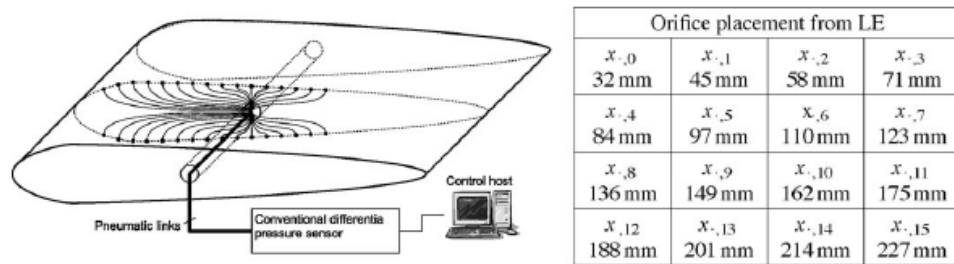
Figure 6.7: Model airfoil equipped with orifice arrays for the proposed experiments.

6.4.2 Test with conventional instrumentation

Tests with conventional instrumentation consist in creating a realistic wind tunnel setup. The tests employ an airfoil model. However, in this experimental track the airfoil is not yet equipped with capacitive strip sensors. Conversely, orifice arrays are drilled on its surfaces and linked to a conventional multi-point pressure scanner. The orifice arrays are then used to emulate the readings of the capacitive strip sensors. The advantages of this "intermediate" experimental approach are two-fold. First of all, one can check the flight parameter inference algorithm relaying on well-acceded and documented instrumentation. Secondly, one can build data to be used as a benchmark for the further experiments using the real capacitive sensors. In this way, potential issues limited to the capacitive strip sensors can be easily isolated. The experiments herein reported employed a NACA0015 (310mm chord) airfoil model equipped with two symmetrically placed arrays of

orifices emulating the readings of two 16-units PCB strips, as shown in Fig. 6.7. The right side of the figure also reports the position of the individual orifices from the airfoil leading edge. The experiment consisted in a training phase and in a validation phase. In the training phase, data was collected either from simulation or from wind tunnel instrumentation sampling the (α, V_∞) region of interest at regular points (1° and 5 m/s steps). Training data was used to extract two calibration sets **Ks** and **Ke** for **F** (**Φ, E, K**), referring to simulation data and experimental data, respectively. Then, in the validation phase, the profile was placed in the wind tunnel at unknown angle and air speed. A reading **S** was made from the pressure probes and used to infer α and V_∞. Measurement of α and V_∞, were also taken by the wind tunnel scales and compared. It is important to remark that calibration and validation were always practiced on different data sets. Fig. 6.8 helps better perceiving the discrepancy between measurements made by estimation and by the wind tunnel scales, for the case where the calibration vector **Ke** is used. The case with **Ks** is substantially similar, with only slightly larger errors. The x-axis reports α, the y-axis reports V_∞, and the z-axis (vertical) reports the magnitude of the measurement errors. Note the generally good agreement, with errors smaller than 1∘ (~6% of range) and 1 m/s (~2.5% of max tested speed). Also note that although the amount of data is insufficient for statistical considerations, the plots appear to show slightly larger discrepancies at higher speeds. This suggests that aerodynamic effects ignored by simulation may play a significant role. This is interesting, particularly when confronted with data based on error propagation analysis, such as that presented in Section 6.3.3 and Fig. 6, where errors were larger at lower speeds when the errors introduced by the sensors had larger relative importance.

6.4.3 Test with strip sensor

The last experimental track consists in tests based on real strip sensors prototypes in a wind tunnel setup. Hence, all the components of the proposed measurement system are finally
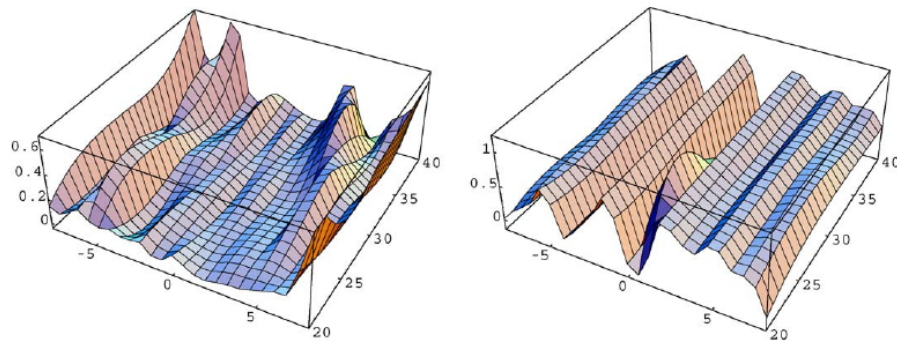
Sensitive spot placement from LE		
$x_{1,0}$ 83 mm	$x_{1,1}$ 110 mm	$x_{1,2}$ 137 mm
$x_{1,3}$ 164 mm	$x_{1,4}$ 191 mm	$x_{1,5}$ 218 mm

Figure 6.8 : Plots of discrepancy among data inferred by estimation and data obtained by conventional instruments. (A) Errors on V∞, in m/s; (B) errors on α in degrees.

included. In this tests, the experimental setup is similar to the above, but a PCB strip sensor is glued on the skin of the model airfoil to be placed in the wind tunnel. As above, the tests exploited a

77

NACA 0015 airfoil (310mm chord). A single prototype PCB sensor was actually employed, being glued on the upper airfoil surface as illustrated in Fig. 9. The right side of the figure also report the exact placement of the sensitive spots. The experiment followed the same guidelines of the previous section, with a notable exception: function $\underline{\mathbf{F}}$ ($\mathbf{\Phi}$, $\mathbf{E}$, $\mathbf{K}$) was taken to model a link between (V_∞, α) and the sensor capacitance readings, not between (V_∞, α) and pressure readings. In other terms $\underline{\mathbf{F}}$ was asked to incorporate the non-linear characteristics of the sensor, as pictured in Fig. 10. This could happen most naturally thanks to the extensive parameterization of $\underline{\mathbf{F}}$ In operation the capacitance value for the sensing elements at rest were approximately 3.4 pF (slightly varying among the many sensitive spots). Capacitance readings were made at V_∞,
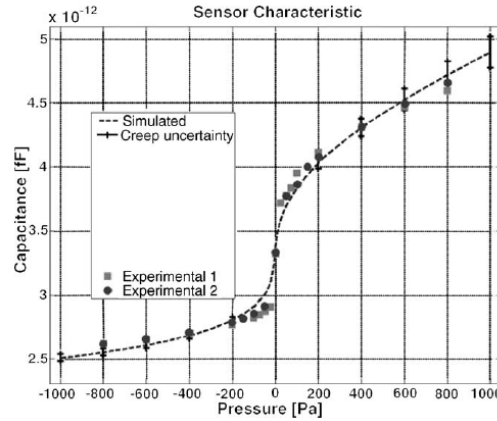
Figure 6.10 : Non-linear pressure to capacitance relationship of the prototype strip sensor used for the experiments.

Setup		Estimation		Error	
V_∞ (m/s)	α (°)	V_∞ (m/s)	α (°)	$|\Delta V_\infty|$ (m/s)	$|\Delta\alpha|$ (°)
30.15	−4	30.08	−4.04	0.07	0.04
40.06	−4	39.42	−4.04	0.63	0.04
29.91	0	29.14	+0.30	0.78	0.30
39.90	0	39.20	+0.14	0.70	0.14
30.10	+4	30.80	+3.17	0.70	0.82
40.08	+4	35.94	+5.80	4.13	1.80
29.91	+8	30.04	+7.97	0.13	0.03
40.03	+8	39.73	+8.15	0.30	0.15
0.09	–	0.45	–	0.37	–

Table 6.1 : Experimental verification of the correct operation of the proposed measurement System In tests, the set of measurements used for calibration was always disjoint from the measurements used in validation.

equal to 0, 25, 30, 35, 40 m/s and α equal to −8◦, −4◦, 0◦, 4◦, 8◦. These test conditions made the sensor capacitance vary in a [−500, +900] fF range around their quiescent value. Capacitance measurements showed a repeatability of approximately ±9 fF (±0.7% of the available range). Table 1 shows the ability of the calibrated system to correctly infer V∞, and α at various speeds and angles of attack, resulting consistent with the theory presented so far. Errors are clearly larger than those presented in the previous section. This last track of experiments provided valuable results. Namely:

- Substantial coherence of the experimental data with data provided by theory and by other experimental tracks proved the generally correct operation of the capacitive sensors and the possibility of effectively using on-skin capacitive sensing for the measurement of high-level flight parameters.

- The possibility of seamlessly incorporating the non-linearities of the sensor model in the estimation procedure was shown.

- The possibility of reliably inferring high-level flight parameters even with the monitoring of a single airfoil surface was proved.

The larger estimation errors, obtained in this experimental track with regard to the previous one can be ascribed to some concurrent causes. First of all, it is worth noticing that the monitoring of a single airfoil surface reduces the diversity among the various sensor reading. From the CRLB-based error propagation analysis it is known that this negatively affects the final accuracy. Secondly, in this experiment the length of the readout vector l was 5, while in the previous track of experiments l was 30. From the CRLB-based error propagation analysis it could also be foreseen that a reduction in the input redundancy could negatively affect accuracy. Finally, the experiments revealed a second order phenomena in the sensors themselves. This is a long-term dynamical phenomena known as creep that derives from the sensor materials, construction and sizing. In the future, results shall be improved also by contrasting this phenomena or accounting for it in the models.

Conclusion

Pressure profiles obtained from the proposed array of aeronautical application differential capacitive sensor match the highly accurate Setra® commercial sensor measurements, validating the sensor figures of merit in terms of sensitivity, resolution, accuracy and drift predicted by the design approach. The goal, during the design phase, is to predict the viscoelastic behaviour, in order to modify the sensor so as to reduce drift. Drift is, in fact, the primary source of imprecision for this kind of sensor. The trade-off between sensitivity and drift, due to creep, is a major issue: increasing the sensitivity leads to increased output drift. Experiment was set up to assess the performance of the strip and its functionality. The first aerodynamic object analyzed was a custom-built, modular and decomposable NACA 0015 airfoil, containing internal electronics and pneumatic pipes. Experiments have been made in a wind tunnel for different angle of attack in a ± 8° range and for different free stream velocities up to 45 m/s. The best sensor prototypes have shown a resolution of 2 Pa in a ±2k Pa range with a ±1,1% precision of full range, due to the creep drift. It has been demonstrated that, by using devices fabricated with polymer technology, one can decrease sensors costs, even when they are used as disposable devices and can provide the same degree of non-invasiveness and resolution as MEMS. This work has introduced a polymer-based, non-invasive and conformable sensor strip, designed for acquiring pressure profiles over the surfaces of aerodynamic bodies. The physical design was assisted by multiphysic FEM simulations, which has shown to be a reliable means to optimize sensor performance. Two kinds of experimental results have been performed and have been compared to multiphysic simulations and state-of-the-art sensors, showing very good agreement with both. These kind of sensors are well suited to fluid dynamic applications which involve monitoring large surfaces in harsh environments.

A novel measurement approach for air data has been presented, enabling the determination of free-stream air speed and flight attitude angles from measurement taken by a redundant set of identical pressure sensors directly applied on the skin of the aircraft. In the proposed methodology the aircraft itself is a part of the measurement system. The theory of operation has been developed with the aid of estimation theory and accuracy bounds have been determined for the proposed approach. Experiments have been practiced in a wind tunnel to confirm the correctness of the theory. While the results obtained so far are satisfactory, research is still in progress, specifically dealing with the following goals: Enhancement of the experimental equipment, to get a better perception of the achievable accuracy, enhancement of the experimental equipment, allowing airfoils to be equipped with many sensors at the same time, to test fault detection/fault tolerance schemes, extension of the methodology to side-slip detection, algorithm refinement and porting to an embeddable computing system, coding of procedures to help finding optimal sensor placement.

Wireless Pressure Sensor Network for Nautical Applications

Introduction

In yacht sailing challenges are concerned, the ability to optimize pressure distribution above sail surfaces, tweaking their shape in the changeable wind and sea conditions, represent one of the key factor to win a yacht race. The aerodynamic field around a sail is characterized by Reynolds numbers lower than the ones typical of aeronautical applications. Moreover, depending on the point of sailing, the flow is affected by boundary layer separation phenomena either partially, when recirculation bubbles are present, or completely when stall occurs. Also, the mechanical behaviour is complex: a sail acts as a membrane with low flexural module, so its shape varies with the variable aerodynamic load acting on it. The properties of the materials are anisotropic due to the different thickness used to reinforce the structure. All the complex aerodynamic and mechanical phenomena involved and the strong uncertain of both wind and sea conditions let the study and the prediction of a yacht sail performance extremely complex and dependent on a large number of parameters. Until a few years ago, sail design was done experimentally through trial-and-error practice of sail makers, full-scale force measurements, and wind-tunnel testing of scale models. In the past, aerodynamic numerical methods were used, but mainly implementing inviscid potential flow, lifting-line, lifting-surface, vortex-lattice methods. All these methods were computationally efficient, largely diffused and well accepted, but were limited to preliminary design and could not be used for predicting viscous separated flows with strong adverse pressure gradient. Today more accurate and advanced numerical prediction of aerodynamic flows around racing yachts are performed by means of Reynolds averaged Navier-Stokes solvers (RANS) [1], [2], [3], [4], accessible with reasonable CPU time because of the continuous increase in computer power available. Experimental studies have been performed both on two-dimensional sails and three-dimensional full yacht models: [6], [7], [8], [9]. Wilkinson performed an experimental data-base in the form of pressure measurement on a two-dimensional rigid mast-sail model varying different parameters like mast diameter, camber ratio, sail profile, incidence, trim angle, and Reynolds number; [10], [11], [12]. Wilkinson's data-base is one of the few data-bases to understand and test the differences between experimental measurements and numerical predictions around mast-sail configurations. Wind-tunnel results on 3D models are useful, but the actual flying shape of sails is difficult to achieve because of the soft materials from which they are made, the difficult problem of rig structural similitude, and the absence of wind-gradient effects in most wind tunnels. Moreover, it is rarely possible to acquire sufficient local measurements, such as wall pressure and skin friction along the sail, to increase the understanding of these complex flows and contribute to the validation of advanced numerical methods. To be able to improve sail design, the performances must be evaluated with sufficient accuracy taking into account all the involved parameters and the real flying shape of the sail surface before being integrated into the aerodynamic model for a velocity prediction program (VPP).

Aim of the developed sensor network is to sense the weak pressure field acting on the sail plan of a full batten sail by means of instrumented battens, providing a real time differential pressure map over the entire sail surface. By means of static non-linear coupled mechanical-electrostatic simulation, it is possible to predict the pressure versus capacitance static characteristic suitable for the transduction process and to tune the geometry of the transducer to reach the required resolution, sensitivity and time response in the appropriate full scale pressure input ranging from +/- 250 Pascal. A time dependent viscoelastic error model has been inferred and developed by means of experimental data in order to model, predict and reduce the inaccuracy bound due to the viscolelastic phenomena affecting the Mylar® polyester film used for the sensor diaphragm. The

wireless sensor network is composed by three main element pressure sensing units wireless nodes, instrumented battens. The pressure sensing unit is the core of the network, it is a capacitive differential non-MEMS sensor built in PCB technology, its aim is to sense and transduce static pressure by means of deformation of a thin and very sensitive film of Mylar840®. Wireless nodes host the sensing unit, the sensing electronic circuit, and the power supply battery, are built in PCB technology too. Any nodes is fabricated to ensure the sensing unit to be set in the instrumented battens and to let the sensor not to be affect to the battens curvature and strain. Instrumented battens let the nodes to be positioned on the sail surfaces, its principal aim is to reduce the intrusivity of the whole network over sail and to let a quick and easy installation. By means of any instrumented battens is therefore possible to acquire a discrete differential pressure distribution across the sail chord from the sail luff to the leech .Combining the measurement of all battens it is possible to get the pressure profile at different height along the mast from the base to the top. By means of the network it is therefore possible to compute pressure maps over full battens sails, potentially these data can be used with two distinct approach: a real time elaboration , and/or a post processing computing. The real time pressure data could used by different users as challenger or amateur sailors; the pressure data if coupled with parameters directly connected with the helmsman choices such as sail attitude, trim, and course sailed, may be used to evaluate the man sailing ability to get maximum performance of the yacht in terms of sail-plan efficient , maximum velocity or VMG velocity made good to wind. Other important applications related to the real time acquisition are concerned with the navigation and automatic control of yacht sails. Pressure may be use as input of a control system dedicated to the self trim of sails for autonomous navigations. The post-processing of pressure data could be used both by a sail maker or a researcher, the former can test the efficient of new sail shape and trim actions, the latter can use the data to better understand the complex fluid dynamic phenomena such as the iteration of the mast-sail junction or sail overlap, moreover new sail flow model could be validate and/or boundary conditions implemented. The proposed sensor network is also a suitable tool to enhance the developed of the sails aerodynamic module of the VPP, useful to evaluate the complex performance of a yacht sail.

Charter 7

Sails pressure measurements

Yacht sails are an ancient invention, at first sight efficient and easy devices. Anyway, if observed from a scientific point of view they reveal many complex phenomena. Yachts deeply interact with two fluids: water and air. The sail is a moving body characterized by an aerodynamic behaviour ranging from the one similar of a parachute in the broad reach courses, to that of a wing in the close reach ones. Moreover, the sail surface presents many peculiar characteristics. Geometrically a sail presents a very thin thickness, a marked aspect ratio, a strong curvature of the profiles, and a deformable surface due to the elasticity of the material used. The aerodynamic field around a sail is characterized by Reynolds numbers lower than the ones typical of aeronautical applications. Moreover, depending on the point of sailing, the flow is affected by boundary layer separation phenomena either partially, when recirculation bubbles are present, or completely when stall occurs. Also, the mechanical behaviour is complex: a sail acts as a membrane with low flexural module, so its shape varies with the variable aerodynamic load acting on it. The properties of the materials are anisotropic due to the different thickness used to reinforce the structure. All the complex aerodynamic and mechanical phenomena involved and the strong uncertain of both wind and sea conditions let the study and the prediction of a yacht sail performance extremely complex and dependent on a large number of parameters. Shaping a sail is many reason more complex than designing an aircraft wing of high aspect ratio cause the ambient conditions are usually known and less dynamic. To estimate the performance of yachts sail, Velocity Prediction Program (VPP) are often employed. The VPP solves a set of equations that govern the motion of the yacht. However modelling the aerodynamics of the yacht remains a large problem. Sail performance characteristics usually come from CFD for upwind sails, whereas for downwind sails wind tunnel tests are the preferred method due to the high computational cost of downwind CFD simulations. At present, VPPs use semi-empirical data to calculate the forces on the hull and sails. When available experimental database of sail properties and characteristics allow the validation of Computational Fluid Dynamics (CFD) codes and their implementation in the VPP. The fluid dynamics of sails is poorly understood, even if as reported in the content of this short review some experiments in open literature provide a base from which the knowledge of sail flow field can be further enhanced. The main reason for investigating two-dimensional sails is that the flow around three-dimensional sails is highly dependent upon the sail geometry and sailing conditions. For upwind sailing, the sail performance is highly sensitive to sail trim. A three-dimensional model sail is very difficult to trim, and the trim required would change with the varying flow angles and boat heel and direction. A three-dimensional sail experiment requires that the free stream flow direction change with increasing distance from the foot to the top of the sail. This is necessary to simulate the change in effective wind angle that the sail experiences as it travels through the earth's atmospheric boundary layer. Flow is therefore twisted using a set of turning vanes, but the twist has to be changed for any change in the boat's speed or heading. For the reasons mentioned, upwind testing of the sail is unfeasible. Experimental investigations of two-dimensional, high-aspect-ratio sails using sail sections representative of that used on modern yachts is aimed to provide database suitable to provide a database for CFD validation and also enhancing the sail designer's physical understanding

of the complex fluid dynamics involved. The state of the art in sail design differ from upwind to downwind sails. As far as upwind conditions are concerned the camber of the sail and the angle of incidence of the apparent wind to the sail are small, resulting in largely attached flow. A leading-edge separation bubble may be present, especially in the presence of a mast. Wind tunnel testing by racing teams is rare due to the problem of trimming at model scale. Upwind sail performance is highly sensitive to trim because of the small angles of incidence involved, meaning that small changes affect the performance significantly. Upwind sail flow analysis is generally performed using panel methods, and sometimes Euler codes. The design starts as a series of two-dimensional sections that vary with the height of the sail, and that are then blended together to form a three-dimensional sail. The three-dimensional sail is then optimized further by coupling 3D panel methods, some of which can implement twisted onset flow, to a finite-element structural-analysis program to try to predict the flying shape. Physical understanding of the flow around generic sail sections at representative Reynolds numbers is limited. An enhanced understanding of the flow physics around sail sections is required as a first step to understanding the more complex flow around a three-dimensional upwind sail. Three-dimensional upwind sails may have separated flow at the head of the sail whilst the flow remains attached elsewhere as a result of the twisted onset flow. This greatly influences the sail design and trim. To reduce separation near the head, the sail is usually twisted, too. Generally, strong tip vortices are shed off the head and the foot of the sail. As a result, the induced drag is large, and may contribute as much as 15% of the total boat drag (including hull, rigging and wave drag). Heeling of the boat also significantly affects the performance of the sails. It is also important to understand the sensitivity of the two-dimensional flow to Reynolds number, wind direction, camber and the effects of the mast and its orientation with respect to the sail. Such parameters will affect the transition behaviour of the flow, the size of the leading edge separation bubble if any, and the location of the trailing-edge separation. A correlation of these flow characteristics coupled to the sail pressure distribution, lift and drag will enhance the understanding of how to better design sails in order to maximize the forward thrust and to minimize the lateral force producing responsible for heeling moment. In reaching (i.e. partial-downwind conditions), the angle of incidence is larger. The flow on the main sail and gennaker or spinnaker is complex due to the presence of large scale separation for higher incident wind angles. If the flow is separated at the leading edge it is important to know the extension of bubbles and also for what conditions the flow reattaches. At higher angles of incidence, the flow is often unsteady. This unsteady behaviour affects the dynamic behaviour of the sail. In the past, aerodynamic numerical methods were used, but mainly implementing inviscid potential flow, lifting-line, lifting-surface, vortex-lattice methods. All these methods were computationally efficient, largely diffused and well accepted, but were limited to preliminary design and could not be used for predicting viscous separated flows with strong adverse pressure gradient. Today more accurate and advanced numerical prediction of aerodynamic flows around racing yachts are performed by means of Reynolds averaged Navier-Stokes solvers (RANS) [6], [7], [8], [9], accessible with reasonable CPU time because of the continuous increase in computer power available. Flow simulation requires the use of viscous solvers and turbulence models. Because of their expense and limited expertise in the sailing industry, wind tunnel testing is the preferred method of testing. However, the same limitations of many upwind experiments such as low aspect ratio and purely force and moment data are also seen for the downwind experiments. For the downwind case, it is therefore important to provide flow topology and force/pressure data on sails with realistic camber and high aspect ratio for a range of wind angles and Reynolds numbers. There have been two valuable series of experiments that have attempted to address some of the fundamental questions regarding 2D sail flows, with and without masts, these were carried out by Milgram [10-14] and Wilkinson [15-17]

85

7.1 Sails experimental studies

Experimental studies have been performed both on two-dimensional sails and three-dimensional full yacht models: [10-17], [6], [7], [8], [9]. One of the earlier experiments concerned with 2D sail coefficient measurements was performed by Milgram (1971) [10, 11], he investigated highly-cambered thin airfoils, without masts. Two thin profile were chosen for testing, a NACA 65 and NACA a = 0,8 mean lines. The experiments were conducted in a water tunnel at three different Reynolds numbers of 6,9 and 12×10^5. These high Reynolds numbers were achieved through the use of water as the working fluid and by the use of relatively large-chord sections. The relatively small dimensions of the water tunnel meant that the aspect ratio of the airfoils was low, being equal to approximately 2.2. Data for the highly-cambered sections is in the form of lift, drag and pitching-moment coefficients for a range of angles of attack. The experimental setup uses dynamometers to measure the forces and moment, with one side of the airfoil clamped and the other side pinned. A consequence of such a kind of arrangement is that the airfoil twists under load, with two degrees of twist reported for angles of attack greater than ten degrees. For the range of camber ratios investigated by Milgram, for the NACA 65 and a = 0,8 mean line , the aerodynamic characteristics are similar and do not vary greatly over the limited Reynolds number range in which the tests were conducted. A typical Cl-α plot shows a linear increase in Cl up to 4 degrees angle of incidence, followed by a small drop in Cl and then a recovery in Cl up to approximately 20 degrees as shown in Fig 7.1 The maximum value of Cl increases with camber ratio for a given thickness distribution as one would expect and ranges between approximately 2 and 2.6.
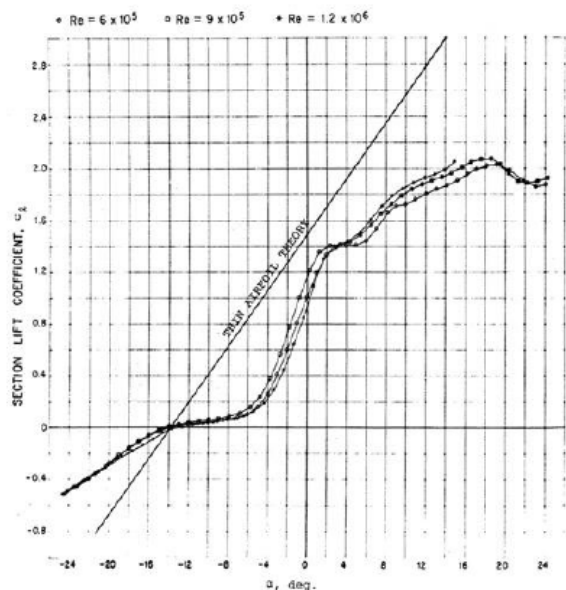
Figure 7.1: Lift coefficient versus incidence

The aerodynamic coefficient behaviour for the proposed thin section found by Milgarm are different from those of conventional, airfoils with low camber and moderate thickness, the data for which can be found in Abbott and von Doenhoff [18]. Thin airfoil theory predicts pre-stall lift versus angle of incidence fairly well for these sections. For highly cambered, thin sections, the Cl is always less than predicted, with the slope of the curve greater than 2π radian for angles of attack less than the theoretical ideal angle of incidence . The slope is less than 2π radian for angles of attack greater than the ideal angle of incidence as shown in Fig 7.1. In 1978 Milgram [12] tested one mean line (NACA a = 0:8) for two different camber ratios (0.12 and 0.15) with circular and elliptic-shaped masts of different diameters. The data are again limited to lift and drag coefficients,

although the longitudinal location of the centre of pressure is included as a function of Cl. The tests were carried out in the same water tunnel as used Milgram (1971), but without the turbulence screens, which resulted in measured values of Cd for the sections without a mast being 10% higher than in the earlier tests. The addition of a circular mast with a diameter to chord ratio (d/c) of 0.15, does not significantly change the Cd-Cl behaviour for CR=0.15, and extends the Cl range of the CR=0.12 section before the onset of the sharp drag rise. The difference in Cd between the two different camber ratio sections is a slowly increasing function of Cl for the circular mast (d/c=0.15). However the addition of an elliptic mast (d/c=0.17, where d in this case is the square root of the mast cross-section area), causes the Cd-Cl curve to be shifted to the right for the lower camber ratio meaning that the CR=0.12 section has a lower Cd over the whole range in Cl and the difference in Cd between the two increases rapidly with increasing Cl. Milgram concludes that a common range of mast-sail geometries for a broader range of camber ratio still need to be investigated. Also since the value of d/c is typically large near the head of sails, further study of sections at high Cl for large values of d/c is required. The addition of a mast to the sail raises the friction and form drag to the same order of magnitude as the induced drag of the sail, whereas without the mast the friction and form drag would be small by comparison. Another important experimental test concerning mast-sail profiles has been performed by Wilkinson. He performed an experimental data-base in the form of pressure measurement on a two-dimensional rigid mast-sail model varying different parameters like mast diameter, camber ratio, sail profile, incidence, trim angle, and Reynolds number; [15], [16], [17]. Wilkinson's data-base is one of the few data-bases to understand and test the differences between experimental measurements and numerical predictions around mast-sail configurations. Wilkinson [15] (1984) took Milgram's experiments with the mast attached one step further, and measured pressure distributions and velocity profiles for NACA a = 0:8 and 63 mean lines with a circular mast attached. Tests with the NACA 63 mean line investigated the effect of moving the point of maximum camber forward. Wilkinson conducted the tests in the 7' x 5' tunnel at Southampton University, England at Reynolds up to $1,6 \times 10^6$.
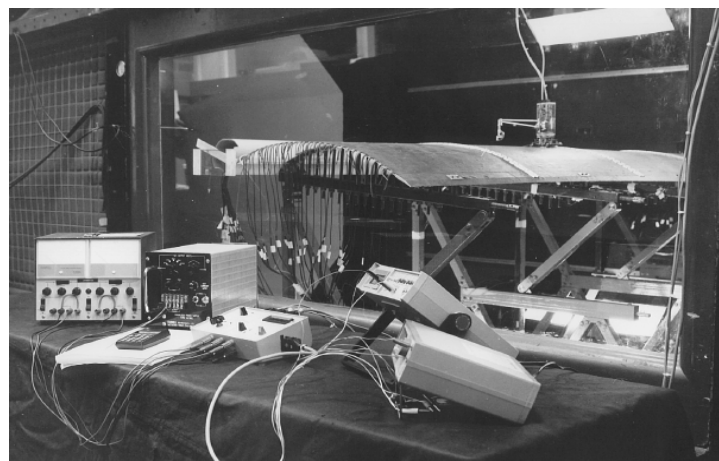
Figure 7.2 : Wilkinson's experimental wind tunnel set up

Such as with Milgram's tests, a low-aspect-ratio sail was tested to achieve high Reynolds numbers, and therefore three-dimensional flow at high angles of attack cannot be ruled out. The experiment set out to look at the effects of sail camber distribution, camber ratio, Reynolds number, angle of incidence, mast diameter/chord ratio and mast angle, on the pressure distribution Fig 7.3.
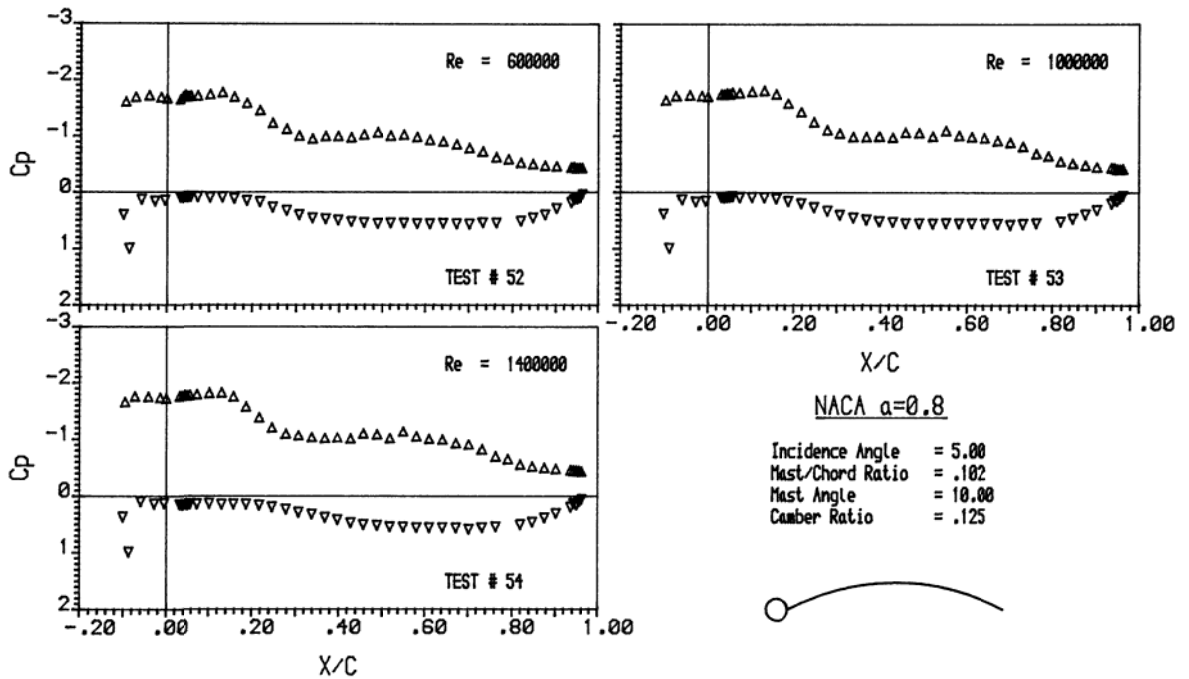
Figure 7.3 : Typical pressure coefficient results for a series of parameters

A total number of 216 tests were carried out, and it was concluded that all the pressure distributions could be represented by one universal form of pressure distribution that could be divided into nine regions as shown in Fig. 7.4. Increasing angle of incidence tended to decrease the base pressure in the upper-surface separation bubble and to shorten the length of the bubble. The pressure distribution also fattened out on the upper surface (region IV), and the position of the trailing-edge separation moved upstream. Increasing d/c has the effect of increasing the size of the separation bubble, fattening out the pressure distribution in region IV and reducing the extent of the trailing-edge separation. Finally, the effect of the two sail shapes tested on the aerodynamic characteristics appears to be small. The pressure recovery at reattachment is larger for the NACA 63, the minimum pressure in region IV occurs further forward, and on the lower surface the pressure distribution is much fuller.

REGION	DESCRIPTION
I	Upper Mast Attached Flow Region
II	Upper Separation Bubble
III	Upper Reattachment Region
IV	Upper Aerofoil Attached Flow Region
V	Trailing Edge Separation Region
VI	Lower Mast Attached Flow Region
VII	Lower Separation Bubble
VIII	Lower Reattachment Region
IX	Lower Aerofoil Attached Flow Region
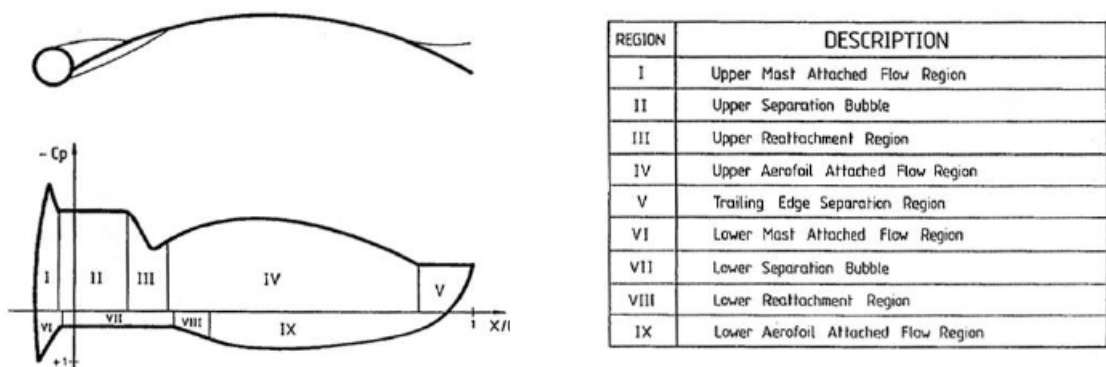
Figure 7.4: Universal pressure distribution for a 2D-Mast sail profile

Wind-tunnel results on 3D models are useful, but the actual flying shape of sails is difficult to achieve because of the soft materials from which they are made, the difficult problem of rig structural similitude, and the absence of wind-gradient effects in most wind tunnels. Moreover, it is

88

rarely possible to acquire sufficient local measurements, such as wall pressure and skin friction along the sail, to increase the understanding of these complex flows and contribute to the validation of advanced numerical methods. To be able to improve sail design, the performances must be evaluated with sufficient accuracy taking into account all the involved parameters and the real flying shape of the sail surface before being integrated into the aerodynamic model for a velocity prediction program (VPP). From the review of Milgram and Wilkinson's works, it is obvious that the sections and even the masts tested may not be representative of real sails and masts. Furthermore, the data gained in both series of experiments provided a foundation for understanding more about sail flows but is limited because three-dimensional flow effects may be large due to the low aspect ratio of the airfoils tested. With modern testing techniques the understanding gained from these basic experiments is useful to further enhancing the understanding of this most complex flow.

7.2 Pressure sensitivity paint

Pressure sensitivity paint is a smart techniques used to investigate pressure filed above aerodynamic surface. These paints need a reasonable dynamic pressure to work well. A. Crook [62] made used of pressure sensitivity paint to performed an experimental investigation concerning the measurements of pressure in bi-dimensional model of six mast-sail profile configurations, conducted in the NASA Ames 70 x 100 wind tunnel. The six mast sail model were made of thin cambered steel sheet put under tension to reduce the risk of buckling in the tunnel, and formed to the desired shape using matching machined blocks place in compression. PSP has been used on the upper and lower surface of the sail to determine the pressure distribution around the section, and also by integrating the pressure distribution, to calculate the section lift coefficient. PSP is applied to a highly-reflective surface and luminesces when excited molecules in the coating return to a lower energy state due to the collision with an oxygen molecule in a process known as oxygen quenching. Excitation is commonly provided by a UV lamp. The rate of quenching is proportional to the partial pressure of oxygen, which is in turn proportional to the air pressure. PSP is therefore most sensitive to changes in pressure when the dynamic pressure is high and the percentage change in pressure is high with respect to atmospheric pressure. A typical setup for PSP is shown in Fig 7.5.
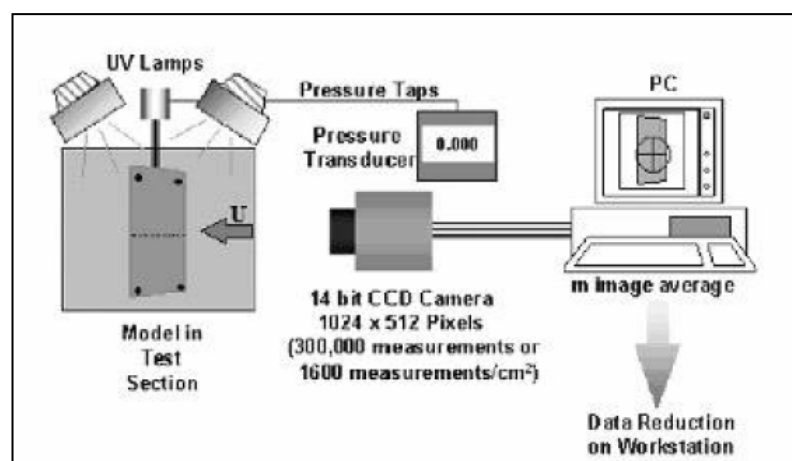
Figure 7.5 : Setup for PSP

The ratio of wind-on to wind-off intensity of the emitted light from the PSP is proportional to the ratio of respective pressures under conditions of constant excitation. The constants in the governing equation are derived either before the experiment by measuring the intensity of the PSP for various

89

pressures and temperatures and/or during the experiment by using a reference pressure on the model such as that provided by a pressure transducer. Photogrammetry may then be required to associate the points in the PSP image with those on the model. Uncertainty in the measurement of pressure can be due to errors in the calibration of the response of the paint to pressure, spatial and temporal variations in illumination and errors in the data processing. Anyway the largest source of error comes from the uncertainty in the paint's temperature. The accuracy of PSP is about 1 mbar with a resolution of 0.5 mbar, and that the typical time response is 0.5 seconds, although 1 μs has been demonstrated. Illustrations of the ability of PSP to capture the pressure distribution with high resolution over a large area and range of pressure are given in Fig 7.6.
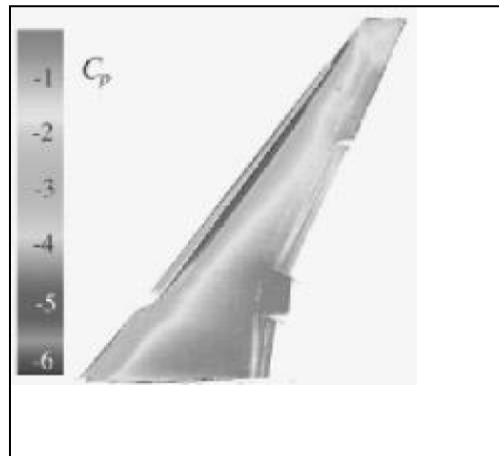
Figure 7.6 : PSP above a wing model.

7.3 Conclusion

Pressure measurements are of great importance in almost all fields of engineering and industrial applications, as far as yacht sailing challenges are concerned, the ability to optimize pressure distribution above sail surfaces, tweaking their shape in the changeable wind and sea conditions, represent one of the key factor to win a yacht race. The amount of open literature concerned with experimental pressure measurement is poor and relate to few mast sail configuration and attitudes. Nowadays, the only affordable and easy to set system, able to monitor the qualitative flow conditions in the real yacht sailing harsh environment, are the well known tell tales; these simply woven lines can provide a general visualization of recirculation bubbles and separated areas over sail surfaces, but don't represent a scientific tool able to investigate the behaviour of flow.
Aim of the pressure sensor network developed in this artwork is to provide a means to depict the weak pressure field acting on the sail plan of a full batten sail by means of instrumented battens, providing a real time differential pressure map over the entire sail surface. A common specification in such a kind of applications is related to the large size of the surfaces that has to be monitored, leading to the use of a large number of robust and conformable sensors in order to achieve the required spatial resolution. In this scenario, a real-time pressure distribution represents an important means for the analysis of the aerodynamic behaviour of the body and for its correct trim. The wireless sensor network has been developed to get the following requirements : small dimensions to increase spatial accuracy, low environment-invasion-level; high resolution, robustness and low cost.

Chapter 8

Nautical pressure sensor

Aim of the network is to sense the weak pressure field acting on the sail plan of a full batten sail by means of instrumented battens, providing a real time differential pressure map over the entire sail surface. These kind of experiments if performed with classic laboratories techniques would require long set up procedures and time consuming acquisitions. The already mentioned approach appears to be suitable just for scientific experiments where the data collected are post-processed. Instead the main goal of the proposed wireless sensor network has been developed for, is the real time and on-situ acquisitions of differential pressure over sail surfaces in harsh sea environments.

8.1 Wireless sensor network structure and working principle

The wireless sensor network has been developed in collaborations with other colleagues and particularly it has been projected by Ing. Rossano Codeluppi. The wireless sensor network is composed by three main element described in detail in the next paragraph :

- Pressure sensing units

- Wireless nodes

- Instrumented battens

The pressure sensing unit is the core of the network, it is a capacitive differential non-MEMS sensor built in PCB technology, its aim is to sense and transduce static pressure by means of deformation of a thin and very sensitive film of Mylar840®.
Wireless nodes host the sensing unit, the sensing electronic circuit, and the power supply battery, they are built in PCB technology too. Any nodes is fabricated to ensure the sensing unit to be set in the instrumented battens and to let the sensor not to be affect to the battens curvature and strain. Any Instrumented battens let the nodes to be positioned on the sail surfaces, its principal aim is to reduce the intrusivity of the whole network over sail and to let a quick and easy installation.By means of any instrumented battens is therefore possible to acquire a discrete differential pressure distribution across the sail chord from the sail luff to the leech as shown in Fig 8.1.
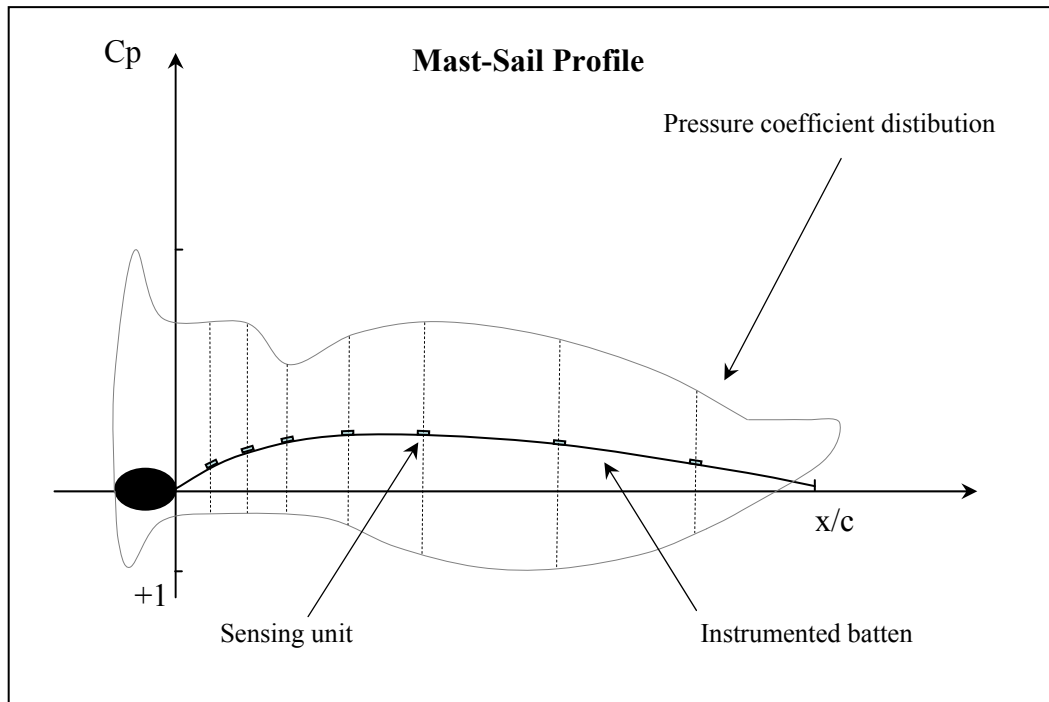
Figure 8.1: Pressure acquisition in a mast-sail profile

Combining the measurement of all battens it is possible to get the pressure profile at different height along the mast from the base to the top as shown in Fig.8.3. The wireless network and the component of which it is composed let the real time acquisition of static pressure be smart and reliable. By means of the network it is therefore possible to compute pressure maps over full battens sails, potentially these data can be used with two distinct approach: a real time elaboration , and/or a post processing computing.
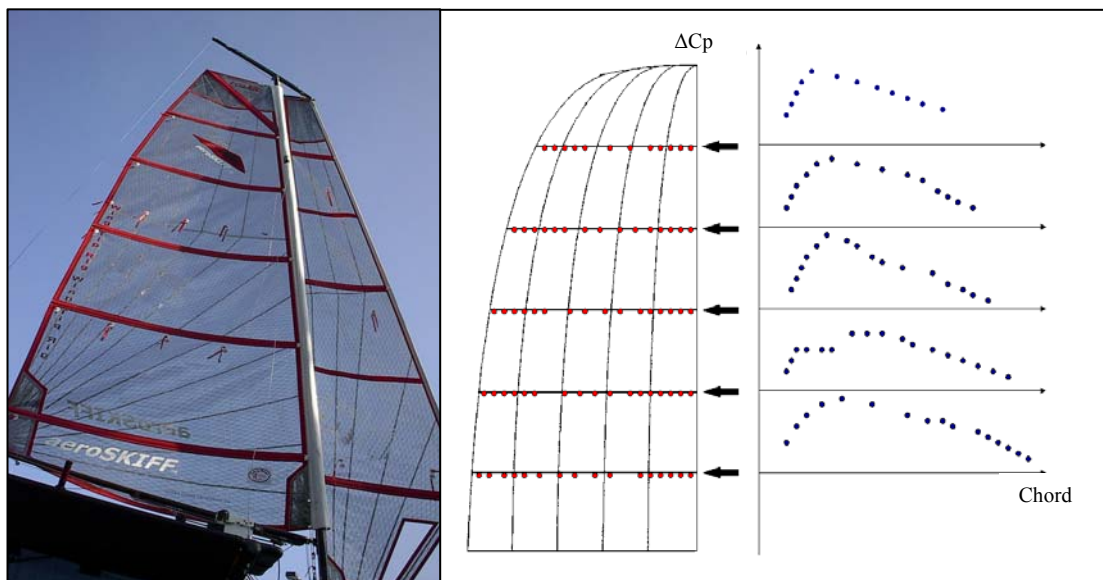
Figure 8.3 : Differential pressure acquisition for different height station along the mast

The real time pressure data could used by different users as challenger or amateur sailors; the pressure data if coupled with parameters directly connected with the helmsman choices such as sail attitude, trim, and course sailed, may be used to evaluate the man sailing ability to get maximum

performance of the yacht in terms of sail-plan efficient , maximum velocity or VMG velocity made good to wind. Other important applications related to the real time acquisition are concerned with the navigation and automatic control of yacht sails. Pressure may be use as input of a control system dedicated to the self trim of sails for autonomous navigations. The post-processing of pressure data could be used both by a sail maker or a researcher, the former can test the efficient of new sail shape and trim actions, the latter can use the data to better understand the complex fluid dynamic phenomena such as the iteration of the mast-sail junction or sail overlap, moreover new sail flow model could be validate and/or boundary conditions implemented. The proposed sensor network is also a suitable tool to enhance the developed of the sails aerodynamic module of the VPP, useful to evaluate the complex performance of a yacht sail.

8.2 Wireless sensor network

The wireless sensor network developed is composed by a certain number of nodes and a controller. Nodes are devoted to sense and transmit, the static pressure above the sail surface; they house the pressure sensing unit, the sensing electronic, the antenna, and a battery. Whereas the controller is devoted to collect the pressure data transmitted by any nodes, to switch the operation mode of the network, to create and feed the data stream to a graphical interface. The general network layout can be modelled as a star Fig 8.4, where the middle position is interested by the controller, the others by nodes,[63],[64],[65].

Zensys Node

Network Controller
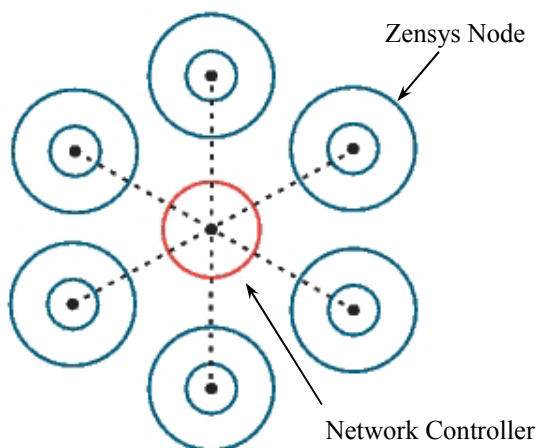
Figure 8.4 : network topology

The network has been developed to handle a maximum number of 50 nodes, it can provide a sail pressure map every 3 seconds. Any nodes of the network and transmits the differential pressure related to its point of measurement, this actions require a certain power, to be performed. To reduce as much as possible the power consumption of the battery of every node, anytime the controller asks nodes for the pressure value measured, this is transmitted only when the sensed pressure differs from the previous value of a pre-set threshold, otherwise it "sleeps" until the next request from the controller,[66]. These procedure is necessary to save battery and not to overcrowd the transmission band. Data from the network nodes create an information stream received on yacht board by the controller and lid to a computer by cable to be processed and displayed in real time. The network controller can also switch on or switch off any nodes of the networks. WSN were originally created to collect data from sensors or transmitting control commands in industrial applications, therefore if compared with other application the WSN do not operate with high data rate (actual-throughput) or long radio range, but with a low power consumption ,[67], [68], [69], [70], [71],this feature is useful to let the use of small and thin battery achievable.

93
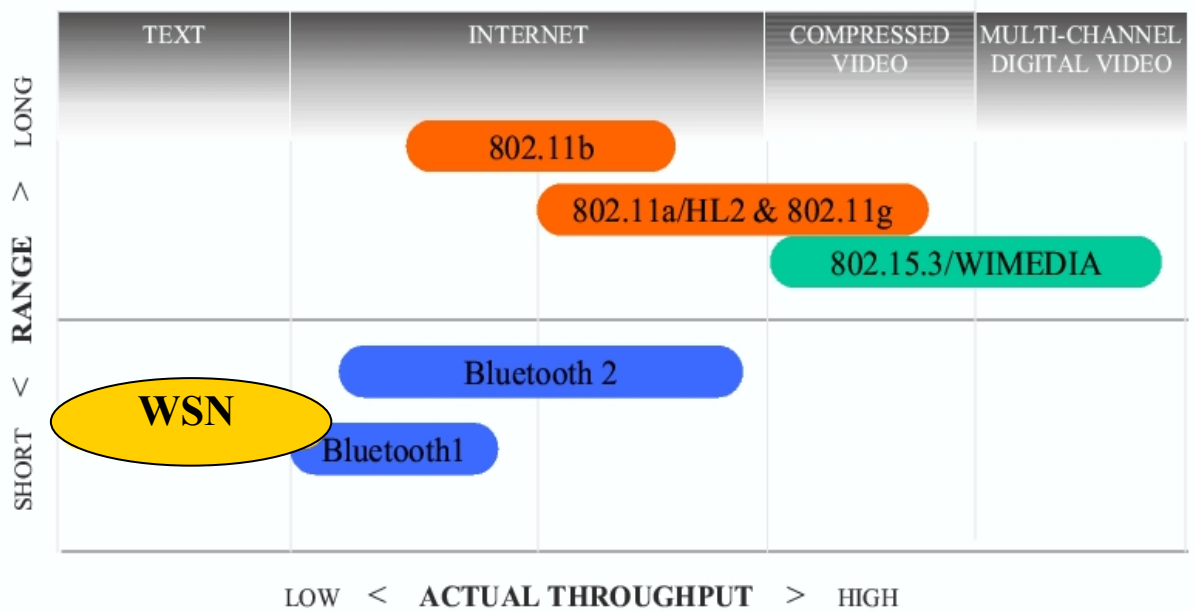
Figure 8.5 : WSN compared with other wireless system

Nowadays it's possible to choose between different WSN platforms on the market. They differ for characteristics as transmission bands, data rate, available electronic in the node and readiness of use. The WSN transmission features are also dependent on the country where they are employed, because of allowed transmission band.

BAND		COVERAGE	DATA RATE	# OF CHANNEL(S)
2.4 GHz	ISM	Worldwide	250 kbps	16
868 MHz		Europe	20 kbps	1
915 MHz	ISM	Americas	40 kbps	10

Table 8.6 : WSN bands in the world and characteristics

WSN transmit on ISM band (Industrial, Scientific and Medical band): the band is free, but changes its frequency according to the country. Table 8.6 summarizes bands and transmission characteristics for different countries. The WSN platform chosen for the proposed application is a Zensys ZW2101 board Fig. 8.7 it is mounted on board of every node of the network .
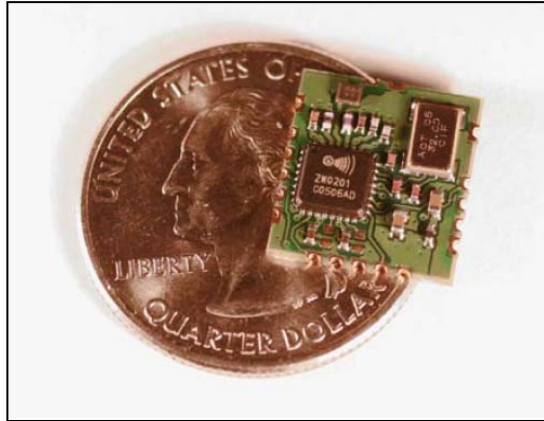
Figure 8.7 : ZW2101, mounted on every node

The sensing electronics implemented in any nodes of the Wireless Sensor Networks (WSN) is built in a small single-chip, where a microcontroller manage an electronic system and a radio section allows a radio communication. Every single-chip is programmable to suit the requirements of the network. The network can handle many hundreds of nodes. Node are driven by a network controller devoted to receive pressure data transmitted by any nodes; a network collector unit is located on the yacht board Fig 8.8.

Figure 8.8 : Network controller

The Zensys ZW2101 is not a single-chip device but a micro board with integrated, [72] electronics. The ZW2101 is, 14mm x 16mm width and 2mm thick. The transmission frequency used in Europe by Zensys is 868MHz, this parameter can be set by the user according to the country rules. The radio transmission range, depends on the antenna type and power of transmission (programmable), generally the maximum range varies between 30 metres indoor, to 350 metres outdoor. The WSN developed transmits its data in a range of at least 30 meters; this distance has been set taking into account a yacht equipped with a mast height of 30 meters and with the data controller positioned on board. In the proposed NWS the network controller is able to broadcast every nodes displaced on the sail.

8.3 Sensing unit structure and working principle

The sensing unit has to cope with the weak pressure field acting over the sail surface. The sensor presented in this artwork is a differential capacitive pressure transducer built in PCB technology. The sensing unit implemented in each nodes of the wireless network is a robust and 'non-MEMS' device able to monitor the differential pressure field acting on wide surfaces and in harsh environment. Capacitive sensors have been chosen because of some clear advantages when compared to other types, i.e. higher sensitivity, better temperature performance, and lower power consumption. The latter is a suitable characteristic for a wireless network. The use of PCB technology has several advantages over other approaches, it allows the hosting of electronic sensing and signal processing components by means of smart packaging, such as the chip onboard technology. Moreover, it is possible to obtain devices achieving most of the specifications required at very low cost. The sea is in fact a very harsh environment and the sensing element is the weaker component of each node of the network, therefore it must be cheap and easy to be replaced. In spite of the low cost, the PCB technology, during the last few years, has greatly improved its resolutions, allowing the design of precision devices and transducers with a resolution of tens of micrometers. Moreover, by its nature, the PCB structure can provide a support for smart packaging, hosting both analogue and digital signal processing circuits.

The structure of the sensing unit Fig 8.9 consist of a 12 μm thick conductive Mylar840® diaphragm stretched over a circular cavity . The deformable diaphragm film will deform itself downward and/or upwards with respect to external pressure acting as the movable plate of the capacitor producing a capacitance output related to pressure changes.
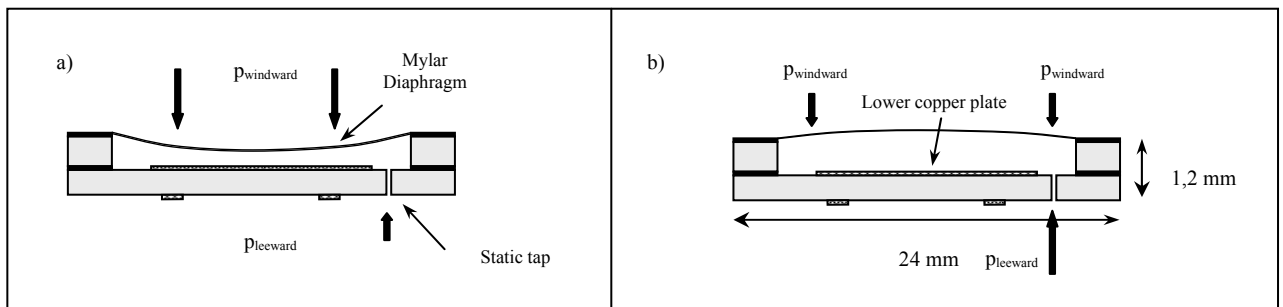
Figure 8.9: Sensor working principle and dimensions

The fixed plate of the capacitor is a circular copper electrode obtained in the base of the sensor Fig. 8.9 (b). The sensor measures the differential pressure exerted between the external side of the membrane, directly exposed to the flow, and the pressure inside the cavity of the sensor connected to the other side through of a static tap Fig.8.9 (a).
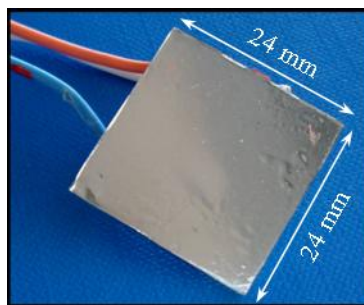
Figure 8.10: Sensor dimensions

The membrane represents a measurement point that can be monitored electronically by collecting a set of surface differential pressure profiles acting through the sail surface that are dependent upon the environmental conditions. Since the membrane area is usually much smaller than the monitored aerodynamic surface, the corresponding pressure distribution over the deformable film can be considered constant. The device length and width is 24 mm, the total thickness is below 1.2 mm as illustrated in Fig.8.10 b.

8.4 Wireless node

Such as any sensing units is developed to sense the pressure acting on the sail surface, any nodes on which it is mounted has to guarantee important issues. Nodes are devoted to:

- Host the electronic sensing circuit, and the power unit, by means of smart packaging and chip onboard technology.

- Transmit the pressure data to the data collector

- Let the static pressure to be lead inside the sensor cavity and above the thin diaphragm.

- Let the sensing unit to be insensitive to the curvature and strain acting in the battens.

Nodes are housed in special instrumented battens, described in brief in the following chapter. Any node is a thin and flexible base layer of FR4; it is 90 mm long and 30 mm width with a thickness of just 460 um in which are implemented: a pressure sensor unit, the sensing electronic circuit, and a battery, as shown in Fig 8.11. The sensing electronics of the Wireless Sensor Networks (WSN) is built in a small single-chip, where a microcontroller manage an electronic system and a radio section allows a radio communication.
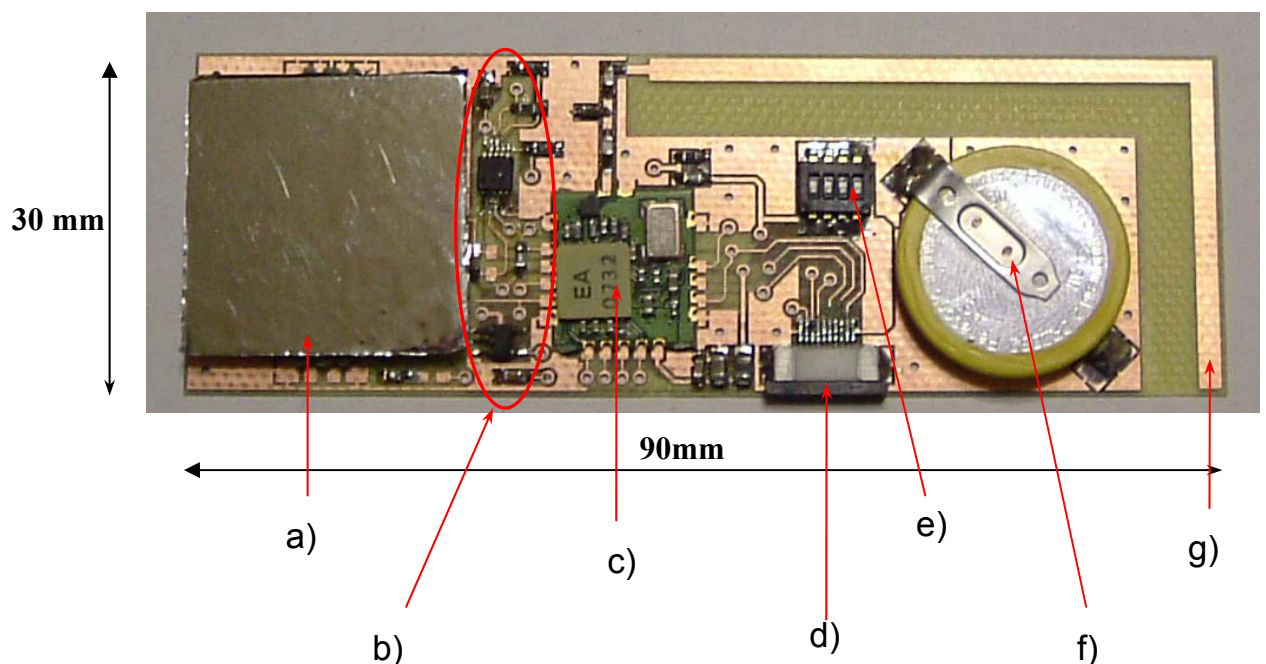
Figure 8.11 : WSN node layout

Every single-chip is programmable to suit the requirements of the network. The network can handle many hundreds of nodes and every node can send its data to the data controller. Every nodes of the network is equipped with the following principal component Fig. 8.11 :

a) **Sensing unit :** The sensing unit is positioned in the forward part of the node and linked to the base by means of a 2 mm thick plinth of FR4 on which it is bonded. The thick plinth of FR4 due to its short dimension in the direction of maximum curvature of the battens let the effects of battens deformations to be greatly reduced. It also allows the electrical signal to be led to the sensing circuits by means of an appropriate numbers of vias.

b) **Sensing electronic** : The sensing circuit is directly mounted on board, the sensing circuit chose is a charge amplifier (CA), a very special class of circuits often employed in capacitive sensing device to convert voltage signals from low capacitive variations. It performs the translation from a capacity value induced by the diaphragm deformation to a voltage value.

c) **Zensys ZW2101 node:** This device translates the voltage value sensed by the charge amplifier in a pressure value, manages the sensing electronic, and process the data to be transmits by the antenna the data rate is 9,6kbps.

d) **Programming connector** : It is used to program the ZW2101 before using the node.

e) **ON/OFF switch**: It's the physical on/off switch . When in ON position the node is started and set in stand-by mode thus wait for the wake up command from the controller and transmit a pressure data when the sensed pressure differ from the previous value of a certain pre-set threshold.

f) **Battery** : It's the supply of whole node. It is a 3V, 220mAh, coin battery, with a diameter of 32 mm and thickness of 2.6 mm, once bonded on board the battery and node height is 3.5mm Fig. 8.12.
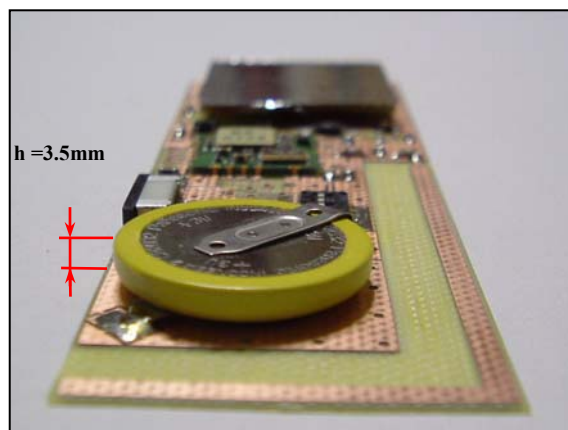
Figure 8.12 : WSN node and battery

g) **Antenna** : It's a "L" $\lambda/4$ monopole [73], [74], [75],created directly on the PCB and it has been tuned to the transmission frequency of 868MHz (the wave length λ is 34,5cm). It has been chosen between four different kind of antenna :

98

1. <u>Whip antenna</u>: generally it's a wire long $\lambda/4$, $\lambda/2$ or λ bonded on the board at the RF output of ZW2101. Simple to design and to use, it is an good omnidirectional antenna with a good antenna gain, but it's too fragile to be used on a sail.

2. <u>External $\lambda/4$ monopole</u>: it's hard antenna setting perpendicular to board. It is a good omnidirectional antenna with a good antenna gain and we use it in the controller, but it's impossible use it on the wireless node because too large to implement physically.

3. <u>Chip antenna</u>: it's an antenna build into a chip. It is very small and easy to implement on a board, but it is a poor omnidirectional antenna with low gain.

4. <u>$\lambda/4$ monopole on PCB</u>: it's the antenna with the most complex design, its behaviour is strongly influenced by the node physical structure. It represent a good trade-off: it is a good omnidirectional antenna with a fairly good antenna gain and board-compatible dimensions . It has been designed as a "L", $\lambda/4$ monopole : this topology allows to reduce of 20% the full antenna length ($\lambda/4$) simplify the board design, without decrease significantly the antenna gain.

In the standby state any node needs 10,5uW; whilst to perform a measurement (sensing and transduction) 15,3mW are required; if the pressure values differ from the pre-set threshold the transmission is allowed and 66mW are required . A node spend about 2,8 seconds in the standby state and require about 200 millisecond to acquire and transmit the pressure value. The already mentioned time intervals are averaged values and are strictly dependent on the band use due to the number of nodes that perform a transmission. Working on average time we can estimate the node life time by the capacity of battery used. A 3V 220mAh coin battery has been chosen. If the network is held active eight hours in a day, every node needs an equivalent battery per day of 4,2 mAh. So we can estimate the node life time in more than 1.5 months working eight hours per day. Another important aspect the nodes is called to assure, is to let the static pressure to be sensed. The pressure distribution acting on the two sides of the sail in fact will be sensed in one face by means of a static tap drilled in the bottom part of the base layer Fig 8.13. Through the static tap the pressure of the windward side (or leeward depending on the course sailed) will be lead inside the cavity of the sensor by means of a small pipe drilled in a special FR4 plinth to allow the pressure to be shared in the cavity of the sensor .The pressure acting on the opposite side of the sail will be sensed by the thin membrane facing directly with the flow. It is important to point out that, in order to guarantee the concentric alignment of the static tap on the sail cloth (1mm of radius), with the pipe drilled in the bottom side of the node, the latter has been realized with a larger radius of 3mm.
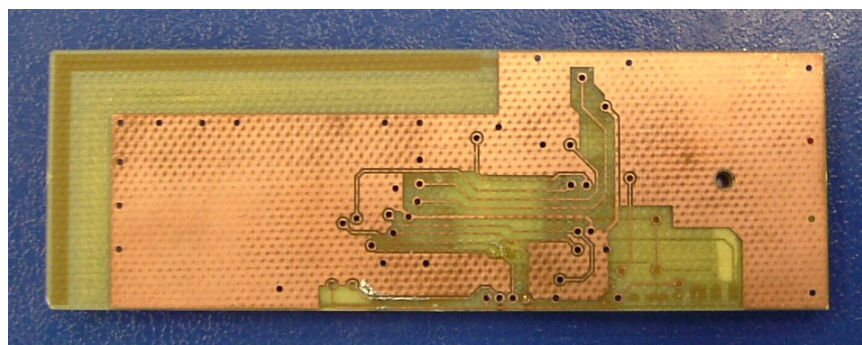
Figure 8.13 : WSN node – bottom view

The last requirement the node has to guarantee is to let the sensing unit be insensitive to the strain induced by battens camber. Battens are designed to produce a predefined shape in the sail plan

form, anyway these objects are semi-rigid bodies thus changing their shape according to helmsman adjustment and pressure distribution over the sail surface. The sensing unit has been built over a 760 um thick frame of FR4 while the node board shown in Fig.8.13 is just 460 um thick, thus more flexible and able to follow the batten camber. The sensing unit which is 24 mm width and 24 mm long and is bonded to the node Fig 8.16 board by means of a 5 mm width and 24mm long FR4 plinth, its thickness is 1,6 mm Fig.8.14.
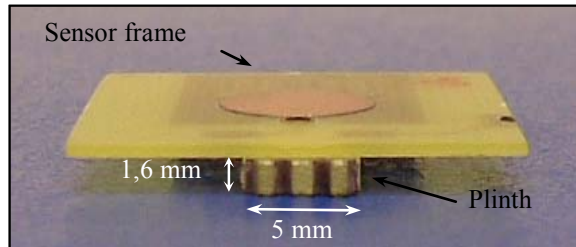
Figure 8.14 : Plinth bonded to the sensor frame

The thick plinth of FR4 due to its short dimension in the direction of maximum curvature of the battens (5mm) let the effects of the battens deformations on the sensing unit to be greatly reduced. It also allows the electrical signal to be led to the sensing circuits by means of an appropriate numbers of vias Fig 8.15. Inside the plinth a circular pipe is drilled to led the static pressure inside the cavity of the sensor.
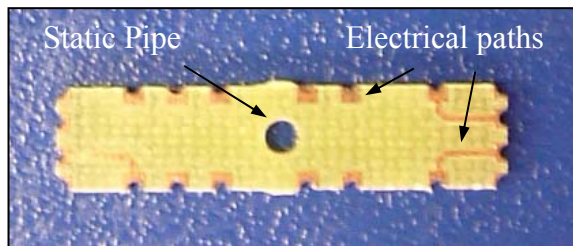
Figure 8.15 : plinth electrical paths , and static pipe

Once the sensing unit is bond on the plinth it is the higher component of node the maximum thickness of the node is about 4 mm the width is 30mm an the length is 90mm.
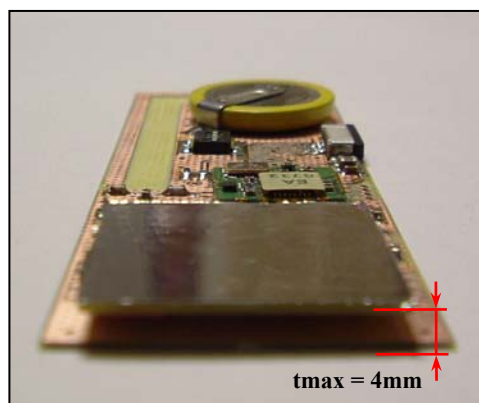
Figure 8.16 : wireless pressure monitoring node – sensor side

100

8.5 Instrumented Battens

Battens are usually employed to provide to sails a pre-defined shape and to avoid excess of deformations. Battens are inserted inside special pockets, therefore the thickness of sails is not uniform along the surface but present variations in the proximity of the battens pockets . The thickness of battens ranges from two to four millimetres and the length and width vary according to the shape and requirements for any type of sails. Moreover battens are not fixed to sail but it is possible to slip off the battens in order to adjust their length to trim the local camber of the sail . These peculiarity of modern full battens sails let the battens to be a useful and non-intrusive device where to place the nodes of the wireless network . According to these considerations, special instrumented battens has been developed and fabricated to house nodes. As a consequence the nodes layout has been chosen to be conformable with the shape of battens. As reported by Wilkinson [15-17], the typical pressure distribution along the chord of a mast-sail profile, is characterized by regions where pressure gradients are quickly variable. These regions are those close to the luff and the leech of sail; in the former quick variations of pressure are due to junction between mast and sail here large separation bubbles and flow reattachment points of the flow are present, in the latter turbulent and large separations zone are present. According to these considerations nodes distribution, in any battens, has been chosen to be numerous close to the mast (leading edge) to better depicts the extension of recirculation bubbles and close to the leech (trailing edge) to identify the onset of separation Fig 8.17.
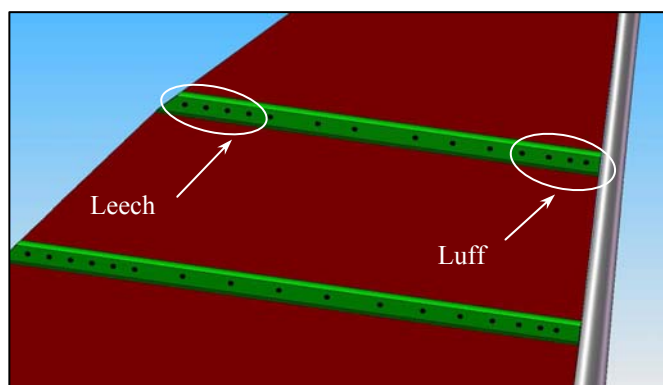
Figure 8.17 : Distribution of nodes along the chord of the batten sail

Battens was built in the laboratory facilities by means of a numeric-controlled milling machine. Any battens consist of two PVC layers a base and a lid., as shown in Fig.8.18 (a) . The base is the thicker layer (2,5 mm) and houses the bottom part of the nodes in preformed cuts, in the bottom side circular holes acting as static taps let the pressure get inside the cavity of the sensor Fig.8.18 (b). The lid is the thinner layer (1,5 mm) of the battens and presents two through cuts, one is circular for the battery the other square for the sensor and let the diaphragm face with the outside flow .
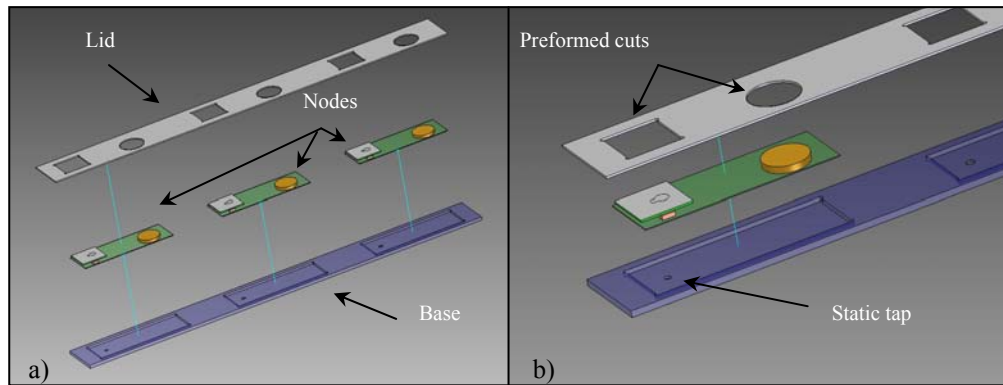
Figure 8.18 : Instrumented battens component (a), Allocation of the node inside the batten (b)

To let the static pressure to be sensed the pockets of any instrumented batten are cut in the point of measurement with two circular holes one in the windward side of the sail the other in the leeway. Holes are respectively some millimetres greater than the sensing unit diaphragm and the static tap diameter Fig. 8.19 in this way the battens and the pocket let the pressure of one side of the sail to get inside the cavity of the sensor and the diaphragm to face the outside flow of the opposite side.
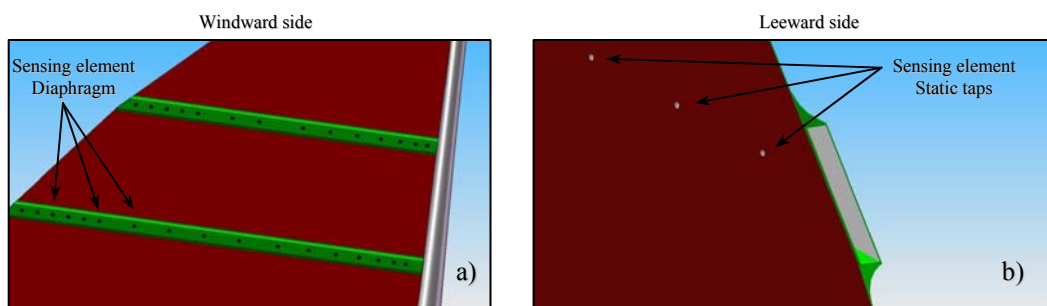
Figure 8.19 : Preformed cuts in the sail, diaphragm (a), static tap (b)

In Fig 8.20 the assembled battens is presented, the total thickness of any batten is 4 mm, in this way the top side of the sensor will lean out from the battens thickness of about 0.5 mm, to let the sensor adhere to border of the preformed cut in the cloth of the sail.
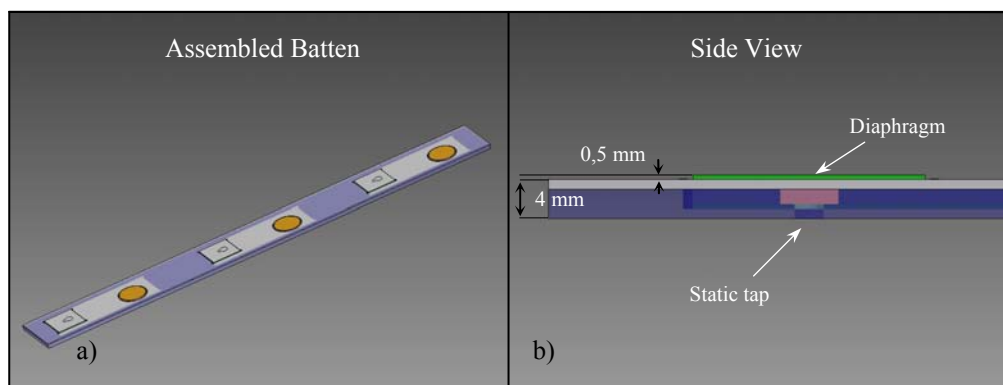
Figure 8.20 : (a) Assembled batten, (b) Side view of the battens and node

In Fig 8.21 Fig 8.22 the fabricated battens composed by the base and the lid are shown, while in Fig 8.23 the nodes is positioned in the batten. The base and the lid shown of the instrumented battens, was built in the laboratory facilities by means of a numeric-controlled milling machine, in Fig.8.21

(a) it's possible to see the square pre-formed cuts fabricated to let the membrane facing the otside flow. In Fig. 8.21 (b) , the assembled base and lid of batten are shown.
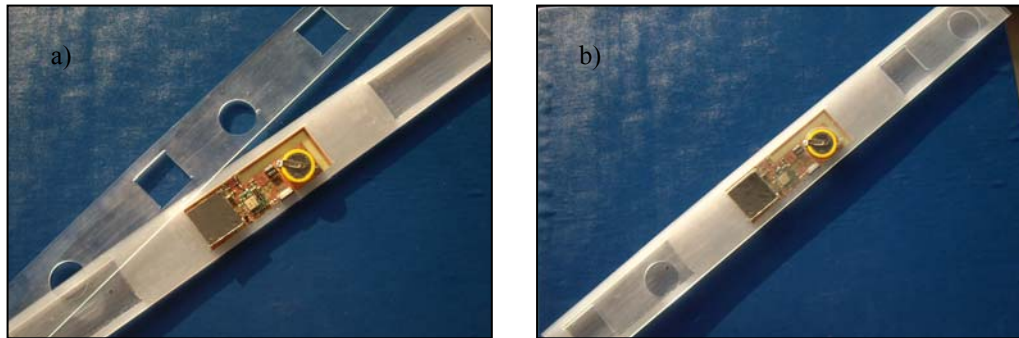
Figure 8.21 : (a) The lid and base of the batten, (b) A node packed inside the batten

In Fig.8.22 (b), the side view of the battens; the senor and the sensing unit, the whole thickness of the battens is 4 millimetres.
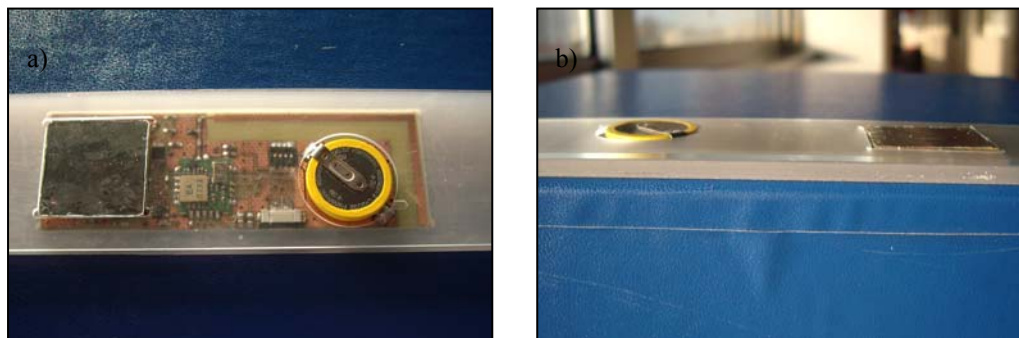
Figure 8.22 : (a) Top view of a node inside the batten, (b) Side view of the batten

Chapter 9

Nautical pressure sensor unit finite element simulations

In chapter 2 was shown how the analytical formulation of the sensor behaviour might be not sufficiently accurate for achieving a good design of the sensor due to the non linearity present both in the pressure-deflections transduction and in the electric capacitance relationship. Numerical FEM simulations are then a fundamental task for the understanding of the sensor behaviour and for comparing the latter to the commonly used silicon-based MEMS structures. The aim of FEM simulations is to describe more efficiently the physical and structural sensor features in order to find an optimum geometry and to satisfy the specific application. Since the output of the sensor is a capacitive information, coupled electrical and mechanical simulation have to be taken into account. Fortunately, simple hand calculations show that, in contrast with typical MEMS structures, electrostatic force is negligible with respect to external forces inducing mechanical deformation: for a parallel circular plate capacitor with a radius of 1 cm, the distance between armatures should be tens of μm for obtaining an electrostatic force, in air, equivalent only to 5 Pa for an applied difference of potential of 5V. As a consequence, electrostatic simulations may follow mechanical ones without coupling. On the other hand, an important difficult issue is due to viscoelastic behaviour of polymers, thus an over-simplified analysis could lead to large errors. This problem is usually referred to as creep and its modeling was described in chapter 3.

A fem static model of the sensor was realized by means of a static non linear coupled model able to predict the mechanical deformation of the membrane an the related capacitance change induced between the two plate of the capacitor, the model was refined in successive iteration by means of a first run of experimental data acquired on sensor prototypes. The Fem static model is a suitable tool to predict different topics concerning the sensor characteristic, as the mechanical and electrostatic sensitivity, potential conditions of saturation, dead band zone, full scale output and resolutions. By means of the fem static tool is then possible to choose the appropriate geometrical dimension in terms of radius and initial distance between plates that better suite to the pressure field the sensor will have to face. Anyway the static fem model is not useful to estimate the error of the sensor in terms of accuracy and repeatability, this problem is due to the non linear and viscoelastic time dependent behaviour of the thin diaphragm. To be able to estimate the inaccuracy bound associated to any of the geometry tested with the static model, a time dependent model of the error affecting the diaphragm is necessary. Unfortunately poor data concerning the creep behaviour of Mylar® are available in open literature or technical datasheet, that's why has been necessary to develop an experimental procedure able to extract this data and to infer a time dependent error model to predict the imprecision of the device, introducing in the fem static model, time dependent parameters to reproduce, with a certain degree of confidence, the inaccuracy bounds related to the pressure input.

Both the fem static model and the time dependent error model have been used to choose among many potential geometries for the sensor ; finally the one associated with the better trade off , in terms of sensor figure of merits parameters, has been chosen.

9.1 Fluid dynamic input variable

Since the fluid dynamic application, chosen for the proposed sensor architecture, is the monitoring of pressure pattern over a sail profile, a first investigation was conduced to explore the typical fluid dynamic variables environment. Airplane wing are composed by typical aeronautical profile, to get data concerning the pressure involved in such bi-dimensional body a vast amount of experimental studies have been conducted and collected in different data base or book. In Abbot [18] a vast amount of parameters such as lifting drag, momentum and pressure coefficient are reported for a large numbers of NACA profiles. Typical flows over aeronautical commonly used profiles are characterized by high Reynolds numbers and low incidence angle, therefore the fluid flux has a high level of kinetic energy and due to the low incidence of typical aeronautical applications the adverse pressure gradient let the flow to separate in a narrow and well discernable range of incidence. Unfortunately sails are not composed by typical aeronautical profile but by the union of a mast and a thin load-deformable cambered lines. Moreover the typical Reynolds numbers involved in yacht sailing are several order of magnitude lower than the aeronautical typical ones. All these factors let the flux over sails profile be characterized by large amount of separate areas and recirculation bubbles, these phenomena are often related with sudden drop in the pressure magnitude in respect with the condition of attached or potential flows. The already mentioned phenomena let an analytical approach not suitable to estimate the pressure over such a surface and flux, for these reason numerical solution and experiments concerning the pressure field acting on a sail has been take into account to get an estimation of the differential pressure field magnitude.

Computational methods are often based on simple algorithm based on the panel method. This methods can be used for computing 2D inviscid, incompressible, irrotational flow solutions. This method is based on the boundary layer equation described in [76]. It uses Thwaites equations for the laminar part of the flow and Head's equations for the turbulent part. Michel's criterion is used to locate transition and the drag coefficient is computed using the Squire-Young formula [77]. The results obtained with the panel method model are quite accurate for pressure distribution but not enough for the evaluation of the shear-stresses, and to identify separation and reattachment point which are not considered in this phase. In more advanced developments, like Xfoil® [78], the model is slightly more complicated, and the solution is more robust and closer to experimental results. Another possibility to calculate the pressure distribution around a wing profile is to use the Thin Airfoils Theory. The main problems concerned with the numeric code developed with these theory are inaccuracies introduced when separated flows are handled, for this reason empirical approach or approximated numerical methods are use to estimate the extension of recirculation bubbles and separated areas. Among the different fem codes the results from MacSail® a vortex-lattice (VLM) methods developed at the Helsinki University of Technology [79], has been analyzed to infer the bound of the pressure field acting over a maxi yacht in close hauled courses with mainsail and head sail. The results of panel methods provides the velocity, pressure, separations and reattachment points in the middle of trapezoidal plane panels over the leeward and windward side of the sail. In table 9.1 and table 9.2 typical results in matrix form are shown for the mainsail and the headsail. The first index of numbers located in the first column of table 9.1 and 9.2 represent the vertical position of the panel considered, starting from the base till the top of the sail, while the second index represent the position along the chord of the sail profile, from the leading to the trailing edge.

No.	C_{plee}	Cp_{wind}	ΔCp	Δp 10Kts	Δp 20Kts	No.	C_{plee}	Cp_{wind}	ΔCp	Δp 10Kts	Δp 20Kts
1,1	-0.498	0.460	0.958	15	62	2,1	0.001	0.001	0.000	0	0
1,2	-1.263	0.616	1.879	30	121	2,2	-0.309	0.017	0.326	5	21
1,3	-1.569	0.688	2.257	30	146	2,3	-1.042	0.092	1.134	18	73
1,4	-1.680	0.720	2.400	38	155	2,4	-1.387	0.273	1.160	26	107
1,5	-1.724	0.747	2.471	39	159	2,5	-1.512	0.363	1.875	30	121
1,6	-1.428	0.726	2.154	34	139	2,6	-1.286	0.427	1.712	27	110
1,7	-0.994	0.675	1.670	27	108	2,7	-0.905	0.461	1.365	22	88
1,8	-0.468	0.570	1.038	16	67	2,8	-0.429	0.439	0.868	14	56
3,1	0.002	0.002	0.000	0	0	4,1	0.003	0.003	0.000	0	0
3,2	0.270	0.016	-0.254	-4	-16	4,2	0.316	0.016	-0.300	-4	-19
3,3	-0.444	0.081	0.525	8	33	4,3	-0.175	0.070	0.245	3	15
3,4	-0.952	0.252	1.203	19	77	4,4	-0.589	0.216	0.805	13	52
3,5	-1.137	0.333	1.470	23	95	4,5	-0.749	0.276	1.025	16	66
3,6	-1.049	0.390	1.440	23	93	4,6	-0.794	0.331	1.124	18	71
3,7	-0.788	0.419	1.207	19	78	4,7	-0.683	0.367	1.050	16	67
3,8	-0.401	0.396	0.798	12	51	4,8	-0.401	0.367	0.768	12	49
5,1	0.373	0.098	-0.275	-4	-17	6,1	0.092	0.497	0.405	6	26
5,2	0.207	0.156	-0.051	0	-3	6,2	0.110	0.360	0.250	4	16
5,3	-0.096	0.317	0.414	6	26	6,3	-0.032	0.319	0.351	5	22
5,4	-0.358	0.345	0.703	11	45	6,4	-0.165	0.319	0.484	7	31
5,5	-0.459	0.340	0.799	12	51	6,5	-0.211	0.313	0.524	8	33
5,6	-0.509	0.345	0.854	13	55	6,6	-0.208	0.300	0.508	8	32
5,7	-0.462	0.328	0.789	12	51	6,7	-0.162	0.263	0.425	6	27
5,8	-0.301	0.280	0.581	9	37	6,8	-0.087	0.192	0.279	4	18

No.	C_{plee}	Cp_{wind}	ΔCp	Δp 10Kts	Δp 20Kts	No.	C_{plee}	Cp_{wind}	ΔCp	Δp 10Kts	Δp 20Kts
1,1	-0.496	0.492	0.988	16	63	2,1	-0.177	0.282	0.459	7	29
1,2	-1.540	0.621	2.161	35	139	2,2	-1.242	0.607	1.848	29	119
1,3	-2.012	0.687	2.698	44	174	2,3	-1.953	0.720	2.673	43	173
1,4	-2.164	0.725	2.889	47	186	2,4	-2.317	0.784	3.101	50	200
1,5	-2.097	0.753	2.850	46	184	2,5	-2.330	0.821	3.151	50	203
1,6	-1.716	0.758	2.474	40	160	2,6	-2.024	0.824	2.847	46	186
1,7	-1.193	0.636	1.829	29	118	2,7	-1.539	0.783	2.322	37	150
1,8	-7620.	0.280	1.041	16	67	2,8	-0.927	0.645	1.572	25	101
3,1	-0.145	0.217	0.362	5	23	4,1	-0.451	0.295	0.747	12	48
3,2	-1.101	0.550	1.651	26	106	4,2	-1.064	0.495	1.585	25	100
3,3	-1.774	0.673	2.447	40	160	4,3	-1.518	0.599	2.117	34	137
3,4	-2.136	0.747	2.882	46	186	4,4	-1.747	0.664	2.411	39	156
3,5	-2.070	0.778	2.848	46	184	4,5	-1.594	0.671	2.265	36	146
3,6	-1.803	0.770	2.572	41	166	4,6	-1.378	0.634	2.012	32	130
3,7	-1.042	0.708	2.110	34	136	4,7	-1.096	0.535	1.163	26	105
3,8	-0.916	0.530	1.447	23	93	4,8	-0.774	0.321	1.095	17	70
5,1	-0.714	0.509	1.223	19	79						
5,2	-1.036	0.454	1.490	24	96						
5,3	-1.185	0.486	1.670	27	108						
5,4	-1.241	0.508	1.748	28	113						
5,5	-1.089	0.477	1.566	25	101						
5,6	-0.937	0.407	1.345	21	87						
5,7	-0.719	0.297	1.015	16	65						
5,8	-0.496	0.144	0.639	10	41						

Table 9.1: Head Saill pressure coefficient   **Table 9.2:** Main Sail pressure coefficient

Another important issue is to set the higher limit of the pressure field which is directly connected with the intensity of wind blowing on the sail. In many sailing contest the higher limit of the wind above which the regatta is aborted is usually twenty knots for this reason the full scale pressure input of the wireless sensor network has been developed to operate in a true wind ranging from zero to twenty knots; a safe factor to allow overpressure has also been considered.

To estimate the higher differential pressure exerts through the sail surface the panel with the maximum difference of ΔCp has been found and the related differential pressure calculated for two conditions of apparent wind of 10 kts and 20 Kts.

$$\vec{V} = 10 Kts \qquad \Delta p_{Max} = 38 \ [Pa]$$

$$\vec{V} = 20 Kts \qquad \Delta p_{Max} = 160 \ [Pa]$$

Mainsail

$$\vec{V} = 10 Kts \qquad \Delta p_{Max} = 23 \ [Pa]$$

$$\vec{V} = 20 Kts \qquad \Delta p_{Max} = 204 \ [Pa]$$

Headsail

The maximum value of the differential pressure exert over the headsail is about 200 Pascal in a true wind of 20 Kts in close hauled condition, with both the sails working.

A literature review concerning experimental pressure measurements over sail surfaces has been carried out. In open literature the only experimental data-base concerned with pressure over mast-sail profile is the one collected by Wilkinson [15-17]. He present a parametric experiment over a scale model of bi-dimensional sail with circular mast of different diameters and two different variable camber NACA mean lines; a NACA 63 and a NACA a=0.8. The typical graphical form of the data is presented in Fig. 9.1
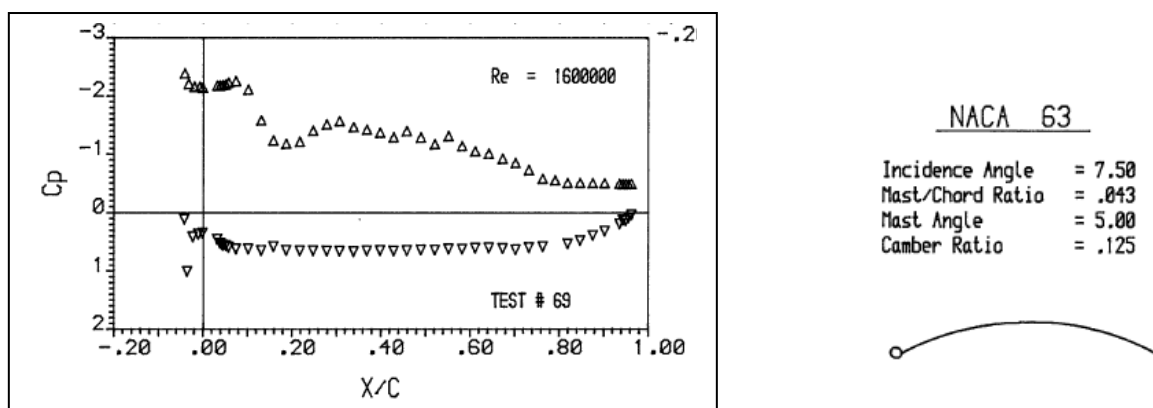
Figure 9.1: Wilkinson Data base

To get an estimation of the maximum difference of pressure exert on the sail among the different experiment, the maximum difference between the pressure coefficient of the leeward and windward side of the sail has been find among the 216 tests performed and the related differential pressure calculated. The maxiumun value of ΔCp equal to 3.4 has been detected over the mast in a

107

configuration of high incidence and small ratio between mast diameter and chord. From the pressure coefficient definition and in the standard atmosphere condition for a wind intensity of 20 Kts (about 10 m/sec) is possible to calculate the maximum differential pressure exert as expressed in Eq. 9.1, Eq. 9.2:

$$Cp = \frac{p - p_\infty}{\frac{1}{2}\rho V_\infty^2} \qquad\qquad \Delta p = \frac{1}{2}\rho V_\infty^2 \Delta Cp \qquad\qquad (9.1)$$

$$\Delta p_{Max} = 0.5 \cdot 1.225 \cdot 10^2 \cdot 3.4 = 208 Pa \qquad\qquad (9.2)$$

Also the experiments performed by Wilkinson present a maximum differential pressure of about 200 Pascal. Both the experimental and numerical data base concerned with static differential pressure exert over sail surfaces show that the higher level of differential pressure is about 200 Pascal, for this reason the full scale input of the pressure sensing unit implemented in the wireless network has been set to a value of +/- 300 Pascal to let the device able to sense the pressure field and to prevent unwanted overpressure.

9.2 Preliminary geometry definition

The proposed wireless sensor network has been developed to operate over sails, it's aim is to detect the pressure field with the lowest intrusive level. Intrusivity is an important issue of the network cause geometrical variations or discontinuity over sail surface may affect the characteristic of the flow and, as a consequence, to modify the pressure field of the sail. For these reasons the most convenient way to take the measurement network above the sail is to integrate it in the battens of sail. This topic due to the natural shape and dimension of battens will dramatically affect the design of any nodes of network and the sensing units. As reported in chapter 8. the sensing unit is a stacked structure created by the union of three layer, the base, the spacer and the diaphragm; the spacer create the circular cavity wherein the membrane deflect while the base which is the thicker layer has a square shape as shown in Fig. 9.2 In a first design phase the maximum and minimum dimension allowed for the frame square base L , the circular cavity of the spacer D , and the initial distance between plate H have been set.
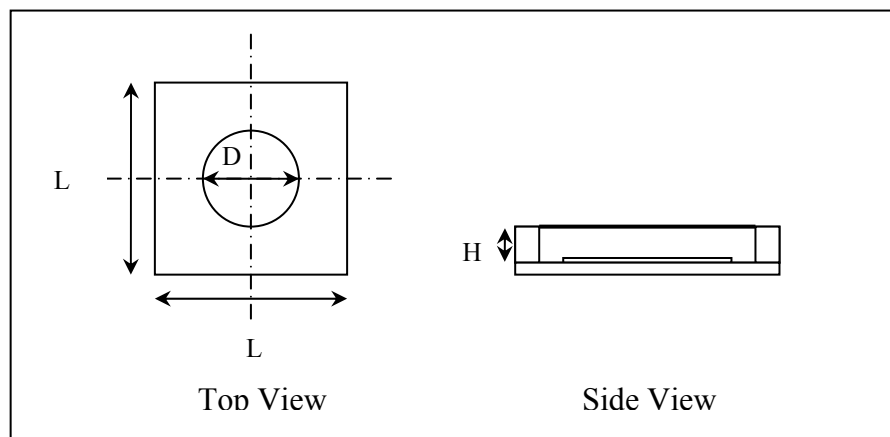
Figure 9.2: Sketch of sensor

The longitudinal extension of battens ranges from the luff to the leech of the sail varying its length according to the height along the mast, this dimension doesn't affect the sensor design as much as the lateral one. Battens width usually ranges from 20 to at least 40 millimetres , for the design of the battens the higher limit of 40 millimetres has been chosen. The width L of the sensing units must lay between this two bounds and the round diameters D must be chosen as trade off among two requirements: it has to be as large as possible to guarantee a certain mechanical sensitivity of the membrane but also as small as possible to guarantee a wide free surface able to ensure a safe and robust adhesion of the glue employed to joint the membrane to the spacing layer. The maximum lateral dimension L will also have to be some millimetres shorter than the width of the battens external edge, to let the sensor not to be damaged when battens are inserted inside the apposite pockets in the sail.Starting from the above considerations the maximum value allowed for the diameter dimension of the round cavity of the sensor D has been set to 20 mm while the external width L to 40 mm . Acting in this way the sensor can be house inside the battens, and a useful free surface for the layers adhesion is present. The minimum diameters for the membrane is set by the mechanical sensitivity of the membrane, a minimum diameters of 4 mm must be set to be able to sense the pressure field. According to the previous consideration the sensor edge length L, must be lower than 40 mm and diameter of the membrane must be 4 mm<D<20 mm . The last parameters discussed in this paragraph is the initial distance between plates of the capacitor, the bounds within it can be chosen depend on the maximum thickness allowed for the battens and the minimum distance of the electrode at which the electrostatic force is no more neglect able. The maximum thickness of a batten is about 4 millimetres but it doesn't affect the dimension H of the sensor cause for values of H greater than 500 um the sensitivity of the device is not appropriate to the FSI proposed. The lower limit of H is limited by the magnitude of the electrostatic force that would cause the conductive membrane to be attracted to the lower electrode, this phenomena imposes to chose a value for the parameter H higher than 10 um.

9.3 Modelling and design

A multi-physic coupled mechanical load-deflection and electrostatic deflection-capacitance numerical analysis of the diaphragm and variable capacitor is necessary for the modelling and design of the sensor structure. The voltage applied on the electrodes is low, as a result, the electrostatic force is very low and can be ignored when compared with the pressure load.
A FEM-based software tool such as FEMLAB® [35] has been used to perform a static non-linear analysis of the multilayered structures under a uniform load. The modelling of the diaphragm deformations with respect to the pressure load has been carefully considered. When small pressure loads are applied, and the maximum displacement of the diaphragm remains within half of its thickness, it acts as a thin plate subjected to small displacement. Therefore, classical mechanical theory of deformation can be used, and a linear stress-strain relationship (Hooke's law) can be applied. In this case, a linear deformation of the plates with respect to the pressure is expected. However, when higher loads are applied, then a specific theory has to be considered [24]. The increase of bending of the circular plate creates a strain in the middle plane that can not anymore be neglected. In this case the diaphragm acts as a membrane. At the same time, large deflections in the diaphragm cause supplementary stresses with respect to the conventional elastic theory and they must be taken into account in the model. This is a geometrical effect producing non linearity between load and deflection: the more a plate is stressed, the less it deflects Fig 9.3.
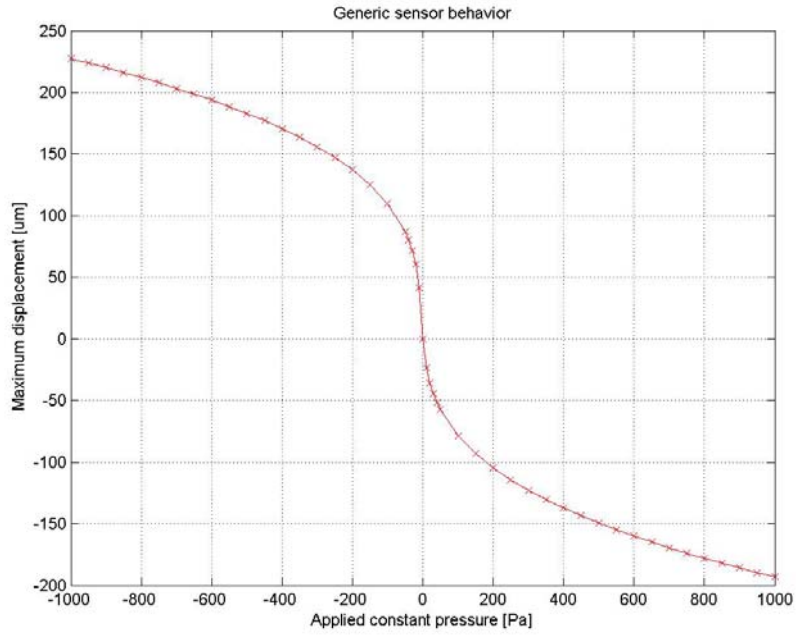
Figure 9.3 : Maximun displacement versus Pressure

The development of the fem model has been carried out by means of useful experimental data in an iterative process. Data acquired by means of a first run of tests on sensor prototypes has pointed out the strong need to pre-stress the diaphragm in order to reduce the tendency of the thin membrane to exhibit different equilibrium shapes when the pressure load is low. This problem manifest high levels of hysteresis at low values of pressure. A radial pre-stress tension is therefore necessary to reduce diaphragm instabilities when the differential pressure is close to zero; this helps the membrane to preserve a steady planar shape in the absence of pressure input. This behaviour is shown in the transduction experimental characteristic of Fig. 9.4 where is visible the reduction of hysteresis at low value of pressure loads.

(a)   (b)
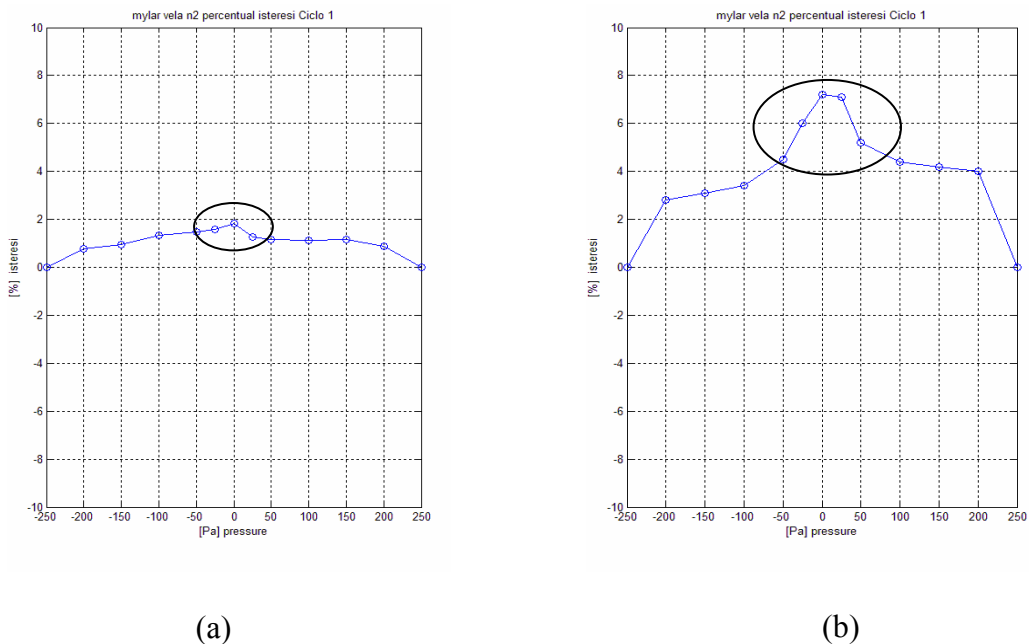
Figure 9.4: (a) Percentage hysteresy pre-stressed diaphragm. (b) Percentage hysteresy un-stressed diaphragm

110

The pre-stress requirement, found with the help of experiment campaign, have been implemented in the boundary conditions of the diaphragm model as a constant radial tension able to reproduce the pre-stress level induced in the diaphragm during the fabrication process. The relation between the pre-stress imposed by the weight used as ballast in the fabrication process has been calculated as follows: first of all the diameter of the circular ring of the pre-stress device built, (this object is described in detail in chapter 11) has been measured and used to calculate the lateral area of the circular membrane joint along the circular edge of the ring. The area of the membrane material that lies inside such circle is the one subjected to the uniform tension induced when the circular cave cylinder, the lead and the ring, slide along the piston as explained in chapter 11. The pre-stress, as indicated in Eq 9.3, is computed dividing the total weight W, of the assembler device and lead, for the lateral area of the membrane Al, computed by means of membrane thickness and radius of the circular ring.

$$Al = \pi \cdot R^2 \cdot t \qquad\qquad \sigma_T = W / Al \qquad (9.3)$$

According to the formula the radial tension σ_T varies from 0 Mpa to 6 Mpa as a function of weights imposed in the assembly procedure ranging from 0 Kg to 4,2 Kg. To let the fem model matches the experimental data the pre-stress imposed in the membrane surface is slightly lower than the one analytically computed with Eq.9.3, of about 12% - 19% depending on the load of the range applied. The relation used to calculate stresses is reliable in case of uniaxial loads while the actual condition of load differ from this ideal condition and moreover is not able to take into account friction between the diaphragm and the material of the pre-stress device.

Soon after the pre-stress level is defined and inserted in the boundary conditions the numerical solutions is obtained solving first the sensor axial-symmetric geometry for the mechanical large deflection problem with a static and non-linear solver capable to provide the deformed shape of the membrane for any load condition in the range +/-250 Pa. Femlab® solves for large deflections using a strain-displacement relation, known as Green or Green- Lagrange strains and defined as in Eq. 9.4 (a):

$$\varepsilon_{GL} = \frac{1}{2}\left(\frac{l^2 - l_0^2}{l_0^2}\right) \quad \text{(a)} \qquad\qquad \varepsilon_E = \frac{1}{2}\left(\frac{l - l_0}{l_0}\right) \quad \text{(b)} \qquad (9.4)$$

where ε_{GL} is the deformation, l_0 the initial length and l the deformed length .This relationship has been used instead of the classical engineering strain, defined in Eq. 9.4 (b). Furthermore Cauchy stresses, are replaced by the second Piola Kirchoff stress:

$$\sigma_{PK} = \frac{l}{l_0}\frac{F}{A} \qquad (9.5)$$

where σ is the stress, F the force and A the surface.

	Thickness (um)	Young's Moduls (GPa)	Poisson's Ratio
Mylar Diaphragm	12	5	0.38
Fr 4 - Spacer	Variable	20	0.22
Copper fix electrode	35	115	0.35

Table. 9.1: Mechanical properties

This model has been used for the whole structure, even for the parts that are subjected to small deformation: this because the large deflections model is valid with a good approximation also for small displacement. In Tab 9.1 the mechanical properties of the employed materials are shown. The deformed shaped for any pressure load of the membrane, which is the mechanical module output, is the input of the electrostatic module Fig.9.5.
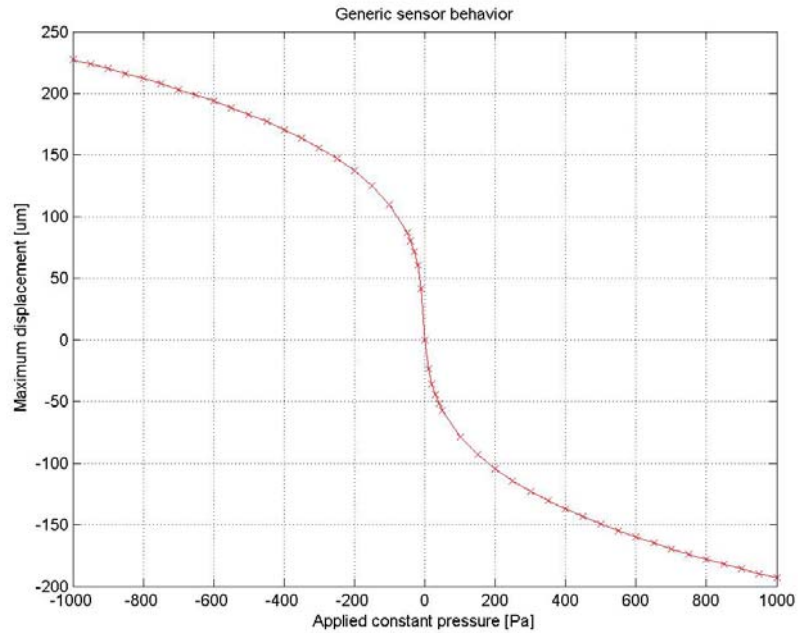
Figure 9.5 : Maximum displacement versus Pressure input

The electrostatic module solve the Poisson equation for the space charge density in the internal chamber of the sensor, is therefore possible to evaluate the capacitance related to any pressure load of the full scale input integrating the surface charge density over the plate area.
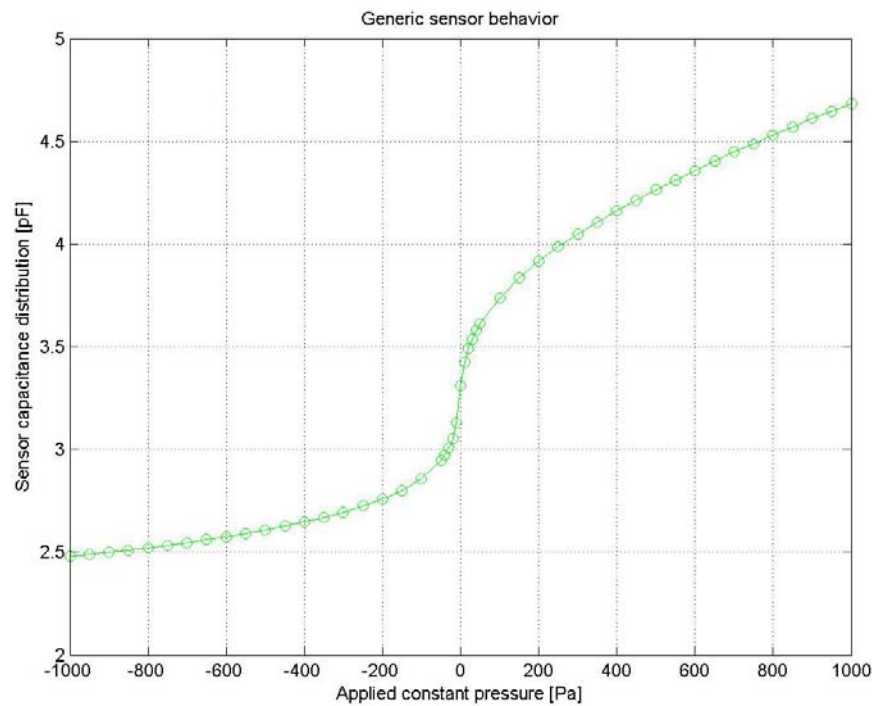
Figure 9.6 : Sensor capacitance versus pressure

112

Acting in this way it is possible to evaluate, by means of the mechanical module, the membrane deflection in response to the applied pressure load finding out, through the electrostatic one, the respective capacitance variation Fig.9.6. After that, the numerical model has been set, a campaign of finite element tests has been performed to investigate the behaviour of the sensor in the full scale pressure input, with different geometry and pre-stress level of the diaphragm. The independent variable of the campaign are :

- **p**: pressure load
- **r** : radius of the cavity
- **h** : initial distance between electrode
- **T** : initial pre-stress level

while the dependent variable are :

- **w** : maximum displacement of the membrane
- **C** : capacity
- **σ** : Von mises stress
- **σmean** : Mean Von Mises stress
- **σp** : Von mises stress induced by pressure
- **σT** : Von mises stress induced by pre-stress

By means of the numerical output provided by the model is possible to infer the classic figure of merit of the sensor as: full scale output, sensitivity, transduction function, saturation, dead band etc. Aim of the numerical simulation is to find the best trade off among the independent variable of the sensor varying the dependent ones.

9.4 Fem data analysis – unstressed diaphragm

The condition of total absence of pre-stress load in the membrane is an ideal condition, this is due to residual stresses, always present in the thin layer, induced during the adhesion of the spray glue in the fabrication process. Anyway comparison with experimental data confirm that these stresses are very low, and the analysis of fem model with a null value of pre-stress tension T provides a good approximation of the membrane behaviour. In Fig. 9.6 half of the deformed shape of the diaphragm Mylar® layer is shown while in Fig. 9.7 the deformed shape versus radial position, is shown, for five step of pressure, each spaced of 50 Pa, starting from 0 Pa to 250 Pa.
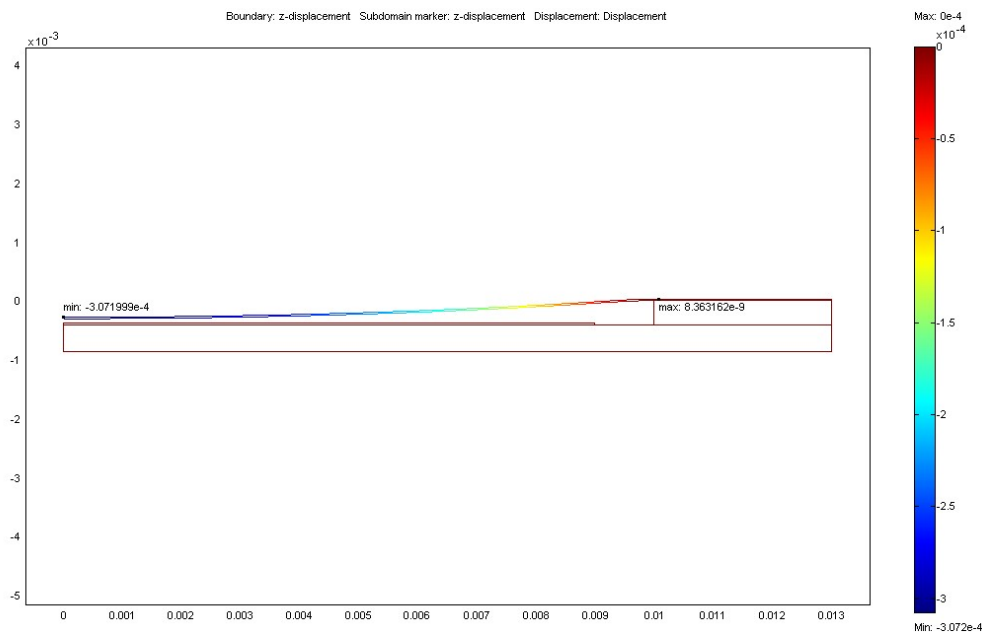
Figure 9.6: Diaphragm deformation
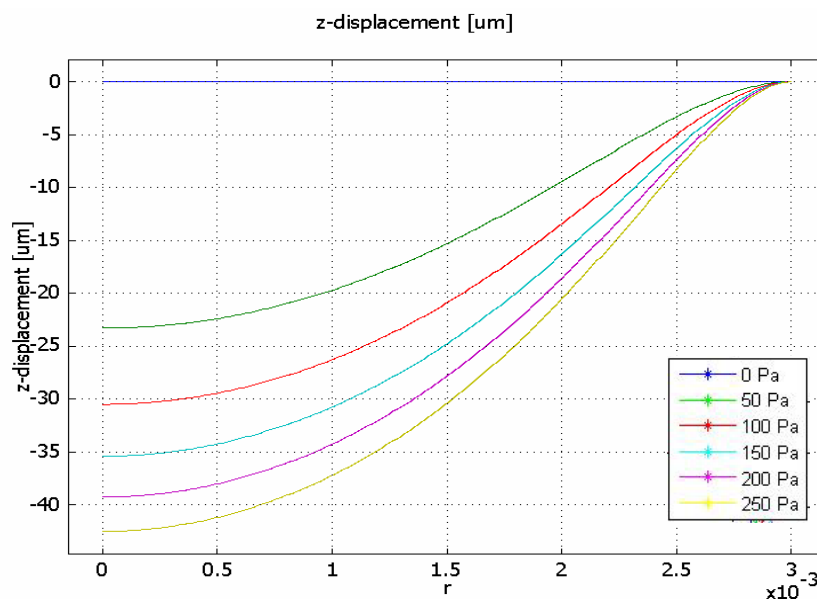
Figure 9.7: Half diaphragm deformed shape for pressure input step of 50 Pascal ranging from 0 to 250 Pascal

The maximum displacement increase as a function of the pressure load but the more a plate is stressed, the less it deflects, and as shown in Fig 9.7 the maximum displacement in the middle of the plate is not proportional to the load but its variation decreases while the variation of the applied pressure is constant. The knowledge of the deformed shape of the plate for every pressure is then suitable to be computed in the electrostatic module where the transduction relation for the proposed geometry is computed Fig 9.8

114
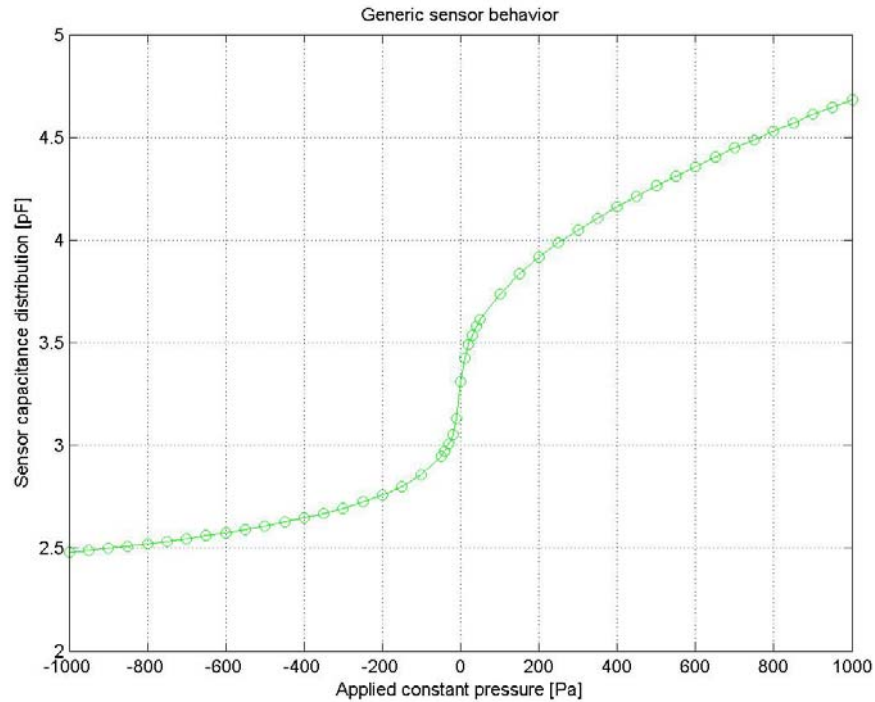
Figure 9.8: Computed transduction characteristic

The last two dependent parameters to analyzed are the local and mean Von Mises stress. In Fig.9.9 the local stresses as function of radial position for five pressure loads are shown.
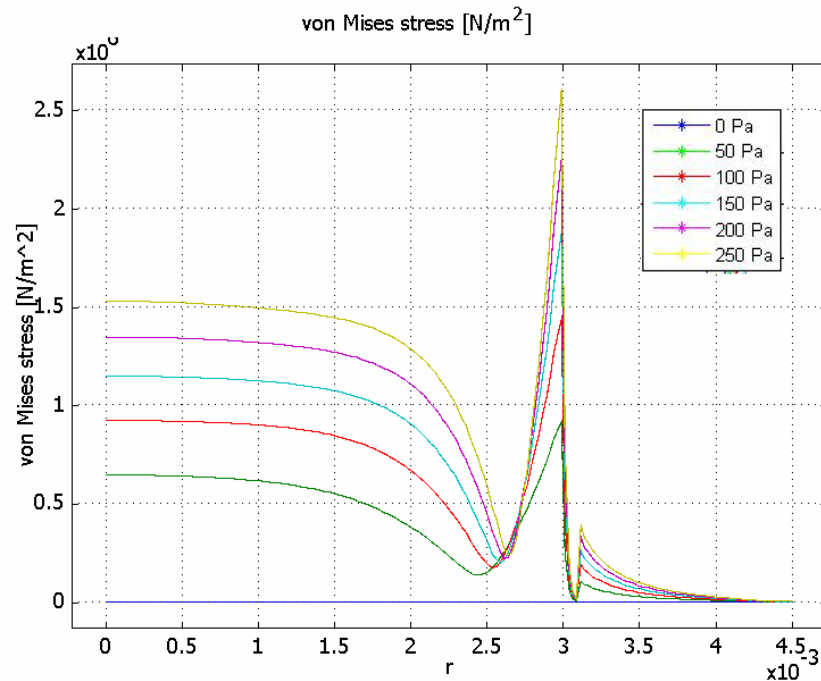
Figure 9.9: Half diaphragm local von Mises stress versusr radial position for pressure input step of 50 Pascal ranging from 0 to 250 Pascal

Analyzing the shape of such function for any of the applied loads it present a maximum in the stress pattern along the edge of the round cavity, corresponding to a value of r equal to 3 millimetres . Such maximum is due to the efforts concentration in the bottom side of the membrane caused by the

115

sharp edge modelled in the geometry module of the fem program; in the real sensor the magnitude of such maximum in strongly dependent on the curvature radius of such edge, a parameters which is difficult to infer. As general rules during the fabrication process the edge of the cavity have been rounded to reduce such effect. The stress behaviour along the radius reach a relative maximum in the middle of the plate and tends to decrease till the edge of the cavity. For values of the radius between 3 and 4.5 millimetres the internal action are the lowest, cause this is the area where the glue is sprinkled to let the plate be joint to the spacer. The last noticeable aspect of the graph are the different stress pattern associated with the five pressure load imposed: the local stress is a function of the pressure load, the shape of the function is the same for any load steps but the magnitude of stresses along the radius increases as the pressure loads increases. The same trend can be noticed if the mean Von mises stresses are computed over the surface of the membrane. In Eq. 9.6 the mean Von mises stresses are calculated in a vertical cross section of the sensor by means of an integration process over the membrane area .

$$\sigma_{Mean} = \frac{1}{A} \int_A \sigma_{Mises} dA \qquad (9.6)$$

In Fig 9.10 the mean stress are plot as a function of pressure, their magnitude increases as the pressure increases, the slightly asymmetry is due to the different behaviour of the deformed shape for positive and negative pressure.
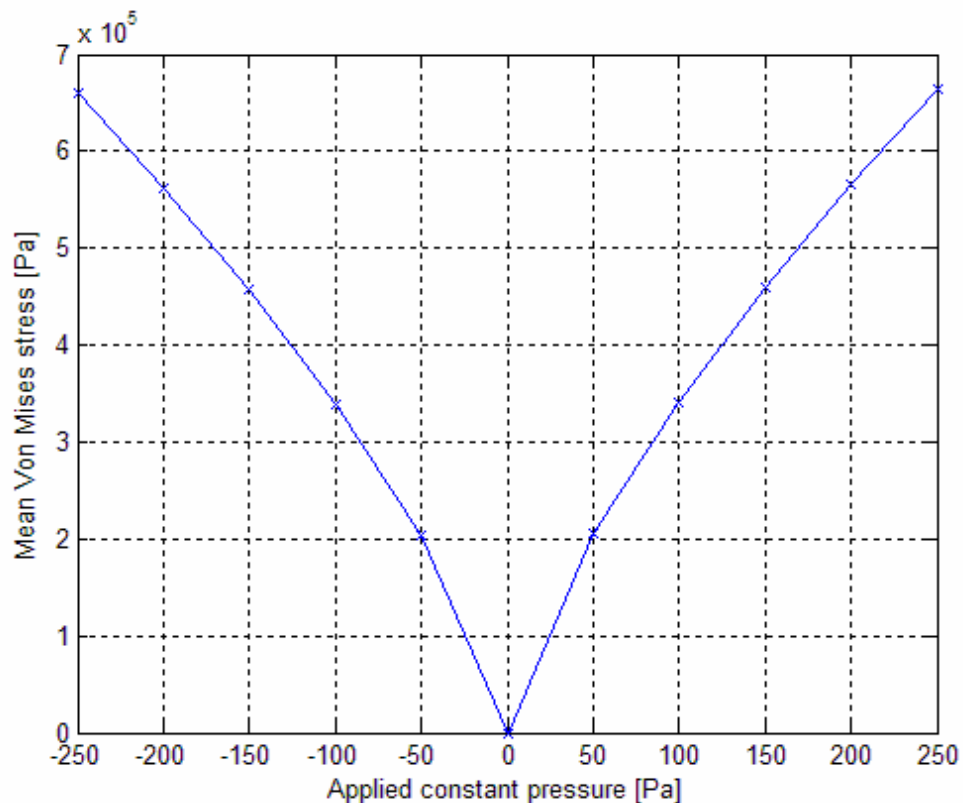
Figure 9.10: Mean von Mise streses in the full scale input

The stresses versus pressure trend already mentioned is at first sight obvious, anyway it's worth to be pointed out if viscoelastic phenomena concerned with polymeric material are considered. Creep affects the diaphragm causing deflections of several micrometers, which manifest themselves during time-scales of tens of minutes: this leads to an undesirable output drift and hysteresis, which has to be estimated when evaluating sensor precision. This phenomenon is evident in the sensor

116

behaviour, i.e. when the membrane is subjected to a constant pressure load it shows an elastic strain followed by a viscous and time dependent deformation with an increasing trend. The time dependent deformation is then transduced by the capacitor relation showing an increasing value of capacity reaching an asymptotic value after a certain period, under constant pressure load. The mechanical deformation of the diaphragm which is subjected to creeping phenomena is a function of the entire loading history of the body itself. In other terms, viscoelasticity let the system gains memory. Moreover as stated in chapter 3 the elastic time dependent strain due to the creep component is a function of the stress magnitude as shown in Fig. 9.11.
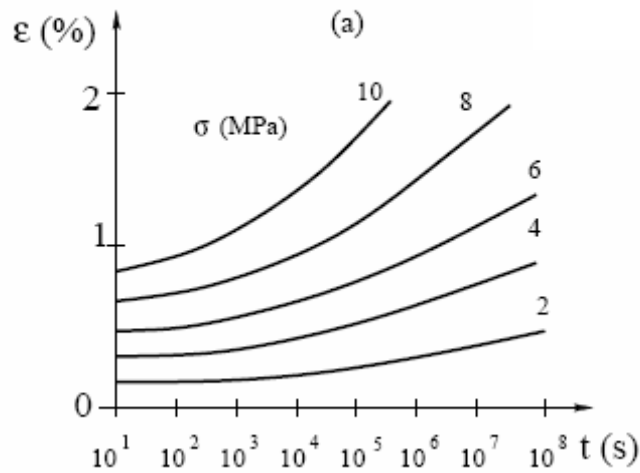
Figure 9.11 : Deformation versus time for different stresses

The main source of hysteresis an inaccuracy for such type of sensor is due to these phenomena. The analysis of mean stresses in the diaphragm in the stationary fem model as function of pressure reveals that they strongly depend on pressure magnitude therefore the time dependent mechanical deformation of sensor has a specific value for every value of pressure. This behaviour introduce a strong complexity in the mechanism governing the error evolution as a function of time: at every pressure is associated an elastic instantaneous deformation related to a certain capacity therefore to a unique value of pressure. After the first instant a secondary elastic time dependent deformation takes place until an asymptotic value is reached, to this deformation is associated a variation of capacity that let not be possible to correlate to the pressure imposed an unique value of capacity but just a range of capacity; this determines the inaccuracy bound of the device. Any inaccuracy bound along the full scale input depends on the working point of the sensor and moreover by the previous load time history, cause to any pressure applied is associated a different magnitude of stress and deformation as shown in Fig. 10.9 and Fig 10.10. Viscoelastic effects, commonly known as creep, also had to be taken into account during the Fem simulations cause Mylar, the material used for the thin sensing element of the sensor is affected such has many plastic material, by creping phenomena at ambient temperature and low stresses. Creep affects the diaphragm causing deflections of several micrometers, which manifest themselves during time-scales of tens of minutes: this leads to an undesirable output drift and hysteresis, which has to be estimated when evaluating sensor precision. This phenomenon is evident in the sensor behaviour, i.e. when the membrane is subjected to a constant pressure load it shows an elastic strain followed by a viscous and time dependent deformation with an increasing trend. The time dependent deformation is then transduced by the capacitor relation showing an increasing value of capacity reaching an asymptotic value after 36 minute, under constant pressure load. The mechanical deformation of the diaphragm which is subjected to creeping phenomena is a function of the entire loading history of the body itself. In

117

other terms, viscoelasticity let the system gains memory. To get an estimation inaccuracy of the diaphragm due to, the viscoelastic behaviour of Mylar has to be considered. The way adopted to model the viscoelastic phenomena is the one proposed by Zagnoni et all in [2], where a time dependent elasticity Young's module has been introduce. This time-varying parameter inferred by means of experimental data take care of describing and estimate the dynamic error effects. Acting in this way is possible to get an estimation of the inaccuracy bound for any geometry and pre-stressed level considered. During the design phase, this was helpful when determining the most suitable materials geometry and pre-stress level for the sensor.

9.5 Fem data analysis – pre-stressed diaphragm

The development of the fem model has been carried out by means of useful experimental data in an iterative process. Data acquired by means of a first run of tests on sensor prototypes has pointed out the strong need to pre-stress the diaphragm in order to reduce the tendency of the thin membrane to exibit different equilibrium shapes when the pressure load is low. This problem manifest high level of hysteresis at low values of pressure. A radial pre-stress tension is therefore necessary to reduce diaphragm instabilities when the differential pressure is close to zero; this helps the membrane to preserve a steady planar shape in the absence of pressure input. The introduction of the pre-stress independent variable T add a new degree of freedom to the optimum design of the sensor. Increasing the magnitude of T involve a deep variation in the deformation of the membrane and in the load-induced local and mean stresses. A fem campaign has been performed to analyze the behaviour of the dependent variable w, C, σ_{mean}, σ.
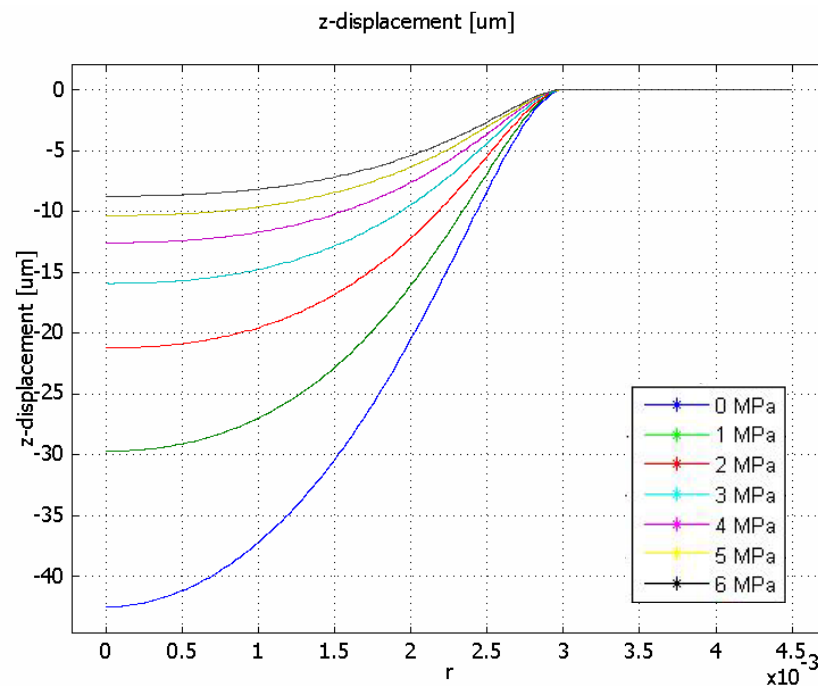
Figure 9.12 : Half diaphragm deformed shape versus radial position for the maximum pressure input of 250 Pascal for pre-stress T step of 1 Mpa ranging from 0 to 6 MPa

In Fig. 9.12 half of the deformed shape of Mylar layer for the maximum value of pressure (250 Pascal) is shown for five step of pre-stress level T ranging from 0 MPa to 6 Mpa :
The higher the value of the parameters T , the lower the maximum deflection of the diaphragm, as expected the tension decreases the diaphragm flexibility. Such as for the relation between pressure

118

and deflection in the case of absence of pre-stress, the relation between deflection and T for a given pressure load is not proportional. The blue line is related to a value of T equal to zero.
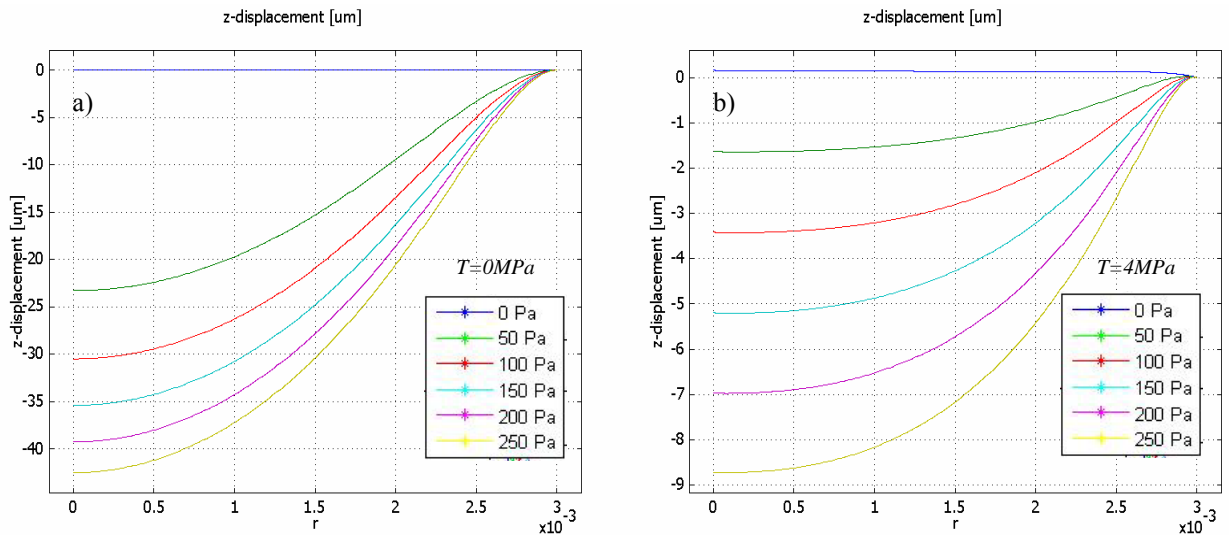
Figure 9.13 : half of the deformed shape of Mylar layer for five step of pressure each spaced of 50 Pa starting from 0 Pa to 250 Pa

In Fig.9.13 (a) and (b) half of the deformed shape of Mylar layer is shown for five step of pressure each spaced of 50 Pa starting from 0 Pa to 250 Pa, the left plot is related to a value of T equal to zero the right plot to a value of T equal to 4 Mpa. It's worth to point out as above a certain level of stress the relation between load and deflection tends to a proportional behaviour Fig.9.13.

The presence of a pre-stress in the membrane material, tends to increase the stiffness of the membrane and to reduce the mechanical sensitivity to the pressure load. Increasing the stress in a certain way acts as increasing the thickness or the Young's module of the material, cause even if subjected to the same loads the maximum displacements of the diaphragm decrease and its behaviour dosen't tends to the membrane model but to the one of a thin plate. This behaviour is shown if Fig 9.13 (b) where the maximum displacement is expressed as a function of the full scale pressure input for different pre-stress level. When the stress induced in the diaphragm is close to 1.5 MPa the magnitude of maximum displacement is equal to the thickness of the diaphragm (20um) and the maximum displacement is proportional to the pressure loads as in the thin plate theory.
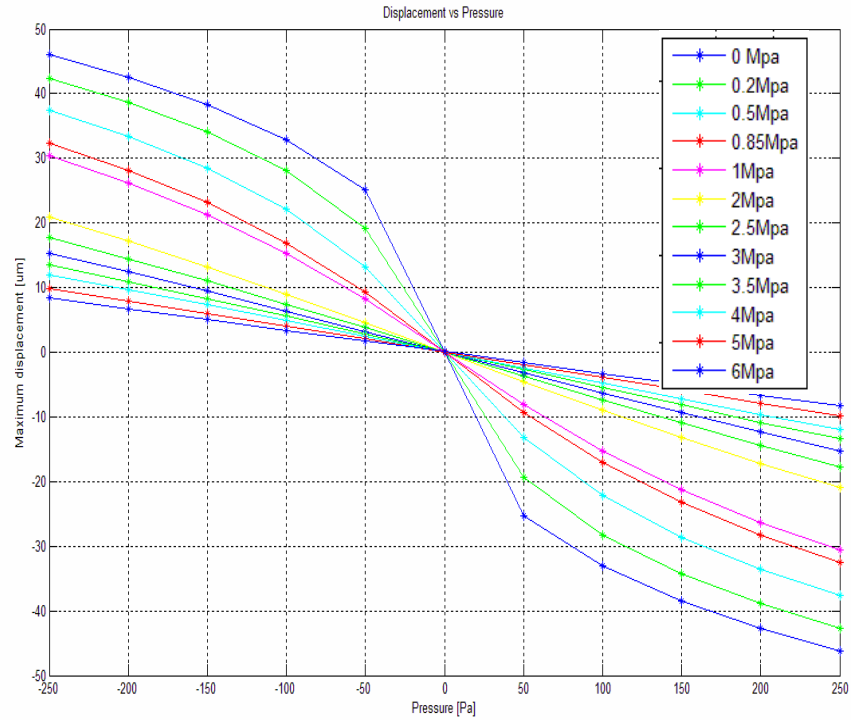
Figure 9.14 : Maximum displacement versus pressure for a pre-stress level ranging from 0MPa to 6 Mpa

The presence of a pre-stress in the Mylar plate decreases the mechanical sensitivity of the sensor but increase the linearity of the relation between displacement and pressure load Fig 9.14. A similar trend can be observed if the transduction curve of the sensor for the same level of tension is plot. The higher tension levels strongly decrease the overall sensitivity of the sensor reducing the full scale output but the transduction curve tend to a linear relation. The deeper difference concerning the pre-stressed diaphragm is related to the distribution of the load dependent stress along the membrane radius and their mean value. If the local stress in the membrane is first analyzed for the whole level of pressure input at different level of tension the key role of the pre-stress tension T in the evolution of creeping phenomena is revealed Fig 9.15 (a,b,c,d).

(a)

(b)
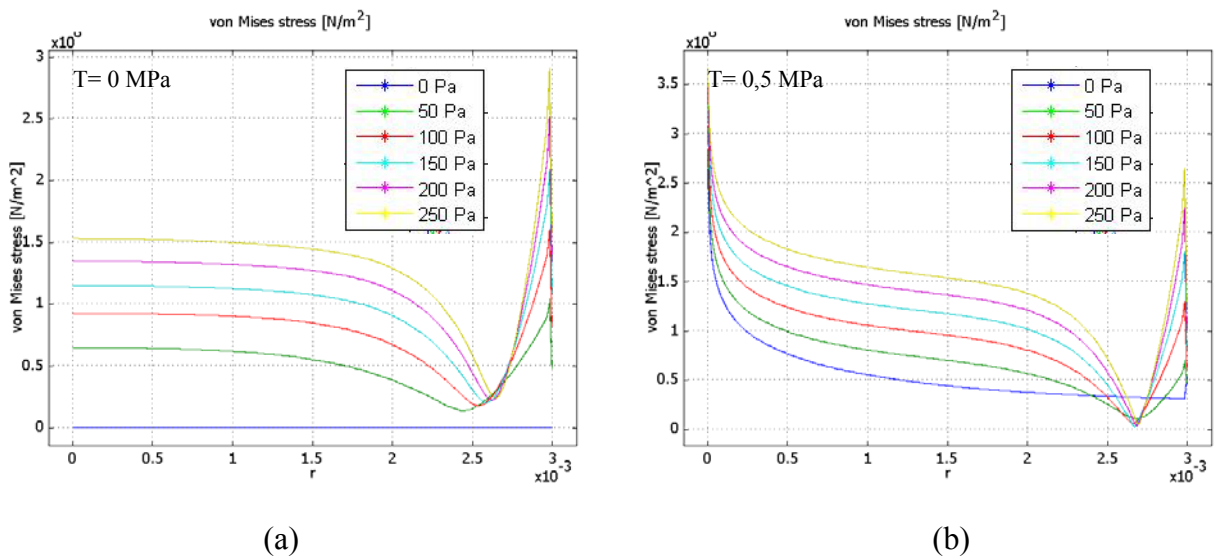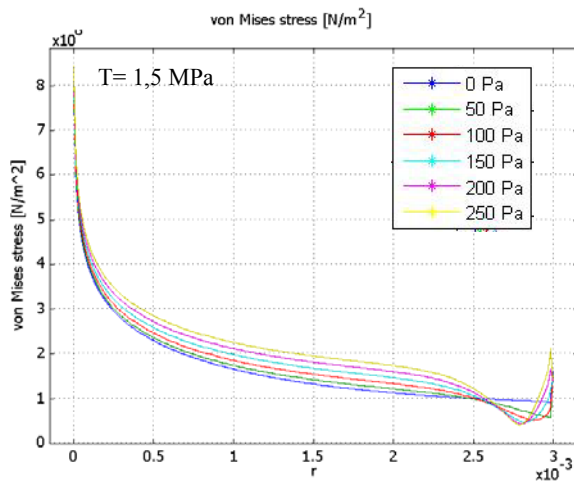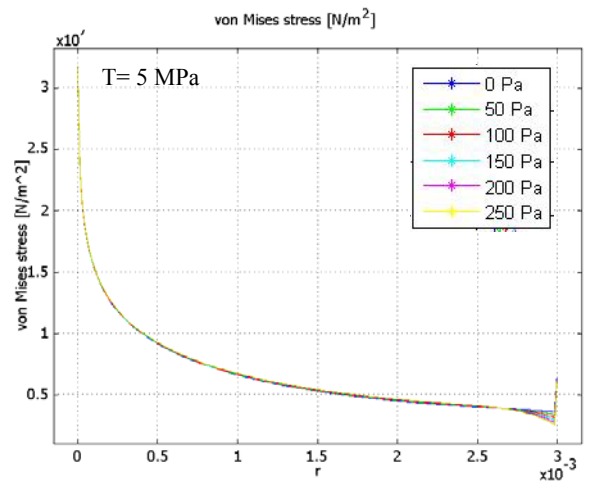
(c)   (d)

Figure 9.15 : Local Von mises streses versus radial position for four pre-stress level.

Each of the four plots shows the evolution of local Von Mises stress along half of the membrane, from the center to the edge of the cavity for six value of pressure ranging from 0 to 250 Pa with step of 50 Pa. From figure a till figure d the parameter T has a magnitude respectively of 0Mpa, 0.5Mpa, 1.5Mpa and 5Mpa. In the case of T equal to zero any pressure loads induce a different local stress in the membrane as reported in the previous paragraph, but a progressively increase of pre-tension let the local stresses to be less and less dependent to pressure loads, Fig 9.15 (b) and Fig 9.15 (c), until above a certain value of T local stresses are independent by the pressure loads Fig 9.15 (d) .
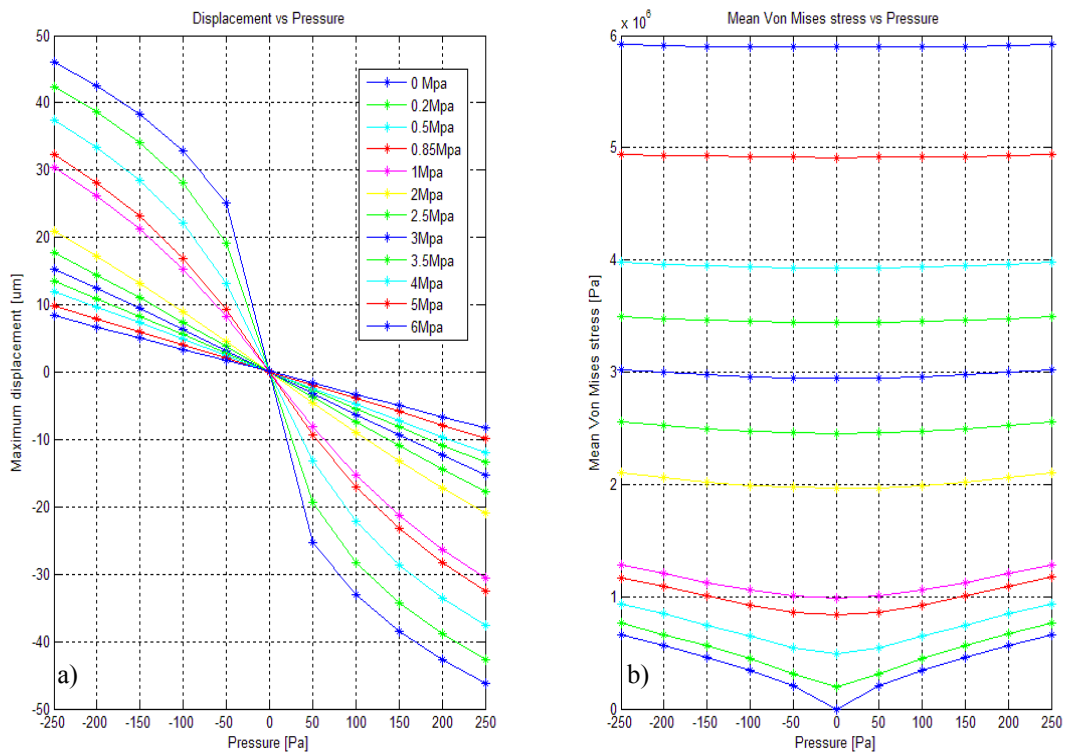
Figure 9.16: Maximum displacement (a), Mean Von mises stress (b) as function of pressure

121

The same trend can be observed if mean Von Mises stresses are computed above the diaphragm surface according to Eq. 9.6. The mean Von mises stresses are dependent to pressure input loads until the parameters T reaches a certain value, in particular the Von mises stress for which this phenomena takes place is around the pre-stress tension for which the behaviour of the diaphragm change to the one of a membrane to that of a thin plate subjects to large displacement i.e. for maximum displacement around the thickness of the diaphragm. This trend is shown in Fig 9.16, where the maximum deflection and the mean Von mises stresses are plot as function of the pressure input load. In Fig. 9.17 the percentage variation of mean stresses in the diaphragm in the whole full span pressure input with respect to the maximum variation of mean stresses for the zero pre-stress condition is shown. For the particular geometry chosen, the pre-stress value, at which the maximum deflection is equal or lower to the diaphragm thickness, lays within 1,5 Mpa and 2 Mpa; above these value both the local and the medium Von mises stresses are not dependent on the pressure load and the percentage variation of mean stresses in the diaphragm is below 15%.
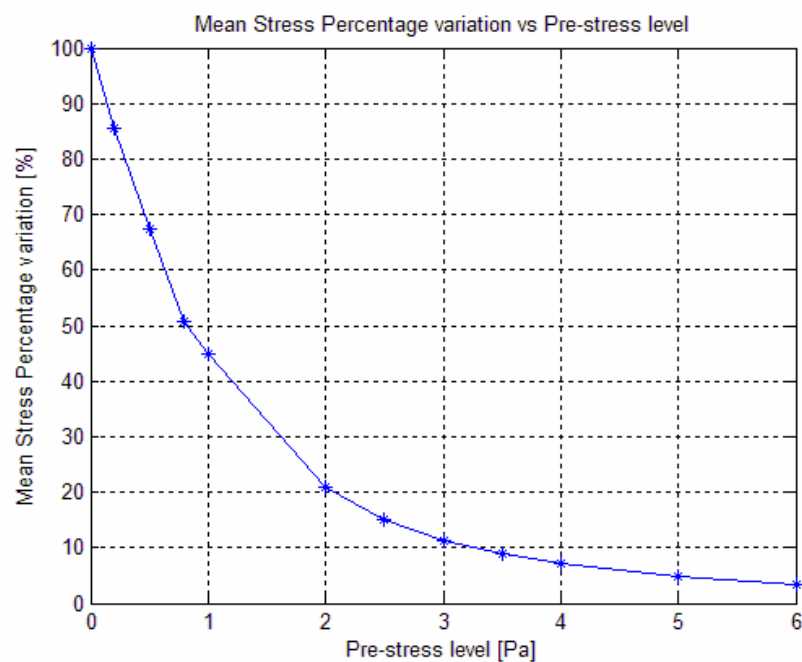
Figure 10.17: Mean Von mises stresses versus pressure

The main consequence concerning the invariant behaviour of stresses with pressure lays in the mechanism by which the viscoelastic phenomena take place. As stated in chapter 3. the time dependent deformation of the diaphragm depends on stresses: when the pre-stress tension T is zero, the stress is strongly dependent on load, so for any pressure input a different time dependent deformation is associated. Whereas if pre-stress tension T is above the value for which the behaviour of the diaphragm is the one of a plate, stresses are no longer dependent on load but constant, this case let the modelling of error induced by creep to be simpler to be inferred cause deformation of such material is still dependent on time and stresses but weakly or independent by the pressure load. When the diaphragm is pre-stress the time deformation has still reached the asymptotic value associated with the pre-imposed stress level and is weakly variable with the pressure load, being the variation of total stress they induce, lower than the value imposed in the fabrication process. Moreover being the pre-stress tension note let be feasible to gather, by means of experimental data and fem models, a time dependent mechanical model concerning the deformation of the plate for different stress levels. As will be explained in next paragraph a time dependent mechanical model able to predict the relaxation of the plate can be inferred and use to estimate the inaccuracy bounds of the sensor.

122

Chapter 10

Viscoelastic dynamic error model

Capacitive pressure sensing can be schematically represented as in Fig. 10.1, where a pressure variation with respect to a reference position is transduced into an electrical capacitance variation. This is typically achieved by the mechanical deformation of the sensitive element (usually a diaphragm or a plate), which is finally converted into an electrical signal. An approach commonly used for pressure sensor design is sketched in Fig. 10.2 (a) in terms of normalised input/output. Every physical quantity in the transduction chain varies within the ranges allowed by the sensor characteristics. The sensor accuracy is defined by the number of detectable levels in which the output range, in the last step of the chain, is divided: the levels being representative of the number of minimum pressure intervals that can be sensed, considering the electrical noise and a chosen signal to noise ratio (SNR) during electrical transduction [80].
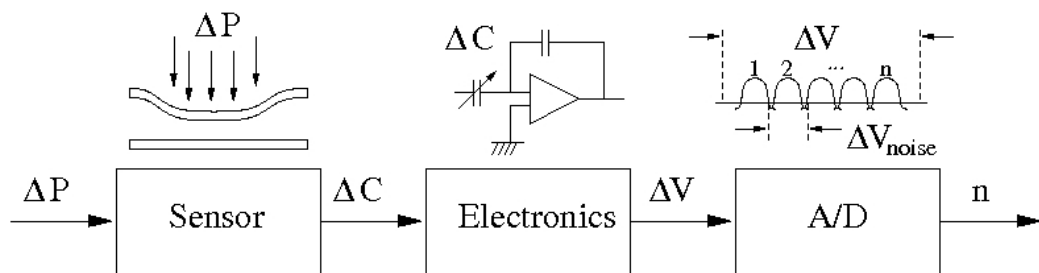
Figure 10.1: (a) Transduction chain in capacitive pressure sensing. Pressure is converted into an electrical capacitance by means of a mechanically deformable element and it is finally translated into an electrical potential which is representative of the input.

As an example, in order to target the sensor to a specific application, the range of pressure values (P_{MIN}-P_{MAX}=ΔP_{MAX}) that shall be measured must be defined. The range of pressure ΔP_{MAX} must be mapped into a capacitance range ΔC_{MAX}, and an opportune electrical circuit will convert the variation of capacitance ΔC_{MAX} in an electrical potential variation ΔV_{MAX}. Ideally, the pressure signal ΔP (considered as a pressure variation between P_{MIN} and P_{MAX} with respect to a reference position) must produce the larger possible variation of every following physical variable in the sensor transduction chain (obtained through the choice of the design parameters), in order to maximise the sensitivity amongst every transduction step Fig. 10.2 (a). This leads to a nominal sensor accuracy represented by the number N of levels (fixed by the estimation of the electrical noise and the choice of the SNR [80]) by which the pressure range is divided, thus defining the minimum detectable pressure variation within the specified range. However, when the sensor shows creep behaviour, a different picture emerges from the previously described design approach. Creep is the tendency of a material to deform over time for relieving a constant applied stress: in this situation, the stress-strain characteristic exhibits a behaviour that appears dynamic and highly non

123

linear, even for small deformations. Depending upon the materials, viscoelastic behaviours can manifest at ambient temperature and for different stress [1,38,27,48,49], thus resulting at the output of a capacitive pressure sensor as a time dependent drift which deteriorates the accuracy of the sensor, as shown in Figure 10.2 (b).
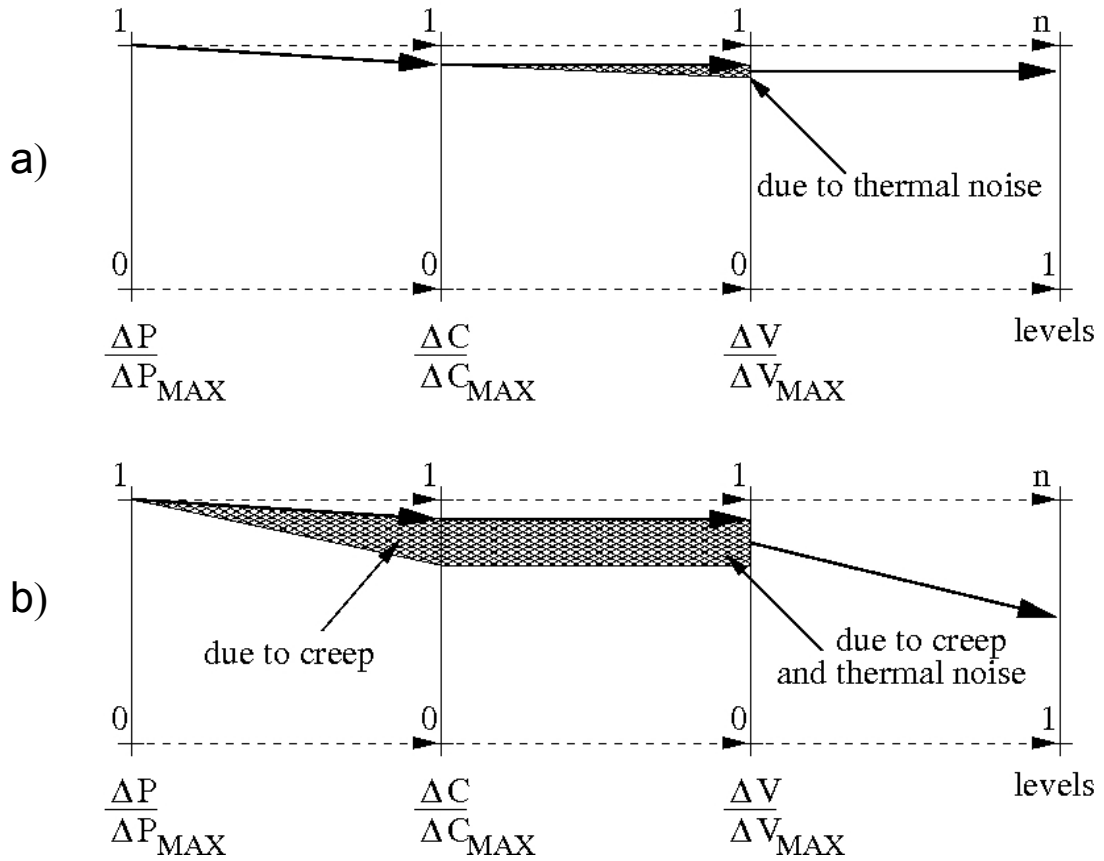
Figure 10.2 : a) Response of a capacitive pressure sensor not affected by creep. The pressure range that has to be sensed is firstly mapped in the maximum capacitance range allowed by the sensor geometry and then into the maximum voltage range allowed by an electrical circuit. The number of levels at the output of the circuit, equivalent to the number of pressure intervals that can be sensed, is dependent on the electrical noise in the circuit. (b) Response of a capacitive pressure sensor affected by creep. Viscoelastic behaviour, which takes part during the deformation of the sensitive element, can be considered as superimposed to the electrical noise, thus decreasing sensor accuracy and lowering the number of detectable levels.

For its nature, creep is very difficult to compensate through mathematical algorithms, due to its long and short memory characteristics [48,49]. In this thesis, for design purposes, viscoelastic phenomena are considered superimposed to the output signal as a random noise instead of being regarded as a drift. Creep is strongly dependent on the material used and on the sensor geometry (especially the sensor membrane), whilst electrical noise is defined by the circuitry parameters, which include amongst them the sensor capacitance. As it will be shown in the next paragraph, the two noise entities are one directly and the other inversely dependent upon the sensor membrane area. Clearly, the trade-off between creep and electrical noise is given by tailoring sensor geometry and circuitry parameters in order to find the condition that minimise both noise quantities.

124

10.1 Estimation of creep in capacitive pressure sensors

As reported in [1,38,39-47], creep manifests primarily in two components of the sensor structure: the deformable membrane and the solder paste (or glue) that, in certain architectures, is used to bond the membrane to the sensor support. The membrane and the gluing substance show viscoelastic behaviour typically when polymeric (polyimides, resins) or composites materials (polymers and thin copper-clad films) are employed, and whenever the stress in a material (plastic, metal or alloy) approaches the yield stress, being also strongly dependent on the temperature. Creep in polymers, at ambient temperature, is due to temporarily conformational rearrangements of the polymer macromolecules under an applied stress, leading to a time dependent deformation. This can be totally recovered [81,49] if the material yield stress inside the specimen is not exceeded, this is the case of both aeronautical Kapton and Mylar films. Creep in thin copper film, as those employed in the aeronautical sensors, instead (0.1 – 10 um thick at ambient temperature) due to dislocation of the copper crystals [82,50] is strongly dependent on crystal size [51-53].

Here, an approximation has been introduced, in order to estimate the sensor contribution to creep, and a method which minimises the viscoelastic effect by tuning opportunely the design parameters. For this, a simplified model of capacitive pressure sensor is given in Fig. 10.3.
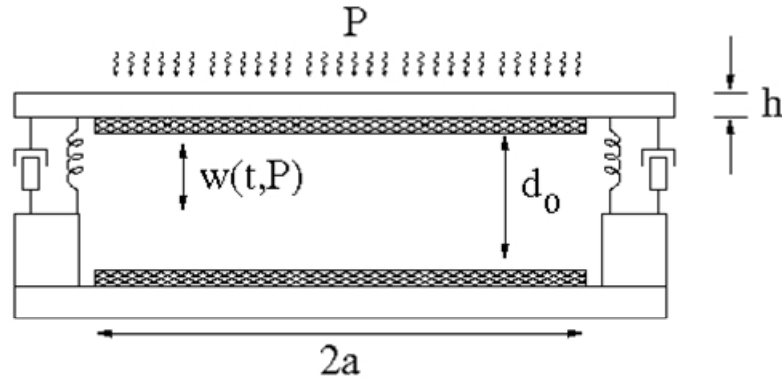
Figure 10.3 : A capacitive pressure sensor is represented as a parallel plate capacitor where the membrane deformation is modelled with a spring and a dashpot in order to consider the elastic and viscoelastic behaviour, respectively, of the structure.

A capacitive pressure sensor, can be represented as a circular parallel plate capacitor of radius a, whose upper plate of an uniform material of thickness h is movable with respect to the fixed lower one, depending upon the response of the parallel spring-dashpot when a pressure P is applied. The initial distance (resting position) between the plates is d_0. The spring is characteristic of the elastic deformation of the system, while the dashpot is representative of the time-dependent viscoelastic behaviour. When a uniform pressure load P is applied to the membrane, a displacement w(t,P) is produced and the sensor electrical capacitance is given in Eq.10.1 :

$$C(t,p) = \varepsilon \frac{\pi a^2}{d_0 - w(t,p)} \tag{10.1}$$

The membrane displacement can be decomposed in two contributes as shown in Fig.10.4 (a): an instantaneous elastic displacement $w_{el}(P)$ and a slower, time dependent displacement (due to creep) $w_{cr}(t,P)$, which give a capacitive response $C_{el}(P)$ and $C_{cr}(t,P)$, respectively, Fig.10.4 (b).

125
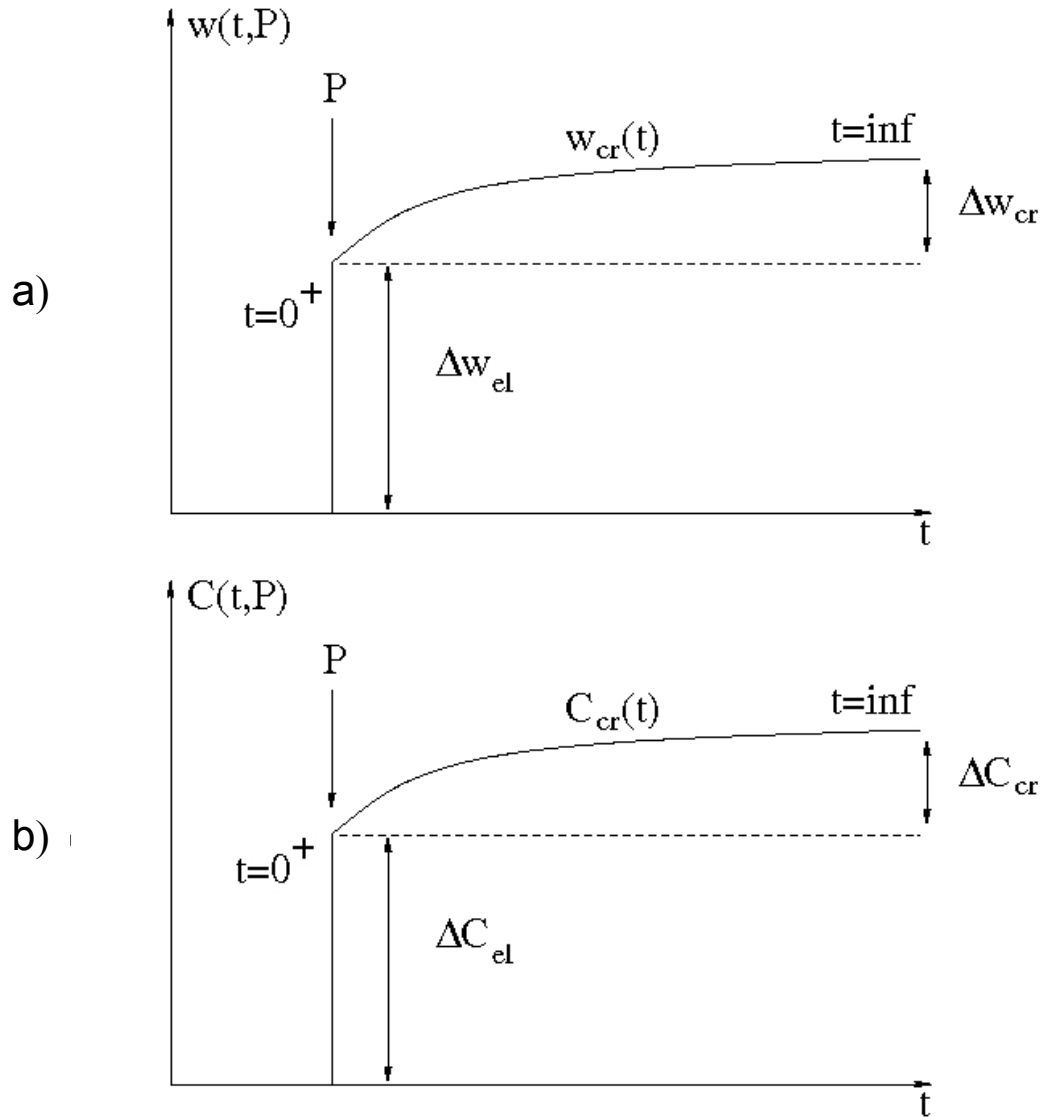
Figure 10.4 : (a) Example of membrane deflection behaviour obtained when a load P is applied, at a certain time, to the sensor: a slow, time dependent displacement Δw_{cr} is superimposed to the displacement Δw_{el} caused by elastic deformation of the membrane. (b) Example of capacitive output derived from the elastic and viscoelastic behaviour of the membrane deflection.

Due to viscoelasticity the system gains memory [49]. Any plate or membrane subject to an applied load will slowly varying its deflection, obtaining an output that deviates from a non-viscoelastic response by no more than a quantity Δw_{cr}, corresponding to ΔC_{cr}. The reason to practice this analysis is to understand how the geometry and the materials employed in the sensor can influence the viscoelastic response, thus defining the error bounds. Such bounds can be roughly interpreted as an uncertainty that should be taken into account during measurements. One of the aims performed in this thesis is to investigate how design parameters can be adjusted to minimise the quantities $w_{cr}(t,P)$ and $C_{cr}(t,P)$ with respect to $w_{el}(P)$ and $C_{el}(P)$.

126

10.2 Mechanic sensor design parameters

Membrane and plate deflection can be described, with a good approximation, by means of well established mechanical theory. Depending on membrane or plate thickness, small deflections (SD) or large deflections (LD) theory can be used [24].
Useful relationships for an appropriate mechanical description of the pressure sensor deforming element are:

$$\text{(SD)} \quad \sigma_{rMAX} = \frac{3}{4}\frac{Pa^2}{h^2}, \qquad \text{(LD)} \quad \sigma_{rMAX} = k'\sqrt[3]{\frac{EP^2a^2}{h^2}} \qquad (10.2)$$

$$\text{(SD)} \quad w_{rMAX} = \frac{Pa^4}{64D}, \qquad \text{(LD)} \quad w_{rMAX} = ak''\sqrt[3]{\frac{Pa}{Eh}} \qquad (10.3)$$

$$D = \frac{Eh^3}{12(1-v)^2}, \qquad (10.4)$$

$$\text{(SD)} \quad w_r = w_{rMAX}\left(1-\frac{r^2}{a^2}\right)^2, \qquad (10.5)$$

valid for a circular plate, clamped at the edge and being subject to a uniformly distributed pressure P, where r is the radius coordinate whose origin is set in the centre of the membrane, σ_{rMAX} is the maximum stress in the membrane, w_{rMAX} is the maximum membrane deflection, E is the modulus of elasticity, v is the Poisson ratio, h is the plate thickness, w_r is the membrane deflection along the radius (only in the case of small deflections) and k' and k'' are experimental constants [24]. Creep behaviour can be described by using different methods [47,27-49]. In this work, the method proposed in [38] is applied. Following this procedure, an estimation of the plate deflection Δw_{cr}, due to creep and superimposed to the elastic deflection Δw_{el}, can be obtained Fig 10.4 (a), Fig 10.4 (b).
Creep is approximately classified as a low-pass phenomenon, so that a typical experiment to estimate its extent consists in applying, at t = 0, a step-like excitation in stress and in evaluating the difference between the response at t = 0^+ and the asymptotic response at t→+∞. A particularly effective way of doing so is by the introduction of a time dependent creep modulus [38], defined as:

$$E_i(t) = \frac{\sigma_i}{\varepsilon_i(t)}, \qquad (10.6)$$

where $\varepsilon_i(t)$ is the time dependent strain, σ_i is the corresponding stress and the index i represents different values of stresses (equivalent to a certain load P applied) and temperature conditions Fig 10.5.
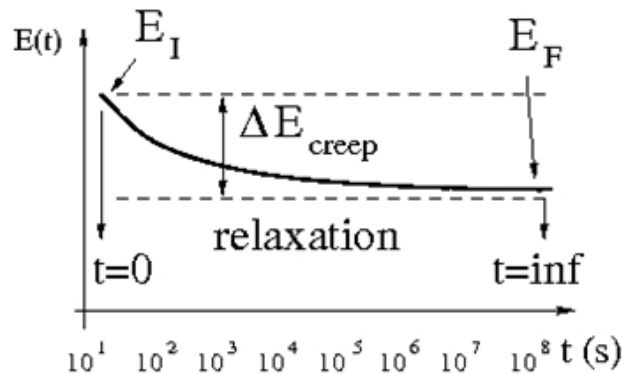
Figure 10.5 : Time dependent creep module
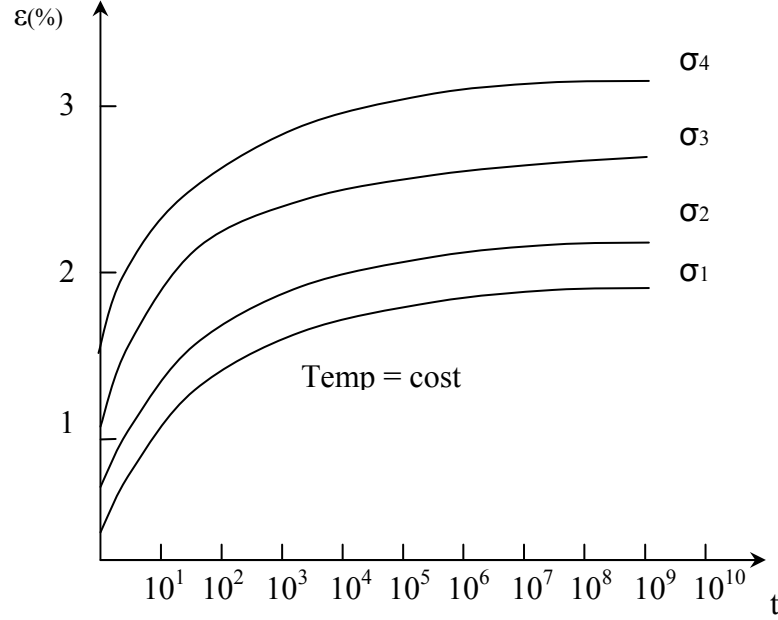
Figure 10.6 : Creep behaviour in materials. Characteristic curves strain versus time for different stresses at constant temperature of a uniformly loaded specimen.

The bigger the stress, the bigger the creep strain for a fixed temperature; the higher the temperature, the bigger the creep strain for a fixed stress. As demonstrated in [38], one can use the strain curves in Fig 10.6 from material datasheets to extrapolate the values $E_I=E(0^+)$ and $E_F=E(+\infty)$ from Eq. 10.6, as shown in Fig. 10.5 E_I is a value representative of elastic deformation, whilst E_F is representative of the deformation due to viscoelastic behaviour when an asymptotic condition is reached and it is dependent upon the load applied. To better understand the viscoelastic role played by creep, an important distinguish concerning stresses must be done. In a pre-stressed diaphragm total stresses can be divided in a part due to the pre-stress tension σ_T and a part induced by the load pressure input and called σ_P, the former defined as the stress magnitude present in the membrane at zero load pressure input, the latter as the stresses added when a pressure load is applied. In order to estimate the uncertainty of the sensor introduced by creep in terms of membrane displacement Eq. 10.5 and the values obtained from Eq. 10.6 can be combined to define the ratio between the displacement due to creep and the displacement due to the elastic response as:

$$\frac{\Delta w_{cr}}{\Delta w_{el}} = \left(\frac{\dfrac{Pa^4 12(1-v)^2}{64h^3 E_F(P,T)} - \dfrac{Pa^4 12(1-v)^2}{64h^3 E_I}}{\dfrac{Pa^4 12(1-v)^2}{64h^3 E_I}} \right) = \frac{E_I - E_F(P,T)}{E_F(P,T)} = \alpha(P,T) = \alpha(\sigma_p, \sigma_T) \qquad (10.7)$$

Eq. 10.7 describes the membrane deflection due to creep with respect to the elastic displacement and it is dependent upon the pressure load P and pre-stress T, which identifies the asymptotic value $E_F(P,T)$. Here, it must be noticed that although when stresses in the membrane are not constant, as

128

demonstrated in [1,38], combining numerical simulations with experimental results allows to extract averaged parameters E_I and E_F for any sensor geometry, while when a certain pre-stress level in the membrane is reached , the asymptotic value of E_F is weakly function of the pressure load P (and therefore stresses σ_P) and greatly of the pre-stress T (and therefore stresses σ_T) imposed in the fabrication process, thus the Eq. 10.7 can be approximated as expressed in Eq. 10.8.

$$\frac{E_I - E_F(T)}{E_F(T)} \approx \alpha(\sigma_T) \tag{10.8}$$

Pre-stressing the diaphragm presents different advantages: it reduces inaccuracy close to the zero pressure inputs as stated in chapter 9, and cause the material of the thin film to operate at a constant or weakly variable stress σ_P (stresses induced by the pressure load), being the dominant stresses the ones induced in the pre-stress fabrication procedure. This let possible to choose in Fig. 10.6 which is the stress level parameter concerned with the operative range of the film, thus defining the deformation-time function related to the diaphragm used and to calculate an unique value of $\alpha = \alpha(T)$ that will depend greatly by the pre-stress actions σ_T for the whole pressure input range. Moreover the pre-stress imposed let the time dependent part of the viscoelastic process to be, in large amount, over and done, letting the diaphragm work close to the asymptode deformed constant value .

10.3 Iterative procedure

Viscoelastic phenomenon are evident in the sensor behaviour, i.e. ,when the membrane is subjected to a constant pressure load, it shows an elastic strain followed by a viscous and time dependent deformation with an increasing trend:

$$\sigma = \sigma_o = \cos t$$
$$\varepsilon_T(t,T) = \varepsilon_E + \varepsilon_{VE}(t,T) + \varepsilon_V(t,T) \tag{10.9}$$

The time dependent deformation is then transduced by the capacitor relation showing an increasing value of capacity reaching an asymptotic value after 36 minute, under constant pressure load. In Fig. 10.7 , it is shown a comparison between the response to a constant load of an ideal sensor and the response of a sensor affected by viscoelastic phenomena.
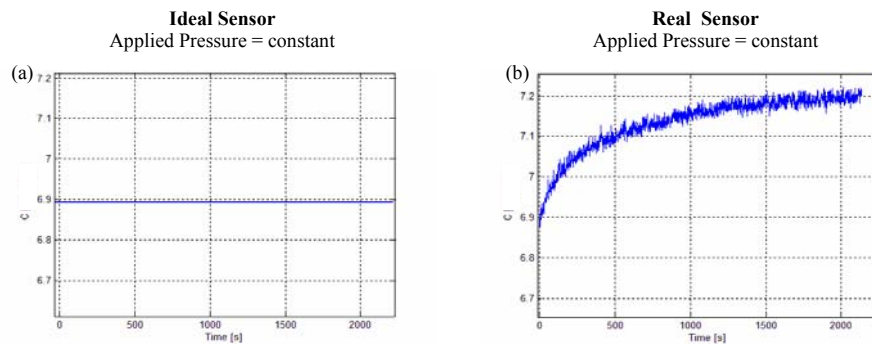
Figure 10.7: Ideal (a), and real (b)sensor response to constant load

The major motivation to obtain a reliable model for the error is to understand how different actions on the geometry and the materials employed in the sensor fabrication could reduce the extent of the

129

viscoelastic response and thus tightening the inaccuracy bounds. In the modelling of creep one should consider that by taking into account the viscoelastic phenomena, the deformation model of a membrane changes from a static, nonlinear, time-invariant model to a dynamic, non-linear, time-invariant model. The viscoelastic behaviour could be modelled introducing time derivatives into the system of partial equations that rule the diaphragm deformation, even if this approach is quite complicated. An effective way to model the viscoelasticity is to introduce a time dependent modulus of elasticity. This kind of approach has already been adopted in the aeronautical pressure sensor to model and set the accuracy limit for pressure sensor [42], but starting from experimental datasheet of Kapton® in which the time variant percentage deformation at difference stress level was reported [43]. Unfortunately Mylar® data concerning creep phenomena were not available, that is why to be able to predict the inaccuracy bound for the Mylar film employed for the nautical sensor, an iterative computational process has been developed. By means of the iterative procedure a time variant Young module inferred from experimental data has been set. The experimental data, useful to get the error model have been collected applying four different constant value pressure to the sensor, respectively 100,150,200,250 Pascal. The pressure load have been held until the capacity value reached the asymptotic value; this happened averaging after 36 minute. Acting in this way the drift capacitance value $\Delta C_{Exp}=f(p(t))$ for each of the four load and for any time interval among t=0 and t=36 minute were available. The fem static model described above has been modified in order to developed the iterative procedure able to figure out the time dependent module of elasticity. The fem static model consist in a mechanical model able to compute the deformed shape of the diaphragm for any pressure load, the output of this module is the input of the electrostatic one able to compute the related capacitance. The fem static model has been modified acting in this way Fig.10.8 starting from the static young module of Mylar®, E_0, for any discrete instant ranging from t=0 to t=36 minute and for the same four pressure load applied in the experiment, the elasticity of the material has been iteratively reduced by an appropriate step quantity ΔE, in this way each new step simulation starts with an elasticity module $E_{trial}= E_0- \Delta E$. For any iteration in time the mechanical fem module evaluates a slightly deeper deformed shape of the membrane ΔW to which a capacity variation ΔC_{Fem} is related. For any time instant and for the four pressure considered the fem capacity variation ΔC_{Fem} is related to the experimental variation ΔC_{Exp} at the instant and pressure considered until the percentage fem error $\varepsilon\%$ is below a preconditioned acceptable level. When the percentage error between the true experimental capacity drift ΔC_{Exp} and the predicted fem capacity $\Delta CFem$ is minimized the related young module E_{trial} is stored for any pressure at any instant
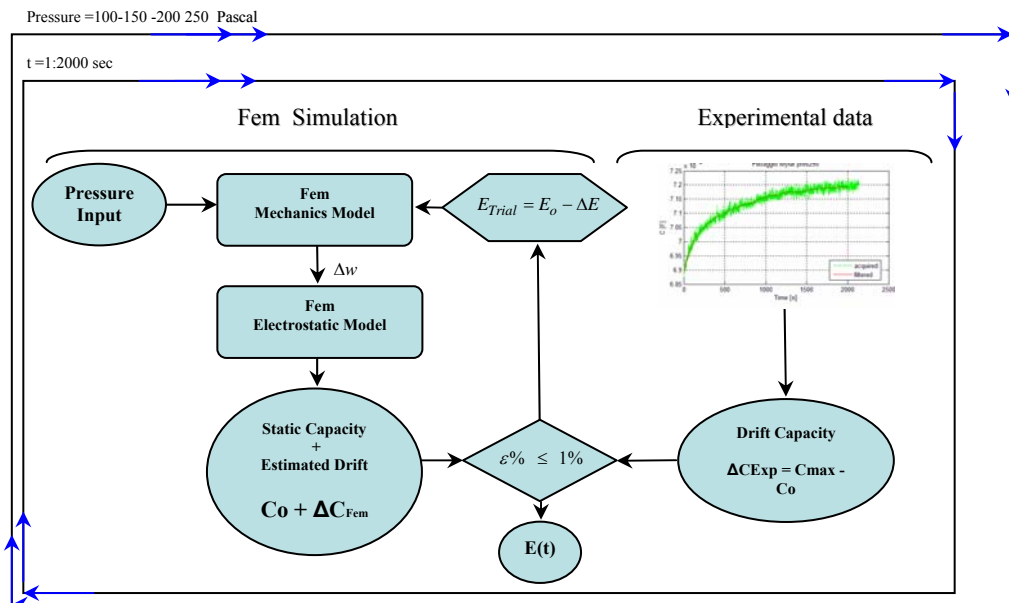
Figure 10.8 : Iterative process diagram

The four fem curves obtained have been fitted minimizing the root mean square difference with a function sum of exponentials and constant Eq. 10.10, where the parameters are representative of the elastic and viscous behaviour of the membrane in particular condition of exerted stress and temperature.

$$E(t) = \sum_i A_i \cdot \exp(B_i \cdot t) + E_{fin} \qquad (10.10)$$

The expressions obtained have been used for time dependent mechanical simulations Fig.10.9.
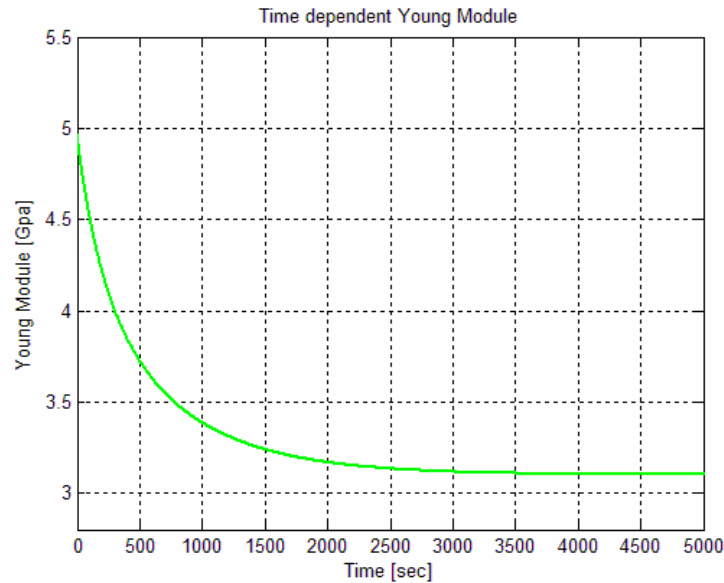
Figure 10.9: Time dependent Young Module

The developed iterative procedure is useful to extract, by means of an experimental test, a relationship able to describe the mechanical viscoelastic phenomena occurring in the membrane. The time dependent deformation transduced by means of the capacitor relation is therefore amplified (or deamplified) according to the initial distance between the plate. The time dependent model of the error and the static model of the sensor are useful tools capable to detect the best trade off between the mechanical error introduced by viscoelasticity, mainly dependent on the radius of the membrane, and the modulation introduced by the non linear relation of the capacitor.

131
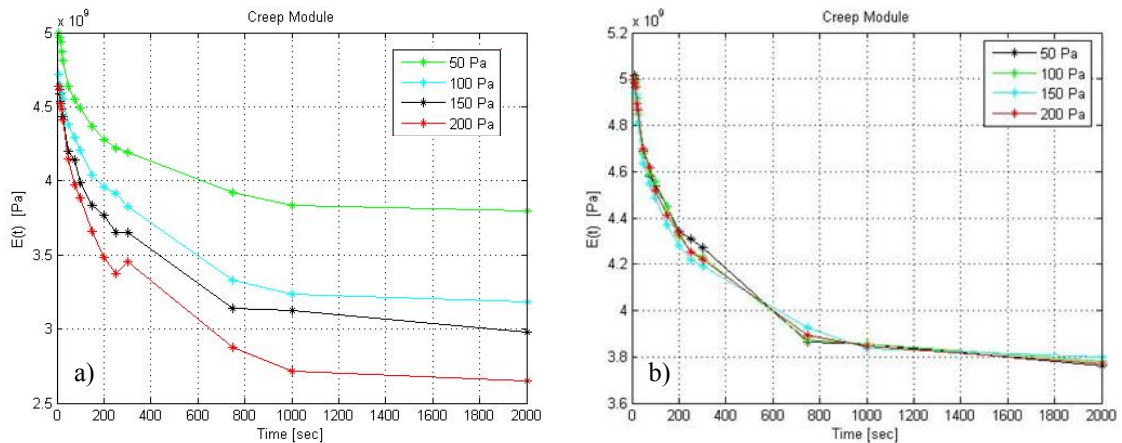
At the end of the process four different function as shown in Fig 10.10 (one for any pressure load) are available to relate the Young module with time. If the iterative procedure is performed with experimental data acquired for an un-pre-stressed diaphragm, four different time dependent creep module are obtained, whereas if it is ran starting from pre-stressed diaphragm experimental data, an unique function for the creep module is obtain being the stress in membrane constant or largely induced by the pre-stress load T. By means of the fem static, and dynamic models is possible to predict the static behaviour and the inaccuracy bounds due to the viscoelastic drift and to extract the value needed in the relation presented in previous paragraph:

$$\frac{E_I - E_F(T)}{E_F(T)} \approx \alpha(T) \tag{10.11}$$

10.4 Electrical sensor design parameters

When the membrane displacement is mapped into a capacitance variation, a further parameter must be considered: the initial distance d_0 between the plates of the capacitor. This parameter is completely uncorrelated to the sensor mechanical response and can be used to alter the ratio between elastic and viscoelastic output, as demonstrated hereafter. Using the expression given in Eq. 10.1, the proportion between capacitance variation due to elastic deformation (ΔC_{el}), and capacitance variation due to creep (ΔC_{cr}), similarly as in Eq. 10.7, is described by the following:

$$\frac{\Delta C_{cr}}{\Delta C_{el}} = \frac{\dfrac{\varepsilon A}{d_0 - w(1+\alpha)} - \dfrac{\varepsilon A}{d_0 - w}}{\dfrac{\varepsilon A}{d_0 - w} - \dfrac{\varepsilon A}{d_0}}, \tag{10.12}$$

where A is the area of the capacitor plate, w the plate displacement and α the ratio obtained in Eq. 10.7. Here, for purpose of demonstration, it is assumed that the displacement due to creep varies linearly with the load P applied, so that the displacement due to creep can be described in percentage of the elastic displacement (generally, numerical simulation could be used to describe accurately the relations between elastic and viscoelastic displacement). Simplifying the common terms in Eq. 10.12, dividing every terms by d_0 and substituting $x=w/d_0$ in the resultant equation, the following can be obtained:

$$\frac{\Delta C_{cr}}{\Delta C_{el}} \Rightarrow f(x) = \frac{\dfrac{1}{1-x(1+\alpha)} - \dfrac{1}{1-x}}{\dfrac{1}{1-x} - 1} = \frac{\alpha(1-x)}{x^2(1+\alpha) - x(2+\alpha) + 1}. \tag{10.13}$$

The variable x is representative of the ratio between the plate displacement and the initial distance between the plates, where it is assumed that w_{MAX} is always smaller than d_0. The previous hypothesis states that the plates will come into contact and that x can only tend to 1. If the limits of f(x) are calculated it is found that:

$$\lim_{x \to 0} f(x) = \alpha \quad \text{and} \quad \lim_{x \to 1} f(x) = +\infty \tag{10.14}$$

The results found in the previous subsections indicate that: creep can not be eliminated by tuning the geometrical design parameters, it can only be reduced. The sensor viscoelastic behaviour is dependent, for a fixed geometry, by the materials used and the part of stresses σ_p induced by the pressure input load, as shown by Eq. 10.7 . Creep can be reduced, for a fixed pressure load, only by decreasing the load dependent stress σ_p induced in the materials by pressure, changing the sensor geometry, thus minimising the variation ΔE_{creep} in the creep modulus Fig.10.5, which is responsible for Δw_{cr} Eq. 10.7. This can be achieved by increasing the membrane thickness h and decreasing its area (proportional to the plate radius a): this also decreases the diaphragm displacement, as clearly stated by Eq 10.3 and Eq 10.5. The transduction step from membrane displacement to electrical capacitance variation, mainly due to its non linear characteristic, can only increase the already existing viscoelastic entity, depending strongly on the quantity x, as shown in Eqs. 10.13 and 10.14. The most favourable condition is achieved when the initial distance between the plates, for a given displacement, is maximum. This occurs when x tends to 0. In doing so, inevitably, the sensor electrical sensitivity deteriorates. For a given geometry and pre-stress level T, fixed the full scale range input and the temperature, the coefficient $\alpha(P,T)= \alpha(P)$ in Eq. 10.7 varies only as function of the pressure input stresses σ_p whose value is influenced by the membrane area A and its thickness h. When A decreases and h increases, the stress lowers and $\alpha(P)$ decreases. Assuming to scale A and h of a factor k with $0<k<1$, α will be scaled by a factor n, with $0<n<1$, due to a lower stress in the material Fig. 10.6 . Substituting the scaled quantities in Eq. 10.12, the following relation is obtained:

$$\frac{\Delta C_{cr}}{\Delta C_{el}}(k,n) = \frac{\dfrac{\varepsilon kA}{d_0 - w(1+\alpha n)} - \dfrac{\varepsilon kA}{d_0 - w}}{\dfrac{\varepsilon kA}{d_0 - w} - \dfrac{\varepsilon kA}{d_0}} \Rightarrow \frac{\dfrac{1}{1 - x(1+\alpha n)} - \dfrac{1}{1-x}}{\dfrac{1}{1-x} - 1} \qquad (10.15)$$

Eq. 10.12 is invariant to the scaling parameter k. While the quantity ΔC_{el} remains the same, the quantity ΔC_{cr} becomes smaller than the one in Eq. 10.15 , due to a factor n induced by a smaller stress σ_p in the material. This demonstrates that, for a fixed value of x, if the stress σ_p in the membrane is reduced, the ratio ($\Delta C_{cr} / \Delta C_{el}$) is decreased. As a summary, it has been demonstrated that in order to reduce the creep contribution, the sensor sensitivity P-C must be reduced both in terms of pressure-deflection characteristic and deflection-capacitance characteristic.

10.5 Design solution

As demonstrated in the previous section, minimising the sensor sensitivity leads to a reduction of the viscoelastic behaviour in advantage of the sensor accuracy. However, another bound is found when the capacitive useful signal produces an output comparable with the electrical noise of the sensor circuit. If we assume Gaussian distributions, in a noisy environment, the error probability P_e in detecting M levels within the signal variation ΔS is given by:

$$P_e = \frac{M-1}{M} erfc\left(\frac{\Delta S}{2\delta_N \sqrt{2}}\right) = \frac{M-1}{M} erfc\left(\frac{SNR}{2\sqrt{2}}\right), \qquad (10.16)$$

where δ_N is the RMS of total equivalent noise in the signal [83]. Applying this theory both to mechanical and electrical behaviour of the sensor in terms of capacitive output (where the viscoelastic output and the electrical noise are both considered as a random noise), a geometrical

trade-off is found, maximising the sensor accuracy by reducing at minimum both creep noise and electrical noise.

10.6 Creep noise

The Boltzmann superposition principle is a useful means of analyzing the creep deformation resulting from several distinct loading or unloading steps of strain or stress [47,49]. Thanks to viscoelasticity the system gains memory: each loading step, appended in the past, contributes to the final response. The above observation implies that in order to know the exact response of a structure subject to creep, a model of its excitation should be available, describing the evolution in time of input stress (or strain). This is normally not possible in many applications where the input loading and its dynamic is unknown. Although the sensor response due to creep, ΔC_{cr} in Fig.10.4 (b), represents an imprecision in the measurement, here is considered as a random noise: the quantity ΔC_{cr} is treated as a random variable superimposed to the elastic sensor response ΔC_{el}. Eq.10.16 can then be used to evaluate the number of detectable levels of pressure, within a certain degree of confidence (DoC) defined as DoC $=1-P_e$, in which the capacitive range can be divided. This yields to the following expression of the SNR:

$$ SNR_{cap} = \frac{\Delta C_{el}}{f(\Delta C_{cr})} \geq \xi \tag{10.17} $$

where ξ is the lower bound for SNR (for example, $\xi = 4.6$ for P_e limited to 1% and M=2, according to Eq.10.16, ΔC_{el} is the sensor signal, due to elastic response, and f(ΔC_{cr}) is the capacitive noise due to creep. The quantity f(ΔC_{cr}) can be defined as:

$$ f(\Delta C_{cr}) = \max(\Delta C_{cr}(P_i)) \quad \text{or} \quad f(\Delta C_{cr}) = \sqrt{\sum_i \Delta C_{cr}(P_i)}, \tag{11.18} $$

where P is the load applied and i is an index which allows to consider different pressure values in the specified range. Since the variation due to creep is not a real Gaussian variable, one can choose to consider it either as the maximum variation induced by a pressure value in a chosen range (thus choosing the worst case) or as a geometrical average of different capacitance variations produced by a set of pressure values in a chosen range. However, if the characteristic pressure-capacitance (P-C) is highly non linear, so leading to a wide range of ΔC_{cr} values with respect to the signal ΔC_{el}, the sensor accuracy will vary non uniformly along the P-C curves and Eq. 10.16 must be applied locally to different working points.

10.7. Electrical noise

Similar considerations can be drawn when an electrical circuit is used to map the range of capacitance in a range of voltage. As an example, an integrated charge amplifier may be used to detect input capacitance variations [84], as shown in Fig. 10.11.

134
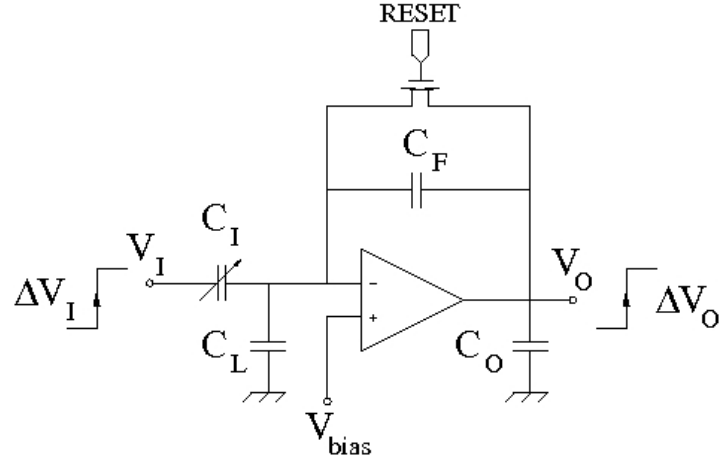
Figure 10.11 : Schematic of an electrical circuit for capacitive sensing. A voltage step ΔV_I at the input produces a voltage step ΔV_O at the output which is proportional to the value of the sensor capacitance C_I.

The following equation describes the circuit:

$$\Delta V_O = \frac{C_I}{C_F} \Delta V_I, \tag{10.19}$$

where ΔV_O is the voltage variation on the output node upon application of input pulses ΔV_I on the circuit inputs V_{IN}, C_I the sensor capacitance measured, C_F the feedback capacitance. The signal that allows distinguishing a pressure applied on the sensor membrane can be expressed as:

$$\Delta\Delta V_O = \frac{\Delta C_I(P)}{C_F} \Delta V_I, \tag{10.20}$$

where ΔC_I is the input capacitance variation due to the applied pressure P. This yields to the following expression of the SNR:

$$SNR_{el} = \frac{\Delta C_I \Delta V_I}{C_F \sqrt{\sum_k V_{kn(rms)}^2}} \geq \xi, \tag{10.21}$$

where the $V_{kn(rms)}$ are the output-referred noise power of different noise sources and ξ is defined as above. This analysis will focus on the intrinsic circuit noise and thus will assume noiseless inputs and power supplies. Assuming a single-pole model, and $C_F \gg (C_I + C_L) / A_0$ (where A_0 is the DC gain of the amplifier stage), the read-out noise introduced by the operational amplifier may be expressed as follows:

$$V_{n(rms)} = \sqrt{\frac{4}{3} \frac{KT}{C_O} \frac{C_I + C_L + C_F}{C_F}} \tag{10.22}$$

where C_L and C_O are the capacitances on the input and output nodes of the operational amplifier, as indicated in Fig. 10.10. Clearly, the intrinsic boundaries for capacitive sensing must be taken into account when choosing the circuit parameters so that $\Delta C_{I\ MAX}$ will produce an output variation $\Delta V_o < V_{DD}$. In this type of circuit, the limit imposed by saturation can be easily overcome by the

135

subtraction of an offset charge as proposed in [84], thus achieving accuracy in the order of tens of aF.

10.8 Discussion

The considerations drawn so far lead to the conclusion that the sensor geometry must be chosen opportunely in order to induce a minimum stress into the pressure sensitive element, thus minimising its creep response. This indicates also that small deflections are preferable to large deflections, lowering the stress in the materials and allowing for a more linear P-C characteristic. As an example, if a circular diaphragm, which bends under the application of an external uniform pressure, is considered, from Eq.10.3 and 10.5, the sensor capacitive behaviour can be described by:

$$C = \varepsilon \int_0^{2\pi} \int_0^a \frac{r}{d_0 \pm w(r,P)} dr d\theta = 2\pi\varepsilon \int_0^a \frac{r}{d_0 \pm w_{MAX}\left(1 - \frac{r^2}{a^2}\right)^2} dr d\theta, \qquad (10.23)$$

where $\pm w_{MAX}$ is the membrane deflection due to positive and negative applied pressure. The capacitive response results in two expressions according to the sign of the deflection. For positive deflections it gives:

$$C = \frac{\pi\varepsilon a^2}{\sqrt{d_0 \frac{3(1-v)^2 Pa^4}{16Eh^3}}} \arctan^{-1}\left(\sqrt{\frac{3(1-v)^2 Pa^4}{d_0 16Eh^3}}\right) \qquad (10.24)$$

and for negative deflections the same expression is obtained where $\arctan^{-1}$ is replaced with $\arctan$. Eqs. 10.22, 10.24 and 10.20 can now be used to evaluate the diaphragm stress, the pressure-capacitance and capacitance-voltage characteristics, where Eqs. 10.17 and 10.21 combined to Eq. 10.16 are used to estimate the number of detectable levels in the capacitive and electrical response, respectively. It must be noticed that, as demonstrated in Eq. 10.15 , the lower the stress in the membrane, the bigger the ratio between ΔC_{el} and ΔC_{cr} and the bigger the SNR_{cap}; Eqs.10.16 and 10.17 allow then for an increased number of detectable levels M when the diaphragm area is decreased and its thickness is increased. Conversely, from Eqs. 10.21, 10.22 and 10.16, the number of detectable levels M increases when the sensor capacitance and its correspondent variation are increased, that is to say when the diaphragm area is increased and its thickness decreased. This set of equations show the geometrical trade-off between viscoelastic and electrical noise behaviour.
In this chapter, a design approach for capacitive pressure sensors affected by creep has been proposed, focusing on the causes that define the mechanical and electrical behaviour of the sensor. The signal output due to creep, superimposed to the sensor response due to the input, deteriorates the output precision, manifesting itself as a drift, dependent on the applied load and on the temperature. The viscoelastic response has been considered as a random noise that can be tuned by the choice of the sensor geometry and the material mechanical properties. The developed method represents a useful means during the design phase in order to estimate the sensor figures of merit.

Chapter 11

Nautical pressure sensor fabrication

11.1 Materials

Standard printed circuit board material layers, were used for assembling the device, providing not only the means for communicating electrically the sensitive units to the read out circuitry through standard lithographic techniques, but especially for achieving the transduction. Polyester layers such as Mylar®, is commonly used for a broad array of applications in the electrical/electronics, magnetic media, industrial specialty, imaging/graphics, and packaging markets and wherever flexible surface with high resistance to cyclic stresses is required. High resistance spray glue were used for assembling the three main part of the sensor (base, spacer and membrane), while the more rigid part of the sensor such as the frame of the sensor were made out of woven fibreglass epoxy layers, which, due to their low thickness and stiffness, guarantee both a low total thicness and a strong frame above which to stretch the sensing Mylar® film.

11.1.1 Epoxy resin

FR4 laminate is the usual base material from which plated-through-hole and multilayer printed circuit boards are constructed. "FR" means Flame Retardant, and Type "4" indicates woven glass reinforced epoxy resin. The laminate is constructed from glass fabric impregnated with epoxy resin and copper foil, which is supplied in different thicknesses proportions usually approximately 18 μm or 35 μm. Foil is generally formed by electrodeposition, with one surface electrochemically roughened to promote adhesion. FR4 laminate displays a reasonable compromise of mechanical, electrical and thermal properties. Dimensional stability is influenced by construction and resin content. Generally, heavyweight glass fabric gives a more dimensionally stable material, although it is necessary to use lightweight fabrics for high layer count multilayer circuits. FR4 DURAVER NEMA 156 (510 μm of thickness with 35 μm copper thickness) laminate was purchased by Photochemie AG (Switzerland).

11.1.2 Mylar®

Mylar® is a biaxially oriented, thermoplastic film made from ethylene glycol and dimethyl terephthalate (DMT). DuPont first introduced Mylar® polyester film in the early 1950s, it has been used in a variety of applications that add value to products found in virtually all segments of the world economy. Its excellent balance of properties and extraordinary range of performance capabilities make Mylar® ideal for a broad array of applications in the electrical/electronics, magnetic media, industrial specialty, imaging/graphics, and packaging markets. Equally important to the versatility of Mylar® is its environmental friendliness. It is one of the most environmentally

137

safe polymer products made today. Mylar® polyester film, only by DuPont Teijin Films, is available uncoated or coated and in a broad variety of gauges and widths.
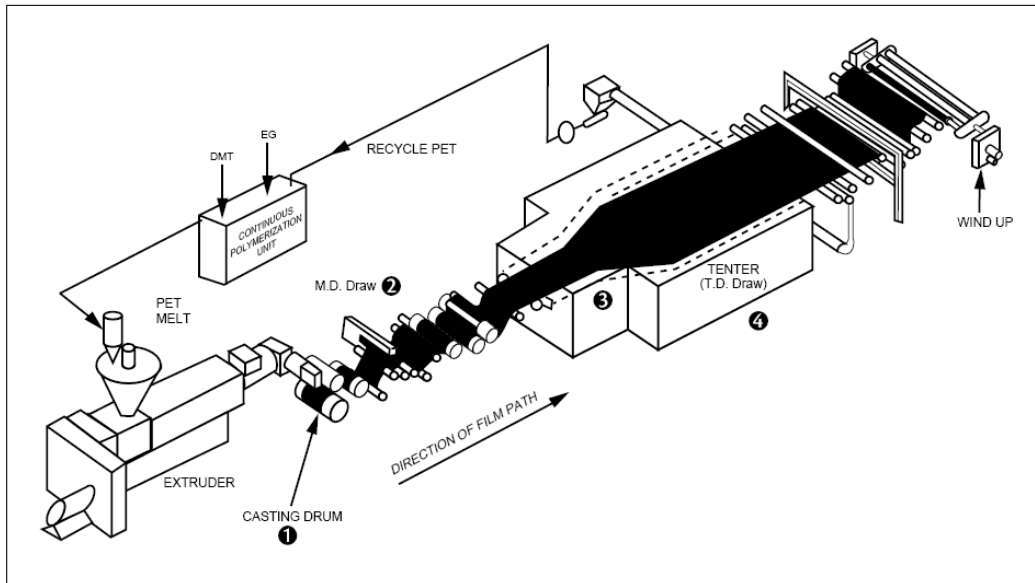
Figure 9.1 : Mylar production process

The production process of Mylar® starts with the extrusion of molten polyethylene terephthalate (PET) polymer onto a chill roll drum to form a film. This film then is biaxially oriented by being stretched first in the machine direction (MD) and then in the transverse direction (TD). The orientation is accomplished by passing the film over rollers that run at increasingly faster speeds (MD orientation), then fed into a tender frame, where it is pulled at right angles (TD orientation). This stretching rearranges the PET molecules into an orderly structure to substantially improve the film's mechanical properties. (Films stretched in the machine direction only are uniaxially oriented; films stretched in both directions are biaxially oriented.) Finally, the film is heat-set to stabilize it. It will not shrink again until exposed to its original heat-set temperature.

11.1.3 Spray Glue

The Scotch-Grip Spray 77 Adhesive is a multi-purpose aerosol adhesive. It is fast tacking and has a long tack range when applied to both surfaces. It is characterised by specific features such as high tensile strength, high shear and peel adhesion, resistance to solvent and moisture, low outgassing and conformability. It is usually employed for bonding a variety of substrates including lightweight boards, foams, plastics, fabric, paper and insulating materials. It is also used for bonding fabric backcloths in studios and window dressing, and bonding polystyrene foam in fabricating packaging units. The adhesive is also widely used in the heating and ventilating industry.

The solvent is a petroleum distillate /cyclohexane its colour clear/pale cream, it shows very good water and UV light resistance but a poor resistance to fuel solvent and oil, this characteristic fit well with the experimental procedures where different pre-stressed membranes where easily glue to the same sensor frame once a quick solvent clean.

138

11.2 Sensor Layers

Four distinct prototypes, differing by dimensions and structures were designed and tested. Since the viscoelastic behaviour was underestimated and a correct procedure was not developed at the very beginning of the project. The first experimental attempts and results were initially useful for validating and optimising the FEM simulation models, however, they main use was for providing a better understanding of the sensor transduction mechanisms from the physical point of view and for shedding new light even on the aspects that regard the parasitic capacitance and the optimisation of the sensor structure and its working principle. The sensing unit consists of a three layer stacked structure: a rigid, copper-clad, glass-fiber base, a rigid, copper-clad, glass-fiber spacer and a 20 μm thick deformable, Mylar® layer as shown in the sketch of Fig. 9.2. Layers were attached to each other by means of either a 5 +/-2 um thick layer of spray glue, patterned in the same shape as the spacing layer.
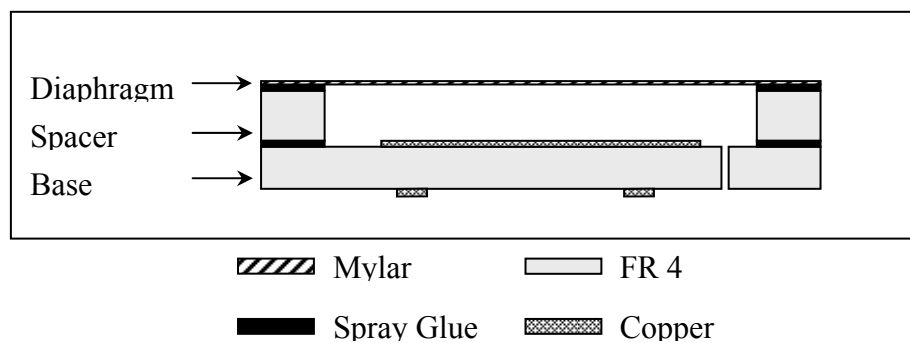
Figure 9.2 : Sensor layers sketch

11.2.1 Base

The base is a three layer sandwich structure; the intermediate layer is glass-fiber while the external ones on both sides are double copper-clad, layers. Base is the bottom part and the thicker layer of the sensing units, and have to guarantee different topics. First of all the base due to its high thickness of 760 um have to act as frame above which the other layers such as the spacer and the diaphragm are glue and pre-stressed. In the upper side of the base, the round fixed plate of the capacitor is realized, and a circular static tap of 1 mm is present Fig. 9.3 (a) The static tap's inner part is copper coated. In this way it leads the pressure inside the cavity of the sensor and lets the electric signal of the fixed plate to be routed to the electrode in the bottom side of the base layer. Moreover not only the copper layer of the upper side is etched but also the glass-fiber inner layer is etched around the square fixed electrode in order to lowering the base-spacer junction surface, this action is crucial to set the initial distance between the plate of the capacitor with a precision of +/-10 um. In the bottom side of the base layer Fig. 9.3 (b) two pads allow the contacts for the two electrodes of the capacitor (movable diaphragm, and square fixed plate) a rectangular guard ring is also present to overcome high parasitic capacitance value. In the rectangular guard ring ten copper connector are realized, to let the sensing unit to be aligned with the static tap pipe and the electric contact of the wireless node. One of the edge of the base perimeter presents a semicircular cut, realized to allows the signal of the conductive membrane to be lead to the bottom side of the base by means of conductive glue, routing the signal through the thickness of the whole unit Fig. 9.3 (a), Fig. 9.3 (b).

139
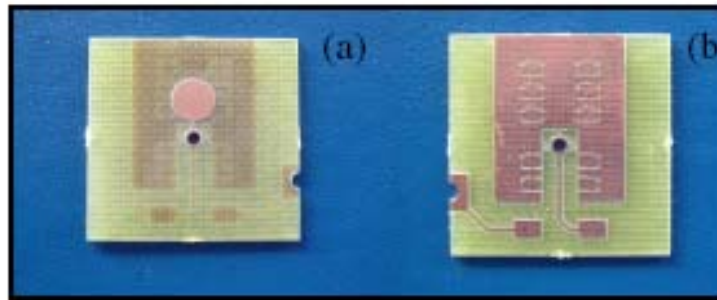
Figure 9.3 : Sensor upper side (a), Sensor bottom side (b).

11.2.2 Spacer

The spacing is the middle layer of the sensing unit as shown in Fig. 9.2 , it is a single fiber-glass planar surface of 125 um; the two sides of the spacer are equal to each others. Principal function of the spacer, is to create the circular cavity in which the diaphragm deflects when pressure loads are applied.
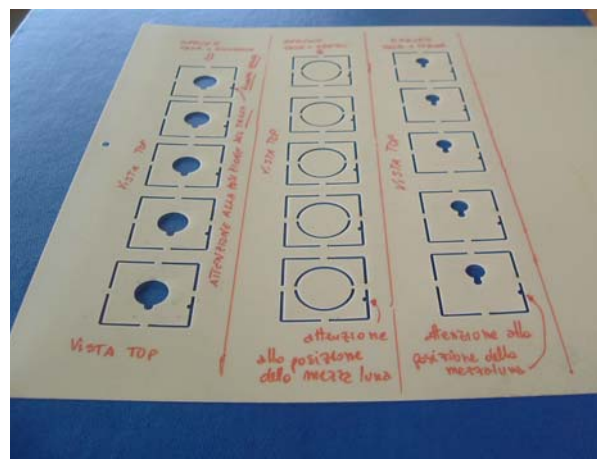
Figure 9.4 : Spacer layers fabricated for different sensor prototypes dimension.

The base-spacer and spacer-membrane junctions are made with special spray glue sprinkled above the surfaces to joint. The most critical aspect of this layer during the assembly process concern with the risk of the liquid glue to penetrate inside the cavity, this event would affect the sensor efficiency both from the electrostatic and mechanical point of view. The presence of glue inside the cavity in fact would alter the dielectric constant of the means between the plate of the capacitor, and would have an effect on the mechanical deflection of the diaphragm inside the cavity. To overcome the two problems, different FR4 shapes, 400 um larger than the cavity of the sensor, have been realized to protect the electrode in the base and the cavity of the spacer Fig. 9.5 (a), (b). The small FR4 shapes are then removed after the sprinkling of the adhesive glue. Also in the spacing one of the edge of perimeter presents a semicircular cut realized to allows the signal of the conductive membrane to be lead to the bottom side of the base through the thickness of the whole sensor.
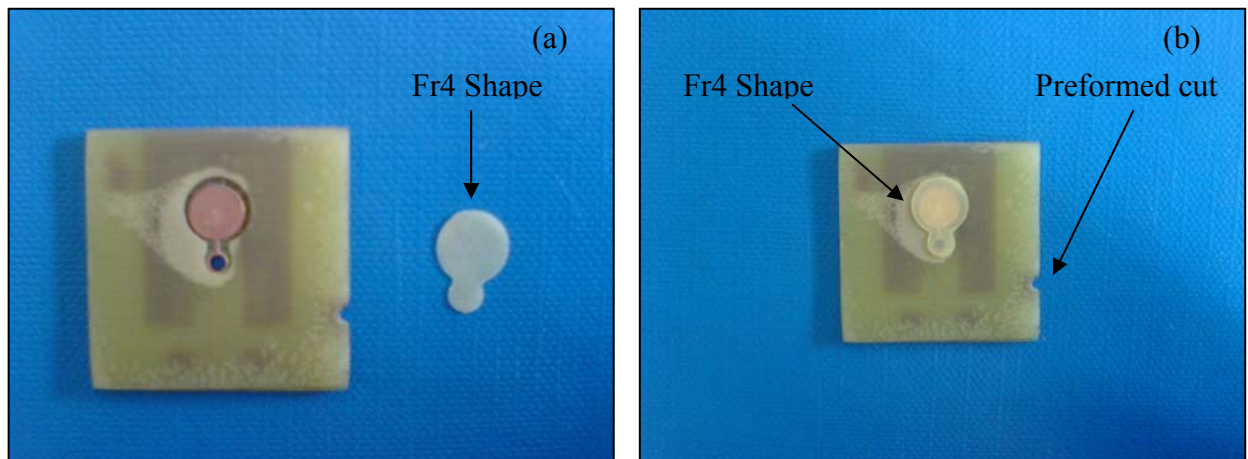
Figure 9.5 : Spacer layers fabricated for different sensor prototypes dimension.

11.2.3 Diaphragm

Mylar is the active layer of the structure it deflects inward and outward the cavity of the sensor, in response to the differential pressure input. The overall sensibility of the sensor is a trade off problem concerning the diaphragm mechanical sensitivity and the modulation of deflection actuated by the capacitor. To be able to improve the mechanical contribution to the overall sensibility of the device, a thin film is required. Others important requirements are : a good dimensional stability, due to low thermal expansion coefficients and resistance to viscoelastic phenomena. Moreover the thin film must be conductive by its nature or able to be coated with conductive coating and nevertheless cheap, to respect the project guideline related to the development of a working macro pressure sensor, realizable with very low economics efforts. Many of the already mentioned features are typical of metals but are more appreciable in special steels which are often employed as sensing element of typical commercial pressure sensors; the only mismatching features is the high manufacturing cost of such thin metal films. A suitable alternative to thin steel film is represented by Mylar, it posses features similar to steel but with a cheaper costs. A wide variety of Mylar are available on market, each one of them have differences in the mechanical characteristics, anyway as indicated in the Dupont Mylar datasheet [1], it is generally not so sensitive to creep. Unfortunately poor data about Mylar viscoelastic behaviour are present in open literature, as consequence an estimation of the viscoelastic behaviour of the thin film is not so easy to be inferred and the inaccuracy bounds of the sensor, largely dependent on these effects, are not predictable with finite element analysis. The particular Mylar chosen for the diaphragm is a Mylar840® type, coated on the bottom side with an aluminium deposition of few Armstrong. The coating let the membrane to be conductive and to operate as the movable plate of the capacitor. The assembly of diaphragm layer is the most critical of the whole fabrication process, this is due to the need of pre-stressing the thin film. The initial stress forced on the film is a key factor in reducing instabilities around the zero pressure loads, and hysteresis along full span pressure input.

11.3 Assembly Methods

11.3.1 Base – Spacer, bonding

Aim of the junction between the base and the spacing layer is to realized the cavity of the sensor, in this phase the concentric assembly of the circular fixed plate and the circular through cut of the spacer must be performed. The second important issue is to avoid glue to penetrate inside the cavity and above the electrode, for these purpose the procedure explained in paragraph 9.2.2 has been followed. The concentric assembly has been performed by means of two precision steel blocks leaned to each other to form a reference square corner Fig 9.6 (a), in this way one of the four corners of the base was leaned to the reference one and after the glue was sprinkled above the upper side of the base, also the spacer layer was leaned to the reference corner above the base Fig 9.6 (b).These easy self alignment of both the edge layers, let the circular cavity and the square copper plate to be concentric.
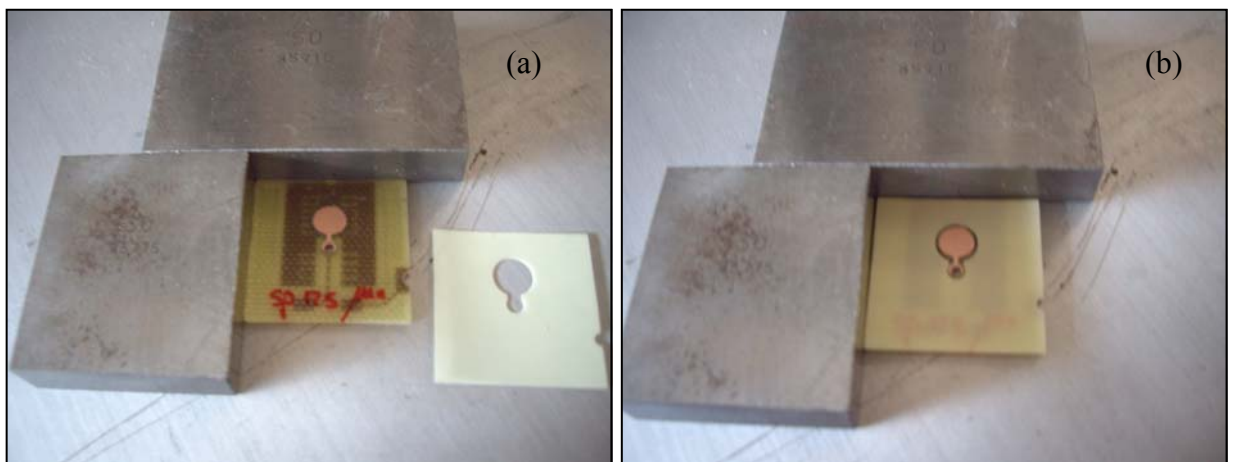
Figure 9.6 : Base self alignment (a), Spacer self alignment (b)
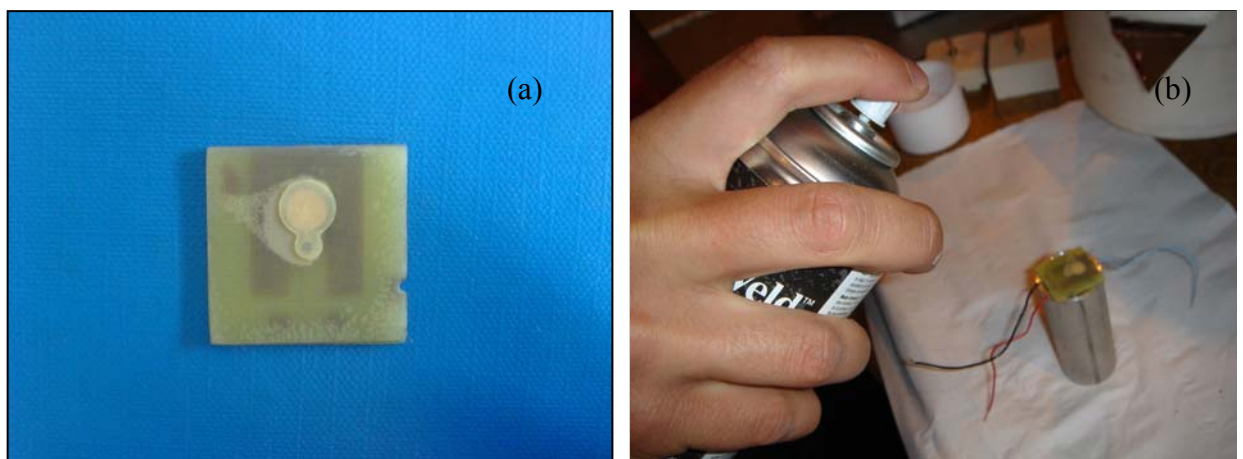
Figure 9.7 : FR4 Glue Shaper (a), Glue sprinkling process (b)

The second issue realized before the alignment procedure is performed by means of an FR4 cavity-shape 400 um larger than the cavity perimeter; the small shape protects the electrode during the

142

glue spraying process, and avoid the glue to penetrate inside the cavity when the adhesion compression load is applied, in Figxx the final assembly is shown. 9.7 (b) and Fig 9.7 (a).
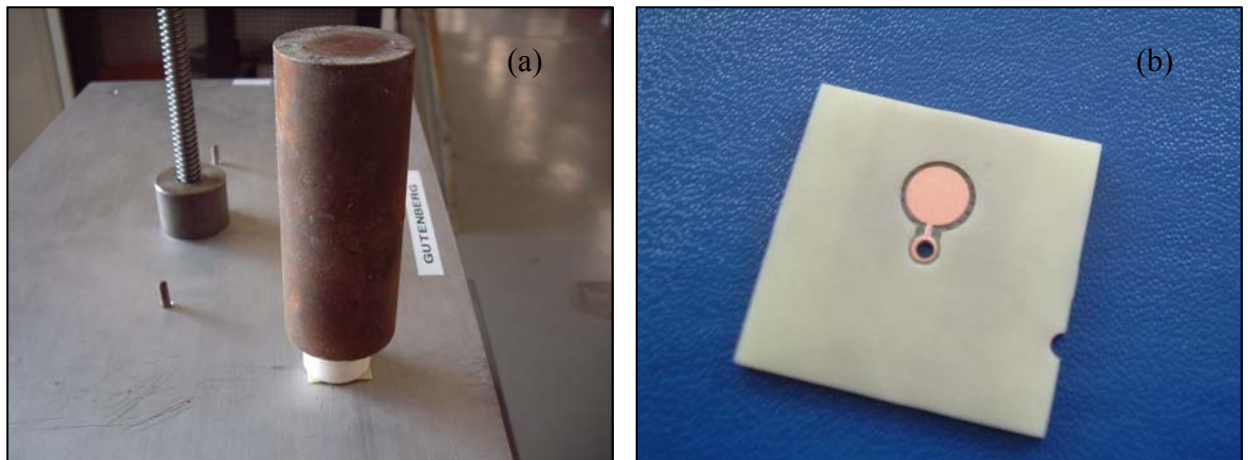
Figure 9.8 : Normal weight to ensure adhesion (a) , Base and spacer Bonded (b)

11.3.2 Mylar – Spacer, bonding

The main critical part of the assembly process is the junction between the membrane and the spacing layer, cause a predefined homogeneous and repeatable pre-stressed level must be forced in order to reduce instabilities of the membrane causing hysteresis error. For the purpose a special pre-tension device has been developed and built. It consist of three different parts : a circular cave cylinder, a circular ring, and a plunger Fig 9.9.
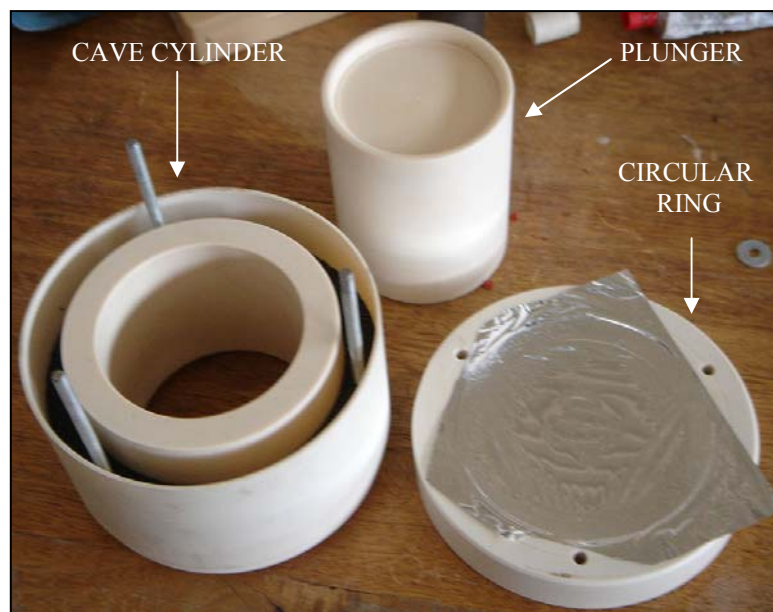
Figure 9.9 : Circular cave cylinder, circular ring, and a plunger

The material used to produce all the above mentioned devices has been manufactured in the laboratories of the faculty. Inside the cylinder a thoroidal cavity is realized to house an amount of lead necessary to let the required tension be imposed Fig. 9.10
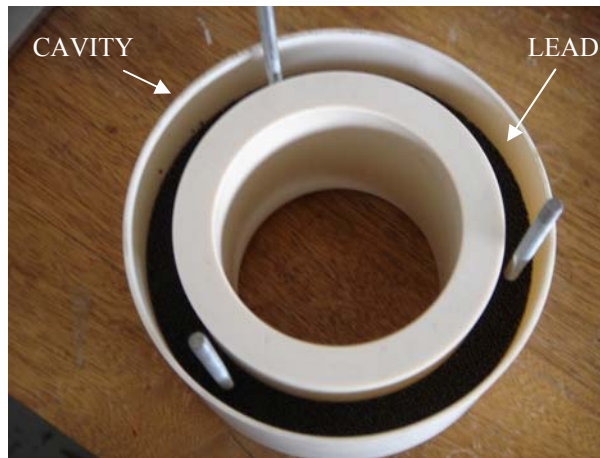
Figure 9.10 : Lead used to impose the pre-stress level in the diaphragm

The assembly routine must be performed with carefully attention in order to guaranty an homogenous and repeatable stress level in the diaphragm. First of all the surfaces to be contact are cleaned and degreased with special cleaner and degreaser to avoid impurity or dirty to affect bonding process. Successively a sheet of Mylar 840 is prepared and pre-stretched by means of a vacuum surface Fig 9.11. By means of an electric tester is necessary to ensure that the non-conductive side of the sheet is the one in contact with the suction surface while the other is free to face the glued spacer surface where it has to be bond.

Figure 9.11 : Mylar sheet above suction surface

At the same time as the air suction is in progress the pre-stretched sheet of Mylar is glued, with a soft adhesive, on the circular ring; this process is used to let the thin sheet surface to be as planar as possible before to be positioned above the cave cylinder which is the device that will impose the required amount of stresses in the diaphragm. Subsequently the Mylar and the circular ring are joint

to the cave cylinder by means of three screws and nuts able to ensure a strong mechanical junction between the circular ring the Mylar sheet and the cave cylinder Fig 9.12.
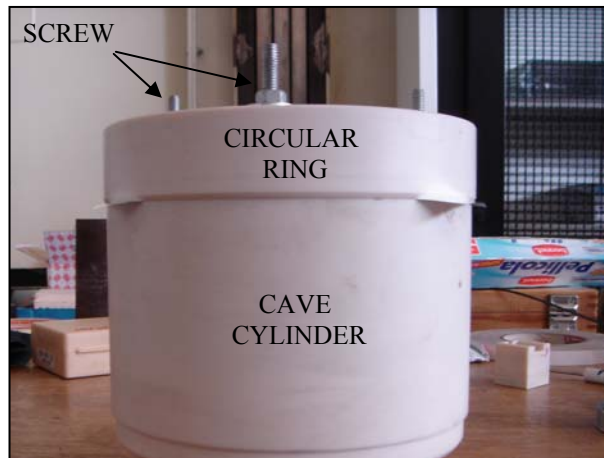
Figure 9.12 : Circular ring and cave cylinder assembled

The two assembled objects shown in Fig 9.10 are then inserted inside the plunger along which vertical translation is allowed.

Figure 9.13 : Circular ring and cave cylinder leaned on the plunger top

The plunger has been built few centimetre longer than the cave cylinder height, so the cylinder slides along the piston later walls until the diaphragm touches the top of the piston, when this condition is reached the cylinder stops its vertical movement and the gravity force acting on it let the thin Mylar film to be pre-stressed Fig 9.14.

Figure 9.14 : Stretched diaphragm

After this action the cavity of the spacer is protected by means of the small shape used in the base-junction and the spray glue is sprinkle over the upper side of the spacer. This action performed before the glue spraying process is fundamental to avoid the glue to penetrate inside the cavity when the adhesion compression load is applied. The small protection shape is then removed and the sensor frame is leaned on the stretched diaphragm. Fig 9.15
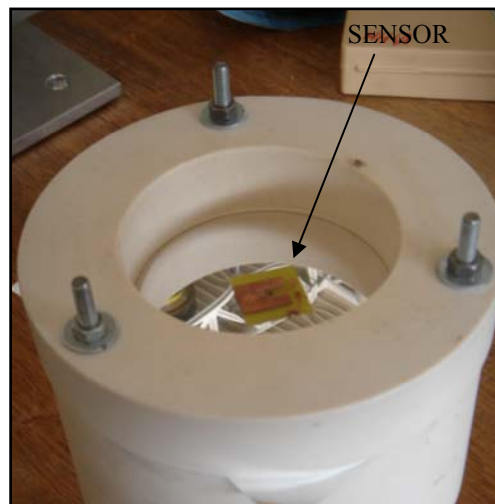
Figure 9.15 : Diaphragm bonding process

Above the bottom part of the base a known weight acts a normal compression stress on the layers to ensure the layer bonding Fig. 9,16. At room temperature, approximately 50% of the ultimate adhesion strength will be achieved after 30 minutes and 100% after 10 hours.
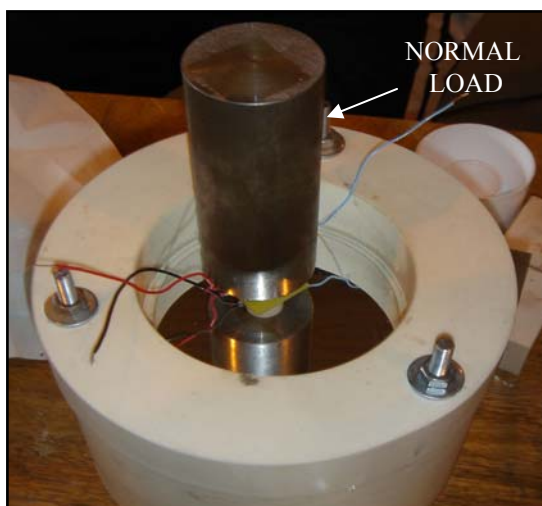
Figure 9.16 : Normal weight to ensure adhesion

When the bonding process is completed a special conductive epoxy CW 2400 is applied in the through cut, shown in Fig 9.3 (b), to let the electric signal of the membrane to be lead through the thickness of the sensor to the relative electrode in the base of the sensing unit. The conductive glue requires, at room temperature, 4 hours to reach the ultimate strength and a low electric resistance.
In the end the weight used to impose the normal action to reach the adhesion of the layers is removed and the Mylar film in excess around the sensor edges is cut away by means of a cutter. The final assembled sensor is shown in Fig. 9.17.
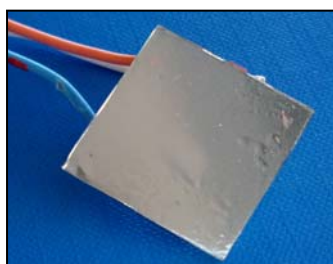
Figure 9.17 : Sensing unit assembled

In Table 5.1 the overall geometrical characteristics of the fabricated prototypes are presented.

	Type 1	Type 2	Type 3	Type 4
With	24 mm	24 mm	24 mm	24 mm
Length	24 mm	24 mm	24 mm	24 mm
Cavità Radius	5 mm	3 mm	5 mm	3 mm
Spacer Thickness	110 um	110 um	75 um	75 um

Table 9.3 : Fabricated prototypes dimension

Chapter 12

Experimental set up and results

Experimental tests have been performed in order to estimate the actual behaviour of the sensor and to validate the fem tool capacity to predict the transduction characteristics of the device. The experimental program have been entirely performed in the laboratory of the Second School of Engineering of the University of Bologna. Two types of analysis were set up. The first test is intended to assess the static characteristic of the sensor and the effect of the pre-stress tension in the transduction chain, while the second was set up to investigate some critically issues emerged from the first run of test in which problems concerned with viscoelastic drift and instabilities of the membrane close to low value of pressure input were observed.

12.1 Experimental setup

The setup, shown in Fig. 12.1, was build in order to perform the previously cited tests and it is composed of a wind tunnel, a Pitot tube, sealed chambers for applying loads independently on the sensor membranes, a conventional silicon-based pressure transducer, an LCR meter, the read-out electronic circuit and a Labview interface control system. In order to apply different pressure values on the membranes, a system composed of a wind tunnel and a Pitot tube was used.
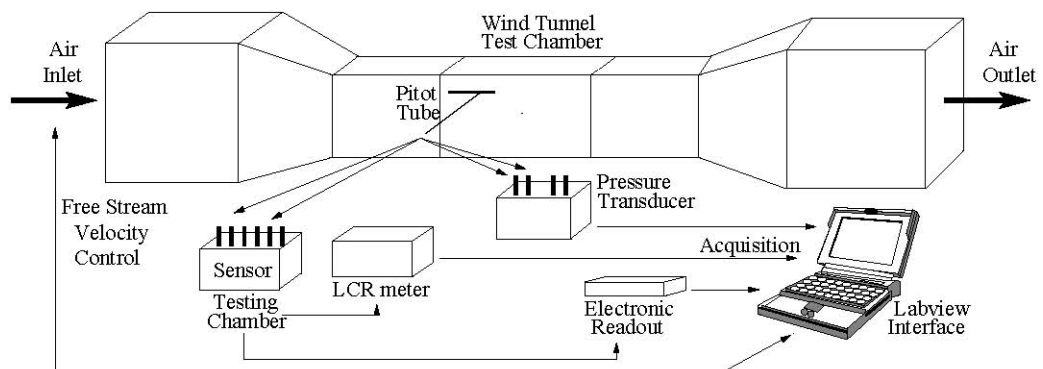
Figure 12.1 : Experimental set up

Low pressure values, such as those in a range of units to hundreds of Pa, are very difficult to obtain statically acting on small volume variations because of the temperature drift and of the pressure waves propagation, which create instabilities in the resulting thermodynamic pressure. This problem was avoided by using, as a referenced applied load, the dynamic pressure obtained from a Pitot tube inserted in the wind tunnel test chamber. Varying the wind tunnel free stream flow velocity, various pressure values can be achieved as the difference between the static pressure and the total pressure, as represented in Fig. 12.2.

148
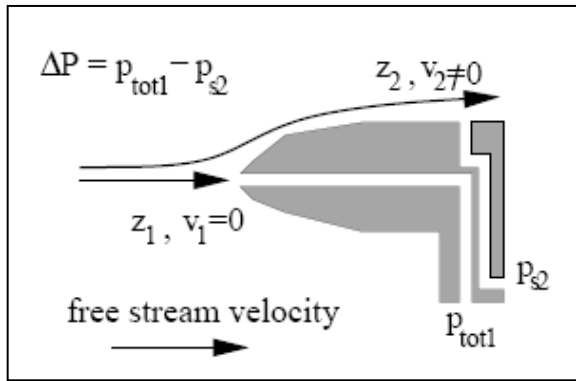
Figure 12.2 : Pitot tube

$$\frac{V_2^2 - V_1^2}{2} + g(z_2 - z_1) + \frac{P_2 - P_1}{\rho} = 0 \tag{12.1}$$

$$P_{Tot} = P_1 = P_\infty + \frac{V_\infty^2 \rho}{2} = P_2 + \frac{V_2^2 \rho}{2} \tag{12.2}$$

Eq. 12.2 states that $P_1 = P_{Tot}$ and $V_2 = V_\infty$ and that by changing V_∞ in the wind tunnel, several pressure values can be obtained by the difference between $P_1 = P_{Tot}$ and $P_2 = P_\infty$ which represent the dynamic pressure of the flow :

$$\Delta P = \frac{V_\infty^2 \rho}{2} = \frac{V_2^2 \rho}{2} \tag{12.3}$$

For these experimental tests, in order to apply several constant differential pressure values on sensor's membrane, a sealed device with two air proof chambers was realized Fig 12.3.
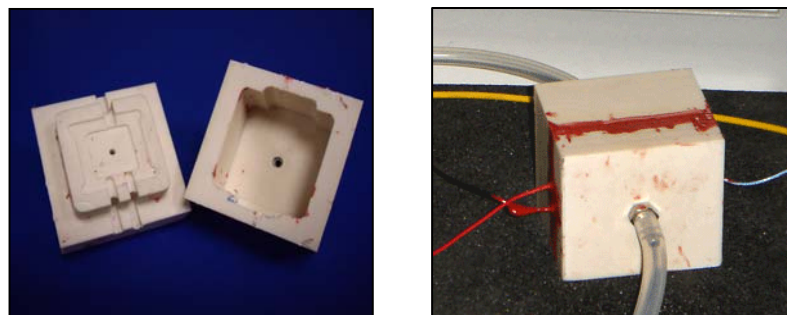
Figure 12.3 : Air proof device

One of the air proof chamber was linked to the total tap of the Pitot tube the other to the static one; in this manner the diaphragm was loaded with the difference of the static and total pressure, therefore the dynamic pressure of the flow. One of the air proof chamber was linked to the total tap of the Pitot tube the other to the static one; in this manner the diaphragm was loaded with the difference of the static and total pressure, therefore the dynamic pressure of the flow. A conventional silicon pressure transducer, a Setra® Capacitive pressure sensor, connected to a National Instrument acquisition board, is used for measuring the pressure associated with the wind tunnel free stream velocity imposed by a dedicated control pad Fig. 12.4.

149

Figure 12.4 : Setra® pressure transucer , Control pad

Data acquisition was performed by mean of a LCR meter and by mean of a capacitive sensitive electronic circuit. The LCR meter is used for measuring directly the capacitance values in order to assess the accuracy of the characteristic evaluated by the theory and by the FEM simulations Fig 12.5. Data have been sampled by a National Instrument PCI-6070E High Performance 1.25 MS/s 12-bit multifunction acquisition board, controlled by a Labview program, written in order to rule automatically the whole setup so far described.

Figure 12.5: Lcr meter

12.2 Static characteristic measurements

The static characteristic of any of the fabricated prototypes has been performed. A set of different constant pressure values were exerted on the sensor membrane, each value being applied for about sixty seconds , by mean of the sealed device shown in Fig. 12.3. The static sensor experimental characteristic is thus obtained and compared with static simulations, in Fig. 12.6 the fabricated prototypes, named Type 4 with the geometrical characteristic specified in table 12.1 and a pre-stress level of 2.8 Mpa, is shown.
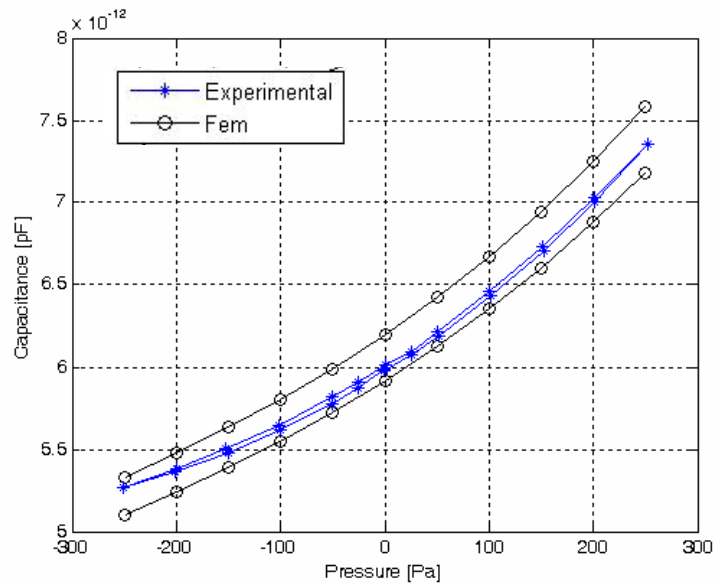
Figure 12.6: Experimetal characteristic – Fem haracteristic

The experimental acquired capacitance signal (blue line) is in good agreement with the FEM static model (black line). The experimental characteristic lies within the two fem bound computed taking into account the geometrical dimensional tolerance of +/- 30 um due to the uncertainty in the thickness of both PCB spacer layer and the glue employed in the bonding process. Defects from the nominal simulated dimensions affects the curve in terms of initial conditions and capacitance variations, because of the non linear relation concerning pressure load and deflection and the hyperbolic relationship describing the capacitance with respect to the distance between the plates. The experimental curve is compose by two closely spaced curves, this is due to the experimental characteristic affected by a certain level of hysteresis as shown in Fig 12.6.
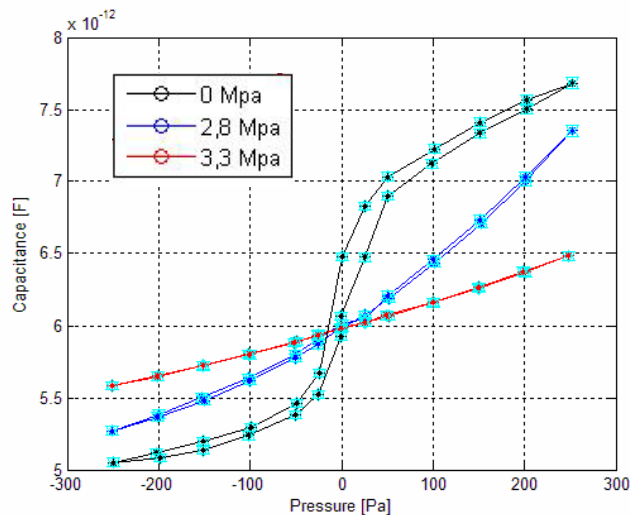
Figure 12.7: Experimetal characteristic for three different pre-stress level

The Mylar diaphragm of the Type 4 prototype sensor discussed above has been assembly with different pre-stress load σ_T, by means of known amount of lead, in order to observe the behaviour of the static characteristic as function of different parameters : mean sensibility, accuracy, percentage hysteresis and the ability of solder glue to keep the required tension in the diaphragm. In Fig12.7 three static characteristics related to three pres-stress loads imposed are presented. As already observed in FEM simulations reported in chapter 9, as the pre-stress load σ_T increase, the

151

transduction function lose its typical highly non linear shapes, cause the displacement became comparable to the thickness and the behaviour of the diaphragm tends to the one of a thin plate subjected to small deflections Fig. 12.7. The linearity error appears as a function of the pre-stress tension and in the performed experiments ranges from 20,96% of FSO with zero pre-stress load to 1.82% of FSO at 2,8 MPa. Increasing the pre-stress load decreases the mechanical sensitivity cause the same pressure input produce a lower output capacitance, the FSO is thus reduce cause the mechanical sensitivity is reduced. A different trend appears if the hysteresis error of the whole cycle and in particular the zero pressure ones is considered. To increase the pre-tension level allow the sensor to manifest a lower hysteresis error at every pressure especially close to the zero pressure input where the percentage error is reduce from 17.34% to 6.49% of FSO. In the absence of initial stresses the thin diaphragm appears to assume different equilibrium shapes depending on the load time history this cause the membrane to present a zero pressure capacity value extremely unpredictable and unrepeatable Fig.12.8.
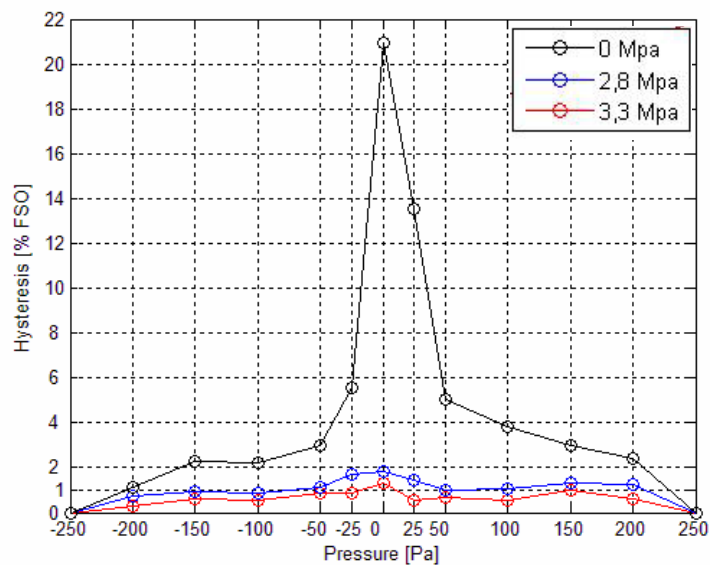
Figure 12.8: Hysteresis vs pressure for three different pre-stress level

Another parameters which is necessary to consider in the trade off process is the ability of the solder glue to keep the adhesion of the diaphragm when subjected to the initial stress and pressure load . In Fig .12.9 a diaphragm stretched with 5.5 Mpa has been tested with several cyclic load within the full scale input, the blue curve relates to the first cycle and present a low sensitivity and the on set of a dead band zone between +/- 50 pascal, causing the sensor to be un-sensitive for low value of pressure. The red line in Fig. 12.9 relates to the fourth cycle of the same sensor and shows how the static characteristic change from the typical linear shape of high pre-stretched diaphragm to the highly non-linear shape of the un-streched ones with great hysteresis in the proximity of the zero input. Experiments on highly pre-stressed diaphragms have shown that for stresses exceeding 5,5 Mpa the solder glue employed is not able to keep the tensions causing lack of long term repeatability or in the worst case the loss of adhesion among diaphragm and solder glue.

152
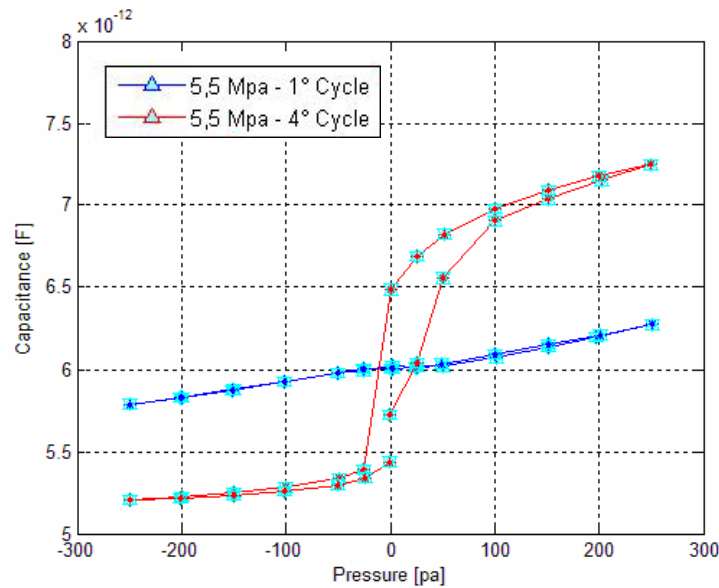
Figure 12.9: loss of repeatability due to lack of adhesion

In Tab.12.1 the hysteresis error, sensitivity, and FSO for the three pre-stress load tested is reported.

Pre-stress Load	Absolute Hysteresis	Percentage Hysteresis	FSO	Mean Sensitivity	Linearity Error
0 MPa	551,58 fF	20,96%	2,63 pF	5,26 fF/Pa	17.34%
2,8 MPa	37,94 fF	1,82 %	2,08 pF	4,16 fF/Pa	12.98%
3,7 Mpa	11,90 fF	1,34%	0,89 pF	1,79 fF/Pa	6.49%

Table 12.1: Static characteristic parameters

Experimental tests have been performed on sensors prototypes with different radius, initial distance between plates and pre-stress level in order to tune the fem static model, and to get parameters useful to infer a first order estimation about the inaccuracy of the sensor due to the viscoelastic phenomena. The geometry of the sensor to be employed in the sensing unit of the wireless sensor network has been chosen as trade off among these parameters to allow a reasonable accuracy an adequate sensitivity, and long term repeatability.

12.3 Creep behaviour experimental result

In order to understand the viscolelastic behaviour of the sensor a series of long term experimental tests has been carried out. The experiments was performed by applying four different steps of constant pressure over the membrane, for the whole time interval required to reach an asymptotic constant value of capacitance output. The four pressure loads imposed in the test procedure was +50, +100 +150 +200 Pascal. The loads chosen are defined positive when the membrane deflect itself inside the cavity of the sensor thus producing the higher value of capacity output. Positive constant pressure loads was chosen cause cause this is the condition where the time dependent

viscoelastic deflection of the membrane is more amplified by the closer distance between electrodes.
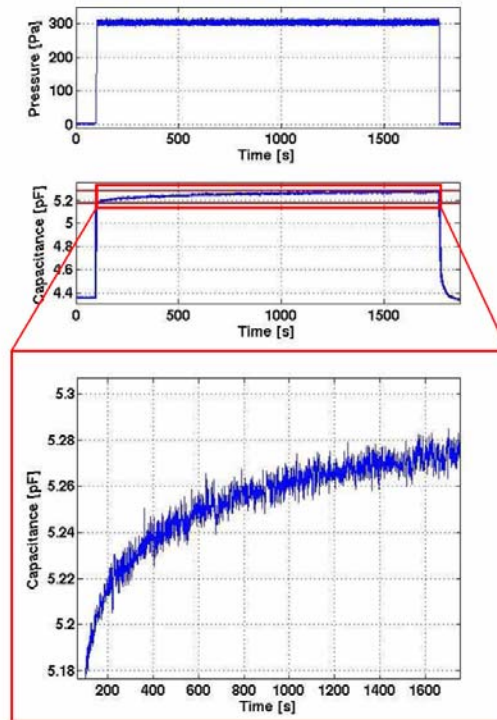
Figure 12.10 : Membrane capacitive response to an applied pressure step of 250 Pa. Twosuperimposed dynamic are distinguished: one, faster, representative of the elastic behaviour of the membrane and one representative of thviscoelastic behaviour of the membrane (enlarged at the bottom).

As represented in Fig. 12.10, it is possible to distinguish two superimposed dynamics: an instantaneous response due to the elasticity of the membrane and a slower one due to the viscoelastic behaviour. In order to simulate the latter phenomenon, a time dependent creep modulus was used, as described in chapter 10. With the iterative procedure describe in chapter 10 a set of experimental testing is required to find out the creep modules parameters describing the mechanical time dependent error evolutions Eq. 10.10: any coefficient can be extracted directly from the results of the procedure for the particular pre-stress level imposed in the fabrication. Thus by means of a series of experimental test with different pre-stress levels is possible to extract the mechanical parameter $\alpha(\sigma_T)$ described in Sec. 10.4. And create a dedicated reference table for every pre-stressed membranes. The experimental data related to a certain numbers of pre-stress level in the membrane and the creep modules inferred by means of the iterative FEM procedure represents a means through which a more accurate description of the viscoelastic error introduce by the material can be given depending upon the stress present in the membrane. In conclusion coupling the FEM static model and the FEM viscoelastic error model described by the creep module it is possible to find out the better sensor characteristic trade off in terms of cavity radius, initial distance between plate, and pre-stress level, able to minimize the creep dependent error in the whole FSO.

12.3.1 Unstressed diaphragm - Creep results

A series of long term experimental tests have been performed to investigate the behaviour of unstressed diaphragm. As already mention in chapter 11 f unstressed diaphragm are bond to the sensor frame by means of a suction surface therefore a certain low residual stress in the diaphragm is imposed but its magnitude is unknown and unrepeatable. The static Fem model fail to evaluate

154

the membrane behaviour in the proximity of zero pressure input this is due to the un-planar shape form of the membrane, this cause high value of hysteresis error close to zero pressure inputs. Long term experimental test has shown a creep dependent variations of approximately 330 fF resulting in a 17% degradation of dynamic scale in 36 min for a pressure of 250 Pa. Fig. 12.11.
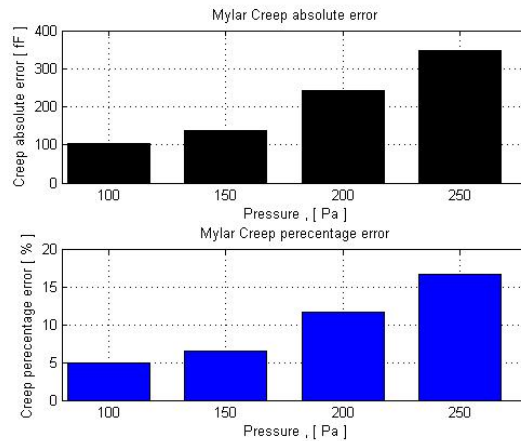
Figure 12.11 : Un-stressed diaphragm: absolute and percentage creep error

It is important to point out that the main error affecting unstressed diaphragm is the un-repetability due to the different unplanar shapes assumed whenever the zero pressure input is crossed as shown in Fig. 12.8.The experimental data acquired in the long term tests have been feed inside the iterative procedure to infer the creep time dependent module describing the mechanical error model of the diaphragm. The creep module provided as output of the procedure Fig. 12.12 shows how for the four pressure input applied four different module are computed, in particular the higher is the pressure load thus the mean stress in the membrane the higher is the module degradation in the time interval.
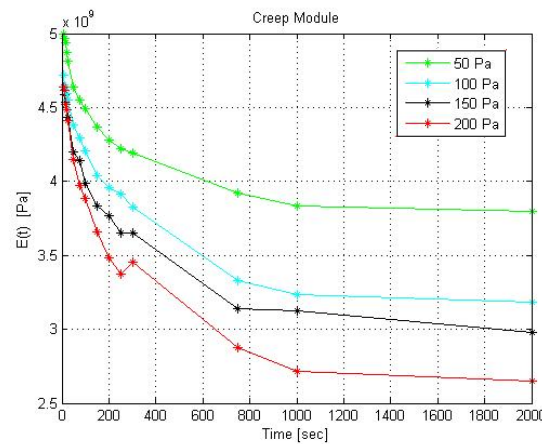
Figure 12.12: Time dependent creep modulo for un-stressed diaphragm

Finally if the fem static model and the associated viscoelastic time dependent error model are compared with the experimental acquisition is possible to point out how the static model fail to estimate the sensor behaviour for the lowest pressure input both in terms of trend and absolute value. For higher values of pressure input the static model function match the slope of experimental data but the still fail in evaluate the capacitance output value.

155
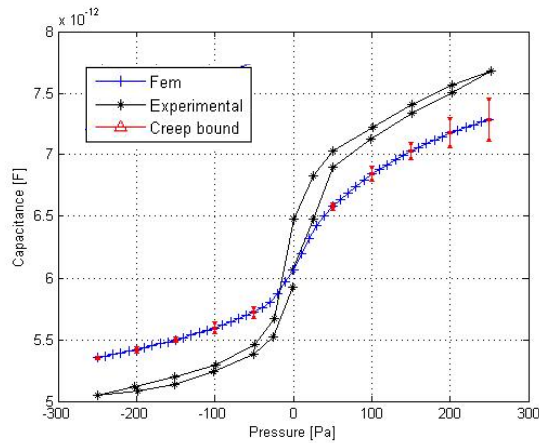
Figure 12.13: Un-stressed diaphragm : Fem static model, Creep Fem estimation, Experimental characteristic

As far as the error bound predicted by the viscoelastic model they appear to underestimate the experimental error bound.

12.3.2 Stressed diaphragm - Creep results

The behaviour of sterssed diaphragms have been also investigated. By means of the device described in chapter 11 , a repeatable pre-stress level was imposed, the actual magnitude of the pre-stress levels has a certain degree of uncertain if compared with the analitycal calculated value Eq. 9.3 , this is mainly due to mechanical frictions induced by the pre-stress device. When a certain pre-stress level is imposed to the diaphragm the fem static model is able to reproduce with sufficient accuracy the experimental behaviour, both in terms of trend and capacity output values. . Long term experimental test has shown a creep dependent variations of approximately 135 fF resulting in a 6.3% degradation of dynamic scale in 36 min for a pressure of 250 Pa. Fig. 12.14.
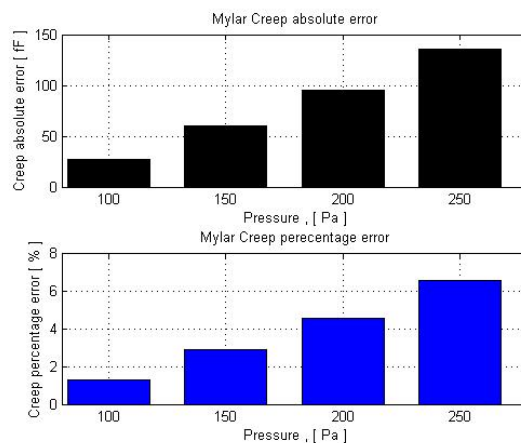
Figure 12.14 : Pre-stressed diaphragm Time dependent creep modulo for pre-stressed diaphragm

Also the experimental data acquired in the long term tests for stressed diaphragms have been feed inside the iterative procedure to infer the creep time dependent module. The creep module provided as output of the procedure Fig. 12.14 shows how for the four pressure input applied the four function associated with the four module are, within the experimental acquisition error,

superimpose, this behaviour, as exposed in chapter 10, is due to the large magnitude difference between stresses induced in the fabrication process and those related to the pressure input load, this aspect let the senor plate to work for the whole full scale input in the fabrication pre-set stress level.
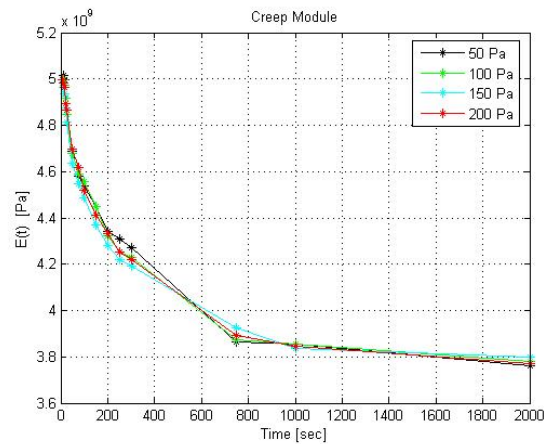
Figure 12.15 : Time dependent creep module for stressed diaphragm

If the experimental characteristic is observed is possible to appreciate how the high hysteresis value associated with the unstressed diaphragm disappears. The fem static model reproduce the experimental shape and is able to predict the reduction of sensibility and full scale output due to the new behaviour of the diaphragm, acting no more as a membrane with a maximum displacement six or seven times the thickness of Mylar but as a plate for which the maximum displacement doesn't exceed the thickness of the plate.
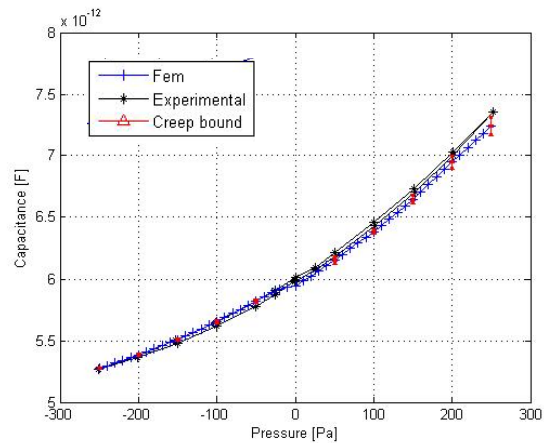
Figure 12.16 : Pre-stressed diaphragm : Fem static model, Creep Fem estimation, Experimental characteristic

If the error bound predicted by the viscoelastic model are superimposed to the fem static model and compared to the experimental uncertainty due to the actual viscoelastic behaviour it is possible to see how the fem error bound slightly overestimate the actual error Fig 12.16. The reported data concern with the best sensor geometry and pre-stress level, provided as output of a numerical campaign performed by means of the static Fem model and viscoelastic error model inferred by means of data acquired through four pre-stress experimental tests.

Conclusion

A differential pressure sensing unit implemented in a wireless sensor network has been developed fabricated, assembled and tested. The sensor designed for aerodynamic applications is capable to operate in the weak pressure field acting on a sail plan. The device is targeted to detect the differential pressure acting between the leeward and windward side of the sail in a full scale input of +/- 250 Pascal.

A fem static model of the sensor has been realized by means of a static non linear coupled model able to predict the mechanical deformation of the membrane an the related capacitance change induced between the two plate of the capacitor, the model was refined in successive iterations by means of a first run of experimental data acquired on sensor prototypes. In the Fem static model the pre-stress tension induced in the fabrication process has been implemented as boundary condition. The Fem static model is a suitable tool to predict different topics concerning the sensor characteristic, as the mechanical and electrostatic sensitivity, potential conditions of saturation, dead band zone, full scale output sensitivity and resolutions. By means of the fem static tool is then possible to choose the appropriate geometrical dimension in terms of radius and initial distance between plates, that better suite to the pressure field the sensor will have to face. Anyway the static fem model is not useful to estimate the error of the sensor in terms of accuracy and repeatability, this problem is due to the non linear and viscoelastic time dependent behaviour of the thin Mylar® diaphragm. To be able to estimate the inaccuracy bound associated to any of the geometry tested with the static model, a time dependent model of the error affecting the diaphragm is necessary. Unfortunately poor data concerning the creep behaviour of Mylar® are available in open literature or technical datasheet, that's why has been necessary to develop an iterative numerical procedure able to extract this data and to infer a time dependent error model to predict the imprecision of the device, introducing in the fem static model, a time dependent parameters to reproduce, with a certain degree of confidence, the inaccuracy bounds related to the pressure input. Both the fem static model and the time dependent error model have been used to choose among many potential geometries for the sensor; finally the one associated with the better trade off , in terms of   sensor figure of merits parameters, has been chosen.

A fabrication procedure has been developed to procedure and to assembly the single layers of the sensor. Moreover a dedicated assembly device able to guaranty an homogenous and repeatable stress level in the diaphragm has been developed and fabricated. The ability to confer to the diaphragm a known and repeatable pre-stress level is a key factor in reducing the diaphragm instabilities close to low pressure input, but also a parameters to chose as trade off with respect to sensitivity. The pre-stress tension associated with the best sensor prototypes tested results of 2,8 Mpa. Two kinds of experiment has been performed and discussed, the former aimed to examine both the ability of the fem static model to predict the experimental static transduction characteristic, the latter, targeted to investigate the long term viscoelastic drift of the stretched diaphragm, and to acquire the necessary experimental data to be set in the numerical iterative procedure, exploit to infer the dynamic error model of the diaphragm. Comparison between the fem static prediction and the experimental characteristic behaviour are reliable for pre-stress level greater than 0,65 MPa, for lower value of pre-stress the fem model fail to estimate the shape of the transduction characteristic around the lower pressure input, due to instabilities of the diaphragm. For pre-stress value higher than 0,65 MPa the fem model gains its prediction ability, and also inaccuracy error bounds are well estimated by the fem error model. Experimental tests has shown that the higher pre-stress level

reachable with the adhesive glue employed in the fabrication is 5,5 Mpa, beyond this value the diaphragm adhesion is not affordable. The geometry associated with the type 4 sensor (see chapter 11), for a pre-stress level of 2,8 Mpa has shown, as predicted by the fem tool, a mean sensitivity of 4,16 fF/Pa with a FSO of 2,08 pF with an hysteresis error of 1,82% FSO, and a non linearity error of about 13%. Long term experimental test has shown a creep dependent drift of approximately 135 fF resulting in a 6.3% degradation of dynamic scale in 36 min for a pressure of 250 Pa.

Whereas experimental test conducted on the same geometry but with the absence of pre-stress has shown a higher mean sensitivity of 5,26 fF/Pa with a FSO of 2,63 pF with an high hysteresis error of 20,96% FSO for null pressure input, and a non linearity error of about 17,34 %. Long term experimental test has shown a creep dependent drift of approximately 330 fF resulting in a 17% degradation of dynamic scale in 36 min for a pressure of 250 Pa. On the basis of experiences gained in modelling such devices a design approach for capacitive pressure sensors affected by creep is also described and proposed, (chapter 10) focusing on the causes that define the mechanical and electrical behaviour of the sensor. The developed method represents a useful means during the design phase in order to estimate the sensor figures of merit.

Finally the layout of nodes in the network has been set and instrumented battens able to house any nodes have been developed and fabricated. Any nodes is fabricated to ensure the sensing unit to be set in the instrumented battens and to let the sensor not to be affect to the battens curvature and strain. The numbers of nodes in any battens are concentrated close to the mast (leading edge) and close to the leech (trailing edge) according to the typical pressure distribution. Each node of the battens is 90 mm long and 30 mm width and just 4 mm thick. Battens are 4 mm width a 4 mm thick while their length varies according to the height at which they are positioned along the mast.

Future works

At present the sensing unit of the Wireless Capacitive Pressure Sensor Network for Nautical applications has been developed and testes by means of air proof device, the next step in the experimentation of such device is to test the system over the surface of a sail model in the wind tunnel. For this purpose a bi-dimensional model of a wing-mast-sail section has been developed. The wing-mast has been chosen to be able to exploit the model for coupled aims. The former is to test the wireless sensor network in a flow field as much as possible similar to the actual one, the latter is to point out the pressure distribution above a sail section equipped with a wing-mast in comparison to a circular mast. At present the bi-dimensional sail profile model is under construction.

159

Bibliography

[1]   S. Callegari, M. Zagnoni, A. Golfarelli, M. Tartagni, A. Talamelli, P. Proli, and A. Rossetti, Experiments on Aircraft Flight Parameter Detection by on- Skin Sensors, Sensors and Actuators A: Physical, in press.

[2]   M. Zagnoni, A. Golfarelli, S. Callegari, A. Talamelli, V. Bonora, E. Sangiorgi, M. Tartagni, A non-invasive capacitive sensor strip for aerodynamic pressure measurement, Sensors and Actuators A: Physical, Vol. 123-124, 2005, pp. 240-248.

[3]   K. E. Petersen, Silicon as a Mechanical Material, Proceedings of the IEEE, Vol. 70, No. 5, 1982, pp. 420-457.

[4]   M. H. Tanielian, N.P. Kim, Pressure belt: an integrated multisensor system, Sensors, Proceedings of IEEE, Vol. 2, 2002, pp. 1182-1187.

[5]   M. B. Cohn, R. Roehnelt, Ji-Hai Xu, A. Shteinberg, S. Cheung, MEMS Packaging on a Budget (fiscal and thermal), Electronics, Circuits and Systems, 2002. 9th International Conference on, Vol. 1, 2002, pp. 287-290.

[6]   Cowles G., Parolini N., Sawley M.L., "Numerical Simulation using RANS-based Tools for America's Cup Design", 16th Chesapeake Sailing Yacht Symposium, Annapolis, Maryland, March 2003.

[7]   Graf K., Wolf E., "CFD investigations and design integration for IACC yachts", High Performance Yacht Design Conference, Aukland, 4-6 December 2002.

[8]   Jones & Korpus, "International America's Cup Class Yacht Design Using Viscous Flow CFD", 15th Chesapeake, Sailing Yacht Symposium, 2001.

[9]   Durbin P., "Separated Flow Computations with the k-_-v2 Model", AIAA J. vol 33(4), 1995.

[10]   Milgram J.H., "Section Data for Thin Highly Cambered Airfoils in Incompressible Flows", NASA CR-1767, July 1971.

[11]   Milgram J.H., "Sail Force Coefficients for Systematic Rig Variations", September 1971.

[12]   Milgram J.H., "Effects of Masts on the Aerodynamics of Sail Sections", Marine Technology, vol. 15(1), 35-42, 1978.

[13]   Milgram J.H., Peters D.B., Eckhouse D.N., "Modelling IACC Sail Forces Combining Measurements with CFD", 11th Chesapeake Sailing Yacht Symposium, 1993.

[14] Milgram J.H., "Fluid Mechanics for Sailing Vessels", Annual Review of Fluid Mechanics, 30, 613-653,1998.

[15] Wilkinson S., "Partially separated flows around 2D masts and sails", PhD Thesis, University of Southampton, 1984.

[16] Wilkinson S., "Static Pressure Distributions Over 2D Mast/Sail Geometries", Marine Technology, vol 26(4),333-337, 1989.

[17] Wilkinson S., "Boundary Layer Explorations Over a 2D Mast/Sail Geometry", Marine Technology, vol 27, 250-256, 1990.

[18] Abbot W.Y.,S.C. SPRING, R.J. Stewart. Flight evaluation of J-Tec VT-100 vectormairspeed sensing system, final report. USAAEFA Proj. No. 75-17-2, May 97

[19] US Army. Final Report 1, USAASTA, Project No.71-30, Flight Evaluation Pacer System, Inc. Loras low airspeed system. March 74

[20] US Army. Final Report 3, USAASTA, Project No.71-30, Flight Evaluation Pacer System, Inc. Lassie low airspeed system. September 75

[21] S.A. Whitmore, Development of a pneumatic high-angle-of-attack flush air data sensing (HI FADS) system, NASA, Memorandum 104241, November 1991.

[22] Myron Kaiton, Walter R. Fried, Avionics navigation system, second edition, E.D. Willey Intrscience , 1996

[23] M.Zagnoni, Mixed Domain Sensor System, Alma Mater Studiorum University of Bologna, March 06

[24] S. P. Timoshenko, S. Woinowsky-Krieger, Theory of plates and shells, second ed., McGraw-Hill International Editions, 1959.

[25] H. Hencky, Z. Math, Uber den Spannungszustand in kreisrunden Platten, Z. Math. Physik., Vol. 63, 1915, 311-317.

[26] Y. C. Shiah, J. H. Huang, Characterization of the Effective Elastic Modulus of an Integrated Sandwich Composite, Journal of Composite Materials, Vol. 37, No. 13, 2003, 1131-1147.

[27] N. G. Mc Crum, C. P. Buckley, C. B. Bucknall, Principles of Polymer Engineering, seconded, Oxford University Press, Oxford, 2000.

[28] DuPont Kapton DataSheets, downloaded at http://www.dupont.com/kapton/.

[29] Encyclopedia of Polimer Science and Engineering, Vol. 9, Mechanical Properties, p. 390, Copyright r 1987, by John Wiley and Sons, Inc.

[30] V. E. Smirnova, N. A. Dolotova, V. I. Aleshin, V. P. Volodin, Study of creep in polyimide film, Polym. Sci., Ser. A 40, Is. 7, 1998, pp. 730-735.

[31] N. Soin, B. Y. Majlis, An Analytical Study on Diaphragm Behavior for Micromachined Capacitive Pressure Sensor, ICSE 2002, IEEE International Conference on Semiconductor Electronics, Proceedings, 2002, pp. 505-510.

[32] J. Moran, An introduction to Theoretical and Computational Aerodynamics, John Wiley and sons, 1984.

[33] H. B. Squire and A. D. Young, The calculation of the profile drag of aerofoils, R. & M., No1838, A.R.C., Technical report, 1938, London.

[34] M. Drela, An Analysis and Design System for Low Reynolds Number Airfoils (Xfoil), Low Reynolds Number Aerodynamics, Springer-Verlag, Lecture Notes in Eng. 54, 1989.

[35] http://www.comsol.com.

[36] A. Becker, Background to Finite Element Analysis of Geometric Nonlinearity Benchmarks, Benchmark Test, NAFEMS, 2000, Sec. 5.2.

[37] W. C. Young, Roark's Formulas for Stress and Strain, 6th edition, McGRAW-HILL, INTERNATIONAL EDITIONS, General Engineering Series, 1989.

[38] M. Zagnoni, A. Golfarelli, P. Proli, S. Callegari, A. Talamelli, E. Sangiorgi and, M. Tartagni, A Non Invasive Capacitive Sensor Strip for Aerodynamics Pressure Measurement, Sensors and Actuators A, Vol. 123-124 (2005), pp. 240-248.

[39] M. H. H. Meuwissen, E. P. Veninga, M. W. W. J. Tijdink, and M. G. H. Meijerink, Design study of a capacitive pressure sensor in non-silicon materials, Proc. IMechE, Part C, J. Mechanical Engineering Science, Vol. 220 (2006), pp. 1633-1643.

[40] M. Pedersen, M. G. H. Meijerink, W. Olthuis and P. Bergveld, A capacitive differential pressure sensor with polyimide diaphragm, J. Micromech. Microeng. Vol. 7 (1997), pp. 250–252.

[41] M.G.H. Meijerink, E. Nieuwkoop, E. P. Veninga, M. H. H. Meuwissen, M. W. W. J. Tijdink, Capacitive pressure sensor in post-processing on LTCC substrates, Sensors and Actuators A, Vol. 123–124 (2005), pp. 234–239.

[42] K. I. Arshak, D. Morris, A. Arshak, O. Korostynska, E. Jafer, Development of a wireless pressure measurement system using interdigitated capacitors, IEEE Sensors Journal, Vol. 7 (2007), pp. 122-129.

[43] Y. Z. Zhu, K. L. Cooper, G. R. Pickrell, A. Wang, High-temperature fiber-tip pressure sensor, Journal of Lightwave Technology, Vol. 24 (2006), pp. 861-869.

[44] T. N. Tun, T. S. Lok, T. C. Jui, R. Akkipeddi, A. Rahman, Contact pressure measurement using silicon-based AlxGa1-xAs semiconductor pressure sensors, Sensors and Actuators A, Vol. 118 (2005), pp. 190–201.

162

[45] N. K. S. Lee, R. S. Goonetilleke, Y. S. Cheung, G. M.Y. So, A flexible encapsulated MEMS pressure sensor system for biomechanical applications, Microsystem Technologies, Vol. 7 (2001), pp. 55-62.

[46] R. A. F. Zwijze, R. J. Wiegerink, G. J. M. Krijnen, T. S. J. Lammerink, M. Elwenspoek, Low creep and hysteresis load cell based on a force-to-fluid pressure transformation, Sensors and Actuators A, Vol. 78 (1999), pp. 74–80.

[47] A. Artndt, Correction for sensor creep in the evaluation of long-term plantar pressure data, Journal of Biomechanics, Vol. 36 (2003), pp. 1813-1817.

[48] J.D. Ferry, "Viscoelastic Properties of Polymers", 3rd ed., John Wiley, N.Y., 1980.

[49] Encyclopedia of Polimer Science and Engineering, Vol. 9, Mechanical Properties, p. 390, Copyrightc 1987, by John Wiley & Sons, Inc.

[50] R. W. Evans and B. Wilshire, Introduction to creep, London, Institute of Materials (UK), 1993.

[51] B. Cai, Q. P. Kong, L. Lu, K. Lu, Low temperature creep of nanocrystalline copper, Materials Science and Engineering, Vol. A286 (2000), pp. 188-192.

[52] Shou-Yi Chang, Yu-Shuien Lee, Ting-Kui Chang, Nanomechanical response and creep behaviour of electroless deposited copper films under nanoindentation test, Materials Science and Engineering, Vol. A423 (2006), pp. 52-56.

[53] R. P. Reed, N. J. Simon, R. P. Walsh, Creep of copper: 4-300 K, Materials Science and Engineering, Vol. A147 (1991), pp. 23-32.

[54] M.A. Menzies, Integrated air data sensors, Aeronaut. J. 105 (2001) 223–229.

[55] F.J. Centolanzi, Characteristics of a $40\circ$ cone for measuring Mach number, total pressure and flow angles at supersonic speeds, NACA, Technical Note 3967, 1957

[56] J. Choisnet, L. Collot, N. Hanson, Method for determining aerodynamic parameters and method for detecting failure of a probe used for determining aerodynamic parameters, US Patent Application 2004/0011124 A1, January 2004.

[57] DSA 3217/3218 Digital Sensor Array (data sheet G511), Scanivalve Corporation, 2003, available at http://www.scanivalve.com.

[58] N.P. Kim, M.J. Holland, M.H. Tanielian, R. Poff, MEMS sensor multichip module assembly with TAB carrier-pressure belt for aircraft flight testing, in: Proceedings of the Electronic Components and Technology Conference, 2000, pp. 689–696.

[59] S.M. Kay, Fundamentals of statistical signal processing Estimation Theory, vol. 1, Prentice Hall, Upper Saddle River, NJ, 1993.

[60] H.A. Eiselt, G. Pederzoli, C.L. Sandblom, Continuous Optimization Models, de Gruyter, Berlin, 1987.

163

[61] H.A. Eiselt, G. Pederzoli, C.L. Sandblom, Continuous Optimization Models, de Gruyter, Berlin, 1987.

[62] A. Crook, M. Gerritsen y AND N. N. Mansour, An experimental investigation of high aspect-ratio rectangular sails, Center for Turbulence Research Annual Research Briefs 2002

[63] Fgfg ZigBee Technology Documents; www.sigbee.org

[64] Min R. and Chandrakasan A.;Top Five Myths about the Energy Consumption of Wireless Communication. Mobile Computing and Communications Review, Volume 7, Number I

[65] Prophet G.;Is ZigBee ready for the big time?;EDN, Agust 2004

[66] Rhee, S.; Seetharam, D.; Liu, S.;Techniques for minimizing power consumption in low data-rate wireless sensor networks.Wireless Communications and Networking Conference, 2004. WCNC. 2004 IEEE Volume 3, 21-25 March 2004 Page(s):1727 - 1731 Vol.3

[67] S.Rhee, S. Liu, An Ultra-low Power, Self-organizing Wireless Network and Its Applications to Noninvasive Biomedical Instrumentation, 2002 IEEE/Sarnoff Symposium on Advances in Wired and Wireless Communications West Trenton, NJ, USA, Mar. 13, 2002

[68] Nicholas Crovatta, " Eyes and easrs every where", EDN, January

[69] Uyiuyi M. Tubaishat, S. Madria.; Sensor networks: an overview , Potential, IEEE volume 22, Issue 2, Apr-May 2003 Page(s):20-23 Digital Object Identifier 10.1109/MP.2003.1197877 .

[70] Torfs, T.; Sanders, S.; Winters, C.; Brebels, S.; Van Hoof, C.; Wireless network of autonomous environmental sensors; Sensor, 2004. Proceeding of IEEE 24-27 Oct. 2004 Page(s):923 - 926 vol.2 Digital Object Identifier 10.1109/ICSENS.2004.1426322

[71] Polastre, J.; Szewczyk, R.; Culler, D.; Telos: enabling ultra-low power wireless research.Information Processing in Sensor Networks, 2005. IPSN 2005. Fourth International Symposium on. 15 April 2005 Page(s):364 - 369 Digital Object Identifier 10.1109/IPSN.2005.1440950

[72] Z-WAVE Developper's kit documentation

[73] Buckley, J.; Aherne, K.; O'Flynn, B.; Barton, J.; Murphy, A.; O'Mathuna, C.;Antenna performance measurements using wireless sensor networks. Electronic Components and Technology Conference, 2006. Proceedings. 56th.30 May-2 June 2006 Page(s):6 pp.

[74] Warren L. Stutzman, Gary A. Thiele Antenna Theory and design. 1981 John Wiley and sons

[75] Smith,K.Antennas for low power applications. RFM, RF Monolithics inc. technical documentation

164

[76] J. Moran, An introduction to Theoretical and Computational Aerodynamics, John Wiley and sons, 1984.

[77] H. B. Squire and A. D. Young, The calculation of the profile drag of aerofoils, R. & M., No1838, A.R.C., Technical report, 1938, London.

[78] M. Drela, An Analysis and Design System for Low Reynolds Number Airfoils (Xfoil), Low Reynolds Number Aerodynamics, Springer-Verlag, Lecture Notes in Eng. 54, 1989.

[79] www.WB-sail.fi

[80] A. Romani, R. Guerrieri, M. Tartagni, N. Manaresi and G. Medoro, Beyond the Microscope: Embedded Detectors for Cell Biology Applications, IEEE International Symposium on Circuits and Systems (ISCAS), 2005, Vol. 3, pp. 2911-2914.

[81] J.D. Ferry, "Viscoelastic Properties of Polymers", 3rd ed., John Wiley, N.Y., 1980.

[82] R. W. Evans and B. Wilshire, Introduction to creep, London, Institute of Materials (UK), 1993.

[83] John G. Proakis, Digital communications, McGraw-Hill, NewYork, 1995.

[84] N.G. Mc Crum, C.P. Buckley, C.B. Bucknall, Principles of Polymer Engineering, second ed., Oxford University Press, Oxford, 2000.